

Uncertainties in millimeter-wave antenna design, modeling and characterization

Citation for published version (APA):

Reniers, A. (2022). *Uncertainties in millimeter-wave antenna design, modeling and characterization: The observer effect*. [Phd Thesis 1 (Research TU/e / Graduation TU/e), Electrical Engineering]. Eindhoven University of Technology.

Document status and date:

Published: 11/05/2022

Document Version:

Publisher's PDF, also known as Version of Record (includes final page, issue and volume numbers)

Please check the document version of this publication:

- A submitted manuscript is the version of the article upon submission and before peer-review. There can be important differences between the submitted version and the official published version of record. People interested in the research are advised to contact the author for the final version of the publication, or visit the DOI to the publisher's website.
- The final author version and the galley proof are versions of the publication after peer review.
- The final published version features the final layout of the paper including the volume, issue and page numbers.

[Link to publication](#)

General rights

Copyright and moral rights for the publications made accessible in the public portal are retained by the authors and/or other copyright owners and it is a condition of accessing publications that users recognise and abide by the legal requirements associated with these rights.

- Users may download and print one copy of any publication from the public portal for the purpose of private study or research.
- You may not further distribute the material or use it for any profit-making activity or commercial gain
- You may freely distribute the URL identifying the publication in the public portal.

If the publication is distributed under the terms of Article 25fa of the Dutch Copyright Act, indicated by the "Taverne" license above, please follow below link for the End User Agreement:

www.tue.nl/taverne

Take down policy

If you believe that this document breaches copyright please contact us at:

openaccess@tue.nl

providing details and we will investigate your claim.

Uncertainties in millimeter-wave antenna design, modeling and characterization

The observer effect

Uncertainties in millimeter-wave antenna design, modeling and characterization
The observer effect / by
A. C. F. Reniers – Eindhoven : Technische Universiteit Eindhoven, 2022 –
Proefschrift

A catalogue record is available from the Eindhoven University of Technology
Library
ISBN: 978-90-386-5509-3
NUR: 959

This thesis was prepared with the $\text{\LaTeX} 2_{\epsilon}$ documentation system
Reproduction: TU/e print-service, Eindhoven, Nederland
Cover design: "Spherical Millimeter-wave Anechoic Chamber" (Thanks to Bart
van Overbeeke, <http://www.bvof.nl/>)
Copyright ©2022 by A. C. F. Reniers. All rights reserved.

Uncertainties in millimeter-wave antenna design, modeling and characterization

The observer effect

PROEFSCHRIFT

ter verkrijging van de graad van doctor aan de Technische Universiteit Eindhoven, op gezag van de rector magnificus prof.dr.ir. F.P.T. Baaijens, voor een commissie aangewezen door het College voor Promoties, in het openbaar te verdedigen op woensdag 11 mei 2022 om 13:30 uur

door

Ad Reniers

geboren te Eindhoven

Dit proefschrift is goedgekeurd door de promotoren en de samenstelling van de promotiecommissie is als volgt:

| | |
|-------------|---|
| Voorzitter: | prof.dr. M. Matters - Kammerer |
| Promotoren: | prof.dr.ir. A.B. Smolders prof.dr.ir. M.J. Bentum |
| Copromotor: | dr.ir. M.H.A.J. Herben |
| Leden: | prof.dr.ir. M.C. van Beurden prof.dr.ir. P.G.M. Baltus prof.dr.ing. A.J.M. Pemen dr.ir. R. Maaskant (Chalmers, electromagnetics) |

Het onderzoek of ontwerp dat in dit proefschrift wordt beschreven is uitgevoerd in overeenstemming met de TU/e Gedragscode Wetenschapsbeoefening.

“The electromagnetic wave propagating through space and time, encountering refraction on its path slowing it down, just to continue, after a brief moment, with incredible speed, diffracting in different directions to end up in self-reflection just to find out that it briefly existed affecting many lives.”

The Observer

This thesis is dedicated to my sons

Owen & Noah.

Contents

| | |
|--|-------------|
| Summary | xiii |
| Samenvatting | xv |
| List of abbreviations | xvii |
| 1 Introduction | 1 |
| 1.1 Introduction | 1 |
| 1.2 Antennas at millimeter waves | 2 |
| 1.2.1 History of the antenna | 2 |
| 1.2.2 Examples of millimeter-wave antennas and applications | 4 |
| 1.3 Classical antenna analysis and design process | 5 |
| 1.4 The essence of measurement | 7 |
| 1.5 The observer effect | 9 |
| 1.6 Antenna design, analysis and measurement process | 11 |
| 1.7 New millimeter-wave anechoic chamber | 14 |
| 1.8 Objective and outline of this thesis | 15 |
| 2 Applying statistical analysis to antenna research and design | 19 |
| 2.1 Introduction | 19 |
| 2.2 Terms and conditions in statistics | 20 |
| 2.2.1 Subareas in statistics | 20 |
| 2.2.2 Level of measurement | 20 |
| 2.2.3 Definition of higher order statistics | 22 |
| 2.3 Probability function | 22 |
| 2.3.1 Probability distribution function versus cumulative distribution function | 23 |
| 2.3.2 Central limit theorem and law of large numbers | 24 |
| 2.3.3 Student's <i>t</i> -distribution | 29 |
| 2.4 Analysis of variance and correlation | 31 |

| | | |
|----------|--|-----------|
| 2.5 | Design process | 33 |
| 2.6 | Creating a reference | 34 |
| 2.6.1 | Modeling process | 35 |
| 2.6.2 | Truncated probability distribution function | 36 |
| 2.7 | Antenna measurement reliability | 37 |
| 2.7.1 | Definition of errors, accuracy and uncertainty | 39 |
| 2.8 | Expressing and evaluating uncertainty in antenna measurement | 41 |
| 2.8.1 | Classification of components of uncertainty | 41 |
| 2.8.2 | Comparing methods for evaluating measurement uncertainty | 43 |
| 2.8.3 | Uncertainty in antenna measurement expressed step by step | 45 |
| 2.9 | Conclusions | 47 |
| 3 | Verifying the simulation model to define an antenna reference | 49 |
| 3.1 | Introduction | 49 |
| 3.2 | Definition of an antenna reference | 50 |
| 3.3 | Verification and validation method of an antenna simulation model | 51 |
| 3.4 | Functional parts of an antenna | 52 |
| 3.5 | Case study 1: linearly polarized rectangular inset-fed microstrip patch antenna | 55 |
| 3.5.1 | Design requirements | 55 |
| 3.5.2 | Outcome of the probabilistic sensitivity analysis | 57 |
| 3.5.3 | Design of the antenna excitation | 61 |
| 3.5.4 | Simulation results of the rectangular inset-fed microstrip patch antenna | 64 |
| 3.6 | Case study 2: Circularly polarized dielectric rod antenna | 70 |
| 3.6.1 | Design parameters | 71 |
| 3.6.2 | Simulation model | 72 |
| 3.6.3 | Simulation results | 73 |
| 3.7 | Summary and conclusions | 78 |
| 4 | Analysis and design of the RF-connector | 79 |
| 4.1 | Introduction | 79 |
| 4.2 | Connected antenna measurement | 80 |
| 4.3 | Case study: Uncertainties in the characteristics of a rectangular inset-fed microstrip patch antenna caused by an RF-connector | 81 |
| 4.3.1 | Various RF-connectors | 81 |
| 4.3.2 | Functional decomposition of a rectangular inset-fed microstrip patch antenna with an RF-connector | 83 |
| 4.3.3 | Illustrating the physical phenomena with help of contour plots | 87 |
| 4.3.4 | Effect of the RF-connector on the antenna characteristics | 90 |
| 4.4 | Analysis of the cause of unwanted radiation | 93 |

| | | |
|----------|---|------------|
| 4.4.1 | Uncertainties caused by transmission line transitions | 93 |
| 4.4.2 | Determining the effect of the unwanted radiation on the antenna characteristics | 95 |
| 4.4.3 | Antenna radiation versus unwanted radiation | 97 |
| 4.5 | New RF probe design | 101 |
| 4.6 | Contactless antenna measurement | 105 |
| 4.6.1 | Determining the input impedance | 106 |
| 4.6.2 | Determining the realized gain pattern | 106 |
| 4.6.3 | Uncertainties and usability of this method | 107 |
| 4.7 | Conclusions and recommendations | 110 |
| 5 | Uncertainties in the measured dielectric properties of solid materials with help of a Fabry-Pérot open-cavity resonator | 113 |
| 5.1 | Introduction | 113 |
| 5.2 | Overview of methods for characterizing dielectric materials | 114 |
| 5.3 | Principle of the Fabry-Pérot open-cavity resonator | 116 |
| 5.3.1 | Condition for a stable Fabry-Pérot open-cavity resonator | 118 |
| 5.3.2 | Different focal distances that meet the stability criterion | 120 |
| 5.3.3 | Development of various Fabry-Pérot open cavity resonator configurations | 121 |
| 5.4 | Design of the Fabry-Pérot open-cavity resonator with spherical mirrors | 123 |
| 5.4.1 | Design parameters of the Fabry-Pérot open-cavity resonator | 125 |
| 5.4.2 | Quality-factor of the unloaded cavity | 126 |
| 5.5 | Derivation of the relative permittivity and loss tangent | 127 |
| 5.5.1 | Determination of the relative permittivity | 128 |
| 5.5.2 | Determination of the loss tangent | 130 |
| 5.6 | Realized Fabry-Pérot open-cavity resonator | 130 |
| 5.7 | Probabilistic sensitivity analysis | 132 |
| 5.8 | Measuring the relative permittivity of air for assessing the measurement significance and accuracy | 136 |
| 5.9 | Causes of uncertainty in characterizing dielectric materials | 140 |
| 5.9.1 | Measurement stability | 140 |
| 5.9.2 | Post-processing the resonance peak in case of a limited number of frequency points | 142 |
| 5.10 | Measured permittivity and loss tangent of PTFE and FR-4 including the combined standard expanded uncertainty | 144 |
| 5.11 | The advantages and disadvantages of using different focal distances to determine relative permittivity and loss tangent | 147 |
| 5.12 | Conclusions | 149 |

| | | |
|----------|---|------------|
| 6 | Conclusions and Recommendations | 151 |
| 6.1 | Conclusions | 151 |
| 6.2 | Recommendations | 154 |
| A | Appendix A | 157 |
| A.1 | Metrological terms used in this thesis [1], [2] | 157 |
| A.2 | Skewness and kurtosis | 162 |
| A.3 | Transformations for skewed data | 163 |
| A.4 | Kernel density estimation | 163 |
| A.5 | Coverage factor k_p with a certain level of confidence p for a limited amount of degrees of freedom v | 165 |
| A.6 | Bootstrap resampling | 166 |
| A.7 | Antenna characteristics | 167 |
| B | Appendix B | 169 |
| B.1 | Patch antenna dimensions | 169 |
| B.2 | Circular polarization | 173 |
| B.3 | Uncertainties affecting the behavior of the circularly polarized rod antenna | 176 |
| B.4 | Misalignment in the layer registration of the PCB | 177 |
| B.5 | Polarization pattern methods | 178 |
| B.6 | Measurement results of the circularly polarized rod antenna | 182 |
| B.7 | Effect of the waveguide port on the realized gain pattern | 185 |
| C | Appendix C | 187 |
| C.1 | Surface waves | 187 |
| D | Appendix D | 189 |
| D.1 | Dielectric material properties and characteristics | 189 |
| D.2 | Optimization of a coupling aperture or iris | 191 |
| D.3 | Relationship between the size of the mirror and the size of the Gaussian beam | 191 |
| | D.3.1 Simulation settings of the Fabry-Perot open-cavity resonator . . . | 192 |
| | D.3.2 Simulation results of the Fabry-Perot open-cavity resonator . . . | 193 |
| D.4 | Amount of q 's with maximum Q -factor per frequency | 194 |
| D.5 | Measurement results of the temperature, humidity and resonance frequency | 195 |
| | Bibliography | 199 |
| | List of publications | 213 |
| | Acknowledgements | 217 |
| | Curriculum Vitae | 221 |

Summary

In the last few decades much progress has been made in new wireless technologies. With the introduction of new standards like, 5G and 6G, the autonomous car for example, becomes a reality. Some necessary features for such an application are low latency and high data rate. The necessary frequency bandwidth can be found at higher frequencies in the so-called millimeter-wave frequency band (>30 GHz). By using the higher frequencies the antennas will become smaller, creating the possibility to integrate them into a system-on-chip or in-package, which on itself are relatively new technologies. With the decreasing size of the antenna and the possibility to integrate them into a complete system, new challenges emerge in both modeling and measuring. The strategy to design and validate antennas at lower frequencies appears to be insufficient at higher frequencies. That is why a different strategy is necessary. Therefore, a more detailed design and experimental validation process is required wherein for each step possible influences are recognized that correlate with uncertainties that affect the behavior of the antenna under test.

This thesis describes the root causes of these influences and uncertainties, shows the impact on the antenna characteristics and demonstrates effective solutions to minimize these. To be able to do so it is necessary to use a statistical framework. Because the use of statistical analysis is not common in antenna research, the statistical terms and conditions are summarized first. Secondly, two design strategies are presented that use statistical tools to quantify the uncertainties in both modeling and measuring a millimeter-wave antenna. With the help of these design strategies, the causes of the uncertainties become clear, which means that possible solutions can be worked out or at least be explained.

The design and validation process that includes environmental influences and uncertainties is tested on two specific case studies. The first case is a linear-polarized patch antenna wherefore analytical equations are used to calculate the proper dimensions. A probabilistic sensitivity analysis simulation is then used to perform a sensitivity analysis on these dimensions to account for manufacturing tolerances such that the effect on the

antenna characteristics is visualized. In the second test case, a circularly polarized rod antenna operating at 60 GHz is studied using a full-wave electromagnetic model to vary input parameters such as dielectric material properties. Both antennas are modeled starting from a basic design without RF-connectors, evolving to more detailed models including different forms of RF-connection. To understand the causes that effect the behavior of the antenna, the RF-connection has been investigated in more detail. A comparison has been made between a coaxial connector, a millimeter-wave probe and a waveguide connection all connected to a same antenna structure.

Another important source of uncertainty in antenna design is formed by the material properties at millimeter-wave frequencies. Since permittivity and dielectric losses are frequency dependent, they need to be determined at the frequency of interest. Most of the time the material properties (permittivity and loss tangent) are unknown or inaccurate at millimeter-waves. As material properties are determining most of the electromagnetic conditions, measuring these properties will be discussed extensively. An in-house developed Fabry-Pérot open-cavity resonator with concave spherical mirrors is developed to determine the material properties at millimeter-wave frequencies. The system has been analyzed with respect to uncertainties caused by, for example, the tolerance on the shape of the spherical mirrors or placing the sample under test repeatedly in the setup.

Conclusions, recommendations and means to enhance the design procedure are addressed in the final chapter of this thesis.

Samenvatting

De laatste decennia is veel vooruitgang geboekt in nieuwe draadloze technologieën. Met de introductie van nieuwe standaarden zoals 5G en 6G, wordt bijvoorbeeld de autonome auto een realiteit. Sommige noodzakelijke functies voor een dergelijke toepassing zijn lage latentie en hoge gegevenssnelheid. De benodigde frequentiebandbreedte is te vinden op hogere frequenties in de zogenaamde millimetergolf frequentieband (>30 GHz). Door gebruik te maken van de hogere frequentiebanden zullen de antennes kleiner worden, waardoor de mogelijkheid ontstaat om ze te integreren in een ‘system-on-chip’ of ‘in-package,’ die op zichzelf relatief nieuwe technologieën zijn. Met de afnemende grootte van de antenne en de mogelijkheid om ze in een compleet systeem te integreren, duiken er nieuwe uitdagingen op in zowel modelleren als meten. De strategie voor het ontwerpen en valideren van antennes op lagere frequenties blijkt onvoldoende te zijn bij hogere frequenties. Dat is de reden waarom een andere strategie nodig is. Daarom is er een meer gedetailleerd ontwerp en een experimenteel validatieproces vereist waarbij voor elke stap mogelijke invloeden worden herkend die correleren met onzekerheden die het gedrag van de te testen antenne beïnvloeden.

Dit proefschrift beschrijft de hoofdoorzaken van deze invloeden en onzekerheden, toont de impact op de antennekarakteristieken en schetst effectieve oplossingen om deze te minimaliseren. Om dit te kunnen doen, is het noodzakelijk een statistisch kader te gebruiken. Omdat het gebruik van statistische analyse bij antenne onderzoek niet gebruikelijk is, worden de statistische voorwaarden vooraf samengevat. Ten tweede worden twee ontwerpstrategieën gepresenteerd die statistische hulpmiddelen gebruiken om de onzekerheden te kwantificeren in zowel het modelleren als het meten van een millimetergolfantenne. Met behulp van deze ontwerpstrategieën worden de oorzaken van de onzekerheden duidelijk, wat betekent dat mogelijke oplossingen kunnen worden uitgewerkt of op zijn minst worden uitgelegd.

Het ontwerp- en validatieproces dat omgevingsinvloeden en onzekerheden omvat, wordt getest op twee specifieke gevalstudies. Het eerste geval dat wordt bestudeerd, is een lineair gepolariseerde patch-antenne, waarvoor analytische vergelijkingen worden ge-

bruikt om de juiste afmetingen te berekenen. Een probabilistische gevoeligheidsanalyse-simulatie wordt vervolgens gebruikt om een gevoeligheidsanalyse uit te voeren op deze dimensies om rekening te houden met fabricagetoleranties, zodat het effect op de anten-nekarakteristieken wordt gevisualiseerd. In de tweede gevalstudie wordt een circulair gepolariseerde staafantenne, die op 60 GHz werkt, bestudeerd met behulp van een volledig elektromagnetisch model om inputparameters te kunnen variëren, zoals diëlektrische materiaaleigenschappen. Beide antennes zijn gemodelleerd uitgaande van een basisontwerp zonder aansluitverbindingen, evoluerend naar meer gedetailleerde modellen met inbegrip van verschillende vormen van aansluitverbindingen. Om de oorzaken die het gedrag van de antenne beïnvloeden te begrijpen, is de aansluitverbinding verder onderzocht. Er is een vergelijking gemaakt tussen een coaxiale connector, een millimetergolf probe en een golfpijp aansluiting die allemaal verbonden zijn met eenzelfde antenne-structuur.

Een andere belangrijke bron van onzekerheid in het ontwerp van de antenne wordt gevormd door de materiaaleigenschappen op millimetergolffrequenties. Omdat de permittiviteit en diëlektrische verliezen frequentieafhankelijk zijn, moeten ze worden bepaald aan de hand van de gebruikte frequenties. Meestal zijn bij millimetergolven de materiaaleigenschappen (permittiviteit en verlieshoek) onbekend of onnauwkeurig. Daarom is een deel van dit proefschrift gewijd aan het onderzoeken van materiaaleigenschappen. Een in eigen huis ontwikkelde Fabry-Pérot open-holte resonator met concave spiegels is gerealiseerd om de materiaaleigenschappen te bepalen bij millimetergolffrequenties. Het systeem is volledig geanalyseerd met betrekking tot onzekerheden die zijn veroorzaakt door bijvoorbeeld de tolerantie op het maken van de sferische spiegels of het herhaaldelijk plaatsen van het te testen dielectrische materiaal in de opstelling.

Conclusies, aanbevelingen en middelen om de ontwerpprocedure te verbeteren komen aan bod in het laatste hoofdstuk van dit proefschrift.

Nomenclature

| Abbreviation | Description |
|---------------------|---|
| 2D | Two dimensions |
| 3D | Three dimensions |
| ac | Alternating current |
| AiP | Antenna in package |
| AiS | Antenna in system |
| ANOVA | Analysis of variance |
| AoC | Antenna on chip |
| AR | Axial ratio |
| AUT | Antenna under test |
| BW | Bandwidth |
| CBCPW | Copper backed co-planar waveguide |
| CDF | Cumulative distribution function |
| CIPM | International committee for weights and measures |
| cm | Centimeter |
| CLT | Central limit theorem |
| CP | Circularly polarization |
| CST | Control systems technology |
| dB | Decibel |
| dBi | Decibel with respect to an isotropic radiator |
| dBm | Decibel with respect to an isotropic milliwatt |
| dBV | Decibel isotropic voltage |
| dc | Direct current |
| DP | Discrete port |
| EDA | Exploratory data analysis |
| EM | Electromagnetics |
| EPC | Electronic Prototype Centrum |
| FD | Frequency-domain solver |
| FEKO | Feldberechnung für körper mit beliebiger oberfläche |
| G | Generation i.c.w. 5G or 6G |
| GHz | Gigahertz |

| | |
|----------|---|
| GND | Ground |
| GO | Geometrical optics |
| GPU | Graphics processing unit |
| GSG | Ground-signal-ground |
| GTD | Geometrical theory of diffraction |
| GUM | Guide to the Expression of Uncertainty in Measurement |
| h | Hour |
| HFSS | High-frequency structure simulator |
| HOS | Higher order statistics |
| HPBW | Half power beam width |
| iid | Independent and identically distributed |
| IC | Integrated circuit |
| IF-BW | Intermediate frequency bandwidth |
| IRQ | Interquartile range |
| KDE | Kernel density estimation |
| LHCP | Left-hand circular-polarization |
| LoLN | Law of large numbers |
| LP | Linearly polarization |
| MACM | Multiple amplitude component method |
| MAPCM | Multiple amplitude phase component method |
| MR | Measurement range |
| MWS | Microwave studio |
| μ SL | Microstrip line |
| NEC | Numerical electromagnetics code |
| NIST | National institute of standards and technology |
| OEWG | Open ended waveguide |
| OtA | Over-the-air |
| PAM | Phase amplitude method |
| PCB | Printed circuit board |
| PDF | Probability density function |
| PMF | Probability mass function |
| PPM | Polarization pattern method |
| PSA | Probability sensitivity analysis |
| PTFE | Polytetrafluoroethylene |
| RA | Reference antenna |
| RF | Radio frequency |
| RHCP | Right-hand circular-polarization |
| RSM | Rotating source method |
| SA | Spectrum analyzer |
| SGH | Standard gain horn |
| SI | International System of Units |
| SLLN | Strong law of large numbers |
| SNR | Signal to noise ratio |

| | |
|------|------------------------------------|
| TD | Time-domain solver |
| TE | Transversal electric |
| TEM | Transversal electromagnetic |
| TM | Transversal magnetic |
| TU/e | Eindhoven University of Technology |
| UTD | Uniform theory of diffraction |
| VIM | Vocabolary of Metrology |
| VNA | Vector network analyzer |
| VSWR | Voltage standing wave ratio |
| WGP | Waveguide port |
| WLLN | Weak law of large numbers |

| Symbols | Description |
|-------------------------|--|
| a | Variable |
| a | Radius of a planar mirror |
| A | Amplitude of the electric field |
| α | Significance level |
| α_d | Fractional power loss per reflection |
| $ A_{dB} $ | Maximum amplitude of the resonance frequency |
| b | Variable |
| B | Susceptance |
| B_m | Radius of the Gaussian beam waist on the spherical mirror |
| BW_{samp} | Frequency points with which the frequency bandwidth is reconstructed |
| BW_{-3dB} | Frequency bandwidth at -3dB |
| c_0 | Speed of light in vacuum |
| c_{air} | Speed of light in air |
| c_{cav} | Speed of light in a resonant cavity |
| C | Kurtosis |
| d | Distance between mirror and the edge of the dielectric material |
| d_0 | Distance between mirror and half the dielectric material |
| d_{ant} | Distance between two antennas |
| d_{iris} | Diameter of an iris |
| d_{mirror} | Distance that a spherical mirror has traveled |
| D | Distance between two spherical concave mirrors |
| D_{app} | Diameter of an aperture of an antenna |
| D_{rs} | Diameter of a radiating surface |
| δ | Time phased angle |
| δ_s | Skin depth |
| Δ_t | Measurement time |
| δ_{fi} | Difference between two consecutive resonance frequencies of an unloaded cavity |
| δ_{fs} | Difference in resonance frequency |
| Δd_{ant} | Variation in distance between two antennas |
| δf_{sa} | Difference between anti-symmetric resonances for an unloaded and loaded cavity |
| δf_{ss} | Difference between symmetric resonances for an unloaded and loaded cavity |
| ΔL | Extra length due to fringe fields |
| ΔP_x | Measured value of uncertainty |
| $^{\circ}\text{C}$ | Degrees Celsius |
| E | Electric field |
| \mathbf{E} | Electric field vector |
| $E[x]$ | Expected value of x |
| E_i | Incidence wave of an electric field |
| E_r | Reflected wave of an electric field |
| E_t | Transmitted wave of an electric field |
| $E[x]$ | Expected value of x |
| ϵ | Absolute permittivity |

| | |
|---------------------------|--|
| ϵ_r | Relative permittivity |
| $\epsilon_{r\text{-air}}$ | Relative permittivity of air (measured) |
| ϵ_{eff} | Effective permittivity |
| ϵ_0 | Vacuüm permittivity |
| f_i | i^{th} resonance frequency |
| f_p | Focal point |
| f_{si} | i^{th} resonance frequency with dielectric material |
| $f_{\delta f}$ | Derived resonance frequency |
| f'_i | Moved resonance frequency f_i |
| f_{left} | Frequency point left from the resonance frequency |
| f_{right} | Frequency point right from the resonance frequency |
| f_{locav} | Resonance frequency of a loaded cavity |
| f_{ulcav} | Resonance frequency of a unloaded cavity |
| φ_{dm} | Angle of the dielectric material |
| φ_{pol} | Polarization angle of the reference antenna |
| φ_B | Brewster's angle |
| φ_L | Angular distance in a spherical coordinate system |
| $^{\circ}F$ | Degree Fahrenheit |
| G | Antenna gain |
| g_i | i^{th} g -parameter in a stability diagram |
| G | Conductance |
| G_r | Realized gain |
| G_{rp} | Realized gain pattern |
| G_{AUT} | Gain of an antenna under test |
| G_{RA} | Gain of a reference antenna |
| γ | Gamma function |
| Γ | Reflection coefficient |
| Γ_{in} | Reflection coefficient of a reference antenna |
| Γ_{zn} | Reflection coefficient of loads with known values |
| Γ_{RSI} | Reflection coefficient of a reflected signal of interest |
| h | Planck's constant |
| \hbar | Reduced Planck's constant |
| h_{PCB} | Height of the printed circuit board |
| h_s | Smoothing factor |
| h_{wg} | Height of a waveguide |
| H | Magnetic field |
| \hbar | Reduced planck's constant |
| i_{ac} | Time varying current |
| k | Scaling factor of the waveguide port |
| K | Kernell |
| k_p | Coverage factor |
| k_w | Wave number in air |
| k_0 | Wave number in free space |

| | |
|------------------------|---|
| l_{gap} | Length of the gap in an inset-fed patch antenna |
| l_{PCB} | Length of the printed circuit board |
| L | Angular mode |
| L_p | Length of the patch antenna |
| λ | wavelength in air |
| λ_0 | Wavelength in free space |
| λ_{cav} | Wavelength in a resonant cavity |
| M | Amount of samples from a population |
| M_v | Measurement value |
| μ_a | Absolute permeability |
| μ_e | Expectation |
| μ_{eff} | Effective permeability |
| μ_r | Relative permeability |
| μ_0 | Vacuüm permeability |
| μ | Population mean |
| n | n^{th} random variable |
| n_r | Refractive index |
| N | Total amount of observations |
| N_{fres} | Fresnel number |
| \mathcal{N} | Normal density function |
| O_p | Total amount of ports |
| p | Radial mode |
| p | Level of confidence |
| p | The momentum of a particle |
| P | Power |
| P_0 | Total power |
| \mathbb{P} | Probability |
| ψ | Truncated probability distribution function |
| q | Axial mode |
| Q_L | Quality-factor of an unloaded cavity |
| Q_{in} | Total amount of input quantities |
| Q -factor | Quality-factor of a resonant system |
| Q_{ucav} | Quality-factor of an unloaded cavity |
| r_m | Radius of a spherical concave mirror |
| R | Resistance |
| R_i | Radius of curvature of the i^{th} spherical mirror |
| R_v | Reference value |
| R_{in} | Input impedance |
| ρ | Correlation |
| ρ_m | Reflection coefficient magnitude |
| ρ_p | Radial distance in a spherical coordinate system |
| ρ_r | Resistivity |
| s | Standard deviation of a sample |

| | |
|--------------------|---|
| s^2 | Variance of a sample |
| $s_{\bar{x}}$ | Standard error of a sample |
| S | Skewness |
| s_x | Corrected standard deviation |
| s_y | Corrected standard deviation |
| sw_w | Sliding window width |
| σ | Standard deviation of a population |
| σ^2 | Variance of a population |
| $\sigma_{\bar{x}}$ | Standard error of a population |
| t | Time |
| t | Half the thickness of a dielectric material |
| t_p | Coverage factor of the students t-distribution |
| $\tan\delta$ | Loss tangent |
| T | Transmission coefficient |
| T_{Bias} | Trueness |
| τ_g | Group delay |
| τ_m | Transmission coefficient magnitude |
| τ_r | Tilt angle |
| $u(y)$ | Standard uncertainty |
| $u_c(y)$ | Combined standard uncertainty |
| $u_{c,r}(y)$ | Relative combined standard uncertainty |
| u_m | Uncertainty of a type ‘B’ evaluation |
| u_n | Uncertainty of a type ‘A’ evaluation |
| $u_r(y)$ | Relative standard uncertainty |
| U | Estimated covariance |
| U | Expanded uncertainty |
| U_r | Relative expanded uncertainty |
| v | Degrees of freedom |
| v_{ac} | Time varying voltage |
| v_x | Velocity of a particle before measurement |
| v'_x | Velocity of a particle after measurement |
| w_{tl} | Width transmission line |
| w_{wg} | Width of a waveguide |
| w_{gap} | Width of the gap in an inset-fed patch antenna |
| w_{PCB} | Width of the printed circuit board |
| w_0 | Radius of the Gaussian beam at the center of a cavity |
| W_p | Width of the patch antenna |
| x | Random variable |
| x_p | Location of a particle |
| x - | Axis of a Cartesian coordinate system |
| X | Sample of a population |
| X | Reactance |
| X | Joint distribution |

| | |
|-------------|---|
| \bar{x} | Sample mean |
| \bar{x}_m | m^{th} sample mean |
| y | Random variable |
| y - | Axis of a Cartesian coordinate system |
| Y | Random variable |
| z | Axial distance |
| z - | Axis of a Cartesian coordinate system |
| z_q | Axial distance in a spherical coordinate system |
| Z_{in} | Input impedance |
| Z_L | Load impedance |
| Z_0 | Free space impedance |
| ζ | x to the power of |

CHAPTER ONE

Introduction

“Discovery consists of seeing what everyone saw and thinking what no one thought”

(Albert Szent-Gyorgyi 1893-1986)

1.1 Introduction

New wireless technology is developing at a rapid pace. With new emerging wireless communication standards like 5G and 6G, using frequencies in excess of 30 GHz, the autonomous car, for instance, becomes a reality. Comparable applications demand high data rates and low latency to be able to work according to specification. This is not possible using the common low-frequency bands under 30 GHz. Therefore the millimeter-wave frequency band (30 GHz to 300 GHz) is explored for applications that require a large bandwidth. It has been found that there are various challenges at millimeter-wave frequencies in the area of antenna design, modeling and characterization by measurement [3] - [5]. Challenges are new materials being used of which the properties at high frequencies are yet unknown. Another challenge and not the least is the small size (less than 1 cm) of the antenna or wireless system. This is one of the reasons that the antenna measurement system, which is used in a particular experiment, has a significant influence on the behavior of the antenna under test. This influence is known as the ‘observer effect’ [6] and makes the retrieved results potentially unreliable. In this chapter we will start with a short description of the history of antennas and a preliminary description of some challenges related to millimeter-wave antennas. The second part of this chapter will describe the importance of measurements and its position in the antenna design process. This chapter ends with presenting an extensive design process, the description of the research questions and the outline of the thesis.

1.2 Antennas at millimeter waves

The central theme of this thesis is the accurate design, analysis and characterization of millimeter-wave antennas. Before we go further into this subject, we go back in time to the emergence of the antenna and its development up to this time. The definition of an antenna or aerial is:

“that part of a transmitting or receiving system that is designed to radiate or to receive electromagnetic waves” [7].

1.2.1 History of the antenna

Based on the definition of the antenna one might argue that Michael Faraday, even without knowing, created the first antenna in the 1830s. By moving a magnet through a coil he produced a time-varying magnetic field in the coil. That field induced a time-varying electric field between the ends of the coil. The coil - that can be considered being a loop antenna - was connected to a Galvanometer registering the detected field. With this experiment, he proved the existence of a relation between time-varying magnetic and electric fields. In 1863 James Clerk Maxwell published the now famous Maxwell equations connecting electricity and magnetism [8], [9]. In 1886 Heinrich Hertz created the first wireless setup [10]. This setup incorporated a half-wave dipole as transmit antenna and a loop as receive antenna [11]. After generating a spark in the gap of the dipole he observed a spark-signal received by the loop antenna. That technique (in which the spark on reception side was replaced by a coherer) was used on December 12th, 1901, by Marconi, transmitting from Poldhu in Cornwall (United Kingdom) to Newfoundland (Canada) over a distance of 3553 km [12]. Marconi had improved on the transmitter and especially the receiver, mainly by optimizing the antennas. He used a wire cone monopole as a transmit antenna, and a 200-meter wire monopole held up by a kite as a receive antenna. By transmitting and receiving the letter ‘S,’ in Morse code (three dots), the first transatlantic wireless communication was a fact. Since then, both frequency use and antenna types have evolved to fulfill the needs for new wireless applications. A rough outline of antenna development over the years is shown in Fig. 1.1.

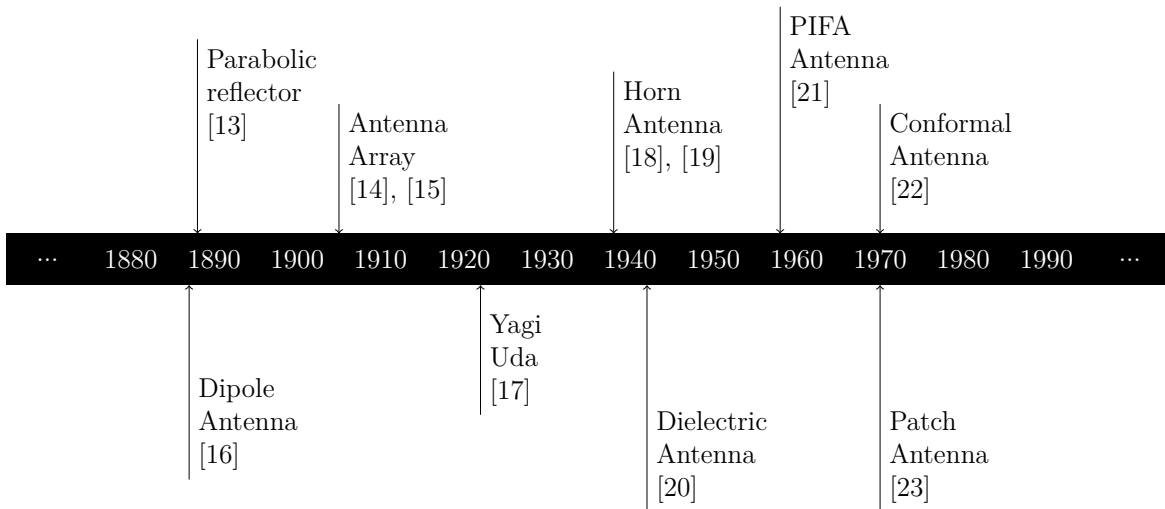


Figure 1.1: Timeline of the development of various types of antennas.

Some of the antennas mentioned in Fig. 1.1 such as the dipole, horn and patch antenna are also used in millimeter-wave applications (see Fig. 1.3). Apart from these well-known antenna types, new antenna concepts have been explored. Some examples shown in Fig. 1.2 are investigated by the electromagnetics (EM) group of Eindhoven University of Technology (TU/e) such as the, antenna-on-chip (AoC), and antenna-in-package (AiP).

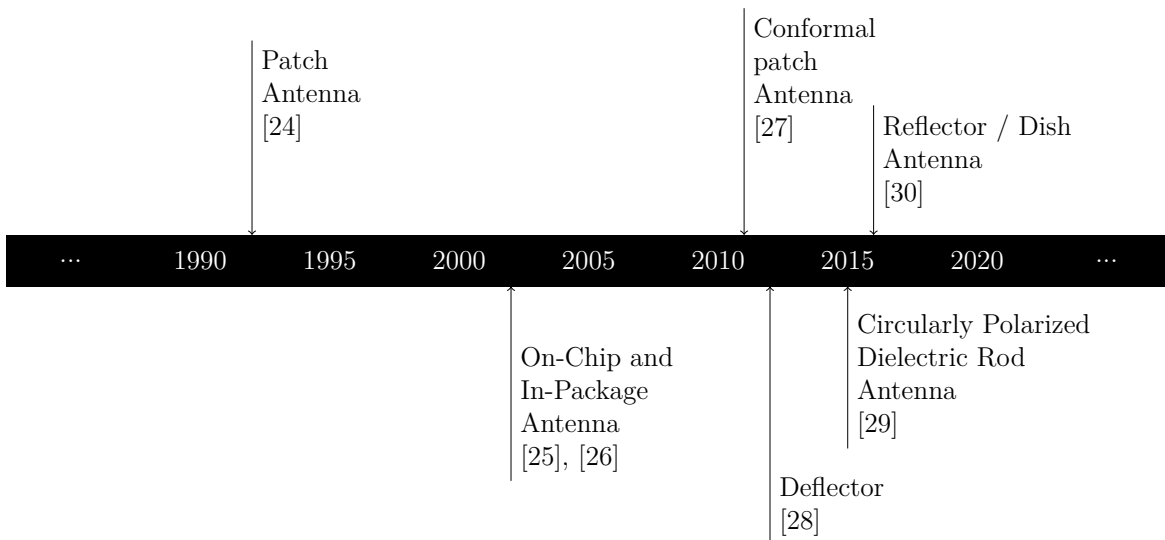


Figure 1.2: Timeline of millimeter-wave antennas investigated by the electromagnetics group of Eindhoven University of Technology.

1.2.2 Examples of millimeter-wave antennas and applications

In Fig. 1.3 various examples of millimeter-wave antennas are shown. These examples show that due to the size of the antenna it is a challenge to set up a connection with a measurement system. In general the antenna is equipped with a coaxial connector and the connection with the vector network analyzer (VNA) is realized via an RF-cable. Although, in some cases, this is also possible for millimeter-wave antennas [see Fig. 1.3(b) where the location of the connector interface is depicted by the red ellipse] it is more common now to opt for an RF-probe connection [see Fig. 1.3(a) and Fig. 1.3(c) where the RF-probe interface is depicted with a yellow ellipse]. This means that the transmission line, coming from the antenna, ends in a co-planar waveguide where the connector is normally located. The RF-probe can also be used to connect a wireless system to a VNA. Fig. 1.3(d) shows an example of such a wireless system with the antenna integrated on an integrated circuit (IC), a so-called antenna-on-chip. Here the connection between transceiver and antenna is realized with a Ground-Signal-Ground (GSG) RF-probe transition. It should be noted that in order to be able to measure this antenna, the connection with the transceiver is removed with a laser. The advantage of measuring the antenna in a system is that you take the influences of the IC into account

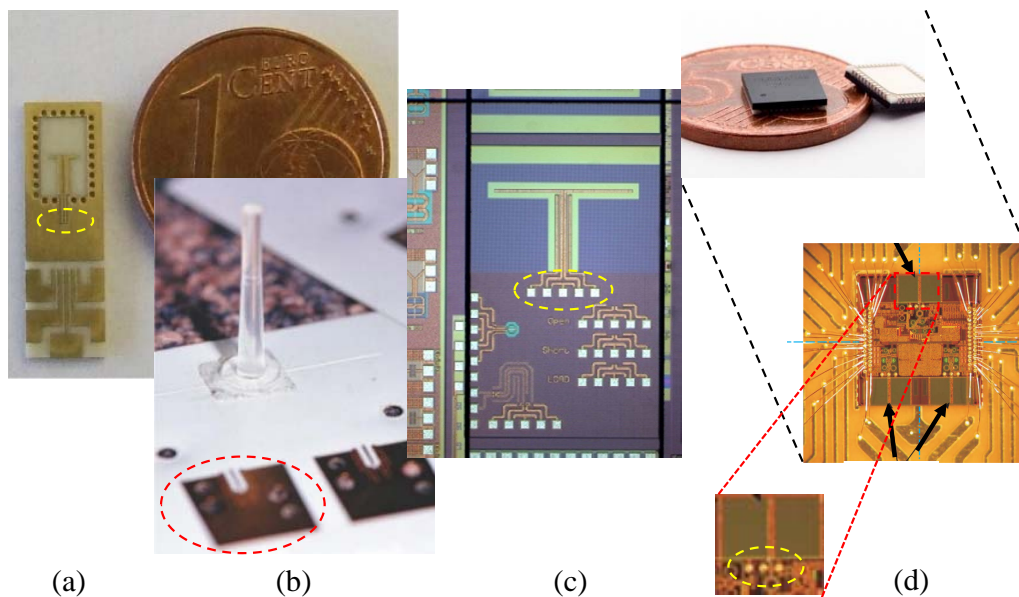


Figure 1.3: Various types of millimeter-wave antennas (a) dipole, (b) dielectric rod [29], (c) dipole on-chip [25], and (d) complete integrated system on-chip [26] with three cavity-backed monopole antennas (indicated by the black arrows). The RF-connection interfaces are RF-probe-pads depicted with the dashed yellow ellipses and an RF-coaxial press-fit connector-pad depicted with the dashed red ellipse.

when determining the behavior of the antenna. In other words, the measurement is performed closer to the real world environment of the antenna.

1.3 Classical antenna analysis and design process

In the first part of the 20th century, radio and television were some of the first wireless applications [see Fig. 1.4(a)]. Since then, not only the diversity but also the complexity of wireless systems has increased. At the same time also the methods for modeling antennas [see Fig. 1.4(b)] and the instruments to measure them [see Fig. 1.4(c)] have been developed.

Fig. 1.4 shows per timeline (row) the interaction between the products, the available analytical and numerical tools and the antenna measurement systems. The thick black arrows show the design process where it is assumed that the product is leading towards the antenna design. The thin black arrows show the iteration between measurements and model.

The mapping of Maxwell's equations, illustrates in the first timeline, means that one used approximate calculations and experiments to design new antenna concepts. An example is the Yagi-Uda antenna as discussed in [31]. In the absence of an anechoic room, which was only developed in the second half of the 20th century, antennas were measured outdoors with a pick-up antenna and apparatus measure the electric field strength [32], [33]. In order to minimize effects of the environment, the antennas were placed on towers, buildings or mountain peaks with a valley in between, as illustrated in Fig. 1.4(c).

In the second time-line, the appearance of the computer is depicted. The computer made it possible to perform complex calculations near-instantaneously. The first computer analysis programs were tested in 1959 [34], thus giving birth to the science of 'computational electromagnetics.' In the same time-line we do see the introduction of indoor anechoic (i.e., reflection-suppressing) antenna measurement chambers. With these developments came the understanding of performing antenna measurements wherein the environmental influences are minimized. This understanding has been laid down in several books, see for example [35].

The third timeline shows the increase of the variety of wireless applications, an important example being the mobile telephone. Due to the increase in computational power since the 1990s, it has now become feasible to model and simulate detailed three-dimensional (3D) antenna structures. It is the author's strong believe that this capability has led in the past to a tendency to omit antenna measurement in the design process. This is depicted in Fig. 1.4 by the red arrow. Antennas are designed and optimized (made to meet the research requirements, see Fig. 1.5) through performing

calculations for many input values (so-called ‘parameter sweeps’), believing that the results represent the actual antenna to be realized. This process is illustrated in Fig. 1.4(b) by the ‘blurred’ Maxwell equations. It is also possible that measurements are being performed, but that the simulation results are believed to represent to be the truth. If and when this assumption is correct will be discussed in this thesis. Finally, the red question-mark shown in Fig. 1.4(c) represents the danger of a decreased physical insight onto following this procedure, making it more difficult to explain differences that may or will occur between simulation and measurement results.

A question that arises, specifically for millimeter-wave antennas, is if differences between simulation and measurement results will be different from those for low frequency antennas, i.e., for frequencies below 30 GHz? A potential distinguishing factor will be the RF-connector(s) used. A Sub-Miniature-A RF-connector for instance [36] fits at a

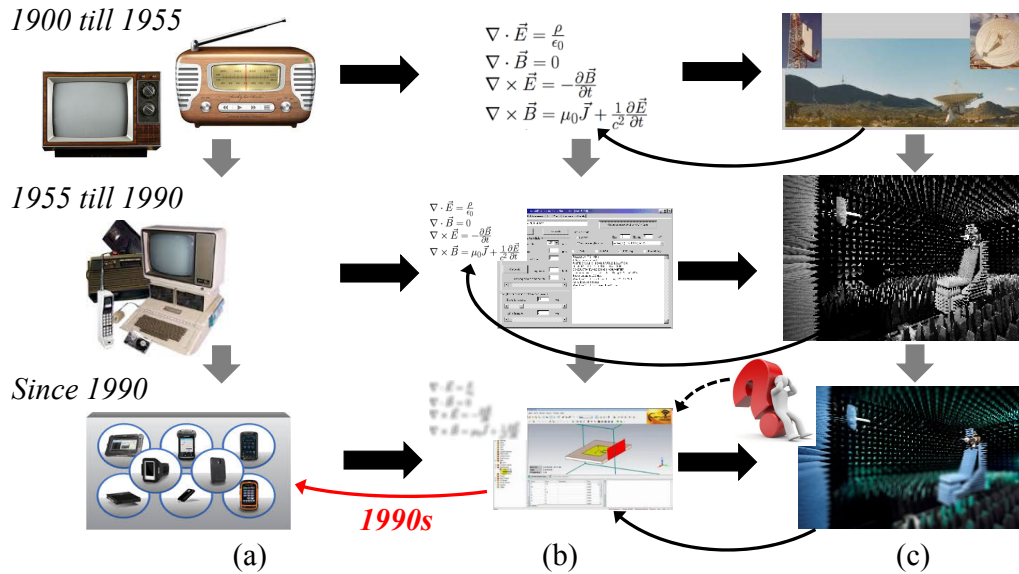


Figure 1.4: Over the years (a) wireless applications, (b) modeling tools and (c) measurement facilities have changed in both variety and complexity. The design process from product idea till modeled and characterized antenna is illustrated horizontally and depicted with the thick black arrows. From 1900 to 1955 the modeling and design was mainly analytical and experimental. From 1955 onwards the first computational simulation tools were introduced together with indoor measurement facilities. From the 1990s on, the computational simulation tools support 3D structures. The red arrow depicts that measurements might be considered less important because of the assumed accuracy of the simulation results. The blurred Maxwell equations represent missing insight into the physics of electromagnetics and the question-mark depicts the situation that where simulations and measurement are performed, simulations are considered the truth.

frequency of 2.4 GHz about four times in the wavelength (0.125 m) where that is exactly the other way around at a frequency of 60 GHz with a wavelength of 0.005 m. Effects of reflection of waves against this connector will therefore be more pronounced in the measurement results (e.g. impedance, gain pattern, etc.) at millimeter-waves. Possible causes and effects of the environment on the antenna as well as possible solutions will also be discussed in this thesis.

1.4 The essence of measurement

To understand the importance of antenna measurements in the design process, we must first understand what is meant by measuring. According to the International Vocabulary of Metrology (VIM), [37] a measurement is defined as a:

“process of experimentally obtaining one or more quantity values that reasonably be attributed to a quantity,”

and a quantity as the:

“property of a phenomenon, body, or substance, where the property has a magnitude and reference.”

In other words, the measurement provides a ‘quantity value,’ also known as a measurand¹, consisting of a ‘magnitude’ and a ‘reference’. If we apply this definition to antenna measurements, we can say that the magnitude may be an electric field represented by an electric current measured with a VNA or spectrum analyzer (SA). However, what a traceable² ‘reference’ could be will be discussed further in this thesis.

With measuring instruments, like the VNA and SA, we are able to gather knowledge about the behavior of an antenna under test (AUT). This way of gaining knowledge, by using measuring instruments, is fairly new. Dating back to ancient Greece, the cradle of philosophy, knowledge was acquired by making abstract models. These abstract models would help, through logical steps, to understand certain phenomena and creating our own philosophical abstraction. On the other hand it was understood that we live in a physical or empirical world that presents itself via occurrences, facts and events which, at that time, could only be perceived through our senses. Therefore, creating abstract models was the way to understand the world. An example is geometry where the first steps in abstraction were made by the ancient Greeks with Euclid’s Elements [38]. The

¹A particular quantity subject to measurement.

²The term measurement traceability is used to refer to an unbroken chain of comparisons relating an instrument’s measurements to a known standard. Calibration to a traceable standard can be used to determine an instrument’s trueness, precision, and accuracy.

geometry abstraction continued up till the 19th century, when scientists developed the n -dimensions, projective geometry, affine geometry and finite geometry [39]. Observation was only used to start speculation. Validation of abstract models was not part of the approach to science. The effect of the ancient Greek point of view on observation or empiricism still holds a negative connotation today [40].

It would take until the 19th century before scientists would take a different view on the importance of measuring. In 1871 James C. Maxwell wrote [41]:

“If, then, we wish to obtain standards of length, time, and mass which shall be absolutely permanent, we must seek them not in the dimensions, or the motion, or the mass of our planet, but in the wave-length, the period of vibration, and the absolute mass of these imperishable and unalterable and perfectly similar molecules”.

Here Maxwell expresses his desire to create a coherent system of standards (references) for measurement. Three base units were identified that could be used, namely: mass³, length⁴ and, time⁵. These quantities form the basis for the International System of Units (SI)⁶ and is the most widely used system of measurement⁷.

These days, experimental activities, from which measurements are the most important part, are considered as being essential in the advancement of knowledge. We have learned to understand what Lord Kelvin in 1883 unambiguously spoke about when he said [42]:

“I often say that when you can measure what you are speaking about, and can express it in numbers, you know something about it; but when you cannot express it in numbers your knowledge about it is of meager and unsatisfactory kind; it may be the beginning of knowledge, but you have scarcely, in your thoughts, advanced to the stage of science, whatever the matter may be. So, therefore, if science is measurement, then without metrology there can be no science”.

Since several decades measuring instruments to ‘take measurements’ are used. The

³first reference in 1889

⁴first reference in 1795

⁵first reference in 1967

⁶The new SI came officially into effect on the 20th of May 2019, precisely a dozen dozen (144) years after the first international treaty on units of measurement – the Metre Convention – which was signed on the same day in 1875.

⁷A system of measurement is a collection of units of measurement and rules relating them to each other. Systems of measurement have historically been important, regulated and defined for the purposes of science and commerce. Systems of measurement in use include the SI, the modern form of the metric system, the imperial system, and United States customary units.

question that now arises is, are we 'reading an instrument' or do we 'make an [antenna] measurement' to gain knowledge? This important question underlies the research that is described in this thesis.

1.5 The observer effect

An important phenomenon related to 'making a measurement' is the effect of the observer. In 1928 Niels Bohr, Werner Heisenberg and other physicists defined the 'observer effect'⁸. The observer effect states that the outcome of an experiment is affected by the experimental setup or experimenter, i.e. the observer [44], [45]. This effect was first described based on observations in quantum mechanics (particle physics). For an electron to become detectable, a photon must interact with it. This interaction will influence the electron's velocity and momentum. The following equation (one dimensional for simplicity) expresses this effect of change in velocity due to the interaction with a photon [44]:

$$\left|v'_{x_p} - v_{x_p}\right| \Delta p_{x_p} \approx \hbar / \Delta t, \quad (1.1)$$

where v'_x is the velocity of the particle after, and v_x is the velocity of the particle before measurement, Δp_x the 'uncertainty in measured value of momentum', Δt the duration of the measurement, and \hbar is the reduced Planck constant $h/2\pi$. Here x_p is the location of the particle and p its momentum.

The observer effect can also be applied on a macroscopic level. This is illustrated by a thought experiment that was described by Erwin Schrödinger in 1935 [46]. The thought experiment is commonly known as 'Schrödinger's cat'. Schrödinger wrote the following explanation [46]:

“One can even set up quite ridiculous cases. A cat is penned up in a steel chamber, along with the following device (which must be secured against direct interference by the cat): in a Geiger counter, there is a tiny bit of radioactive substance, so small, that perhaps in the course of the hour one of the atoms decays, but also, with equal probability, perhaps none; if it happens, the counter tube discharges and through a relay releases a hammer that shatters a small flask of hydrocyanic acid. If one has left this entire system to itself for an hour, one would say that the cat still lives if meanwhile no atom has decayed. The first atomic decay would have poisoned it. The psi-function of

⁸The observer effect is sometimes confused with the uncertainty principle [43], [6] described by Werner Heisenberg in 1927.

the entire system would express this by having in it the living and dead cat (pardon the expression) mixed or smeared out in equal parts.

It is typical of these cases that an indeterminacy originally restricted to the atomic domain becomes transformed into macroscopic indeterminacy, which can then be resolved by direct observation. That prevents us from so naively accepting as valid a ‘blurred model’ for representing reality. In itself, it would not embody anything unclear or contradictory. There is a difference between a shaky or out-of-focus photograph and a snapshot of clouds and fog banks.”

In the case of the electron the change in momentum is caused by an observer. This is different for the story of ‘Schrödinger’s cat’ where an observer does not seem to affect the state of the cat. However, according to quantum theory, we cannot know, the cat is both alive and dead for as long as the chamber is sealed, in a superposition of states. It is only when we open the chamber and observe the condition of the cat (thereby collapsing the wave function⁹), that the superposition is lost and the cat becomes either alive or dead. This paradox demonstrates that observation itself affects the outcome, as the outcome, as such, does not exist until it is observed [48].

In the case of an antenna measurement for instance, a gain pattern measurement can be influenced by reflections caused by objects, which are part of the measurement setup, in the vicinity of the AUT. It can be imagined that as the wavelength becomes smaller, under the same environmental conditions as for lower frequencies, the effect of the reflection on the gain pattern will become larger. An example of objects in the vicinity of the radiating part of the antenna are the interconnection and support structure to hold the antenna in place during measurement. Therefore both objects are becoming part of the antenna and thus also part of the result.

Another point of view with regard to the observer effect is the ‘observer-expectancy’¹⁰. This *confirmation bias* can make the experimenter misinterpret results, and overlook information arguing against the experimenter’s hypothesis.

It is inevitable that both the experimental setup and the experimenter will influence the results of a measurement.

⁹In quantum mechanics, wave function collapse occurs when a wave function — initially in a superposition of several eigenstates — reduces to a single eigenstate due to interaction with the external world. This interaction is called an “observation” [47].

¹⁰The observer-expectancy effect, also called the experimenter-expectancy effect, expectancy bias, observer effect, or experimenter effect, is a form of reactivity in which a researcher’s cognitive bias causes them to subconsciously influence the participants of an experiment. Confirmation bias can lead to the experimenter interpreting results incorrectly because of the tendency to look for information that conforms to their hypothesis, and overlook information that argues against it. [49]

1.6 Antenna design, analysis and measurement process

The design process shown in Fig. 1.5 is illustrated with four different Euler diagrams¹¹ representing four different worlds, namely:

- A) The Influential world colored gray.
- B) The Design world colored green.
- C) The Symbolical world colored red.
- D) The Empirical world colored blue.

In the ‘Design’ world, an antenna is described by so-called research requirements. These research requirements are again linked to an application or research question. The ‘Symbolical’ world, located inside the ‘Design’ world, represents analytical and numerical equations necessary to model / simulate [40] a certain type of antenna structure. The ‘Empirical’ world, also located inside the ‘Design’ world, represents the observation of a quantity with help of a measurement system. Part of this world is the preparation of a sample i.e., an AUT. The overlap between the ‘Symbolical’ and the ‘Empirical’ world represents the validation between the measurement and the analytical or numerical model. It should be emphasized that either the measurement results or the modeling results should serve as a reference, which should be traceable, to enable validation. However, this does impose requirements on either the measurement results or the simulation results, which will be discussed in this thesis.

Zooming in on the design process: It starts with the choice for the desired antenna configuration (see Fig. 1.5). The antenna configuration tells something about what the simulation or realized model looks like and what its purpose is. For instance, an antenna referred to as a ‘Research Antenna’ is considered to be ideal and the simulation model consists only of an antenna. When an antenna is referred to as a ‘Measurable Antenna’ it means that the simulation model of the antenna is extended with an RF-connector model. By comparing the results of the ‘Research Antenna’ with the ‘Measurable Antenna’, it will become clear what, for example, the influence of an RF-connector is on the behavior of the antenna. An antenna referred to as a ‘System Antenna’ means that the antenna is integrated, for instance, on-chip. In this case, the effect of the close-by environment

¹¹An Euler diagram is a graphic method employing circles to represent relations between and operations on classes and the terms of propositions by inclusion, exclusion, and intersection [50]. According to [51] other shapes for the Euler diagram are used although this impacts the perception of the Euler diagram. Therefore the author uses rectangular shapes with rounded corners. The difference between a Venn and an Euler diagram is that a Venn diagram shows all possible logical relationships between a collection of sets, but an Euler diagram only shows relationships that exist in the real world.

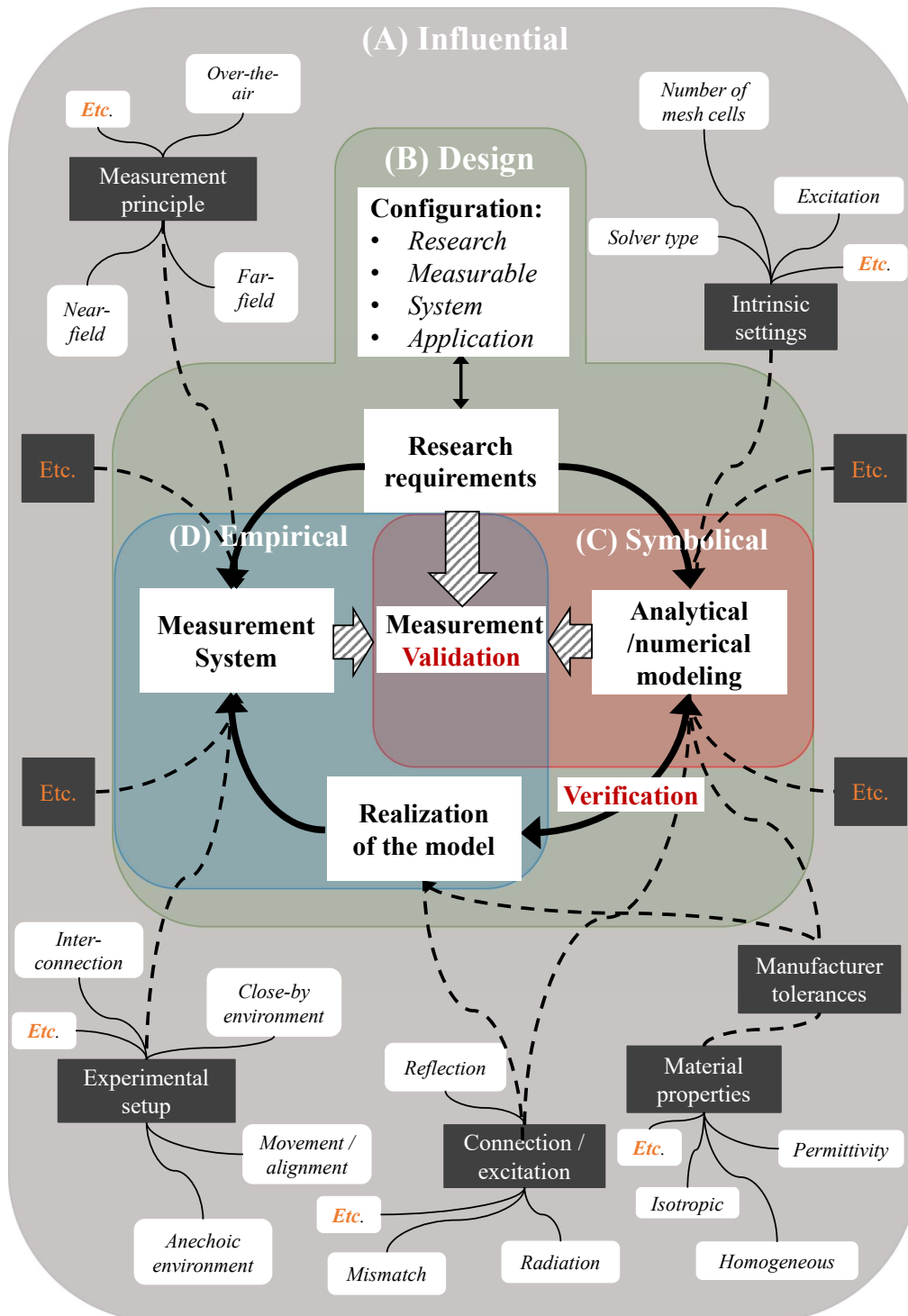


Figure 1.5: The antenna design process is illustrated by four worlds e.g. Euler diagrams [50]. Highlighted are the Design (green), Symbolical (red) and Empirical (blue) world. The research requirements are triggered by the choice to create a research, measurable, system or application antenna. The overlap between the Symbolic and Empirical world contains the antenna measurements and is seen as the validation step. The gray arrows depict that those steps contain information that is used in the validation step. The influential world contains the various causes that influence a certain step in the design process. These are depicted by the dark gray rectangles. Each cause of influence has different uncertainties described in the white rounded rectangles.

on the antenna characteristics can be simulated. An antenna addressed as ‘Application Antenna’ means that the System Antenna is assembled with a package or housing and cannot be accessed from the outside. Therefore, the Application Antenna can only be measured with a so-called Over-the-Air (OtA) testing system. A simulation model will consist of an IC including package, whereby the antenna will be controlled separately. In this case the effect of the package or housing on the behavior of the antenna can be studied.

The design steps are visible within the four worlds in Fig. 1.5 and will be discussed in further detail throughout this thesis. The design steps are defined as:

- Research requirements¹².
- Analytical / numerical modeling.
- Realization of the model.
- Measurement system.
- Measurement.

The bi-directional arrow situated between the ‘Analytical / numerical modeling’ and ‘Realization of the model’ illustrates the verification process. This means that for instance production tolerances obtained from the ‘empirical world’ are used as input parameters in the ‘Analytical / numerical modeling’ step and the outcome verified in the ‘Realization of the model’ step.

The last world called ‘Influential’ shows the external ‘influences’ (dark gray rectangles) and the associated ‘uncertainties’ (white rounded rectangles) in Fig. 1.5. Each influence is connected to a design step. It should be noted that the influences ‘production tolerance’, ‘material properties’ and ‘connection / excitation’ are connected to a design step in the ‘Symbolical’ and in the ‘Empirical’ world. This relationship is expressed with the purple arrow meaning that the model can be tuned iteratively with input from, for instance, the manufacturer for production tolerances. With these input parameters a sensitivity analysis can be performed during the analytical / numerical modeling step to predict the effect of these uncertainties on the behavior of the antenna. This procedure could help to justify the choice for a certain production technology or standard. This will be discussed in more detail in this thesis. Eventually, the influence and uncertainty that are addressed will be investigated on its impact on the characteristic of a millimeter-wave antenna.

¹²The research requirements result in a *true value* (see Chapter 2, Section 2.4) for each antenna characteristics. The antenna characteristics can be, gain pattern, radiation intensity, directivity and gain, radiation efficiency and power gain, input impedance, effective length, bandwidth, effective aperture and antenna polarization, to mention a few.

1.7 New millimeter-wave anechoic chamber

The observer

With all the knowledge and experience gained during this research, a new measuring chamber has been developed. The millimeter wave anechoic chamber is depicted in Fig. 1.6 (half open for illustration purposes). The uniqueness about the design of this antenna measuring chamber is that an attempt has been made to minimize the influences (observer effect) of supporting devices such as the motors, probe-station and frequency extenders. This has been achieved by placing these supporting structures as much as possible outside the anechoic chamber.

A mechanically stable environment has been created by complex mechanical constructions. This makes it possible to probe an AoC or AiP without the RF connection being interrupted during the measurement of, for example, gain patterns. By using electrically conductive cloth connecting the translation table to the chamber and connecting the probe holder to the translation table the concept of the Faraday cage is preserved.

By implementing four cameras the movements of the reference antenna can be tracked such that uncertainties in the movement can be quantified and corrected for.

The capabilities of the chamber are:

- Frequency range of at least 20 GHz to 140 GHz (20 GHz to 300 GHz for far-field measurements),
- $\theta = -125^\circ$ to 125° ¹³, with a resolution of 0.1° ,
- $\varphi = 0^\circ$ to 180° , with a resolution of 0.5° ,
- Far- and near-field measurements (both planar and spherical),
- Integrated probe-station,
- Custom designed antenna carrier for supporting a wide range of antenna structures,
- The physical size of the anechoic chamber is (l × w × h) 200 cm × 150 cm × 280 cm, radius of the sphere = 75 cm,
- Fully-shielded anechoic environment.

¹³For this reserach the angles in the spherical coordinate system are defined as, $\varphi \in [0^\circ, 180^\circ)$, $\theta \in (-180^\circ, 180^\circ]$, $r \in [0^\circ, \infty)$.

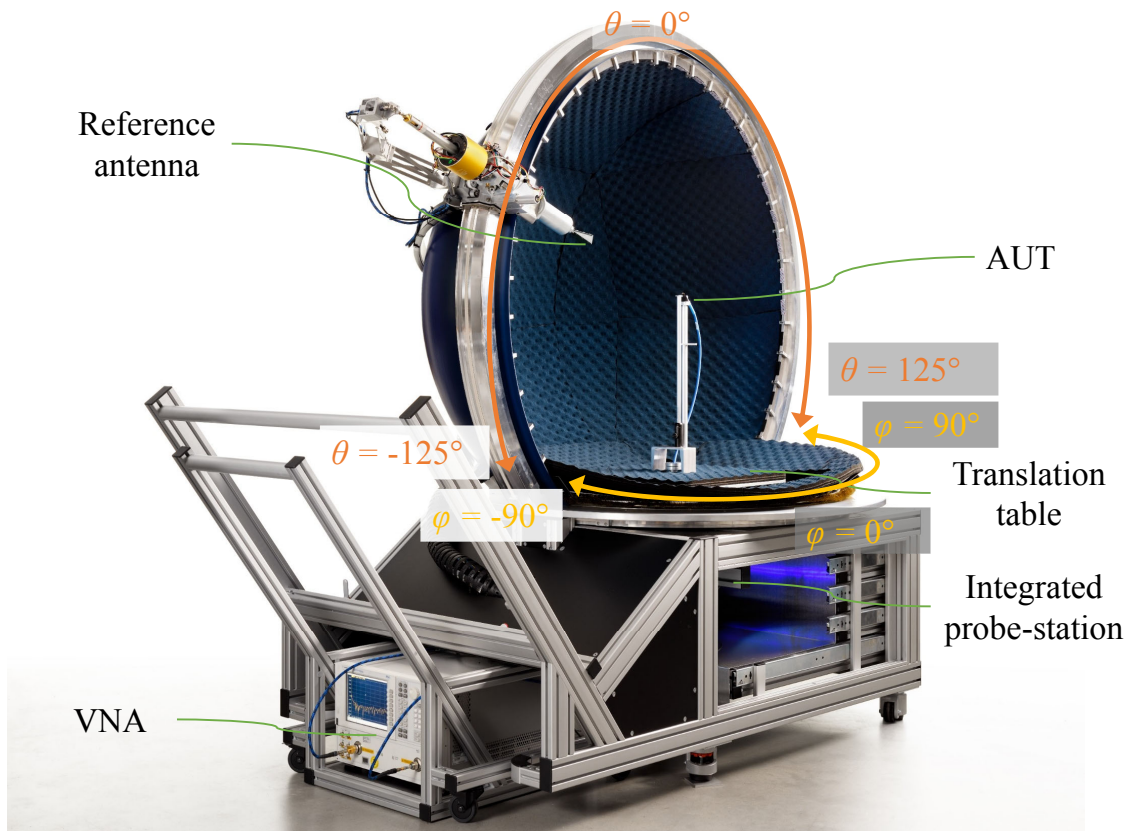


Figure 1.6: The third generation (2022) millimeter-wave anechoic chamber (half open for illustration purposes).

1.8 Objective and outline of this thesis

The aim of this thesis is to investigate the uncertainties in the design and measurement of a millimeter-wave antenna and to propose solutions that minimize the impact of the uncertainties on the antenna characteristics. Thus the research questions are:

“Which uncertainty in the design, modeling and measurement process has the largest influence on antenna characteristics?”

“How accurately can dielectric materials, used to design, support and enclose the antenna structure, be characterized in the millimeter-wave frequency range?”

The outline of this thesis is graphically depicted in Fig. 1.7.

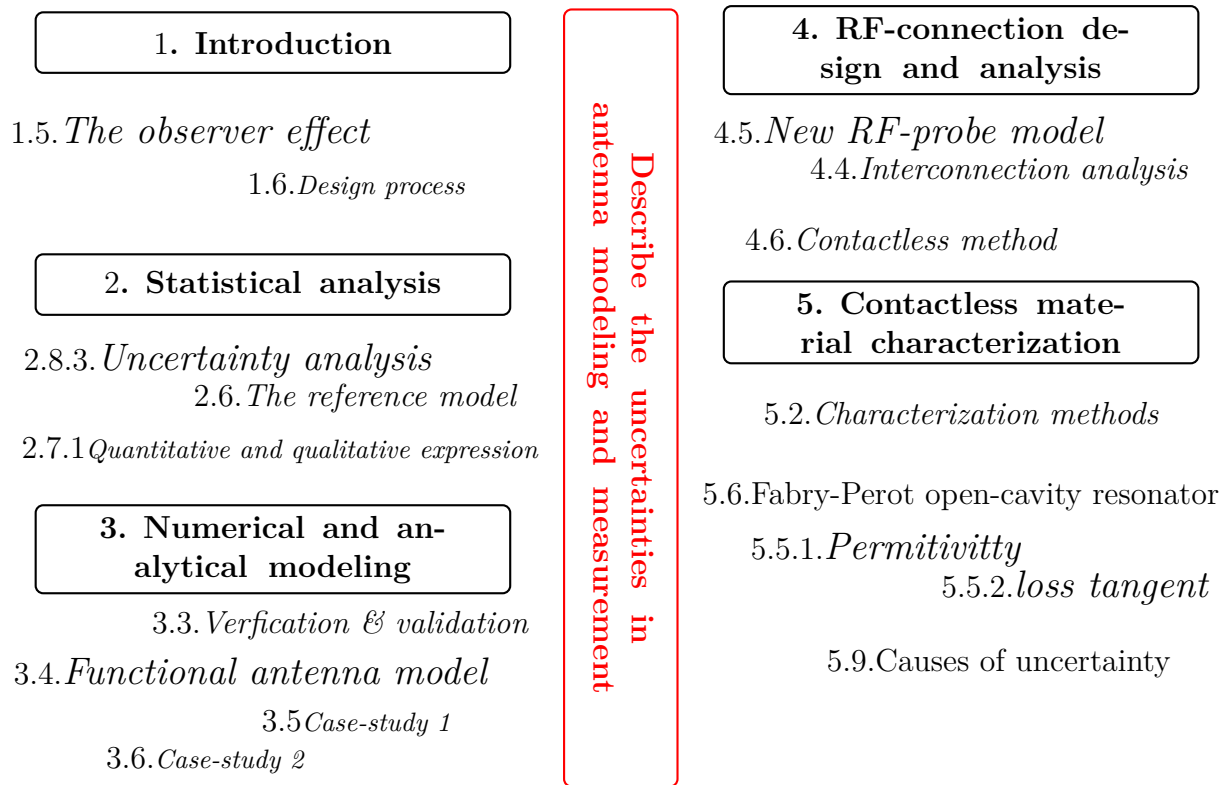


Figure 1.7: Outline of this thesis.

Per chapter the contributions (●) and novelties (■) of this work are indicated:

In Chapter 1 the history of the antenna and the general way of characterizing antennas are described. The essence and value of antenna measurements is emphasized. The main contribution are:

- The definition and importance of measurement in general is described and linked to antenna measurement,
- the understanding of the ‘observer effect’ shows that both measurement instruments as well as the experimenter will influence the measurement results,
- it is concluded that with increasing frequency and thus decreasing wavelength the influence of the close-by environment becomes more distinct than at lower frequencies,
- an extended antenna design process is introduced as a guideline to minimize or to indicate the effect of the observer on the measurement.

Chapter 2 explains how statistical analysis is applied on the results of an analytical or numerical model and on the results of an antenna measurement. The main novelties are:

- Terms and conditions are given of the commonly-used statistical methods and are applied on antenna modeling and measurement,
- two workflows are provided for obtaining both traceable simulation and measurement results.

Chapter 3 introduces verification methods for improving the reliability of the simulation models which are applied to two case studies. The main contribution and novelties are:

- The introduction of a functional decomposition of an antenna system,
- the definition of a reference that could be used for quantifying the antenna characteristics obtained via simulation and or measurement results,
 - explanation of the verification and validation of a simulation model,
- the effect of simulation settings on the outcome of the simulation results of an antenna,
 - results based on a probabilistic sensitivity analysis for gaining insight into which tolerance has the largest influence on the expected behavior of the antenna.

Chapter 4 describes the design and analysis of various types of RF-connectors and their effect on the behavior of the antenna. Because of the complexity, an entire chapter is devoted to this topic. The main contribution and novelties are:

- physical effects like unwanted radiation caused by the transition of a type of RF-connector to a transmission line have been investigated and described,
- a new design of an RF-probe is introduced,
 - the feasibility of a contactless method is studied.

Chapter 5 describes the analysis and outcome of a millimeter-wave Fabry-Pérot open-cavity resonator with two identical spherical concave mirrors. This material characterizing system is used for characterizing dielectric materials that are used for designing and / or enclosing an antenna. As discussed in Chapter 3, limited information of properties of dielectric materials at millimeter wave frequencies (30 GHz to 300 GHz) is available. The main contribution and novelties are:

- A probabilistic sensitivity analysis of the Fabry-Pérot open-cavity resonator with two concave mirrors is performed to determine the achievable significance and accuracy of the measured relative permittivity and loss tangent,

- the permittivity of air is measured to determine the accuracy of the measurement system,
- causes of uncertainty are investigated, described and expressed as a combined standard uncertainty and an expanded uncertainty.

CHAPTER TWO

Applying statistical analysis to antenna research and design

“If your experiments needs statistics you ought to perform a better experiment”
(Lord Ernest Rutherford 1871-1937)

2.1 Introduction

In Chapter 1 it was stated that every step in the antenna design process is subject to uncertainties, except the ‘research requirement’ step¹. These uncertainties must be specified first before they can be correlated with specific antenna characteristics. This approach allows us to determine which uncertainty has the highest impact on a certain antenna characteristic. In order to quantify the impact of an uncertainty, the usage of some form of statistical analysis is necessary. Since the use of statistical analysis is not very common in the antenna community, this chapter will begin with a brief summary of the most common statistical terms and conditions. In the second part of this chapter, two workflows are presented, the first related to analytical and numerical modeling and the second to measurements. In addition, specific statistical tools is described with which the data resulting from modeling and measurement can be analyzed. Finally, the way in which the data should be presented is explained.

¹Although the research requirements themselves can be subject to uncertainties, for example, which value to choose for the antenna gain. This is independent of the uncertainties that arise from modeling, realizing and measuring the antenna compared to the model based on the research requirements.

2.2 Terms and conditions in statistics

Statistics is a branch of mathematics dealing with the collection, analysis, interpretation, presentation, and organization of data [52], [53]. The goal of statistics is to find an answer to a research question. A research question that is discussed in this thesis is:

“which uncertainty has the most significant impact on a certain antenna characteristic during modeling and measurement?”

2.2.1 Subareas in statistics

Data statistics is organized in three subareas. The first subarea is ‘descriptive’ statistics (parametric²), and summarizes a given data set, which can be either a representation of the entire or a sample of a population_{A.1.38}³. Descriptive statistics are broken down into measures of central tendency (mean_{A.1.2}, etc.) and measures of variability (variance_{A.1.61}, etc.).

The second subarea is ‘inferential’ statistics (non-parametric), which uses a random sample of data taken from a population to describe and make inferences about the population.

The third subarea is ‘exploratory data analysis’ (EDA) [54], which is a combination of the other two subareas.

2.2.2 Level of measurement

Statistical measures like standard deviation, mean or mode are categorized in so-called ‘scales of measure’ or ‘levels of measurement’ [55], [56] (see Table 2.1). This topology of classification of data was proposed by S.S. Stevens in 1946 and describes the nature of information within the values_{A.1.60} assigned to variables [57]⁴.

Table 2.1 shows four levels of measurement: nominal, ordinal, interval and ratio. The different levels of measurement are described as follows:

- A nominal variable (e.g. 1), 2), etc.) does not stand for order or numerical significance. For example, labeling an antenna type like 1) monopole and 2) dipole could also be labeled 2) monopole and 1) dipole without changing the content.

²The main difference between non-parametric and parametric data is that from the latter the probability distribution_{A.1.41} (see Subsection 2.3.1), mean and/or standard deviation_{A.1.54} are known.

³These subscripts refer to Appendix A.1.

⁴Other, more detailed topologies are presented in [58], [59] but are seldom used.

- An ordinal variable is a variable for which the order is of importance but not the difference between the values. For example, expressing the happiness you experience when designing an antenna can be done by using a range from 1 to 10 where 1 stands for being unhappy and 10 for being very happy.
- An interval variable is a variable for which the difference between values is of importance like for instance, time or more specific for antennas the directivity function value.
- A ratio variable has all the properties of an interval variable and also has a clear definition of zero. Examples of a ratio variable are temperature in Kelvin (K), height, weight and more specific for antennas, gain.

Table 2.1: Levels of measurement classifying the collected data.

| Level of meas. | Category | Test condition | Condition for the data | Measures |
|----------------|-------------|-------------------------|------------------------|---|
| Nominal | Categorical | Non-parametric | No order | Mode, counts and frequency ^{A.1.26} . |
| Ordinal | Categorical | Non-parametric | Order | Mode, counts, frequency, median, minimum, maximum and range. |
| Interval | Numerical | Parametric ⁵ | No true zero | Mode, counts, frequency ⁶ , median, minimum, maximum, range, mean, variance, and standard deviation. |
| Ratio | Numerical | Parametric | True zero | Mode, counts, frequency, median, minimum, maximum, range, mean, variance, standard deviation, and ratio. |

The columns ‘Category’ and ‘Condition for the data’ in Table 2.1 specify the minimum condition that the data must meet to fall into one of the levels of measurement. The column ‘Test condition’ specifies if the applicable statistical test needs random values for input parameters like the mean, standard deviation etc.. In the column ‘Measures’

⁵In [60] it is noted that for the non-parametric test it is allowed that data can be measured on interval and ratio scale.

⁶In statistics, the frequency (or absolute frequency) of an event is the number of times an observation occurred or was recorded in an experiment or study [61].

mathematical operations that can be applied to a set of data are related to a level of measurement.

As can be seen from the descriptions of descriptive and inferential statistics, both statistical techniques can be used to analyze the data obtained via antenna simulation. This is mainly because computational algorithms or simulations, which rely on repeated random sampling⁷, can generate enough random values. This cannot be said for antenna measurements_{A.1.30}. These types of measurements can only be repeated to a limited extent, otherwise system uncertainties like for instance, frequency drift[63], will play a larger role than the repeatability of the measurements_{A.1.30}. In this case, only inferential statistics can be applied.

2.2.3 Definition of higher order statistics

In statistics, the term higher-order statistics (HOS) refers to measures that use the third or higher power of a sample value. This is in contrast to more conventional techniques of lower-order statistics, which use constant, linear and quadratic terms. Examples of low-order statistics are:

- arithmetic mean (first order),
- variance (second order).

Examples of high-order statistics are:

- skewness (third order),
- kurtosis (fourth order).

HOS is mainly used in estimating shape parameters, such as skewness and kurtosis, such as when measuring the deviation of a distribution from the normal distribution (see Appendix A.2). Because of the higher powers, HOS is significantly less robust than lower-order statistics. During this research the focus will be on the measures of the lower-order statistics.

2.3 Probability function

For all data to which probability analysis can be applied, the probability distribution function must be determined before, for instance, the mean or standard deviation can

⁷Well-known computational algorithms supplying random values are the probabilistic sensitivity analysis and Monte Carlo method [62].

be derived. The probability distribution function may refer to, a cumulative distribution function (CDF) , probability mass function_{A.1.42} (PMF) or, probability density function_{A.1.42} (PDF). The CDF can be used for both continuous and discrete (integers) data. Unlike the CDF, the PMF can only be applied to discrete and the PDF only to continuous data. Because the data obtained for this research is always continuous only the CDF and PDF will be used.

2.3.1 Probability distribution function versus cumulative distribution function

Illustrated in Fig. 2.1 is an example of a normal or Gaussian PDF (black-line) and CDF (blue-line). Indicated in this figure on the x -axis are the standard deviation σ of the population, the significance interval α , the confidence interval_{A.1.6} or _{A.1.7} p, and the Z-score⁷. The population mean μ is illustrated with the vertical dashed dotted black line and the confidence interval with the horizontal ticks. The dashed blue line illustrates the probability correlation_{A.1.10} between the CDF and PDF for variable x .

The PDF shown in Fig. 2.1 is used to specify the probability that a random variable_{A.1.45} x falls within a particular range of values. The normal density function \mathcal{N} is given by [1]:

$$\mathcal{N}(\mu, \sigma^2) = \frac{1}{\sqrt{2\pi\sigma^2}} e^{-\frac{(x-\mu)^2}{2\sigma^2}}, \quad (2.1)$$

where x is a random variable (observation) and σ^2 is the variance. The normal cumulative distribution function is used to express the probability that a random variable takes on a value less than or equal to x and is given by [1]:

$$\text{CDF} = \frac{1}{2} \left[1 + \text{erf} \left(\frac{x - \mu}{\sigma\sqrt{2}} \right) \right], \quad (2.2)$$

where ‘erf’ is the error function⁸ [65], which is expressed as [1]:

$$\text{erf}(a) = \frac{2}{\sqrt{\pi}} \int_0^a e^{-t^2} dt. \quad (2.3)$$

⁷A Z-score is the number of standard deviations a data point is away from the average.

⁸James Glaisher (1809 - 1903) introduced the symbol ‘erf’ in 1871. The abbreviation ‘erf’ was proposed on account of its connection with “the theory of Probability, and notably the theory of Errors”. [64]

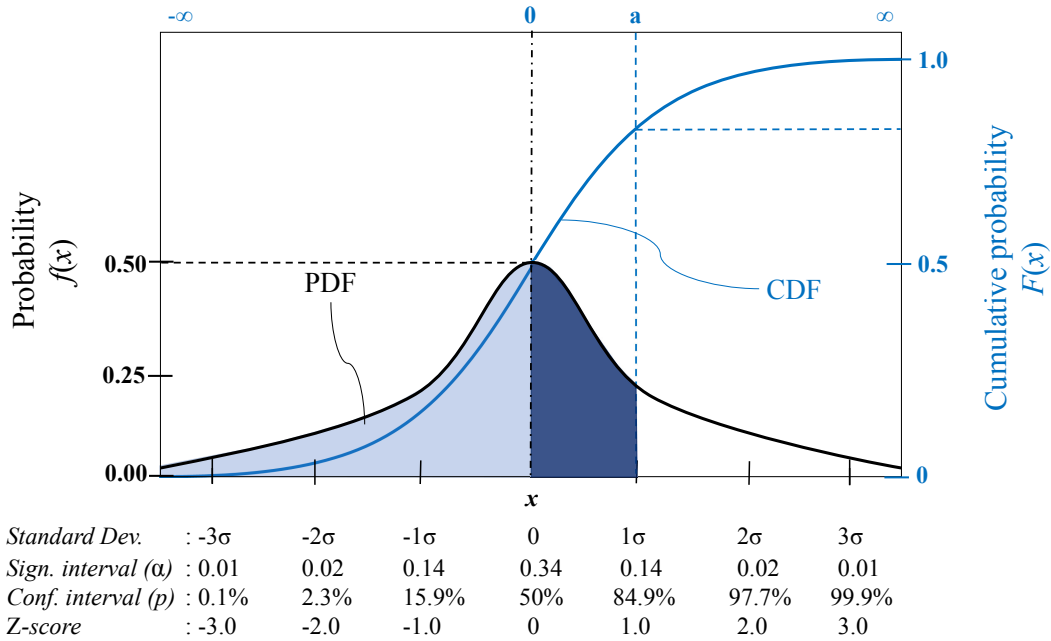


Figure 2.1: The black line illustrates a normal probability distribution function (PDF). The standard deviation σ , significance interval α , the confidence interval p (expressed with the confidence coefficient $A_{1.5}$ $[(1 - \alpha)100]\%$), and the Z-score (see Section 2.3.3) are shown on the x -axis with mayor ticks representing the interval. The dashed/dotted line represents the mean μ . The blue solid line illustrates a cumulative probability function (CDF) with error function $erf(x)$ to determine, for instance, the dark blue area, of the PDF falling in the range $[0, a]$.

2.3.2 Central limit theorem and law of large numbers

In statistics, a population is:

“the totality of items under consideration” [1].

Fig. 2.2, illustrates such a population with an Euler diagram [50] (ellipse with a solid black line).

The items or random variables⁹ x are illustrated with the solid gray dots. The samples are illustrated as elliptic diagrams (solid line colored blue, red and green) filled with a certain number of measurements belonging to the population. Each sample could have a PDF and sample mean \bar{x} that is different from the population PDF and mean.

⁹Other synonyms are observations or measurements.

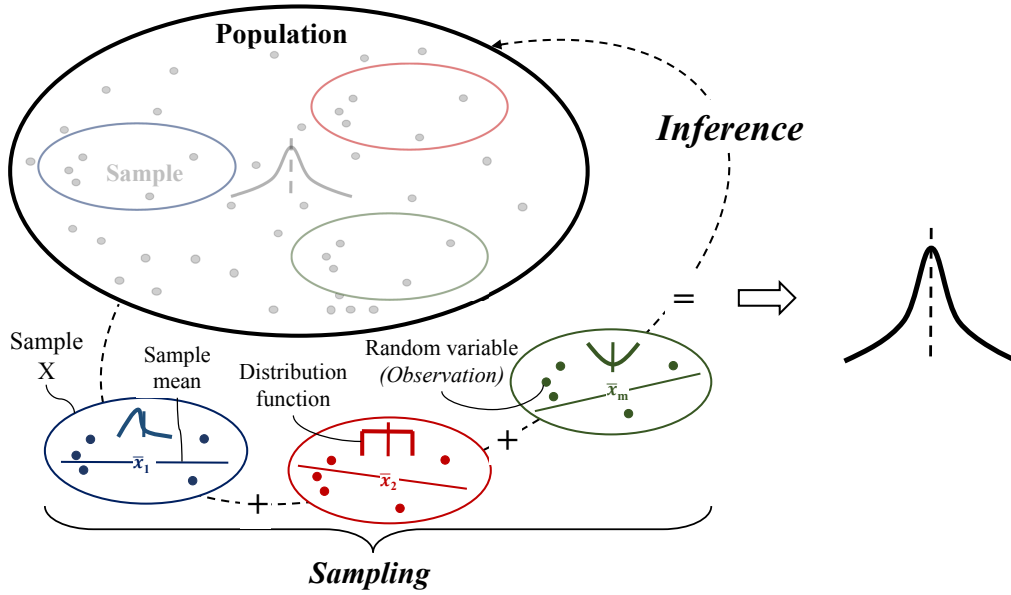


Figure 2.2: The population is illustrated with an Euler diagram (solid black ellipse) with ‘the totality of items’ as solid gray dots. The samples (ellipses with solid colored lines) withhold x_n items (solid colored dots) from the population and have a certain distribution function. Here \bar{x}_m , where $m = 1, 2$, etc., is the m^{th} sample mean illustrated with a solid colored line. From the sampling of sample means the inference is made that the distribution of the sample means is assumed to be normally distributed if N goes to ∞ .

In Fig. 2.2, it is assumed that the distribution of the sample means is normal regardless of the distribution function of the individual samples. This assumption is justified as is described by one of the most important theorems in probability, the Central Limit Theorem (CLT), which states that [66]:

when a large number of independent and identically distributed (i.i.d.) random variables x are selected from the population and the mean is calculated for each sample then the distribution of these i.i.d. sample means \bar{x} will assume the normal probability distribution.

Suppose that x_1, x_2, \dots, x_n are i.i.d. random variables with expected values $E[x_n] = \mu < \infty$ and variance $\text{Var}(x_n) = \sigma^2 < \infty$. Then according to the above, the sample mean [1]:

$$\bar{x} = \frac{x_1 + x_2 + \dots + x_N}{N}, \tag{2.4}$$

approaching mean $E[\bar{x}] = \mu$ and variance $\text{Var}(\bar{x}) = \sigma^2/N$. Thus the normalized random variable [1]:

$$Z_m = \frac{\bar{x} - \mu}{\sigma/\sqrt{N}} = \frac{x_1 + x_2 + \dots + x_N - N\mu}{\sqrt{N}\sigma}, \quad (2.5)$$

has mean $E[Z_m] = 0$ and variance $\text{Var}(Z_m) = 1$. Z_m ‘converges in distribution to the standard normal CDF as N tends to go to infinity.

It is impossible to meet the definition of a population for a specific antenna measurement because the totality of an antenna measurement is not bounded.¹⁰ In addition, the definition of the central limit theorem states that the number of variables (items, measurements) taken from a population must be large. With an unbounded population the number of variables would grow to infinity.

As an illustration, the CLT is evaluated with complex-valued data (\Re , \Im) obtained via a transmission measurement S_{12} between two standard gain horn antennas, placed at a fixed position, at 85 GHz in an anechoic environment. The data is processed with different sample sizes and M sample means \bar{x} as shown in Fig. 2.3.

Comparing the results of Fig. 2.3(a) and 2.3(b) it becomes clear that the PDF in both cases is positive or right-skewed. This means that, only adjusting the sample size N is not sufficient for the measured data to become normally distributed. It should be noted that the width of the right-skewed (see Appendix A.3) distribution becomes narrower with increasing sample size. However, when the number of sample means is increased with a limited sample size, the data tends to become normally distributed as shown in Fig. 2.3(d) (see Appendix A.4). It appears that there is a limit with regard to the number of sample means as shown in Fig. 2.3(c) before it becomes normally distributed. The boxplots show that the number of outliers (purple circles) decreases with increasing number of samples.

The mean (green cross) and median (red line) become equal, which is a mandatory condition for a normally distributed function (see Appendix A.2). The bin size of the histograms shown in Fig. 2.3 is determined by using the Freedman–Diaconis rule [67] $2 \left(\text{IQR}(X) / \sqrt[3]{N} \right)$. The $\text{IQR}(X)$ is the interquartile range (25% to 75%) of the data and N is the number of observations in the sample X .

¹⁰For example, all male with blue eyes in the Netherlands is a bounded population based on three criteria namely, male, the Netherlands and blue eyes.

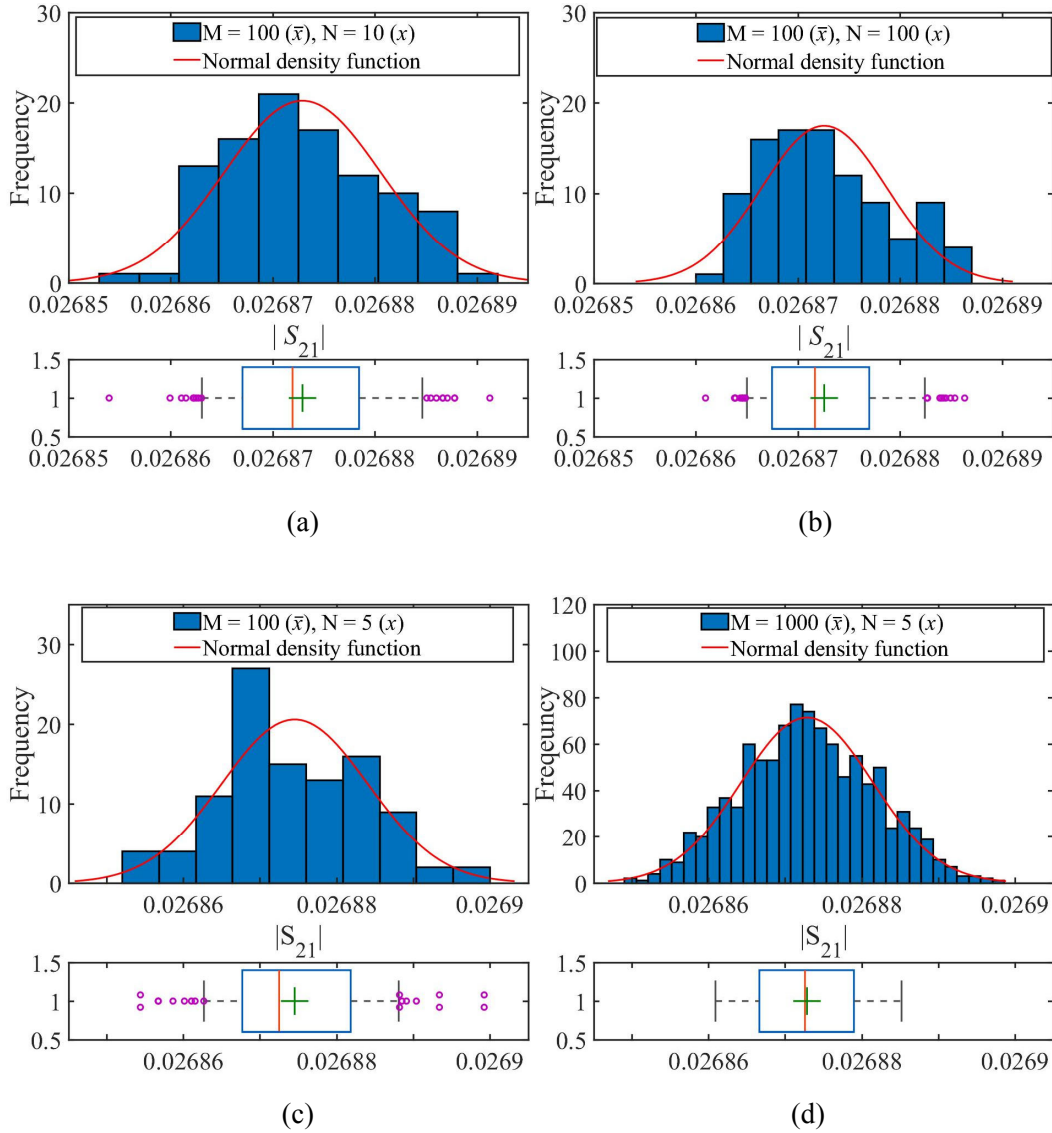


Figure 2.3: Measurement data is obtained with a transmission coefficient S_{21} measurement between two horn antennas, placed in a fixed position, at 85 GHz. The measurement data is used to show how difficult it is to determine if the data is normally distributed. The results are plotted in histograms. The data consist of 100 sample means \bar{x} for (a) $N = 10$ observations x and, (b) $N = 100$ observations. The data consist of $N = 5$ observations for (c) $M = 100$ sample means and, (d) $M = 1000$ sample means. The normal distribution $\mathcal{N}_{\mu, \sigma}$ (red solid line) is for comparison. The box plots underneath the histogram show the difference between the median (red line) and the mean (green cross). The outliers are depicted by purple circles.

Because of the limited number of random variables x , the mean is also an estimation_{A.1.22}. Therefore, another important theorem, the law of large numbers (LoLN), also known as Bernoulli's theorem states [68]:

for a sample of i.i.d. random variables x , as the sample size N grows, the sample mean \bar{x} will tend toward the population mean.

This theorem consists of two versions namely the weak law of large numbers (WLLN) and the strong law of large numbers (SLLN). The difference between them is that the WLLN refers to convergence in probability \mathbb{P} , whereas the SLLN refers to almost sure convergence. The WLLN is expressed as [68]:

$$\lim_{N \rightarrow \infty} \mathbb{P}(|\bar{x} - \mu| \geq \epsilon) = 0. \quad (2.6)$$

With this equation it is expressed that if N approaches infinity, the probability that the sample mean \bar{x} deviates from the population mean μ with error ϵ , equals zero. The SLLN is expressed as [68]:

$$\mathbb{P}\left(\lim_{N \rightarrow \infty} \bar{x} = \mu\right) = 1. \quad (2.7)$$

The difference between the weak and strong law is very subtle and mainly in the definition of convergence. The same measured data that is used for the CLT (see Fig. 2.3) is now used to illustrate the effect of using a limited number of samples as shown in Fig. 2.4. It can be clearly seen that the deviation from the population mean¹¹ is greatest when the fewest number of sample means are used.

This section has shown that even with a significant number of measured S_{21} data, it is difficult to determine with the help of histograms whether the data is normally distributed. The use of box plots gives more insight into the normality of the data than the histogram by visualizing the mean and the median, for instance. Mathematical techniques to test the data for normality do exist. However, this is out of the scope of this research.

There is another method that can be used to make inferences, even if the data set is small. This method uses re-sampling of the obtained data. This method is called 'bootstrap re-sampling' and is discussed in Appendix A.6. Most of the time the repeated data set obtained via a certain antenna measurement will be much smaller, between 10 and 30 times, as compared to the 10000 repeated S_{21} measurements_{A.1.30} used in

¹¹For illustration purposes the population mean in this case is based on the total number of observations.

this section. A statistical method that can be used on such a small amount of data, recommended by [1], is called Student's t -distribution.

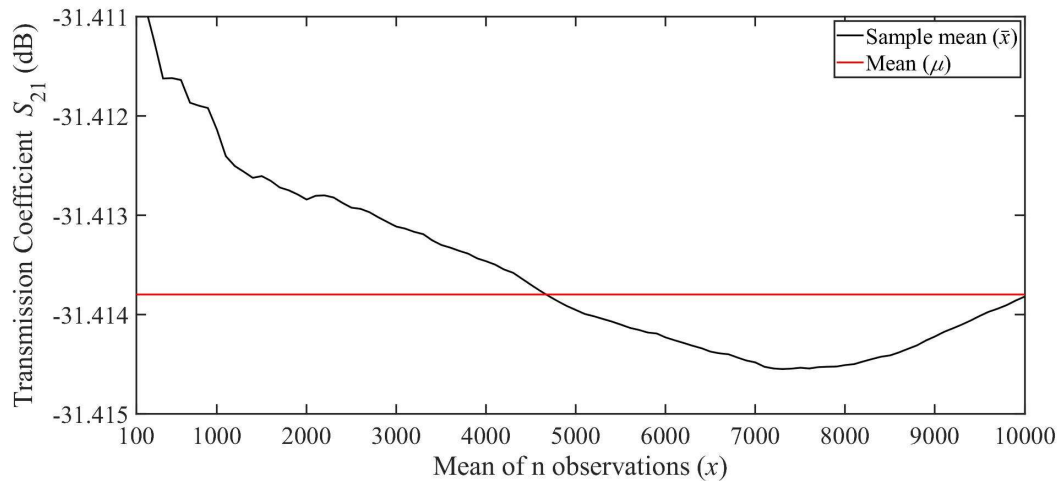


Figure 2.4: The convergence of the sample mean \bar{x} to the population mean μ when the number of independent and identically distributed random variables x increases.

2.3.3 Student's t -distribution

An antenna measuring system_{A.1.36} or antenna characterization can be analyzed on uncertainties by using repeated_{A.1.47} or reproduced_{A.1.48} antenna measurements. However, due to the fact that the number of repeated measurements will be limited, the inferences about the obtained data of a specific antenna characteristic_{A.1.4} will be unreliable.

A statistical tool that can be used for analyzing the data based on a limited number of repeated measurements is the so-called Student t -distribution¹². Student's t -distribution resembles the normal distribution (see Fig. 2.5) depending on the number of observations x and has a probability distribution that can be written as [1]:

¹²In 1908 William Sealy Gosset published a paper [69] about this distribution function under the pseudonym 'Student'. He worked at the Guinness Brewery in Dublin, Ireland and was interested in problems with sample sizes as small as three. Gosset's paper refers to the distribution as the "frequency distribution_{A.1.27} of standard deviations of samples drawn from a normal population". Through the work of Sir Ronald Fisher it became known as Student t -distribution, where the t stands for test value [70].

$$f(t) = \frac{\gamma\left(\frac{v+1}{2}\right)}{\sqrt{v\pi}\gamma\left(\frac{v}{2}\right)} \left(1 + \frac{t^2}{v}\right)^{-\frac{v+1}{2}}, \quad (2.8)$$

where $v = N - 1$ is the number of degrees of freedom¹³_{A.1.13}, t is the test value e.g. observation and γ is the gamma function which generally is defined as [1]:

$$\gamma(N) = \int_0^{\infty} x^{N-1} e^{-x} dx. \quad \Re(N) > 0 \quad (2.9)$$

Equation (2.8) shows that v is a dominant factor shaping the distribution and when v goes to ∞ it approaches a normal distribution as is illustrated in Fig. 2.5.

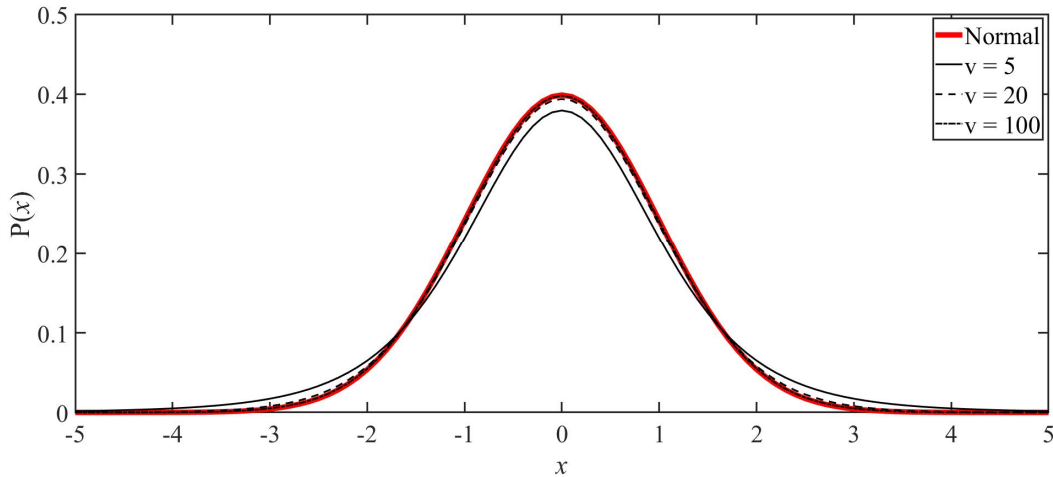


Figure 2.5: Student t -distribution function (normal) with varying degrees of freedom v compared to a normal distribution function (red solid line).

With help of the Z- and T-score the actual coverage factor_{A.1.12} k_p can be determined based on a limited number of observations x . The Z-score is used when the standard deviation is known and the sample size N is larger than 30 observations, otherwise the T-score is used [72].

The Z-score is obtained using [1]:

$$Z = \frac{x - \mu}{\sigma}. \quad (2.10)$$

¹³In statistics, the number of degrees of freedom is the number of values in the final calculation of a statistic that are free to vary [71].

The T-score with a sample estimation of a population, is calculated with [1]:

$$T = \frac{\bar{x} - \mu}{s/\sqrt{N}}, \quad (2.11)$$

where \bar{x} is the mean of a sample and s the standard deviation of a sample. Derived from this equation the T-score can be reconstructed with [1]:

$$\bar{x} = \pm T \left(\frac{s}{\sqrt{N}} \right). \quad (2.12)$$

Instead of calculating the Z- or T-value (k_p) it is possible to use the so-called Z- or T-table (see Appendix A.5) and take one of the values corresponding with the number of observations. Depending on k_p the standard deviation s can be multiplied by this value. For example, when a measurement is repeated 21 times this will lead to a k_p of 1.03 for $1s$ with a $\mathbb{P} \approx 68\%$ and 2.09 for $2s$ with a $\mathbb{P} \approx 95\%$.

2.4 Analysis of variance and correlation

One of the goals of using statistics during this research is to quantify the uncertainties in both the simulation and measurement results of an antenna. If two or more uncertainties are defined then it is important to understand the relationship between the two or more corresponding data sets. There are three important measures to analyze the relationship between the data sets. Two of the three measures are not mentioned in Table 2.1, which are the covariance_{A.1.11} and correlation.

The variance mentioned in Table 2.1 is a measure of dispersion in population and can be used to determine if two random variables (x , y) are i.i.d.. Covariance is a measure of variation and direction between two variables (x , y) in a linear relationship and operates on the values (x_n , y_n) for $n = 1, \dots, N$. With equal probability for x_n , y_n the covariance is generally written as [73]:

$$\text{COV}(x, y) = E[(x - \mu_x)(y - \mu_y)], \quad (2.13)$$

and estimated from samples:

$$\text{COV}(x, y) = \sum_{n=1}^N \frac{(x_n - \bar{x})(y_n - \bar{y})}{N - 1}. \quad (2.14)$$

A positive covariance value means that there is an increasing linear relationship and a negative value indicates a decreasing linear relationship between the two variables (x, y). When the covariance value is zero there is no statistical relationship at all. The covariance matrix is a helpful tool that provides in one overview both variances and the covariances between the various random variables.

Correlation_{A.1.10}, on the other hand, adds not only the direction, as with the covariance, but also the strength of the linear relationship (see Table 2.2) of two random variables (x, y). The correlation ρ is expressed with the following equation [74]:

$$\rho_{x,y} = \frac{\text{COV}(x,y)}{s_x s_y}. \quad (2.15)$$

Where s_x and s_y are the ‘corrected standard deviations’¹⁴ of a sample. The value of the correlation scales between -1 and $+1$. The correlation scale is independent of the scale of the variables themselves where the following apply:

- If $\rho_{x,y} = 1$, then x and y are perfectly, positively, linearly correlated. Positive means they are directly proportional to each other’s mean value, vary in the same direction with the factor of correlation coefficient value.
- If $\rho_{x,y} = -1$, then x and y are perfectly, negatively, linearly correlated. Negative means they are inversely proportional to each other with the factor of correlation coefficient value.
- If $\rho_{x,y} = 0$, then x and y are completely, non-linearly correlated. That is, x and y may be perfectly correlated in some other manner, in a quadratic manner, perhaps, but not in a linear manner.
- If $\rho_{x,y} > 0$, then x and y are positively, linearly correlated, but not perfectly so.
- If $\rho_{x,y} < 0$, then x and y are negatively, linearly correlated, but not perfectly so.

In Table 2.2¹⁵ the classification of the correlation scale¹⁶ is presented.

¹⁴The standard deviation is corrected by applying Bessel’s correction_{A.1.8}, using $N - 1$ instead of N .

¹⁵It should be noted that the scale of the classification of the correlation is dependent on the field of application. For example, there are different scales for the different fields such as politics, psychology and medicine [75].

¹⁶For sake of completeness a correlation of for instance 0.80 is just as high or just as strong as -0.80 .

Table 2.2: Classification of the correlation scale [76].

| # | Correlation | Strength of a linear relationship |
|-----|--------------------------------|-----------------------------------|
| 2.1 | ± 1 | Perfect |
| 2.2 | $\pm(0.80 \text{ till } 1.00)$ | Very strong |
| 2.3 | $\pm(0.60 \text{ till } 0.80)$ | Strong |
| 2.4 | $\pm(0.40 \text{ till } 0.60)$ | Moderate |
| 2.5 | $\pm(0.20 \text{ till } 0.40)$ | Weak |
| 2.6 | 0.00 till ± 0.20 | None to extremely weak |

2.5 Design process

Based on the content and insight gained from the previous sections, statistical terms (see Fig. 2.6 between parantheses) have been added to each design step. The statistical

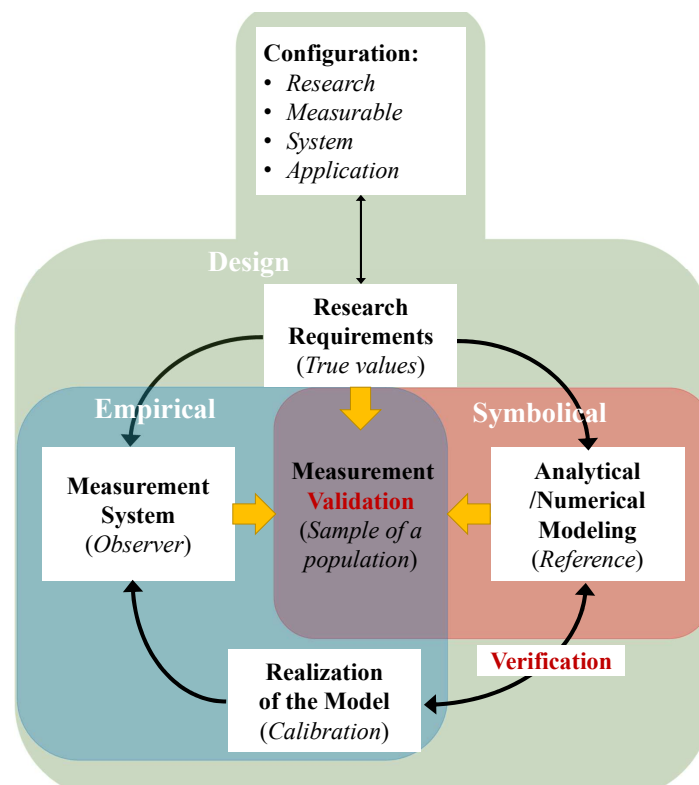


Figure 2.6: The Design paradigm represented by different diagrams with the different design steps as shown in Chapter 1 with statistical terms added, between parentheses, per design step.

term in combination with the relevant design step completes the statistical model. It also indicates the contribution of each step to the design and which data is important to provide. This will be discussed in more detail in the next sections.

2.6 Creating a reference

In sciences like chemistry or biology, it is common to have a so-called ‘reference material’. This reference material is used to check the quality and metrological traceability of products [77], [78]. The reference material is defined as follows [79]:

“Material, sufficiently homogeneous and stable with respect to one or more specified properties, which has been established to be fit for its intended use in a measurement process.”

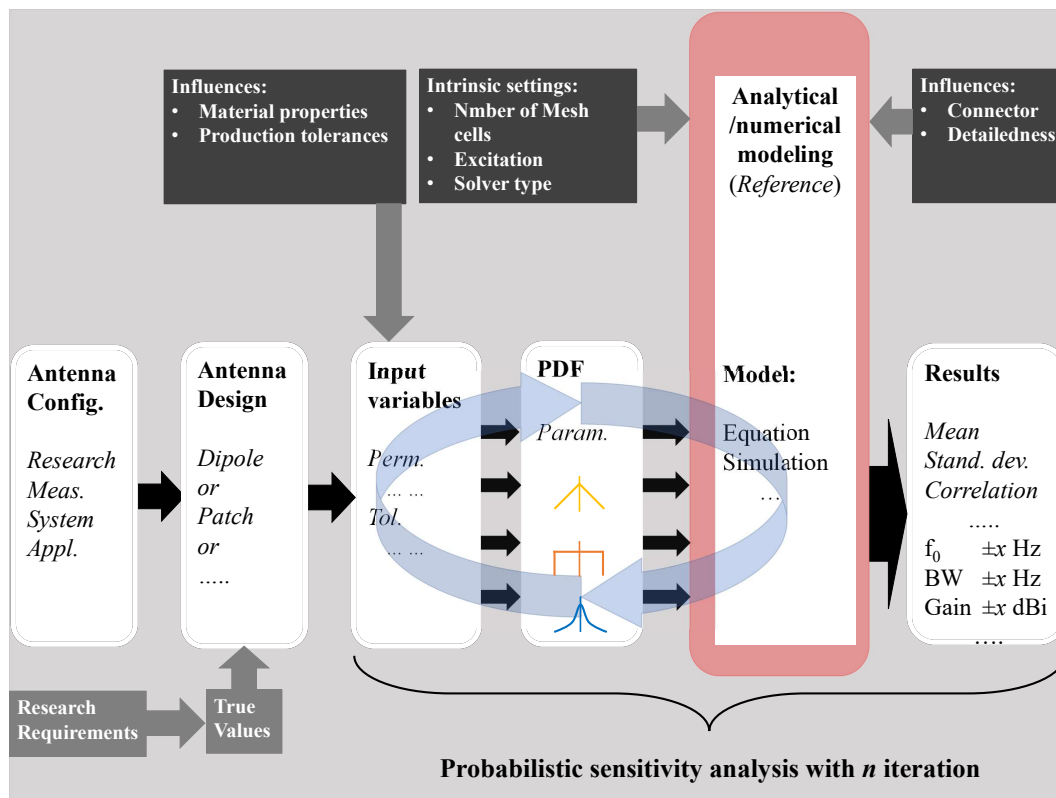


Figure 2.7: Block diagram illustrating the process of creating a reference from an analytical or numerical model. The probabilistic sensitivity analysis (PSA) provides the input data for the model. The probabilistic sensitivity analysis provides output data correlated to the antenna characteristics.

Although creating a standard for a reference (see Chapter 1, Section 1.4) is a topic in

itself, we need to have some sort of reference defined if we want to validate and quantify the measurement results of an antenna under test. In Fig. 2.7 a design process is illustrated enabling to create a reference from an analytical or numerical model.

2.6.1 Modeling process

The purpose of the modeling process as illustrated in Fig. 2.7 is to introduce design choices with settings and values that correspond with reality in a systematic manner as much as possible. This will ultimately result in an accurate, fully described antenna model that can serve as a ‘statistical reference’. It should be noted that although the content of the boxes could vary depending on the type of antenna, the approach of the modeling process remains the same.

In Fig. 2.7 ‘analytical and numerical modeling,’ depicted with the red box, is central. The ‘influences’ are categorized by the dark gray boxes. These influences will somehow affect the antenna characteristics. The extent of the influence will be illustrated with the help of two case studies in the next chapter by using a probabilistic sensitivity analysis. It should be noted that one influence box is made specific and is called ‘intrinsic settings’. This applies only if full-wave simulation software, based on numerical discretization, is used.

The white boxes show - chronologically from left to right - the steps that have to be taken to arrive at a reference model. The first box indicates that a choice must be made as to what type of antenna configuration¹⁷ is used. For example, an antenna on a PCB will need a different design strategy and will have different uncertainties_{A.1.59} than an antenna on a chip will have. To be able to apply a probabilistic sensitivity analysis, both the input variables and their associated PDFs must be determined.

The main idea in this section about making a reference is that as much information as possible about the antenna model should be provided. The antenna characteristics can be described more accurately on the basis of this information. Using error bars, caused by, for example, an uncertainty such as tolerances, the spread caused by these uncertainties can be visualized. If all uncertainties are included in the antenna model, the measurement results of the antenna characteristics must ultimately fall within the error bars. Because there are often several uncertainties, statistical measures such as covariance and correlation can be used to provide insight into the relationship and interaction between the various random variables i.e., input parameters for the antenna model. The input variable with the largest impact requires the highest attention to guarantee a robust antenna design.

¹⁷The selection of the antenna configuration is discussed in more detail in Chapter 1 Section 1.6.

2.6.2 Truncated probability distribution function

As mentioned in Fig. 2.7 the production, in this case of an antenna, is subject to tolerances. The definition of tolerance is:

“the magnitude of permissible variation of a dimension or other measured or control criterion from the specified value.” [80]

When an antenna is produced the production yield is bounded by the chosen tolerance. This means that the PDF must also be bounded [81]. It should be noted that the normal PDF is not bounded. This can be solved by using a truncated PDF from which the mean μ and variance s^2 are those of a normally distributed PDF but now with a truncated range $[a, b]$. The truncated PDF associated with the general normal PDF is created by setting values outside the range to zero, and uniformly scaling the values inside the range so that the integral over the entire range remains unity. The truncation range can be defined for four cases:

- $-\infty = a, b = +\infty$ (non-truncated),
- $-\infty < a, b = +\infty$ (lower truncated),
- $-\infty = a, b < +\infty$ (upper truncated),
- $-\infty < a, b < +\infty$ (double truncated).

The truncated PDF ψ will be symbolized by $(\mu, \sigma, a, b; x)$ where a and b are the truncation interval boundaries. The truncated PDF is evaluated using [82]:

$$\psi(\mu, \sigma, a, b; x) = \begin{cases} 0 & \text{if } x \leq a \\ \frac{\varphi(\mu, \sigma^2; x)}{\Phi(\mu, \sigma^2; b) - \Phi(\mu, \sigma^2; a)}, & \text{if } a < x < b \\ 0 & \text{if } b \leq x \end{cases} \quad (2.16)$$

here,

$$\varphi(0, 1; x) = \frac{1}{\sqrt{2\pi}} e^{(-\frac{1}{2}x^2)}. \quad (2.17)$$

is the probability density function of the standard normal distribution and $\Phi(\cdot)$ is its cumulative distribution function.

$$\Phi(x) = \frac{1}{2} \left[1 + \operatorname{erf} \left(\frac{x}{\sqrt{2}} \right) \right]. \quad (2.18)$$

By definition, if $b = \infty$, then $\Phi((b - \mu)/\sigma) = 1$, and similarly if $a = -\infty$, then $\Phi((a - \mu)/\sigma) = 0$.

After the PDFs are defined probabilistic sensitivity analysis can be used to create a set of random variables by iteration (see Fig. 2.7 blue arrows) as input for the model. Which type of model (analytical or numerical) will be used depends on what model is available for a certain type of antenna.

2.7 Antenna measurement reliability

A typical antenna measurement system_{A.1.36} is illustrated in Fig. 2.8. The setup includes a VNA [see Fig. 2.8(a)]. The VNA is connected to the reference antenna (RA) [see Fig. 2.8(c)] and AUT [see Fig. 2.8(e)] via a cable or waveguide [see Fig. 2.8(b) and Fig. 2.8(f)]. The space between the RA and AUT, illustrated with a dotted circle [see Fig. 2.8(d)], represents the ‘propagation space’ (far-field). The space surrounding the antenna illustrated with the dashed ellipse [see Fig. Fig. 2.8(c) and, Fig. 2.8(e)] represents the ‘reactive space’¹⁸ (near-field).

The objective of an antenna measurement system is to obtain a value of a particular quantity_{A.1.44}, or measurand_{A.1.29}. In this thesis, the quantity to be measured is a time-varying electric field which is the results of a, with an antenna probed, electromagnetic wave.

As illustrated in Fig. 2.8(g) a VNA measures a reflection coefficient S_{11} when a time varying incident electric field is emitted at port 1, and the reflected electric field is obtained at the same port. The VNA measures a transmission coefficient S_{21} when a time varying transmitted electric field is emitted at port 1, and the incident electric field is obtained at port 2. The various antenna characteristics_{A.1.4} that can be measured are summarized in Appendix A.7.

¹⁸Both definitions are described by the author and are not commonly used expressions.

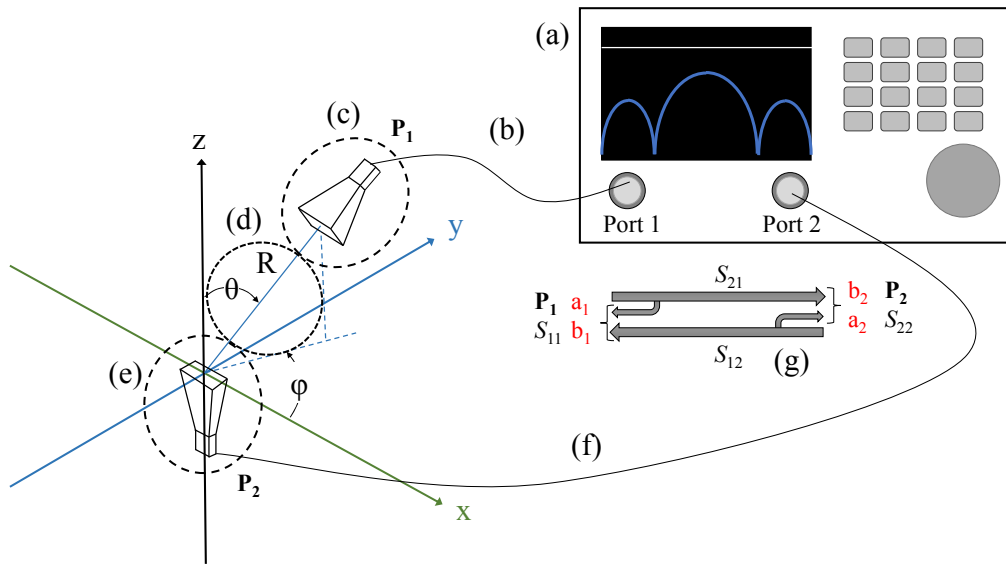


Figure 2.8: Illustration of an over-the-air antenna measurement with: (a) a VNA; (b) transmission medium connected to the reference antenna; (c) The reference antenna and the reactive space (dashed ellipse); (d) propagation space (dotted circle); (e) antenna under test and reactive space (dashed ellipse), and (f) the transmission medium connecting the reference antenna to the VNA. The transmission and reflection coefficients determined with the VNA are illustrated in (g).

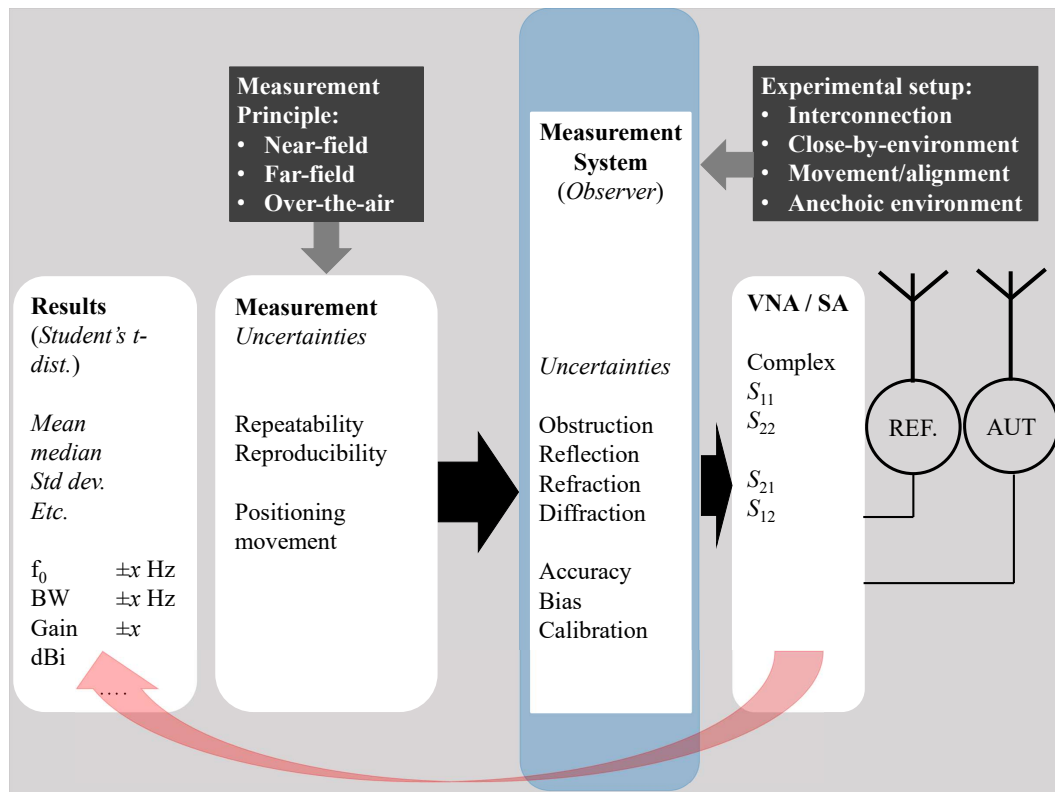


Figure 2.9: Block diagram of obtaining antenna measurement results with help of a VNA.

In Fig. 2.9 the measurement process is illustrated where its purpose and explanation is the same as for the ‘modeling process’ as is discussed in Subsection 2.6.1. The main difference is that a distinction is made between the actual measurement and the measurement principle_{A.1.33}.

2.7.1 Definition of errors, accuracy and uncertainty

The goal of data collection is defined as follows:

“to capture quality evidence that allows analysis to lead to the formulation of convincing and credible answers to the questions that have been posed.” [83]

Therefore, to be able to analyze the data, it needs to be gathered systematically and needs to be thoroughly described. Without a doubt, accurate data collection is essential to maintaining the integrity of the research. Or:

“A formal data collection process is necessary as it ensures that the data gathered are both defined and accurate and that subsequent decisions based on arguments embodied in the findings are valid. The process provides both a baseline from which to measure and in certain cases an indication of what to improve.” [83]

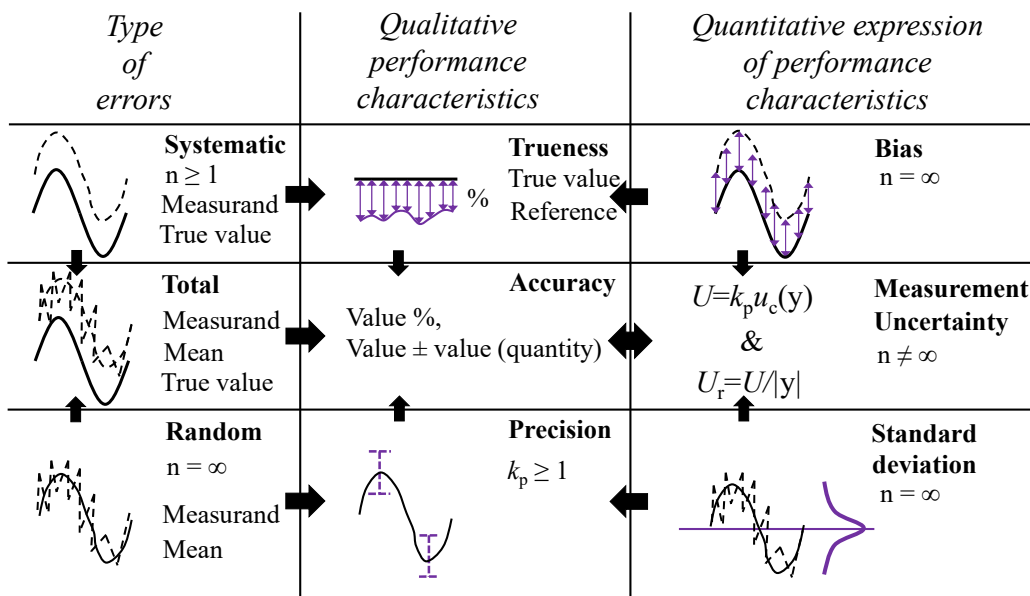


Figure 2.10: Illustration of the interrelations between various error types, the performance characteristics used to estimate_{A.1.21} them and the ways of expressing the estimates quantitatively. n is the number of random variables, k_p the coverage factor, u_c the combined standard uncertainty of a measurement result y , U the expanded and U_r the relative expanded uncertainty.

Unmistakably, the data, collected with a VNA, will have experienced interference on its route, thus introducing both so-called systematic_{A.1.19} and random_{A.1.17} errors. Therefore, detection, as well as quantification of the errors, makes statistical treatment indispensable. However, it has been observed that the understanding, usage and quantification of metrics like trueness_{A.1.53}, accuracy_{A.1.1}, precision_{A.1.39} and measurement uncertainty are not always done consistently [84] -[89]. Fig. 2.10 shows the correct relationship between the various metrics.

The trueness is expressed as a bias_{A.1.3} and can be determined with:

$$T_{\text{Bias}} = \left(\frac{|R_v|}{|R_v - M_v| + |R_v|} \right) 100\%, \quad (2.19)$$

where R_v is the ‘reference value’ and M_v the ‘measured value’. It should be noted that this equation is defined by the author where 100% means true and 0% not true. This equation describes the absolute distance from a certain value to the reference.

The precision, determined with help of the standard deviation σ , is generally expressed with [1]:

$$\sigma \equiv \sqrt{E[(x - \mu)^2]}, \quad (2.20)$$

where μ is the expected value (average) of random variable x . The precision determined with an estimated standard deviation for a population is expressed with [1]:

$$\sigma = \sqrt{\frac{1}{N} \sum_{n=1}^N (x_n - \mu)^2}, \quad (2.21)$$

and the precision determined with a standard deviation for a sample s is expressed with [1]:

$$s = \sqrt{\frac{1}{N-1} \sum_{n=1}^N (x_n - \bar{x})^2}. \quad (2.22)$$

The difference between Equation (2.21) i.e., the standard deviation of a population, and Equation (2.22) i.e., the standard deviation of a sample can be expressed in both quantitative and qualitative differences. The qualitative difference between both equations

is that the population standard deviation is a parameter, calculated from every individual in the population. A sample standard deviation is a statistic¹⁹. It is calculated from some of the individuals in a population. Therefore the standard deviation of a sample will have a greater variability than the standard deviation of a population. The quantitative difference between both equations is subtle. Where calculating the mean, subtracting the mean from each value to obtain deviations from the mean, square each of the deviations, and add together all of these squared deviations are the same. However, we do see a difference in division by N for a population or by $N - 1$ ²⁰ for a sample, which results in an unbiased estimator for the sample variance denoted as s^2 .

2.8 Expressing and evaluating uncertainty in antenna measurement

The content of the ‘International Vocabulary of Metrology’ (VIM) [37] and the ‘Guide to the Expression of Uncertainty in Measurement’ (GUM) [1] forms the basis for this section. The VIM supplies the definition related to measurement in general. For antenna measurements we will adapt the VIM definitions and formulations. The GUM describes the way measurement data can be processed such that the uncertainties_{A.1.59} can be expressed correctly (see Fig. 2.10). Over the years some additions have been developed [92]²¹. An integral part of metrology is evaluating measurement uncertainty. Therefore it could be stated that no measurement is complete without an associated statement of uncertainty. It should be stressed that making inferences about a quantity, for instance an electric field, on the basis of a measurement, is always an estimation_{A.1.22}²².

2.8.1 Classification of components of uncertainty

Uncertainty analysis starts with classifying the obtained data in a Type ‘A’ or Type ‘B’ evaluation²³ where the type ‘A’ evaluation, represented by uncertainty u_n , is defined as a:

¹⁹A statistic (singular) or sample statistic is any quantity computed from values in a sample which is considered for a statistical purpose [90].

²⁰ $N - 1$ is also known as Bessel’s correction [91].

²¹A common rule of thumb is always to repeat your measurement which is based on a saying: “measure thrice, cut once”.

²²A critical remark is that uncertainty is not an error, but an error could be a source of uncertainty.

²³These types of evaluation are not simply corresponding with the classical terms “random” or “systematic” errors (see Subsection 2.7.1).

“method of evaluation of uncertainty by the statistical analysis of series of observations” [37]

The uncertainty component in a Type ‘B’ evaluation, represented by uncertainty u_m , is defined as a:

“method of evaluation of uncertainty by means other than the statistical analysis of series of observations” [37]

A Type ‘A’ evaluation is based on n repeated measurements x where the mean \bar{x} is taken by Equation (2.22). The standard uncertainty $u(\bar{x})_{\text{GUM}}$ in the estimator **A.1.23** is best described by the unbiased²⁴ standard deviation of the mean $s(\bar{x})$ divided by the square root of the number of observations N such that,

$$u(\bar{x})_{\text{GUM}} = s(\bar{x}) = \frac{s}{\sqrt{N}}, \quad (2.23)$$

where s is equal to Equation (2.22).

The sources of $u(\bar{x})_{\text{GUM}}$ for a Type ‘A’ evaluation can be, repeatability **A.1.47**, reproducibility **A.1.48**, tolerances, etc.. The obtained data can be analyzed with the estimated standard deviation termed standard uncertainty $u(\bar{x})_{\text{GUM}}$ and the estimated variance $u^2(\bar{x})_{\text{GUM}}$ of the standard uncertainty. In addition, these sources of uncertainty will be analyzed by carrying out an analysis of variance also known as ‘ANOVA’ (see Section 2.4).

For a Type ‘B’ evaluation the obtained data can be affected by the previous measurement data, experience, knowledge, manufacturer specification, calibration fixture **A.1.25**, tolerance, etc..

The following rule of thumb [93] is often used for classifying the data. When the data is collected by yourself and not older than one year it is categorized as a Type ‘A’ evaluation. If the data is obtained from an external source then it is a Type ‘B’ evaluation.

Combining the classifications of ‘random’ and ‘systematic’ (see Subsection 2.7.1) with categories Type ‘A’ and Type ‘B’ will lead to an alternative nomenclature, namely:

“component of uncertainty arising from a random effect” [94] and,

“component of uncertainty arising from a systematic effect” [94].

Both definitions can be used for either evaluation types, depending on the mathematical process that describes the measurement operation.

²⁴Unbiased standard deviation is symmetric distribution function around the mean where the biased standard deviation is asymmetric around the mean.

2.8.2 Comparing methods for evaluating measurement uncertainty

In [95] it is mentioned that according to the GUM [1] the Type ‘A’ evaluation uses classical probabilistic methods and Type ‘B’ Bayesian probabilistic methods²⁵. The usage of two different methods is inconsistent and is corrected as described in the GUM supplements (SUPP) [97], [98]. However, now there is an inconsistency between the GUM and the SUPP. Although most of the time this inconsistency will not lead to large deviation this is not the case for high frequency electromagnetics where a considerable number of S -parameter inputs can be observed simultaneously. By using the Bayesian approach for the type ‘A’ evaluation the inclusion of the degrees of freedom_{A.1.13} v in the standard uncertainty $u(\bar{x})_{\text{SUPP}}$ of a t -distribution is relevant [95]. The standard uncertainty $u(\bar{x})_{\text{SUPP}}$ is now expressed as:

$$u(\bar{x})_{\text{SUPP}} = \frac{s}{\sqrt{N}} \sqrt{\frac{v}{v-2}}, \quad (2.24)$$

where $v = N - O_p$, with N being the total number of observations and O_p the total number of input quantities,

$$u(\bar{x})_{\text{SUPP}} = \frac{s}{\sqrt{N}} \sqrt{\frac{N - O_p}{N - O_p - 2}}. \quad (2.25)$$

If $O_p = 1$ then Equation (2.24) can be rewritten as:

$$u(\bar{x})_{\text{SUPP}} = \frac{s}{\sqrt{N}} \sqrt{\frac{N-1}{N-3}}. \quad (2.26)$$

The discrepancy between the GUM and the GUM supplements (GUM-S1 and GUM-S2) is clarified by comparing Equation (2.21) with Equation (2.26). For the first equation a minimum of $N \geq 1$ is necessary where in the second equation a minimum of $N = 4$ is enough to define the standard deviation s ²⁶.

When measurements involves multiple complex-valued (\Re , \Im) input quantities, such as the measurement of a vector quantity, a multivariate/joint distribution (\mathbf{X}) should be

²⁵Bayesian statistics is a theory in the field of statistics based on the Bayesian interpretation of probability where probability expresses a degree of belief in an event. The degree of belief may be based on prior knowledge about the event, such as the results of previous experiments, or on personal beliefs about the event. [96]

²⁶For Equation (2.26) it is possible to use $N = 2$. However, this will result in an meaningless square root of -1 .

used according to GUM-S2. The variance and covariance are obtained using a matrix form of Equation (2.26)²⁷ [95]:

$$\mathbf{V}(\mathbf{X}) = \frac{v}{(v-2)} \frac{\mathbf{S}(\mathbf{X})}{N} = \frac{1}{N(N-O_p-2)} \sum_{n=1}^N (\mathbf{x}_n - \bar{\mathbf{x}})(\mathbf{x}_n - \bar{\mathbf{x}})^\top, \quad (2.27)$$

where $\mathbf{S}(\mathbf{X})$, the sample covariance matrix, is expressed as [95]:

$$\mathbf{S}(\mathbf{X}) = \frac{1}{v} \sum_{n=1}^N (\mathbf{x}_n - \bar{\mathbf{x}})(\mathbf{x}_n - \bar{\mathbf{x}})^\top. \quad (2.28)$$

Combining both Equation (2.27) and Equation (2.28) results in the uncertainty matrix [95]:

$$\mathbf{V}(\mathbf{X}) = \begin{bmatrix} u(\mathbf{x}_1)^2 & u(\mathbf{x}_1, \mathbf{x}_2) & \cdots & u(\mathbf{x}_1, \mathbf{x}_n) \\ u(\mathbf{x}_2, \mathbf{x}_1) & u(\mathbf{x}_2)^2 & \cdots & u(\mathbf{x}_2, \mathbf{x}_n) \\ \vdots & \vdots & \ddots & \vdots \\ u(\mathbf{x}_n, \mathbf{x}_1) & u(\mathbf{x}_n, \mathbf{x}_2) & \cdots & u(\mathbf{x}_n)^2 \end{bmatrix}. \quad (2.29)$$

The standard uncertainty $u(\bar{x})_{\text{SUPP}}$ is undefined unless $N > (O_p + 2)$.

For example, the input parameters of a measurement with a VNA are the S -parameters, which represent a single reflection and transmission measurement for a set of ports. Thus a device with O_p ports requires O_p^2 S -parameters to fully characterize the device. Because every S -parameter is complex-valued $S(\Re, \Im)$, $2O_p^2$ of input quantities are required in a measurement model. Because these quantities are correlated with each other, a multivariate distribution must be used (see Section 2.4).

The characterization of a device or antenna with multiple ports O_p could easily result in a large number of measurements N as is illustrated in Table 2.3.

²⁷In Equation (2.27) the $S(X)/\sqrt{N}$ obtained from Equation (2.26) is changed with $S(X)/N$ because the variance is the square of the standard deviation such that the square root in the denominator disappears.

Table 2.3: The minimum number of observations N needed by O_p ports where $Q_{in} = 2O_p^2$ and $N = Q_{in} + 3$ for $u(\bar{x})_{SUPP}$ to be defined [95].

| Ports O_p | Input Q_{in} | Minimum N |
|----------------|-------------------|----------------|
| 1 | 2 | 5 |
| 2 | 8 | 11 |
| 3 | 18 | 21 |
| \vdots | \vdots | \vdots |
| 8 | 128 | 131 |
| 16 | 512 | 515 |

Compared to the number of repeated measurements suggested by the GUM (two observations of any number of input quantities), the number of measurements mentioned in Table 2.3 suggested by the GUM supplement is much larger. In either case, the standard uncertainty of the repeated measurements cannot be obtained accurately enough. In the first case because of the limited number of repeated measurements and in the second case because of the time it takes to perform all the repeated measurements. In [95] it is stated that the GUM supplement approach produces greater uncertainty than the GUM approach. Therefore, further research is needed to find an ideal number²⁸ of repeated measurements from which the standard uncertainty can be accurately obtained.

2.8.3 Uncertainty in antenna measurement expressed step by step

The International Committee for Weights and Measures (CIPM) has provided an approach for expressing uncertainty in measurements. The CIPM approach was adapted by the National Institute of Standards and Technology (NIST) and will also be adapted in this research as follows [94]:

1. **Standard uncertainty** $u(y)$: Express each component contributing to the uncertainty in a measurement as an estimated standard uncertainty.
Relative standard uncertainty u_r : is $u(y)/|y|$ where $y \neq 0$.
2. **Combined standard uncertainty** $u_c(y)$ ²⁹: Combine in u_c all standard uncertainties x_n using the root-sum-of-squares, also known as the error propagation or the propagation of uncertainty.

²⁸In Subsection 2.3.3 Fig. 2.5 it is shown that the Student's t -distribution based on just 20 measurements follows the Normal distribution. The number of 30 measurements is discussed in [99] but in the context of the sample size.

²⁹The combined standard uncertainty is used in Chapter 5, Section 5.7.

The propagation of uncertainty describes the combined uncertainty u_c of multiple sources. This is also called the law of propagation of uncertainty or root-sum-of-squares. The combined standard uncertainty of measurement result y , designated by $u_c(y)$ is the positive square root of the estimated variance $u_c^2(y)$ which is obtained from [94]:

$$u_c(y) = \sqrt{\underbrace{\sum_{n=1}^N \left(\frac{\partial f}{\partial x_n} \right)^2 u^2(x_n)}_{\text{Term I}} + 2 \underbrace{\sum_{n=1}^N \sum_{j=n+1}^N \frac{\partial f}{\partial x_n} \frac{\partial f}{\partial x_j} u(x_n, x_j)}_{\text{Term II}}}. \quad (2.30)$$

‘Term I’ applies to all uncorrelated uncertainties and ‘Term II’ to all correlated uncertainties (see Section 2.4). ‘Term I’ can be rewritten as:

$$u_c(y) = \sqrt{\left[\frac{\partial f}{\partial x_1} u(x_1) \right]^2 + \left[\frac{\partial f}{\partial x_2} u(x_2) \right]^2 + \cdots + \left[\frac{\partial f}{\partial x_n} u(x_n) \right]^2}. \quad (2.31)$$

The approximation for the measurement y is based on x_1, x_2, \dots, x_n input variables. The partial derivatives $\partial f / \partial x_n$, are often referred to as sensitivity coefficients and $u(x_n, x_j)$ is the estimated covariance associated with x_n and x_j .

Relative combined standard uncertainty $u_{c,r}$: is $u_c(y)/|y|$ where $y \neq 0$.

3. **Expanded uncertainty U :** The expanded uncertainty U is determined by multiplying u_c by a coverage factor k_p . U provides an interval with a certain confidence that a value of population Y will fall in. If k_p is not defined we assume $k_p = 2$, following [94].

As discussed in Subsection 2.3.2, the central limit theory states that the distribution of i.i.d. sample means \bar{x} , taken from a population Y , will assume the normal probability distribution. If y is an estimate of Y then the uncertainty can be expressed as $Y = y \pm u_c(y)$.

The uncertainty can be expanded by multiplying it by a k_p :

$$U = k_p u_c(y), \quad (2.32)$$

where U is used to represent a larger confidence interval at level p . Here $k_p = t_p(v)$ where t_p is the t -distribution. The confidence interval is determined from either Equation (2.10) i.e., the Z-score or, Equation (2.12) i.e., the T-score (see Subsection 2.3.3).

4. *Effective degrees of freedom v_{eff}* : The approximation of k_p can be improved by estimating from the effective degrees of freedom v_{eff} . When the different components of uncertainty (Type ‘A’ and / or Type ‘B’) have different values v , then the v_{eff} of each component can be calculated with the Welch-Satterthwaite formula [100]:

$$v_{\text{eff}} = \frac{u_c^4(y)}{\sum_{n=1}^N (u_n^4(y) / v_n)}. \quad (2.33)$$

The coverage factor then becomes $k_p = t_p(v_{\text{eff}})$. For a type ‘B’ evaluation, for which the v is unknown, an estimate of 100 observations can be taken as a conservative estimate [100] (see Fig. 2.5, and Appendix A.5).

5. *Reporting uncertainty*: The following information needs to be included when reporting uncertainty:
- List of components of standard uncertainty with their degrees of freedom v . The components should be identified according to the type ‘A’ and type ‘B’ evaluation.
 - Detailed description of how each component of standard uncertainty is evaluated.
 - Description how the coverage factor k_p is chosen.

2.9 Conclusions

In this chapter the terms and conditions of statistical analysis are described and their applicability to the domain of antenna modeling and measurement is investigated. We have introduced Euler diagrams to describe how to set up an analytical or numerical model so that it can be classified as a reference. An Euler diagram has also been drawn up for antenna measurements. In this case, the description is such that the uncertainties associated with measurements are found, described, qualified and quantified. The procedure based on the uncertainty in measurements which is described by the International Committee for Weights and Measures and used by for instance NIST, is followed.

CHAPTER THREE

Verifying the simulation model to define an antenna reference

“I mean, making simulations of what you’re going to build is tremendously useful if you can get feedback from them that will tell you where you’ve gone wrong and what you can do about it”

(Christopher Wolfgang Alexander 1936 -)

3.1 Introduction

Software packages to numerically solve Maxwell’s equations to simulate antenna designs have been introduced in the past few decades. These software packages have a variety of settings and numerical methods with which it is possible to resolve most antenna structures both quickly and accurately. A good understanding of antenna theory is required in order to make the right choices in software settings, numerical method and mechanical complexity of the antenna design. Moreover, insight and understanding to find the root causes of uncertainties affecting the simulation outcome of the antenna is even more important. A combination of professional knowledge and insight / understanding will lead to an accurate model of an antenna design representing the measurable counterpart, simulation settings and ditto results. In this chapter a schematic representation of the functional parts of a research antenna is presented. On the basis of this schematic representation, a reference of the antenna has been defined. This reference was used to provide insight into the effects of the uncertainties arising from, among other things, the simulation settings and, for example, production tolerances on the behavior of the antenna. This insight into these uncertainties was again done on the basis of two case studies using different verification methods. It will become clear that providing insight into the effect of the uncertainties on the behavior of the antenna by means of a simulation model is necessary in order to provide an accurate prediction of the behavior of the realized antenna.

3.2 Definition of an antenna reference

Analytical methods and numerical simulations are fundamental in science. Simulation, in Latin ‘simulare’, means ‘to copy’. In general, simulation¹ may be defined as creating a model² with a set of conditions in order to study the behavior as it would happen in real-life [101]. In Chapter 2, Section 2.6, Fig. 2.7 the simulation model is illustrated surrounded by different input parameters so that the outcome of the simulation model of the antenna is such that the design can be defined as a reference. The author defines the antenna reference as:

“a simulation model of an antenna design from which all uncertainties are known and the effect from physical phenomena like reflection, refraction³, diffraction⁴ and surface waves [102] (see Appendix C.1) on the antenna characteristics are made insightful.”

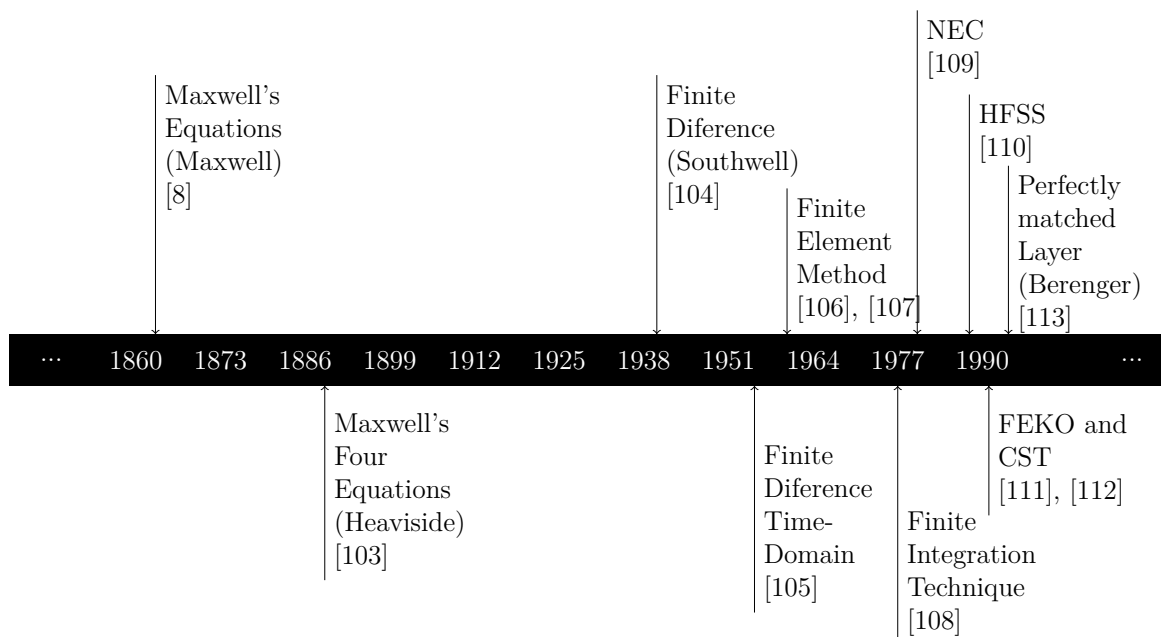


Figure 3.1: Timeline of the evovement of both analytical and numerical methods and different brands of electromagnetic field simulation tools.

¹simulation is the process of using a model to study the performance of a system.

²A simulation model includes its construction and working.

³Deflection from a straight path undergone by a light ray or energy wave in passing obliquely from one medium (such as air) into another (such as glass) in which its velocity is different [50].

⁴A modification which light undergoes especially in passing by the edges of, for instance, opaque bodies or through narrow openings and in which the rays appear to be deflected. A similar modification of other waves (such as sound waves) or of moving particles (such as electrons) [50].

The basis for the simulation model is one of the nowadays available electromagnetic field simulation software tools. Fig. 3.1 shows the evolvment of both analytical and numerical methods related to electromagnetics, making a simulation model of a detailed 3D antenna design possible today.

3.3 Verification and validation method of an antenna simulation model

The ‘verification’ of a model (see Fig. 1.5) is:

“the process of confirming that it is correctly implemented with respect to a conceptual model⁵” [114].

To start, the simulation model of the antenna design must meet the design requirements which form the basis for correctness. Secondly, a verification process must be carried out to gain confidence that the simulation model of the antenna design is an accurate representation of reality. The following verification methods can be used:

- **Using ideal or existing results of a comparable simulation model of an antenna** [115], [116] with which the results of the new antenna can be compared with. This verification step provides reference quantities for antenna characteristics like the antenna gain, gain function, reflection coefficient, half power beam width, etc..
- **Probabilistic sensitivity analysis** which is a study how the uncertainty in the output of a simulation model of an antenna can be attributed to different sources of uncertainty in the inputs. This verification step provides parametric input data according to a certain PDF and can be applied to for instance the material properties [117] of the PCB.
- **Simulation input and intrinsic settings** which are sources of uncertainty [117]. This verification step forces the user to investigate possible effects of certain simulation settings on the behavior of the antenna that are not physical. Consider the type of excitation and port design, the solver type and discretization methods.
- **Contour plots and animating**, for instance, the E - or H -field or current distribution provides insight into what causes certain antenna characteristics to be different than expected. With this method of verification one can conclude whether

⁵A conceptual model is a representation of a system, made of the composition of concepts which are used to help people know, understand, or simulate a subject the model represents. [50]

the unexpected results are due to the simulation settings or are inherent to the new antenna design.

- **Academic (expert) knowledge and expertise** on the topic of antennas and electromagnetics are essential. Although this is the most logical verification step, it sometimes means that more specific knowledge must be acquired before the aforementioned analysis steps can be performed (observer or conformation bias).

The verification process is complemented by a ‘validation process’ (see Fig. 1.5) which is defined as:

“substantiation that a computerized model within its domain of applicability possesses a satisfactory range of accuracy consistent with the intended application of the model” [114], [118].

This means that the antenna measurement results of various antenna characteristics are used to validate the accuracy of the simulated results of the equivalent model of the antenna design.

Another approach is to obtain the measurement results and compare those with the results of a basic simulation model of the equivalent antenna design where differences are expected. By gradually adding more details to the simulation model one gains insight which detail has the most effect on the measurement results i.e.; the antenna characteristics. Examples of details are the RF-connector or the antenna carrier with which it is possible to place the AUT in the antenna measurement setup. This iterative approach will give insight into the uncertainties and its impact on the antenna characteristics.

3.4 Functional parts of an antenna

According to [7] an antenna is ‘that part of a transmitting or receiving system that is designed to radiate or to receive electromagnetic waves’. In Fig. 3.2 we show a functional decomposition of that what we call an antenna⁶. According to the definition from [7] only the part shown in Fig. 3.2(d) is the actual antenna i.e., the radiating part.

However, we usually name all the four parts combined as described in Fig. 3.2 the antenna. These four parts are:

- the radiant part i.e., antenna illustrated in Fig. 3.2(d),

⁶Each type of antenna is composed of the parts described with the functional decomposition model in Fig. 3.2. Depending on the type of antenna the transmission media and / or RF-connector will change. In this chapter, the functional decomposition model is applied to a rectangular inset-fed microstrip patch antenna with a microstrip line.

- the transmission medium illustrated in Fig. 3.2(c),
- the RF-connector interface illustrated in Fig. 3.2(b),
- and the RF-connector illustrated in Fig. 3.2(a).

Because of the unshielded nature of this system the electromagnetic fields, supposed to travel through the transmission line only, also propagate through the air. Physical properties of the wave interaction with the environment are surface waves in the near-field trapped in the substrate, which is part of the transmission medium depicted with the green solid lines. The dashed red lines mimic the reflection on the housing of the RF-connector. The solid purple lines mimic diffraction on the edge of the transmission line corner where the dashed purple circles mimic the resulting unwanted radiating sources close to the antenna. The solid orange circles mimic the unwanted radiation caused by a discontinuity that can be related to the RF-connector interface.

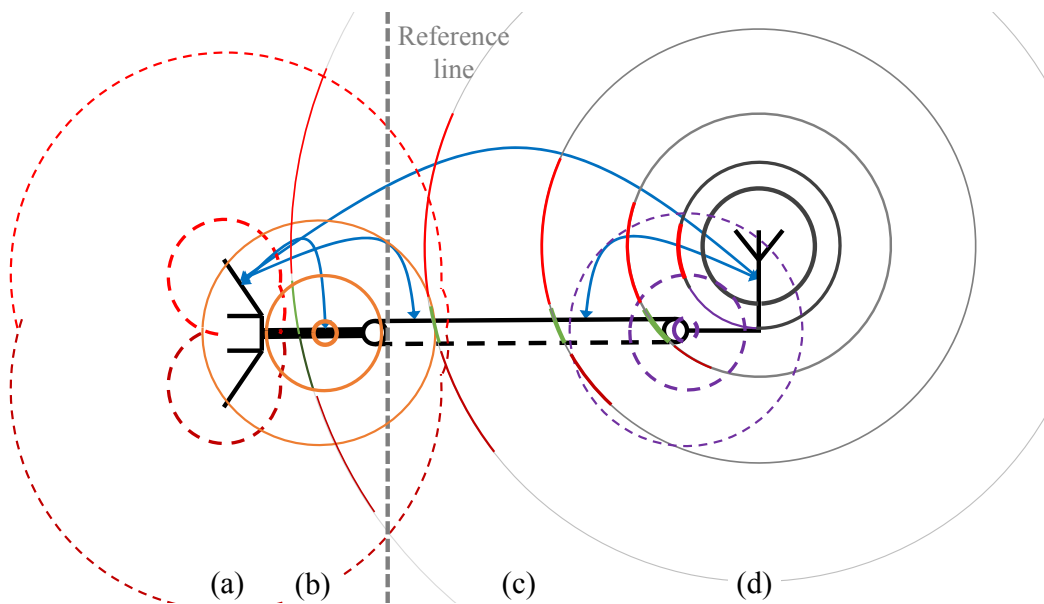


Figure 3.2: Functional decomposition of an antenna system consisting of (a) an RF-connector, (b) an RF-connector interface, (c) the transmission line and, (d) the radiant part i.e., the antenna. All colored lines mimic some sort of radiation except the blue arrows. The green solid lines mimic a surface wave. The dashed red lines the reflection on the housing of the RF-connector. The solid purple lines mimic diffraction on the edge of the transmission line corner where the dashed purple circles mimic the resulting new radiating sources close to the antenna. The solid orange circles mimic spurious radiation caused by a discontinuity that can be related to the RF-connector interface. The solid blue arrows depict the direct coupling between the elements of the measurable antenna and the dashed blue lines the indirect coupling.

The effects of the individual functional parts on the antenna characteristics (direct or indirect coupling, blue lines with arrows) caused by these physical properties have to be investigated. The research that has been done into the coupling between antenna, transmission medium, RF-connector and RF-connector interface will be described in the next chapter.

As discussed in the previous section, an ideal antenna consists of the radiant part only. In reality, there will always be some sort of transmission medium connected to the radiating part. Because we want to determine the influence of the connector, a reference line⁷ has been drawn as shown in Fig. 3.2. It divides the transition of transmission medium to RF-connector interface. Therefore, the antenna will consist of two functional parts namely, the radiating and the guided transmission medium part.

To be able to prove the validity of using a simulation model of an antenna as a reference, two case studies are defined. In both cases the definition of a statistical antenna reference, as presented in Section 3.2, is followed.

In case study 1, which presents a ‘research antenna’ (see Fig. 1.5), the following analysis on the antenna design will be described:

- Random errors (see Fig. 2.10)
 - To show the effect of, for instance, production and material tolerances on the antenna characteristics a probabilistic sensitivity analysis (see Fig. 2.7) is performed.
 - To show which antenna parameter is the most influenced by the tolerance a Pearson-correlation is applied, where the outcome is presented in a correlation matrix (see Section 2.4).
- Systematic errors (see Fig. 2.10)
 - The influence of the simulation software on the predicted behavior of the antenna is investigated, with a specific focus on the choice and design of the port excitation.

In case study 2, which presents a ‘measurable antenna’ (see Fig. 1.5), the following analysis on the antenna design will be described:

- Systematic error (see Fig. 2.10)

⁷Where the reference line is drawn depends on the purpose of the reference. For example, a measurable antenna will have a reference line between the connector and cable coming from the measurement equipment.

- The minimum and maximum values of the tolerance of the material properties and manufacturing tolerances are used as input parameters for the antenna model in the simulation software CST Studio Suite® [112].
- The effect of the port excitation, solver type and model complexity on the antenna characteristics is analyzed (see Appendix B.3)
- Random error (see Fig. 2.10)
 - Repeated antenna measurements of different measurement methods for a circularly polarized rod antenna are performed to show, for instance, the standard deviation of the obtained results (See Appendix B.5 and Appendix B.6).

The goal is to find out how much the various intrinsic software settings and the uncertainties, e.g. tolerances, impact the antenna characteristics. Both cases will present graphs and data, obtained with the simulation model, where from the second case the data will be used to make a comparison with measurements. If the measurement results are within the boundaries or standard deviations of the obtained simulation results of the antenna characteristics then the simulation model is valid.

3.5 Case study 1: linearly polarized rectangular inset-fed microstrip patch antenna

In this case a basic, rectangular inset-fed microstrip patch antenna will be designed, simulated and investigated with help of probabilistic sensitivity analysis simulation. In general the patch antenna (see Appendix B.1) can have one of many shapes and can be excited in different ways. Furthermore, the patch antenna can be implemented in an array or as a single element as is discussed in [119] - [121].

In this case the focus will be on a rectangular inset-fed microstrip patch antenna where its geometry can be determined through analysis with various mathematical methods as is discussed in [122]. These methods include the vector potential approach [123], the dyadic Green's function technique [124], the wire grid approach [125], the radiating aperture method [126], the cavity model approach [127], [128], modal expansion techniques [129] and the differential evolution method [130].

3.5.1 Design requirements

The single element rectangular inset-fed microstrip patch antenna is illustrated in Fig. 3.3. The design requirements are summarized in Table 3.1. It should be noted

that the value of each design requirement is considered a ‘true value’ (see Chapter 2, Section 2.4).

Table 3.1: Design requirements of the rectangular inset-fed microstrip patch antenna.

| # | parameter | Design requirements |
|-----|-----------------------|--------------------------------|
| 3.1 | Center frequency | 85 GHz |
| 3.2 | Bandwidth (-10 dB) | 2% w.r.t. f_0 |
| 3.3 | Gain | 5 dBi |
| 3.4 | Polarization | Linear (vertical) |
| 3.5 | Connection type | Probe, RF-connector, waveguide |

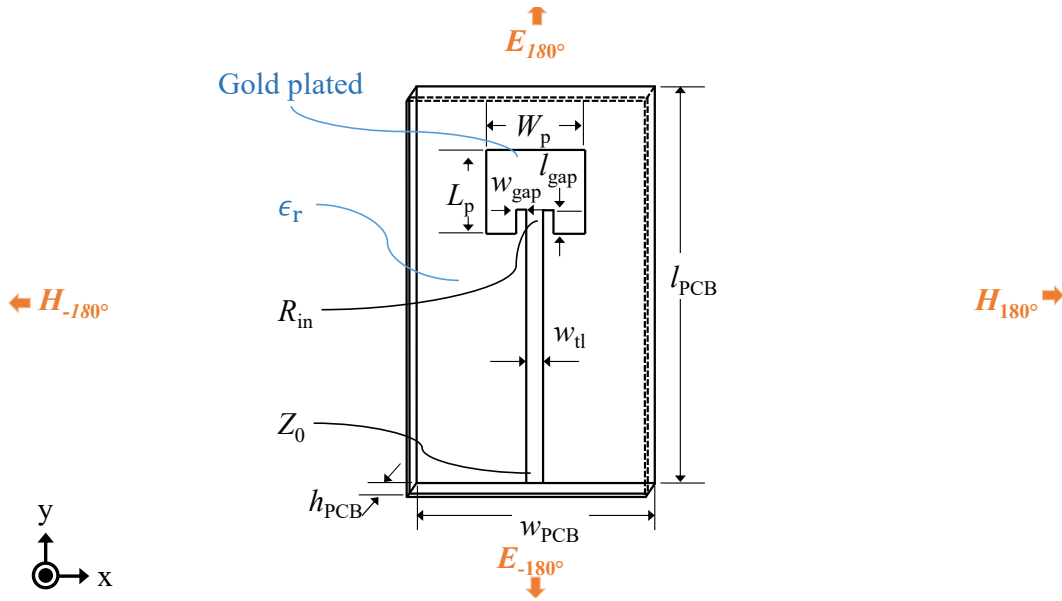


Figure 3.3: Illustration of a rectangular inset-fed microstrip patch antenna with geometrical parameters. The spherical coordinates for the different planes are $\varphi = 90^\circ$, $E_{-180^\circ} < \theta < E_{180^\circ}$ and $\varphi = 0^\circ$, $H_{-180^\circ} < \theta < H_{180^\circ}$.

The ‘transmission line model’ [131] method is used to determine the dimensions of the rectangular inset-fed microstrip patch antenna. The obtained values for the various geometrical parameters (see Fig. 3.3) are summarized in Table 3.2.

Table 3.2: Dimensions of the reference antenna consisting of a transmission medium and rectangular inset-fed microstrip patch antenna (see Fig. 3.3).

| # | parameter | Size (mm) | Equation |
|------|------------------|-----------|----------|
| 3.6 | W_p | 1.210 | (B.4) |
| 3.7 | L_p | 0.940 | (B.8) |
| 3.8 | w_{gap} | 0.080 | (B.10) |
| 3.9 | l_{gap} | 0.394 | (B.12) |
| 3.10 | w_{tl} | 0.240 | |
| 3.11 | w_{PCB} | 10.00 | |
| 3.12 | l_{PCB} | 19.55 | |
| 3.13 | h_{PCB} | 0.102 | |

3.5.2 Outcome of the probabilistic sensitivity analysis

The equations (see Appendix B.1) used to design the geometry of the rectangular inset-fed microstrip patch antenna have in- and output quantities, which are summarized in Table 3.3. The input variables are subject to tolerances caused by material properties and manufacturing techniques. For the tolerances a truncated normal distribution function of $\pm 2s$ will be used, as is discussed in Chapter 2 Section 2.6.2. The values, used for determining the tolerances, are obtained via datasheets, websites of the PCB production companies and scientific literature. Therefore each quantity in Table 3.3 is categorized as a Type ‘B’ evaluation (see Chapter 2, Subsection 2.8.1).

Table 3.3: In- and output parameters of the rectangular inset-fed microstrip patch antenna design.

| # | Eval. Type | Dist. function | Tol. (%) | Input Quantity | Output Quantity | Equation (Appendix B.1) |
|------|------------|----------------|----------|-------------------------|-------------------------|-------------------------|
| 3.14 | B | Trunc. | 3 | ϵ_r | W_p | (B.4) |
| | B | Trunc. | 10 | W_p | f_0 | (B.5) |
| 3.15 | B | Trunc. | 10 | h_{PCB} | ϵ_{eff} | (B.6) |
| 3.16 | | | | ϵ_{eff} | Δl | (B.7) |
| 3.17 | B | Trunc. | 10 | L_p | f_0 | (B.9) |

The tolerances on materials and manufacturing will propagate through the equations, resulting in a spread of for instance the center frequency f_0 .

The results of the probabilistic sensitivity analysis simulation, shown in Fig. 3.4, are presented in a truncated Gaussian distribution (dotted line) which is derived from the

Gaussian distribution (solid line). As can be observed by comparing both distributions the probability is slightly differently distributed and bounded between $\pm 2s$.

Fig. 3.4(a) shows the results caused by varying the width W_p of the patch. The spread of f_0 is 2%. Noteworthy is that the distribution function has a bias of 0.25 GHz. This is believed to be caused by the spread in the width of the patch. As can be observed in Fig. 3.4(b) varying the length L_p of the patch causes a center frequency spread of 9.6%. The difference in frequency spread is obvious because with L_p the f_0 is determined.

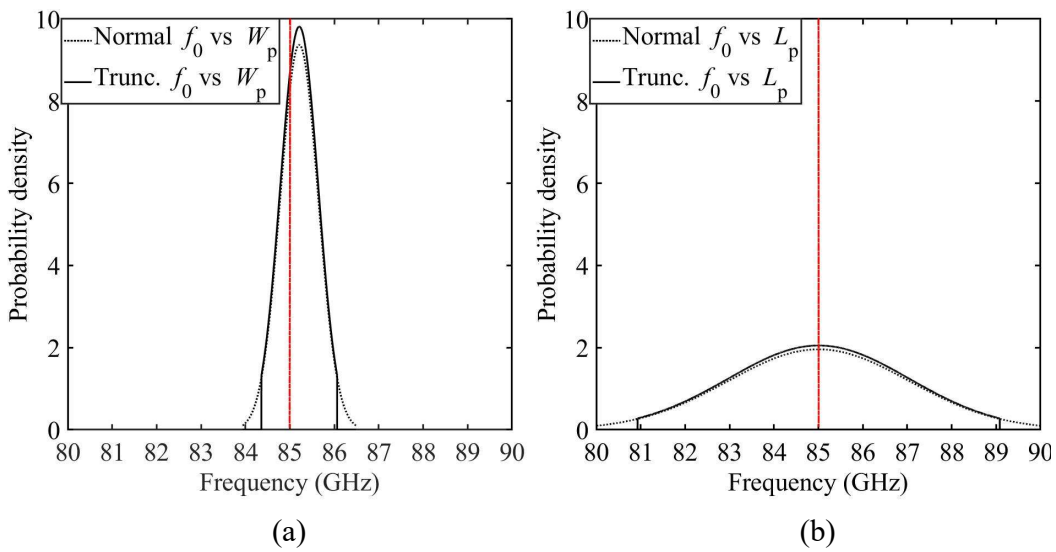


Figure 3.4: The effect of tolerances related to the input variables on the center frequency obtained via a probabilistic sensitivity analysis for, (a) varying width of the patch and, (b) varying length of the patch. The results are presented with a Gaussian (dotted line) and the truncated Gaussian distribution $\pm 2s$ (solid line). The expected mean \bar{x} is illustrated with the red dashed dotted line. The truncation range is indicated by $[a, b]$ (see Chapter 2, Section 2.6.2).

The results for f_0 with a varying W_p based on a tolerance of 10% are shown in Fig. 3.5(a) and f_0 with a varying L_p based on a tolerance of 10% are shown in Fig. 3.5(b).

Each graph in the correlation matrix⁸ shows the association between two random variables related to the geometry of the rectangular inset-fed microstrip patch antenna, shown in Fig. 3.3. Each graph shows the trend [**negative** (descending slope) or **positive** (ascending slope)], the shape [linear, non-linear or no relationship (round)] and the strength [*weak*, *moderate*, or *very strong* (see Chapter 2 Table 2.2)].

⁸The use of correlation in this simple example is intended to illustrate its usefulness.

The following conclusions can be drawn from the correlation matrix:

- **Red colored numbers** in Fig. 3.5, have a **negative** correlation.
 1. There is a *very strong linear* correlation (-0.97) between f_0 and W_p and therefore sensitive to tolerances [see Fig. 3.4(a)]. This means that if f_0 becomes larger then W_p becomes smaller.
 2. There is a *very strong linear* correlation of -0.93 between f_0 and L_p and therefore sensitive to tolerances [see Fig. 3.4(b)]. This means that if f_0 becomes larger then L_p becomes smaller.
 3. With an *moderate linear* correlation of -0.47 between the h_{PCB} and the ϵ_{eff} . This means that the value of the ϵ_{eff} becomes smaller when the thickness of the PCB h_{PCB} becomes larger in both matrices. Tolerances on either ϵ_{eff} or h_{PCB} will affect the center frequency f_0 [see equation B.8] and the dimensions of the microstrip line [see Equation (B.13) or Equation (B.14)].
- **Black colored numbers** in Fig. 3.5, have *no* correlation e.g. no relationship.
- **Green colored numbers** in Fig. 3.5, have a **positive** correlation.
 1. With an *very strong linear* correlation of 0.85 . The ϵ_{eff} is proportional to the ϵ_r in both matrices. This means that tolerances on the relative permittivity ϵ_r affect the effective permittivity ϵ_{eff} and thus the center frequency f_0 and the dimensions of the microstrip line i.e., its characteristic impedance Z_0 .

The combination of the truncated Gaussian distribution and the outcome of the correlation matrix helps to assess which parameter is the most sensitive for the tolerances. For instance, by choosing a manufacturer tolerance⁹ of 5% the frequency spread shown in Fig. 3.4(b) will be reduced to 2% with respect to f_0 . Normally PCB production companies can produce more accurately than specified, but this is at the expense of the yield and that will reflect in the costs.

⁹According to (IPC-A-600G) the 10% manufacturer tolerance is standardly used by companies like [132].

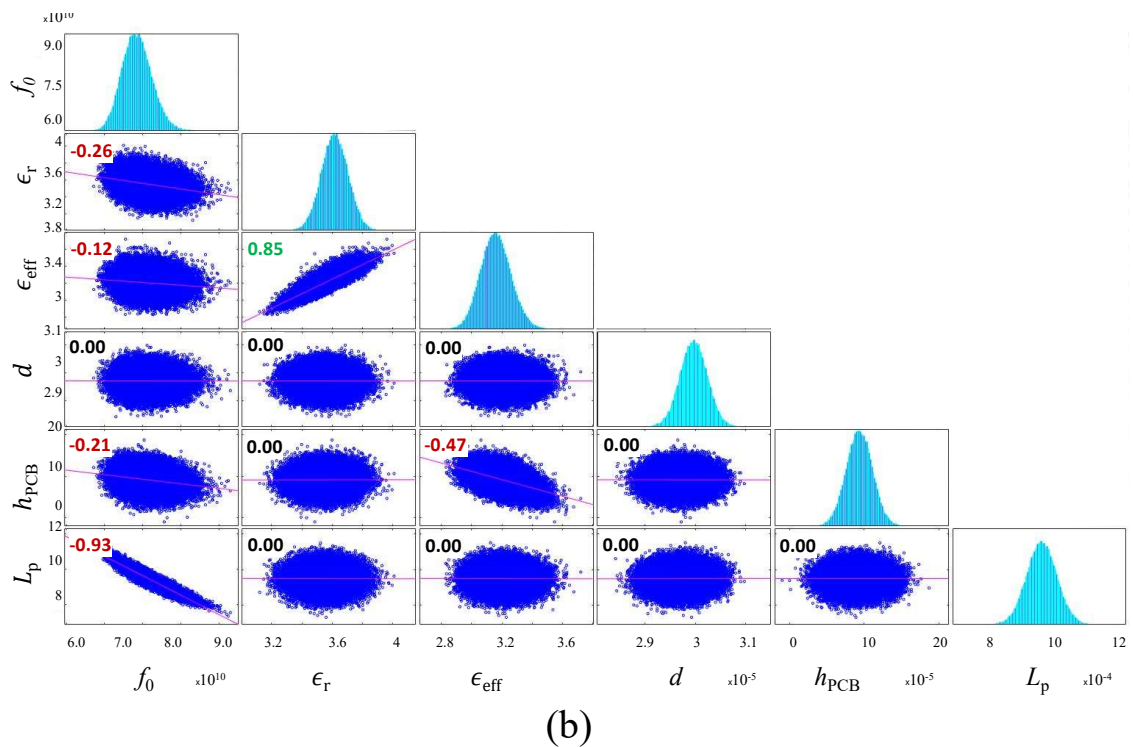
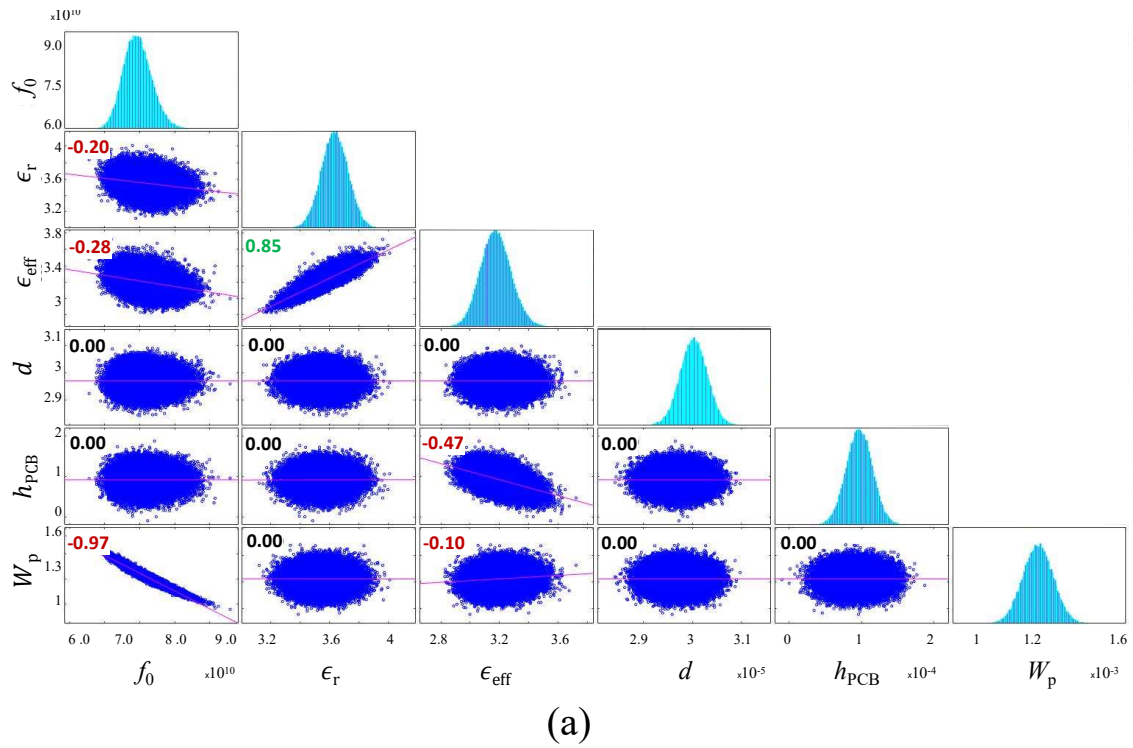


Figure 3.5: Correlation matrix of quantities related to (a) the width of the patch W_p and, (b) the length of the patch L_p , affecting in both cases the center frequency f_0 [see Equation (B.9)].

3.5.3 Design of the antenna excitation

The simulation software [112] provides two types of sources, also known as ports. One source is called ‘discrete’ port and the other ‘waveguide’ port. In this section we want to investigate the influence of the port on the behavior of the antenna. There are three aspects of these ports that cause uncertainty, namely type, location in the design and physical dimensions.

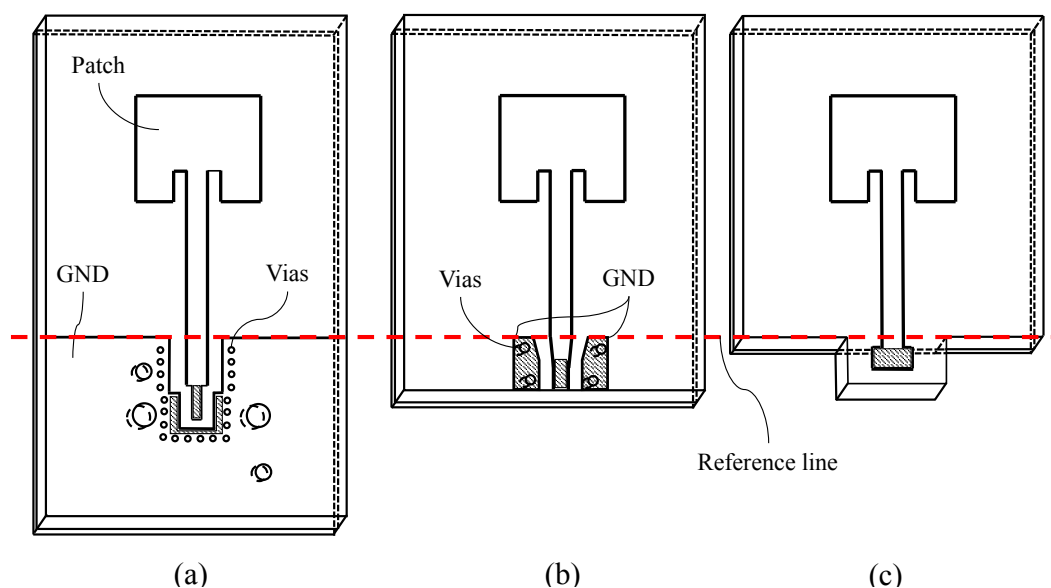


Figure 3.6: The rectangular inset-fed microstrip patch antenna with in (a) a connector interface, (b) a copper backed coplanar waveguide for the RF-probe and, (c) a patch interface for insertion into a waveguide. The red dashed reference line separates the RF-connector interface from the microstrip transmission line and antenna.

Although we ultimately want to investigate the influence of the RF-connector, we want to excite the reference antenna in such a way that the results can be used for three RF-connector variants. The three RF-connector interfaces are illustrated in Fig. 3.6. From left to right are shown the connector interface, the RF-probe interface and the waveguide interface. The red line indicates where the reference antenna physically starts, which is also known as the ‘reference plane’. In all three cases this is at the transition from the RF-connector interface to the microstrip transmission line (see also Fig. 3.2). This is also the location where we will excite the reference antenna.

The port type is more challenging to choose because both types have their own advantages and disadvantages. The discrete port (DP) is illustrated in Fig. 3.7(a) for the ‘edge’ variant and in Fig. 3.7(b) for the ‘face’ variant. The distribution of the current depicted with the yellow and orange arrows in Fig. 3.7(a) shows that the discrete ‘edge’

port introduces an extra discontinuity (indicated by the black arrows) compared to the discrete ‘face’ port shown in Fig. 3.7(b).

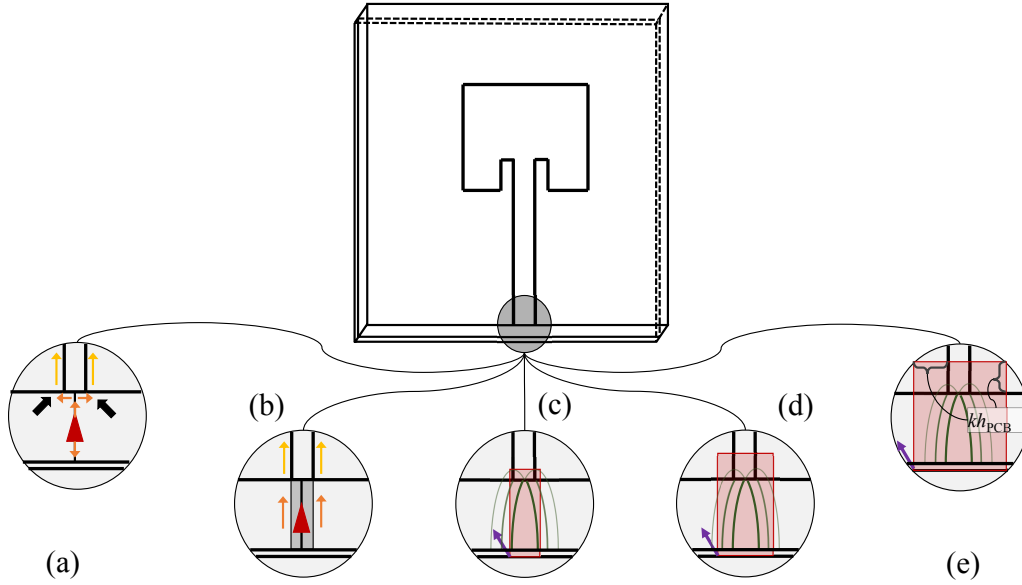


Figure 3.7: The rectangular inset-fed microstrip patch antenna with illustrated in (a) the discrete ‘edge’ port, (b) the discrete ‘face’ port, (c) the waveguide port with size $(kh_{\text{PCB}})/2$, in (d) the waveguide port with size kh_{PCB} and in (e) the waveguide port with size $(kh_{\text{PCB}})2$ (depicted with the accolades). The distribution of the current in (a) and (b) is indicated by the blue arrows (return current dashed light blue). The black arrows in (a) indicate the location where the discontinuity can be observed. The electric field in (c) to (e) are indicated with the decaying green arcs. The purple arrow depicted in (c) to (e) is the Poynting vector [112].

The waveguide port (WGP) is illustrated in Fig. 3.7(c) to Fig. 3.7(e) where the difference between them is the size in both horizontal and vertical direction [see Fig. 3.7(e), depicted with the accolades] of the port defined with factor kh_{PCB} ¹⁰. The challenge in the geometry of the waveguide port is that on one-hand the port needs to excite a field distribution (depicted with the decaying green arcs) that corresponds to a real connected transmission line. On the other hand the port should not be too large such that it influences the realized gain function of the antenna for certain angles.

To illustrate the effect of the port on the behavior of the antenna, a contour plot of the electric field in dBV/m exiting a waveguide port is shown in Fig. 3.8(a) for a time

¹⁰Factor ‘ k ’ is the ‘port extension coefficient’ supplied by [112]. In the case of this simulation model the k -factor is 4.16 with substrate height h_{PCB} (see Table 3.2 #3.13) and microstrip line width w_{t1} (#3.10) (see Fig. 3.3).

domain analysis and in Fig. 3.8(b) for a frequency domain analysis. The contour plot of the electric field exiting a discrete port is shown in Fig. 3.8(c) for a time domain analysis and in Fig. 3.8(d) for a frequency domain analysis. The gray arrows indicate the location of the simulation port, both discrete and waveguide. The purple arrows indicate the location where diffraction occurs. If we compare both waveguide ports then distinctively a hot spot can be observed on the edge of the port in the frequency domain (FD) depicted in the inset figure by the gray arrow in Fig. 3.8(b). The hot spot on the edge of the waveguide port is not present in the time domain (TD) depicted in the inset figure by the gray arrow in Fig. 3.8(a). As a result, the electric field shown in Fig. 3.8(b) is disturbed in the area indicated by the red ellipse compared to the area of the electric field shown in Fig. 3.8(a) by the red ellipse.

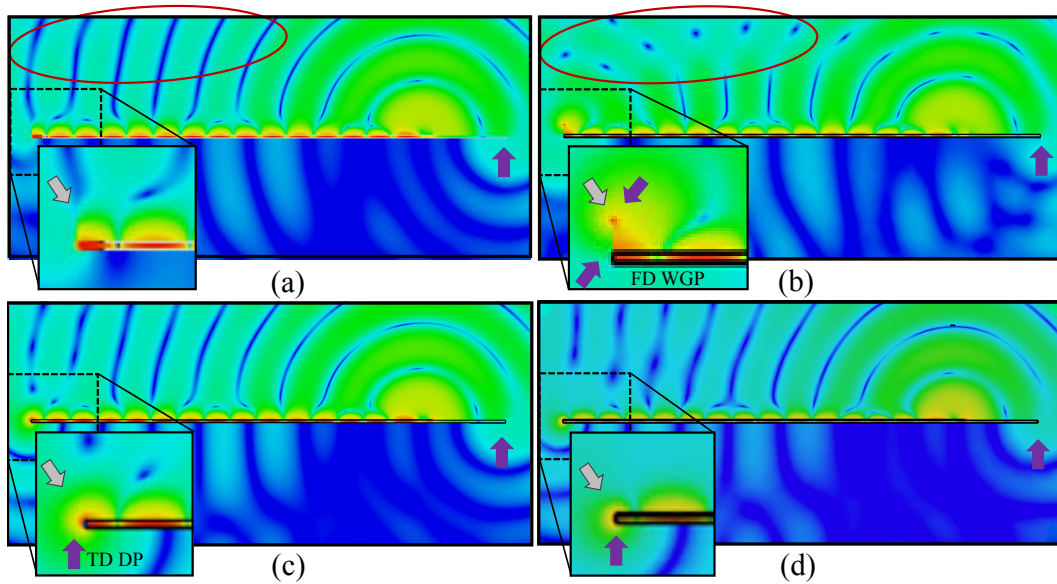


Figure 3.8: Contour plots of the electric-field in dBV/m of a rectangular inset-fed microstrip patch antenna (cross section in the longitudinal direction) exited (a) with a waveguide port with size kh_{PCB} in time domain, (b) with a waveguide port with size kh_{PCB} in frequency domain, (c) with a discrete face port in time domain and, (d) with a discrete face port in frequency domain. The gray arrows indicate the location of the port and the purple arrows the location where an anomaly occurs.

The reason of the difference in behavior of the waveguide port depending on the chosen domain is unknown to the author. In Appendix B.7 the waveguide port shows its effect on the antenna characteristics. In this case the waveguide port is much closer to the antenna than for the antenna design discussed in this section and shows in time domain a blockage and a gain function that has been compromised. However, this effect of the waveguide port is not noticed on the realized gain function of this simulation model

as shown in Fig. 3.10(a) because there is enough distance between the radiating patch antenna and the waveguide port. The discrete port in time domain does not have a blockage but, possibly caused by unwanted radiation [see Fig. 3.8(c)] an effect that can be noticed in Fig. 3.10(a) (blue solid line) by a ripple with a certain periodicity compared to the realized gain function results of the waveguide port.

3.5.4 Simulation results of the rectangular inset-fed microstrip patch antenna

The rectangular inset-fed microstrip patch antenna is simulated as a non-simplified model, meaning that both dielectric and metal losses are taken into account. The discrete port¹¹ and waveguide port models are solved in both time- and frequency domain. The simulation settings are summarized in Table 3.4 and the reflection coefficient and gain pattern results of the reference rectangular inset-fed microstrip patch antenna are shown in Fig. 3.9 and Fig. 3.10.

Table 3.4: Simulation settings concerning the mesh cells for time domain (TD) with regular grid and frequency domain (FD) with irregular grid.

| # | Port | Settings | TD ¹² | Settings | FD |
|------|------|---------------------|------------------|------------------|-------------|
| 3.18 | WGP | Cells per λ | 40 | min. edge length | $254e^{-6}$ |
| 3.19 | WGP | Smallest cell | 0.01 | Max. edge length | 1.44064 |
| 3.20 | WGP | Largest cell | 0.833 | Average quality | 0.79 |
| 3.21 | WGP | Number of | 18,001,440 | Tetrahedrons | 4,409,923 |
| 3.22 | WGP | Nx, Ny, Nz | 271,464,145 | | |
| 3.23 | DP | Cells per λ | 40 | min. edge length | $2e^{-6}$ |
| 3.24 | DP | Smallest cell | 0.01 | Max. edge length | 1.4647 |
| 3.25 | DP | Largest cell | 0.832 | Average quality | 0.80 |
| 3.26 | DP | Number of | 18,164,432 | Tetrahedrons | 3.371.386 |
| 3.27 | DP | Nx, Ny, Nz | 273,468,144 | | |

Time domain results: The reflection coefficient versus frequency results shown in Fig. 3.9(a) of the discrete port edge has a slight offset with respect to the minimum,

¹¹“By selecting the ‘Distributed’ scheme the source and load are uniformly distributed over the entire surface of the face (entire length of the wire, respectively) providing a robust representation e.g. in case of mesh adaptation, as well as supporting coaxial face elements and also discrete current face ports.” [112]

¹²The settings are based on the antenna model with WGP size k and DP face.

compared to the f_0 (See Table 3.1) by approximately 1.7 %.

The realized gain function in the E -plane, shown in Fig. 3.10(a), has a ripple with a certain periodicity with a maximum magnitude of approximately 1.5 dB. Comparing the results for the different ports does not show a significant difference. The ripple with a certain periodicity is caused by the diffraction at the edges of the PCB on either side in the E -plane direction [see Fig. 3.8(c) and Fig. 3.3 ($\pm E_{90^\circ}$)]. Possible blockage or reflection due to the size of the waveguide port cannot be noticed, although the contour plot of the E -field in Fig. 3.8 shows an effect that can be categorized as stemming from an obstruction. Concerning the H -plane shown in Fig. 3.10(c) the results are almost identical for angles smaller than $\pm 45^\circ$ for the different ports. Because of the relatively short distance to the edge of the PCB in the H -plane direction, the periodicity has a lower frequency and is therefore almost not noticeable. For angles larger than $\pm 45^\circ$ there is a difference between the waveguide-port and the discrete-port results. This can be explained from the fact that the waveguide port absorbs more of the fringe fields and the surface waves than the DP.

The trueness [see Equation (2.19)] of the realized gain is summarized in Table 3.5 and shows a minimal variation, less than 5.0%, comparing the different ports. This is because at 85 GHz the reflection coefficient is around -10 dB for all different port types. The largest deviation in realized gain is seen for the discrete edge port and is more than 17%. This is expected to be due to the extra discontinuity introduced at the location of the excitation as shown in Fig. 3.7(a).

Frequency domain results: The reflection coefficient minimum shown in Fig. 3.9(b) for the discrete edge port case and waveguide port $k/2$ case are off compared to the center frequency [f_0 , See Table 3.1, (#3.01)] by $\approx 2.8\%$ and $\approx 2.0\%$, respectively.

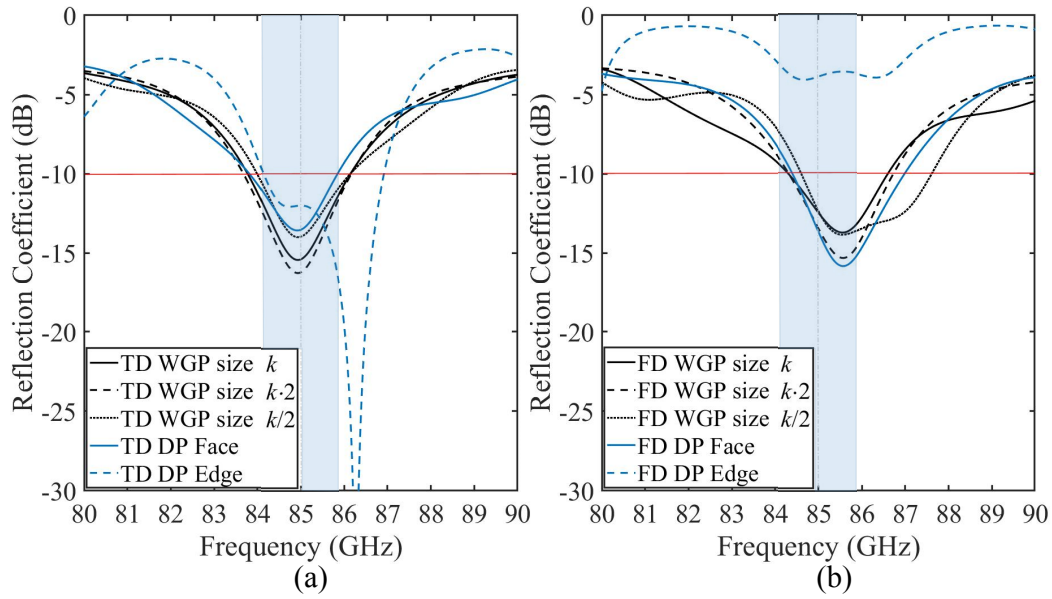
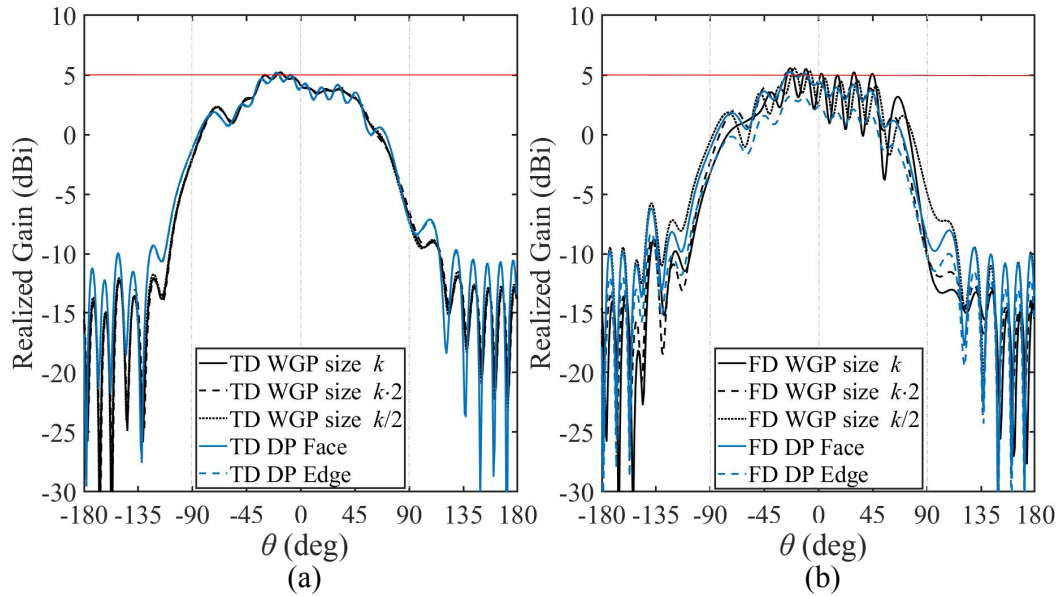


Figure 3.9: The reflection coefficient of the rectangular inset-fed microstrip patch antenna reference for various port configurations for (a) time domain simulation and (b) frequency domain simulation. The red line indicates the -10 dB and the gray dotted line the center frequency f_0 . The transparent blue area is the 2% frequency bandwidth (see Table 3.1).



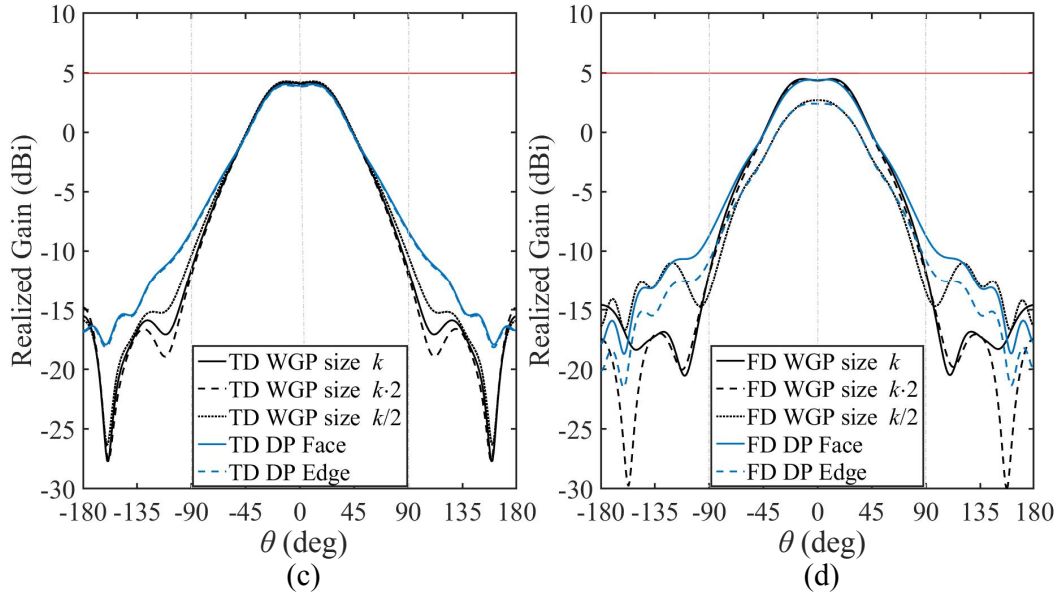


Figure 3.10: The realized gain pattern (dBi) of the rectangular inset-fed microstrip patch antenna reference for E -plane (a) time domain (TD) simulation and, (b) frequency domain (FD) simulation and H -plane (c) time domain simulation and, (d) frequency domain simulation. The vertical gray dotted lines indicate the realized gain at 0° and $\pm 90^\circ$. The horizontal red line indicate the realized gain of 5 dBi (see the design requirements Table 3.1). For all simulation results $f_0 = 85$ GHz

The realized gain function in the E -plane, shown in Fig. 3.10(b), has a periodicity with a maximum magnitude variation of approximately 10 dB. The cause of that magnitude variation can be observed in Fig. 3.8(b). The E -field seems to diffract or caused by a numerical anomaly at the top of the waveguide port indicated by the white arrow causing a constructive and destructive interference pattern. Comparing the results for the different ports does not show significant differences. Therefore, it can be concluded that the periodicity is caused by the diffraction on the edge of the PCB on either side in the E -plane direction [see Fig. 3.3 ($\pm E_{90^\circ}$)]. Possible blockage or reflection effects due to the size of the waveguide port cannot be noticed. Concerning the H -plane, shown in Fig. 3.10(c), the results are almost identical for all ports and for angles smaller than $\pm 45^\circ$. Because of the relatively short distance to the edge of the PCB in the H -plane direction, the periodicity has a lower frequency and is therefore almost not noticeable.

Table 3.5: Trueness (2.19) of frequency f_0 , bandwidth BW and antenna gain with various simulation settings compared with the design requirements [see Table 3.1, (#3.01), (#3.02) and (#3.03)]. The values in bold are representing the minima for the specific antenna characteristic and solver type.

| # | Port | Solver Type | Solving Time | f_0 Trueness (%) | BW Trueness (%) | Gain Trueness (%) |
|------|-------------------------|-------------|-----------------|-------------------------|-----------------|-------------------|
| 3.28 | WGP kh_{PCB} | TD | ≈ 2.0 h | 99.92 | 72.65 | 85.03 |
| 3.29 | WGP $kh_{\text{PCB}2}$ | TD | ≈ 5.5 h | 99.92 | 69.11 | 84.60 |
| 3.30 | WGP $kh_{\text{PCB}}/2$ | TD | | 99.92 | 79.81 | 85.91 |
| 3.31 | DP Face | TD | ≈ 1.5 h | 99.92 | 84.58 | 82.10 |
| 3.32 | DP Edge | TD | ≈ 1.5 h | 98.52 | 61.59 | 81.17 |
| 3.33 | WGP kh_{PCB} | FD | ≈ 7.0 h | 99.35 | 75.56 | 88.42 |
| 3.34 | WGP $kh_{\text{PCB}2}$ | FD | ≈ 4.5 h | 99.35 | 71.73 | 89.35 |
| 3.35 | WGP $kh_{\text{PCB}}/2$ | FD | ≈ 4.5 h | 99.35 | 57.24 | 68.40 |
| 3.36 | DP Face | FD | ≈ 6.5 h | 99.35 | 66.67 | 89.29 |
| 3.37 | DP Edge | FD | ≈ 4.5 h | nd ¹³ | nd | 65.79 |

The trueness of the realized gain is summarized in Table 3.5 and shows a minimal variation, less than 4%, comparing the different ports. This is because at 85 GHz the reflection coefficient is around -10 dB for all different port types. The largest deviation is noticed for the DP edge port case and is more than 18%. This is expected to be due to the extra discontinuity at the location of the excitation as shown in Fig. 3.7(a). The trueness of the center frequency f_0 , frequency bandwidth BW and antenna gain are also shown in Table 3.5 per port type and solver type.

The choice¹⁴ of port type to excite the antenna and its design should be carefully considered¹⁵. For the ‘measurable’ antenna, which can be connected to for instance a VNA, in most cases a waveguide port seems the best option, as illustrated in Fig. 3.11. The ‘research’ antenna, equipped with a microstrip line, could be excited by both a waveguide port or a discrete port.

¹³Not to be determined (See Fig. 3.9(b) blue dashed line).

¹⁴The transmission media mentioned under the heading ‘Transmission media’ in Fig. 3.11 are used in this thesis. There are more transmission media than mentioned in this table. However, most transmission media will eventually switch to a coaxial connection in order to be able to be connected to, for example, a VNA.

¹⁵See Appendix B.7

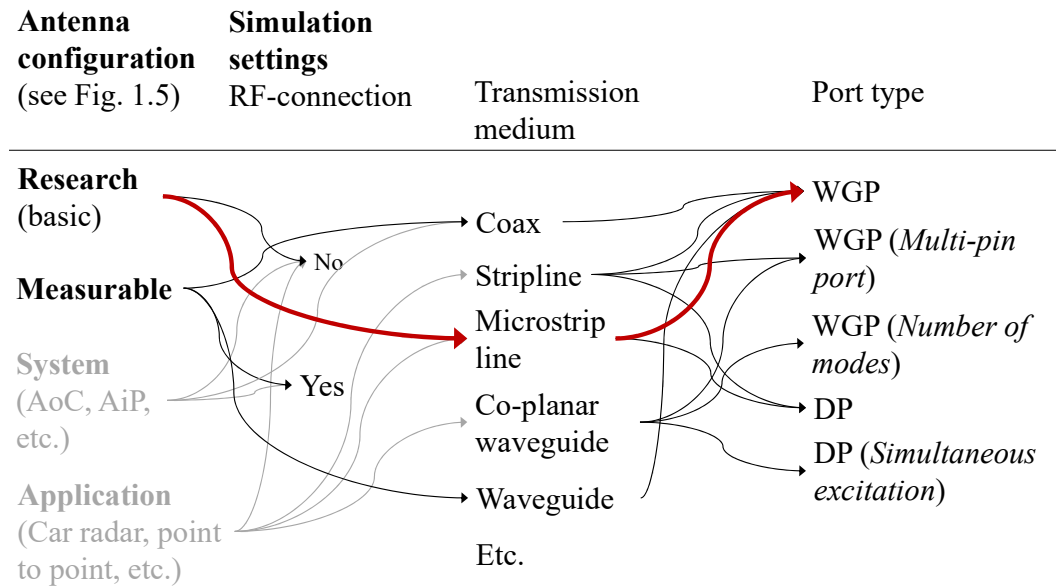


Figure 3.11: Antenna configuration versus the optimal port definition for the antenna investigated in this thesis. The antenna configurations that are not investigated in this thesis are grayed-out. The red colored arrows indicate the path of the transmission line and port used for the reference antenna (rectangular inset-fed microstrip patch antenna) characterized in this chapter.

The advantage of a waveguide port is that it directly excites a TEM- or quasi-TEM-wave into the transmission medium, takes the fringe fields into account and has adaptive impedance matching. A disadvantage is that this port type seems to create numerical anomalies visualized by for instance the contour plot of the E -field [see Fig. 3.8(b)], that could affect several antenna characteristics like the frequency bandwidth and realized gain (see Section 3.5.3).

The advantage of the discrete port is that its interaction with the radiating structure is negligible. A disadvantage is that it does not take the fringe fields into account and needs space to build up the TEM- or quasi-TEM-wave in a transmission medium, which could affect several antenna characteristics like, for instance, the reflection coefficient.

3.6 Case study 2: Circularly polarized dielectric rod antenna

Published in [5]

In this case study¹⁶ a circularly polarized [see Appendix B.2] rod antenna, shown in Fig. 3.12, will be analyzed. This is an already existing antenna, which is described in [133]. The circularly polarized (CP) rod antenna will be verified by performing an extensive tolerance analysis. Given the complexity of the composition of this antenna, we have not opted for a probabilistic sensitivity analysis simulation. In this case we use an analysis based on the minimum and maximum tolerance value per variable. It should be noted that each simulation run, changing one variable takes up to a few days using a Graphics Processing Unit (GPU)¹⁷. The main disadvantage of not using a probabilistic sensitivity analysis simulation is that the covariance of the different input variables can not be taken into account easily. The advantage of using a probabilistic sensitivity analysis simulation and creating a covariance matrix has been shown in the first case (see Section 3.5).

Hence, the PCB, of which the dimensions are shown in Table 3.6 (#3.39), is extended [see Figure 3.13(b)] to what we call a measurable mm-wave CP rod antenna.

Table 3.6: Dimensions of the circularly polarized rod antenna design (see Subsection 3.5.2).

| # | Antenna design type | Dimensions PCB ($w_{\text{PCB}} \times l_{\text{PCB}} \times h_{\text{PCB}}$) |
|------|---------------------|---|
| 3.38 | Application design | 6.72 mm x 8.00 mm x 0.19 mm |
| 3.39 | Measureable design | 34.00 mm x 33.00 mm x 0.19 mm |

¹⁶The results of this case study, presented in this section and Appendix B.2 to Appendix B.6, is based on a published article [5].

¹⁷A computer with a GPU-card can solve the electromagnetic problem 14 times faster than a computer without GPU [134].

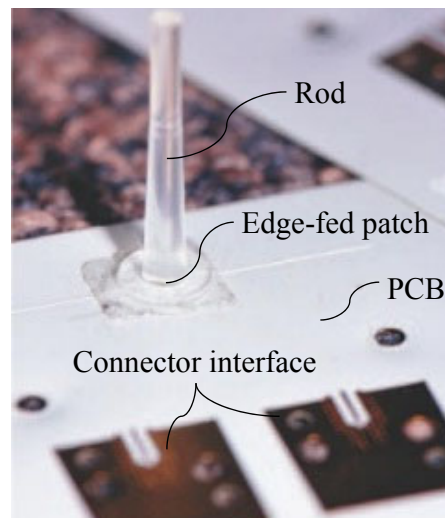


Figure 3.12: Realized circularly polarized rod antenna.

3.6.1 Design parameters

Figure 3.13(a), shows an illustration of the ‘application design’ of a CP rod antenna in transmit and receive mode. The size of the PCB can be found in Table 3.6 (#3.38). As can be concluded, the dimensions of the application design are too small to be able to add an RF press-fit connector or an area for connecting an RF-probe, for example.

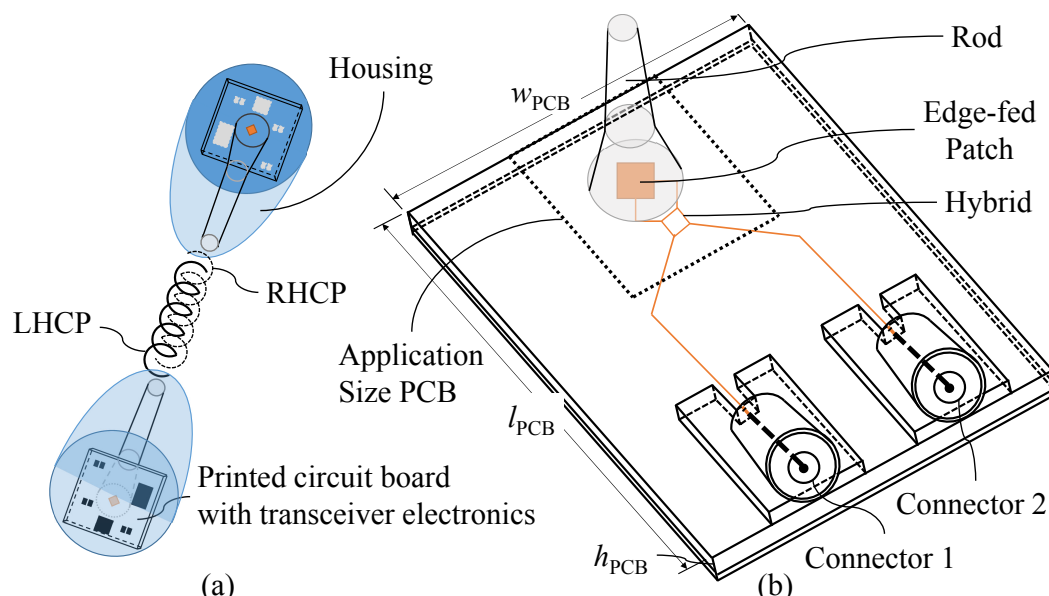


Figure 3.13: In (a) an illustration of a short-range communication application with the circularly polarized rod antenna i.e.; the application design, and (b) the same circularly polarized rod antenna but now in a measurable configuration so that it is characterizable i.e., the measurable design.

The design requirements of the CP rod antenna are shown in Table 3.7.

Table 3.7: Design requirements of the circularly polarized rod antenna.

| # | parameter | Design requirements |
|------|--------------------------|--------------------------|
| 3.40 | Center frequency | 61 GHz |
| 3.41 | Bandwidth (-10 dB) | > 9 GHz |
| 3.42 | Isolation (-20 dB) | > 9 GHz |
| 3.43 | Gain | 9 dBi |
| 3.44 | Half power beamwidth | $< 30^\circ$ |
| 3.45 | Polarization | Circular (RHCP and LHCP) |
| 3.46 | Axial ratio at broadside | $> 0.5 < \text{dB}$ |
| 3.47 | Impedance | 50Ω |
| 3.48 | Connector type | RF press-fit connector |

3.6.2 Simulation model

The CP antenna consists of a rectangular dual edge-fed, microstrip patch antenna, e.g. the CP rod antenna shown in Fig. 3.13(b). The CP rod antenna generates circular polarization with the help of a microstrip hybrid to create the required phase shift of 90° . The hybrid [see Fig. 3.13(b) [135]] makes it possible to excite the antenna for right-hand circular-polarization (RHCP) or left-hand circular-polarization (LHCP). A dielectric rod is placed on top of the patch antenna. The shape and material properties of the rod are chosen to maximize the antenna gain.

Although the rod is part of the antenna, it will not be analyzed separately. This was already done in a previous research and discussed in [135]. To be able to connect the antenna to the VNA, two connectors of type 08K80A-40ML5 [36] are placed on the PCB.

Fig. 3.14(a) shows the measurable simulation model of the CP rod antenna. The transition from a coaxial connector to one of the microstrip transmission lines is shown in Figure 3.14(b). The realization of the antenna, in this case on a multilayer PCB, introduces uncertainties, which are caused by inaccurate material properties at the frequency of operation and manufacturing tolerances [136], [137].

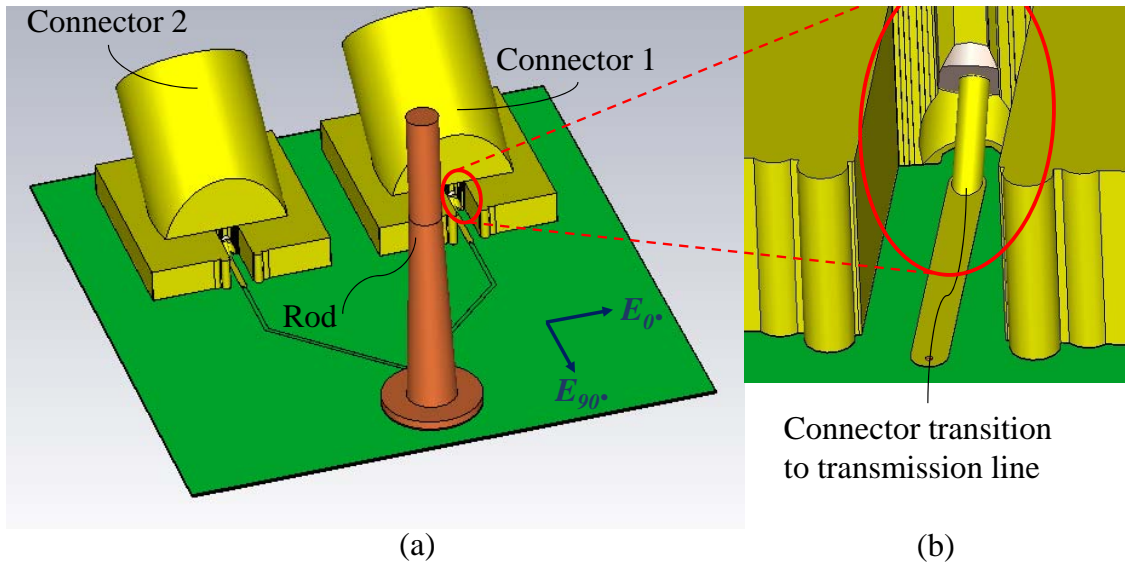


Figure 3.14: Detailed simulation model (a) with the vertical- and horizontal plane perpendicular to the PCB at E_{0° and E_{90° , respectively. Shown in (b) is the connector attached to the transmission line in a close-up view.

3.6.3 Simulation results

Results obtained with full-wave simulation software are already often implicitly suggested to be used as statistical antenna references in literature. This is done by using terms like a ‘good agreement¹⁸’ or ‘we see a trend’ in discussing the graphical representations of simulation and measurement results. However, using simulation results as a reference is justified only when the results come as close as possible to the values presented in the antenna design requirements (see Table 3.7). Round-off errors in the numerical calculations, specific software settings, and external factors will introduce uncertainties [139] that affect the validity of using the results as a reference. Therefore, different aspects concerning the simulation tool and the input parameters are tested. Possible sources for deviations that should be considered are the intrinsic settings of the simulation software [see Appendix B, Table B.1 (#3.49)-(#3.51)]:

- insufficient mesh cells due to specific convergence settings,
- a less efficient solver type [Appendix B, Table B.1, (#3.40)],
- non-physical excitation (port) definition [Appendix B, Table B.1, (#3.39)].

¹⁸“Let’s face it, these phrases have no meaning, and, in my opinion, no place in scientific literature. I’ve used them in papers, before I came to the realization that they have no value. If the agreement is good, tell us how good: use a number, an RMS, a percentage, etc. One researcher’s “good agreement” is another’s “failed to converge.”[138]

Furthermore, external factors causing deviations include:

- inaccurate values for the material properties [Appendix B, Table B.1, (#3.42) - (#3.43)],
- ignored manufacturing tolerances [Appendix B, Table B.1, (#3.46) - (#3.49)],
- over-simplistic simulation model that does not represent the realized antenna (Appendix B, Table B.1, #3.41).

For the external factors, an iteration cycle from simulation to realization is illustrated in Fig. 1.5 (see Chapter 1). In this cycle, the frequency-dependent substrate material properties, e.g., the permittivity and loss tangent and the PCB manufacturing tolerances, are obtained. This iteration between simulation step and realization step is considered as a calibration of the reference.

In Appendix B, Table B.1, the trueness is shown resulting from varying input parameters for angle $\theta = 0^\circ$ i.e., boresight. Fig. 3.15, Fig. 3.17 and Fig. 3.18 show the effect over angles $-30^\circ < \theta < 30^\circ$ for the axial ratio (AR) and $-90^\circ < \theta < 90^\circ$ for the realized gain function resulting from the varying parameters like excitation source, solver domain and material and manufacturer tolerances. The chosen excitation (#3.49), being a waveguide port or discrete port, affects the impedance, the AR [Fig. 3.15(a)] and gain function [Fig. 3.15(b)]. The way the DP is connected to a coaxial feed leads to a mismatch that explains the deterioration of the impedance, AR, and realized-gain (see Appendix B, Table B.1). Using different solvers (#3.50) should lead to the same results. Although the same convergence settings are used, deviations are observed between the frequency domain and time domain solver results for both AR and realized gain function. The simulation time for time domain simulations is approximately 7 hours and for the frequency domain it is approximately 240 hours, a factor of 30 times slower. The increase in simulation time also depends on the design complexity (#3.51). Solving design-complex structures may require specific computational resources such that it can be performed in a reasonable time [134].

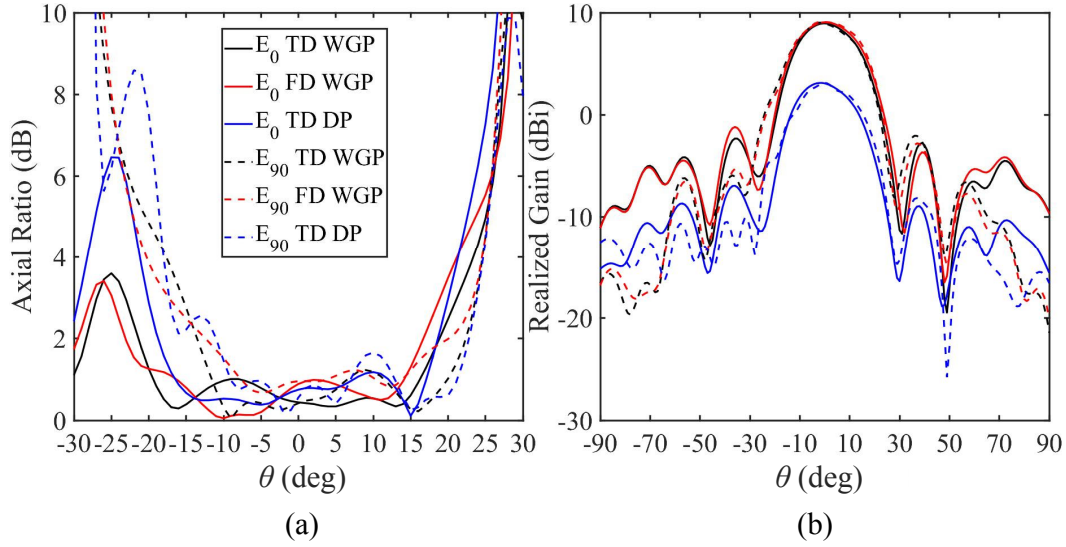


Figure 3.15: Simulated (a) axial ratio and, (b) realized gain function in the $\varphi = 0^\circ$ -plane and $\varphi = 90^\circ$ -plane as a function of (elevation) angle θ for different simulated port excitations. For all simulation results $f_0 = 61$ GHz.

In the $\varphi = 0^\circ$ -plane [see Fig. 3.16(a) and Fig. 3.16(b)] the electromagnetic wave experiences a different environment than in the $\varphi = 90^\circ$ -plane [see Fig. 3.16(c) and Fig. 3.16(d) for the E -field distribution]. In the $\varphi = 90^\circ$ -plane the obstruction of and reflection from the connectors will be more dominant than in the $\varphi = 0^\circ$ -plane, affecting the measured results. In the $\varphi = 0^\circ$ -plane the diffraction from the edges of the PCB will be more dominant than in the $\varphi = 90^\circ$ -plane. This explains why in Fig. 3.15(a) and Fig. 3.15(b) different AR and realized gain function results can be observed for the $\varphi = 0^\circ$ - and $\varphi = 90^\circ$ -planes [see Fig. 3.14(a)].

The results for varying material properties (#3.52) and (#3.53) are shown in Fig. 3.17(a) and Fig. 3.17(b) for the AR and realized gain, as a function of angle θ at a frequency of 61 GHz, respectively. A small effect is noticed for permittivity and loss tangent variations (#3.52) and (#3.53). This is not the case for the manufacturing tolerances (#3.56) to (#3.58). It is observed that these tolerances cause the most considerable deviations so far, especially the tolerances for the layer registration of the multilayer PCB [see Fig. 3.18(a) and Fig. 3.18(b)]. In this case, the misalignment between the microstrip feed line and the patch appears to be disastrous. The PCB layer registration error, measurement methods for the CP rod antenna and measurement results can be found in Appendix B.4, Appendix B.5 and Appendix B.6, respectively.

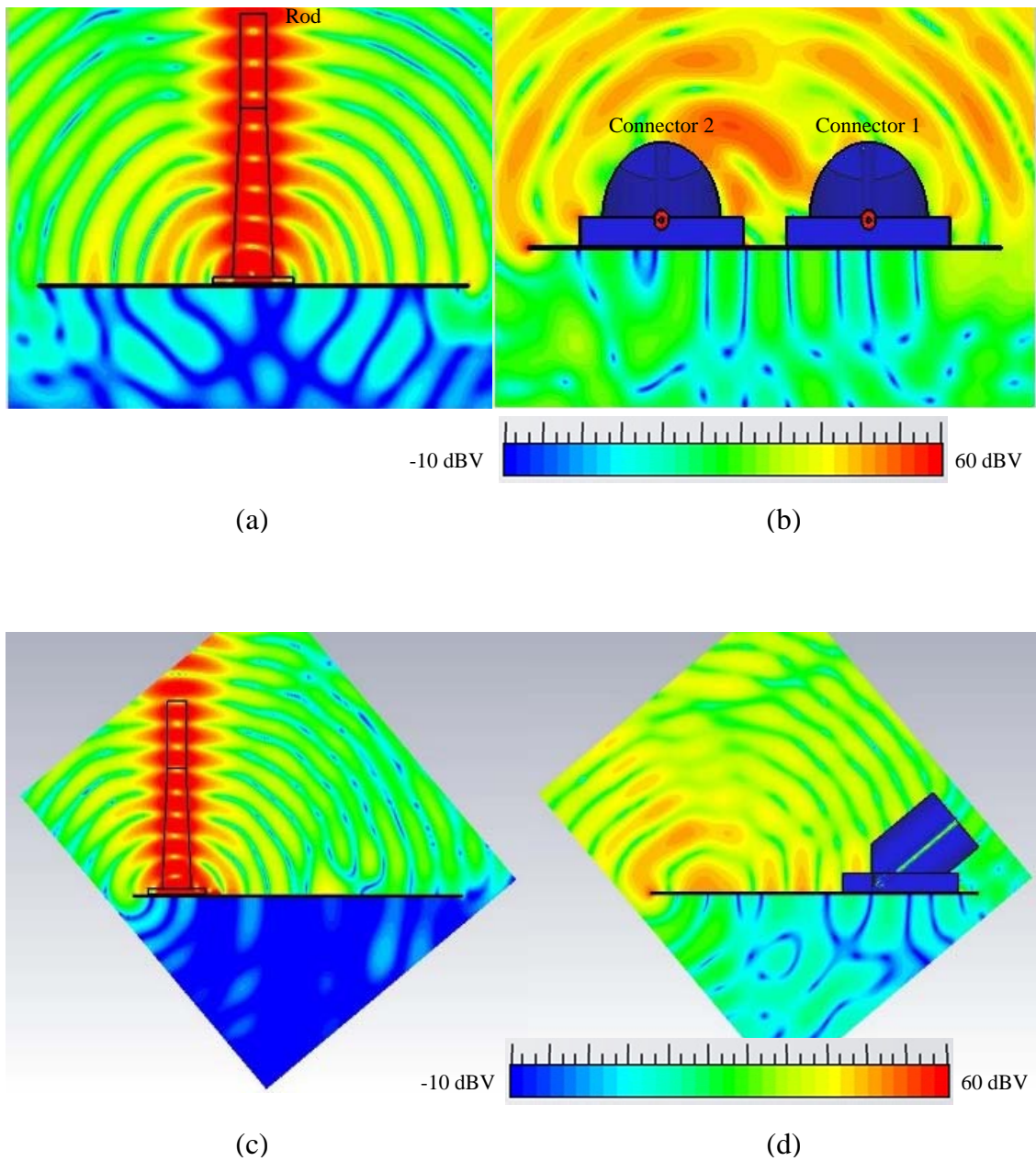


Figure 3.16: Contour plot of the E -field in dBV/m for the $\varphi = 0^\circ$ plane showing (a) diffraction and, (b) obstruction of the connectors. For the $\varphi = 90^\circ$ plane, (c) shows diffraction and (d) obstruction and reflection from the connectors. For all simulation results $f_0 = 61$ GHz.

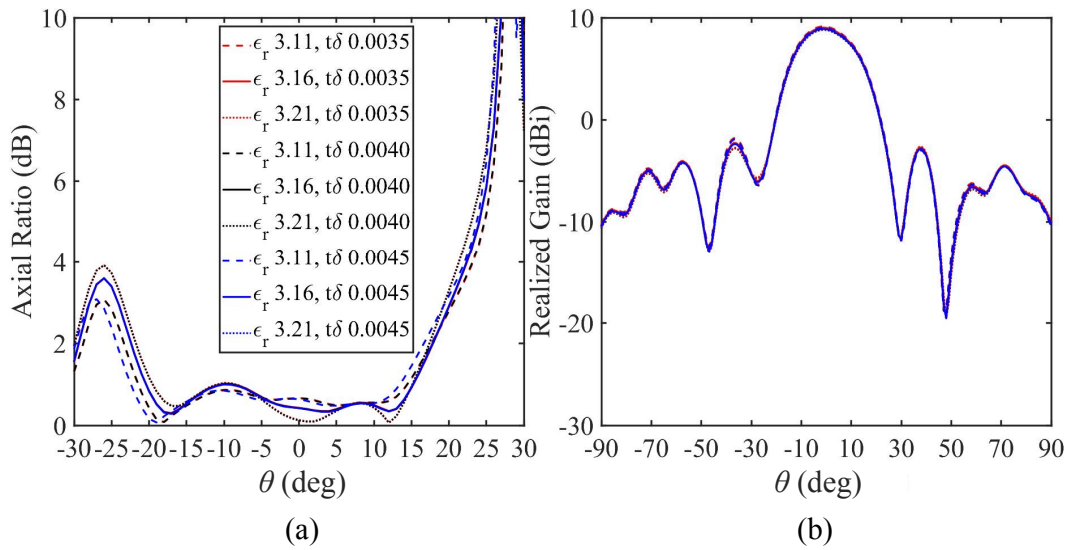


Figure 3.17: The effect of the material properties on, (a) the axial ratio and, (b) the realized gain function for $\varphi = 0^\circ$ -plane. For all simulation results $f_0 = 61$ GHz.

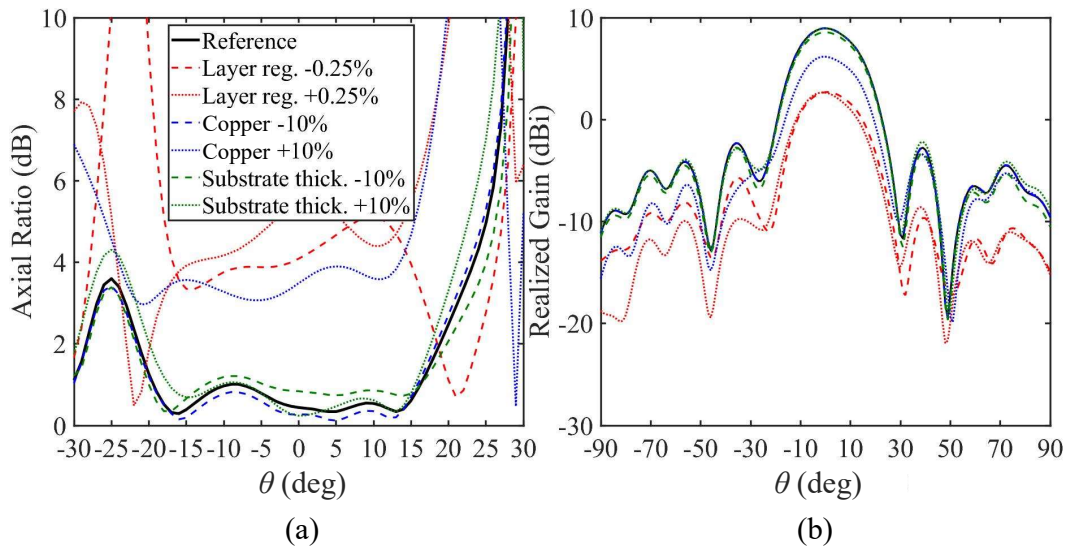


Figure 3.18: The effect of the manufacturing tolerances on, (a) the axial ratio and, (b) the realized gain function for $\varphi = 0^\circ$ -plane. For all simulation results $f_0 = 61$ GHz.

3.7 Summary and conclusions

Setting up a research antenna, e.g. reference showing the actual behaviour of the antenna, starts by pointing out the various functional parts and defining what part belongs to the antenna reference model. The reference antenna is considered without RF-connector but with a transmission medium. The uncertainties (systematic and random errors) that affect the characteristics of the reference antenna are the simulation settings, port type, solver type and manufacturer tolerances have been validated on the basis of two cases.

The first case is based on a linearly polarized rectangular inset-fed microstrip patch antenna. Probabilistic sensitivity analysis (random error) is applied on the available equations (see Appendix B.1) based on realistic manufacturer tolerances. From the truncated normal distribution and correlation matrix it is derived that the permittivity and height of the PCB affect the center frequency and frequency bandwidth the most. It is suggested to reduce the production tolerance from 10% to 5% to reduce the spread of f_0 to 2%.

When investigating the effect of the simulation software settings on the antenna behavior, it has become clear that the port type and antenna excitation design introduce uncertainties (systematic error). Not every port type or design gives the same result. Therefore, a graph is made where the different transmission types are connected to a certain port type that results in the most accurate results of the antenna characteristics with minimal influence of the port.

The second case is based on a circularly polarized rod antenna. The simulation settings, material properties and manufacturer tolerances are used as input parameters for the simulation model to see the effect (systematic error) on the axial ratio and realized gain function. The choice of excitation (port type) gives the most substantial deviation in the simulation results. After varying the earlier mentioned parameters, the accuracy of the axial ratio is expressed with a trueness of 99% and a precision of ± 0.06 dB (1s) the accuracy of the realized gain has a trueness of 98% and a precision of ± 0.1 dB (1s). The layer registration is the most critical concerning manufacturing tolerances.

In conclusion, the antenna design process as described in Chapter 1, Section 1.6, Fig. 1.5 was followed in both case studies. This has led to the design of a simulation model with realistic details and settings whose influence on the behavior of the antenna is understood. But also an improved measurement setup that exerted less influence on the behavior of the antenna during the measurements. Because the antenna design process has been followed the measurement results could be validated with the simulation results, quantified with precision (error bars) and Trueness (%) resulting in an accuracy (see Fig. 2.10).

CHAPTER FOUR

Analysis and design of the RF-connector

**“A perfect interconnection influences neither the quality nor the quantity of the signal.
A perfect interconnection does not exist.”**
(The Observer)

4.1 Introduction

In most commercially available wireless systems, the antenna is integrated. By integrated we mean that the antenna is printed on a PCB, for example, and connected to a transceiver through a transmission line. To characterize these antennas, a measurable variant can be made. An important component to be added to this ‘measurable’ antenna is an RF-connector. In this way the antenna can then be connected to an antenna measurement system. A variety of RF-connector types is available, of which the following will be covered in this chapter: the RF press-fit connector, the RF-probe, and the waveguide-to-PCB connector. Since the aim is to only characterize the behavior of the antenna, attention should be paid on where and how the connector is positioned in the measurable antenna design. Even if the connector has been carefully placed in the measurable antenna design, the question remains whether it still influences the antenna behavior in some way, i.e. the observer effect. The aim of this study is to find out which of the following physical phenomena: surface waves, reflection, diffraction and unwanted radiation cause disturbances on the antenna characteristics and how this correlates with the aforementioned connector types. Based on the obtained results, i.e. which physical phenomenon appears to have the greatest influence, the design of a new RF-connector type will be presented. For this new RF-connector it will be shown that the influence on the antenna characteristics is significantly smaller than obtained with the commonly used RF-connector types. Finally, also a contactless RF-connection will be described that will be analyzed for usability for measurable / integrated millimeter-wave antennas.

4.2 Connected antenna measurement

With an electrically connected antenna measurement, a mechanical contact exists between the antenna to be measured, i.e. an AUT, and the antenna measurement system. This mechanical contact is made by means of RF-connectors. By using an RF-connector, it becomes easy to electromagnetically connect and disconnect the antenna in the antenna measurement setup. For antennas operating in the millimeter-wave frequency band, several RF-connector types exist to establish this mechanical contact as shown in Fig. 4.1.

The first RF-connector, shown in Fig. 4.1(a), is the RF-coaxial-press-fit-connector [see Table 4.1 (#4.1) and (#4.2)]. This RF-connector with a 1 mm screw interface is intended for frequencies up to 110 GHz [36]¹. We will discuss two implementations of this RF-connector applied to the same antenna.

The second RF-connector, shown in Fig. 4.1(b), is the RF-probe² [140]. It was first introduced in antenna measurements at the beginning of this century [141]. The RF-probe consists of a tip with a configuration of contact pins that together form a coplanar waveguide. Furthermore, the RF-probe consists of a semi-rigid coaxial cable, an RF coaxial screw interface and - almost always - a metal housing. Also, in this case, we will discuss two implementations of the RF-connector in the antenna design.

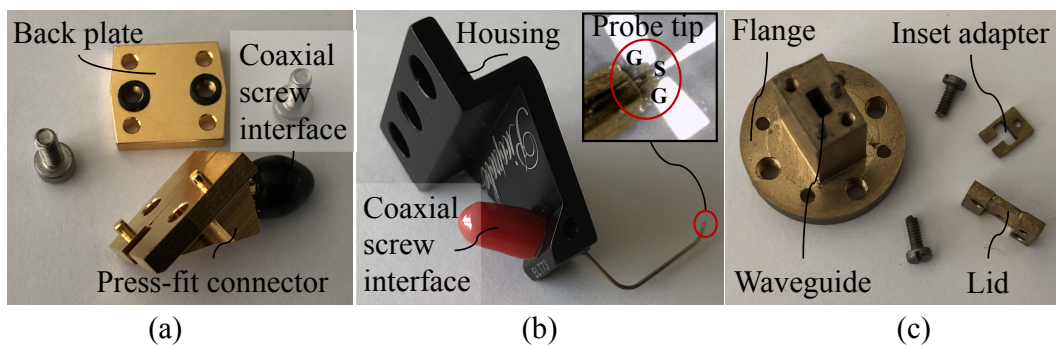


Figure 4.1: (a) RF press-fit connector from [36], (b) an RF-probe [140] with in insert an image of a ground-signal-ground (GSG) probe tip (red ellipse) and, (c) a custom-made waveguide to PCB connector.

The final RF-connector we want to discuss in this chapter, shown in Fig. 4.1(c), is an in-house-designed waveguide-to-PCB connector [142], [143]. This waveguide-to-PCB connector is made specifically for a inset-fed microstrip patch antenna discussed in

¹01K80A-40ML5 right angle jack connector for PCB application.

²Model 110H RVP-style.

Chapter 3 Section 3.5. Only one implementation of this RF-connector type will be investigated.

4.3 Case study: Uncertainties in the characteristics of a rectangular inset-fed microstrip patch antenna caused by an RF-connector

Partially published in [144]

The rectangular inset-fed microstrip patch antenna mentioned in Chapter 3, Section 3.5, is now extended with an RF-connector. A rectangular inset-fed microstrip patch antenna is chosen because it provides insight into most of the physical phenomena introduced in Section 3.4.

4.3.1 Various RF-connectors

Usually a simulation model of an antenna is validated with measurement results. Although the simulation model must be a representation of the actual antenna, often not all components are included. The simulation time can become extremely long by adding certain components to the simulation model. An example of such a component is the RF-connector. It is clear that the absence of the RF-connector in the simulation model can lead to large differences between simulation and measurement results, especially at higher frequencies (>30 GHz). This is mainly due to the RF-connector dimensions, for frequencies from 30 GHz onwards, becoming one to a few wavelengths. The presence of the RF-connector in the simulation model is rarely referred to in the literature to explain the differences between simulation and measurement results [3]. The effect of the RF-connector on the antenna behavior is not specified.

Nevertheless, the results of a simulation model without an RF-connector offer an opportunity to understand how the RF-connector and the RF-connector interface³ influences the behavior of the antenna. The simulation model without RF-connector then becomes an 'ideal' reference (see Chapter 3, Section 3.5).

To analyze the influence of the RF-connector on the behavior of the antenna, a simulation model is made of each RF-connector mentioned in Table 4.1. The simulation models of the RF-connectors have been merged with an existing simulation model of a planar antenna.

³An RF-connector interface is a transmission line on a PCB for the purpose of placing and connecting an RF-connector to an antenna.

The five different RF-connector integrations are divided into two categories, based on intuition and experience in measuring millimeter-wave antennas:

- “Not preferred.” These are the RF-connectors that are expected to have such an influence due to their size / position that the characteristics of the antenna can no longer be correlated⁴ to the results of the simulation model without an RF-connector.
- “Preferred”. These are the RF-connectors that are expected to have a minimal influence due to their size / position so that the characteristics of the antenna can be correlated with the results of the simulation model without an RF-connector.

In order to arrive at an antenna design in which the RF-connector disturbs the antenna characteristics as little as possible, it must be understood which physical phenomena cause the disturbances and how these disturbances occur. These physical phenomena are: surface waves, reflection, diffraction [145], [102] and unwanted radiation. These four physical phenomena are caused by a fifth physical phenomenon namely: antenna radiation. The fifth phenomena is wanted radiation and mentioned here as a possible direct source of an other physical phenomena like reflection. With this in mind we can describe the term ‘direct coupling’⁵ and ‘indirect coupling’⁶ as will be discussed and illustrated in the next Subsection.

⁴The quality of the correlation (good agreement) between measurement and simulation results is determined using trueness, accuracy and precision (see Chapter 2, Section 2.6), the limit is based on the design requirements.

⁵By ‘direct coupling’ it is meant that a physical phenomenon is the primary source influencing the antenna characteristics.

⁶By ‘indirect coupling’ is meant that a physical phenomenon as a second source is the cause of this coupling initiated primarily by the antenna radiation whereby the antenna characteristics are influenced.

Table 4.1: Various physical phenomena that cause uncertainties in the outcome of the measured antenna characteristics related to an RF-connector type.

| # | Connector type | Causes (physical phenomena) | Affects (antenna characteristic) |
|-----|----------------------------------|---|-------------------------------------|
| 4.1 | RF press-fit connector top | Reflection, unwanted radiation | Z, S_{11} G_{rp}, G_r |
| 4.2 | RF press-fit connector bottom | Reflection, unwanted radiation | Z, S_{11} G_{rp}, G_r |
| 4.3 | Top RF-probe | Reflection, diffraction, unwanted radiation. | Z, G_{rp}, G |
| 4.4 | Side RF-probe | Diffraction, unwanted radiation | G_{rp}, G_r |
| 4.5 | Waveguide to PCB connector | Diffraction | Z, G_{rp} |

In Table 4.1, each physical phenomenon is linked to antenna characteristics that may be disturbed. These characteristics are: impedance (Z), reflection coefficient (S_{11}), realized gain pattern (G_{rp}) and realized antenna gain (G_r).

In the following subsection, the five physical phenomena will be described using a schematic illustration of an antenna.

4.3.2 Functional decomposition of a rectangular inset-fed microstrip patch antenna with an RF-connector

In Fig. 4.2 ‘**Antenna radiation**’ is indicated using dark gray circles. Highlighted in the inset figure is the field distribution coming from a rectangular inset-fed microstrip patch antenna (location indicated by black open arrow) by means of a contour plot of the electric field. The antenna radiates mainly in the upper hemisphere due to the ground plane of the rectangular inset-fed microstrip patch antenna. The field distribution coming from the antenna occurs in three regions. These regions are the reactive near-field, the radiating near-field and the far-field. Placing the RF-connector in the first region, the reactive near-field, changes the behavior of the antenna. The placement of the RF-connector in the reactive near-field causes the creation of a structure consisting of the original antenna and RF-connector that together form a new antenna. The current distribution over the antenna and RF-connector together contribute to the radiation.

Finally, antenna radiation is the direct source of some of the physical phenomena that will be described below. This means that there will be a mutual interference between antenna and RF-connector. In the following figures, the mutual influence, direct coupling, will be indicated by a solid blue line with a double arrow. The influence of the

‘indirect coupling’ will be indicated by the dashed blue line with a double arrow.

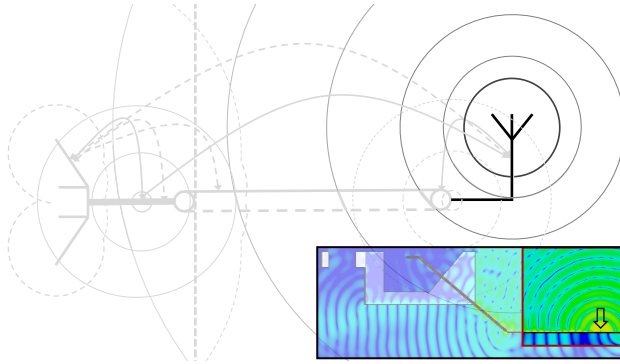


Figure 4.2: Illustration of a radiating antenna indicated by the dark gray circles. The inset figure shows a contour plot of the electric field in dBV/m (The scale can be found in Fig. 4.7). Highlighted in the inset figure is the simulated antenna radiation.

$n = 0, 2, 4, \dots$ for the TM_n modes [122]. Surface wave can be avoided in the antenna design by limiting the thickness of the substrate. This means that the combination of $h_{PCB} = 0.1016$ mm and $\epsilon_r = 3.16$ leads to a cutoff frequency for the $TE_1 = 501.78$ GHz.

For sake of completeness, Fig. 4.3 shows the worst-case situation where, if surface waves (green lines in the substrate) would exist and have indirect coupling (dashed blue lines with arrows) with the RF-connector and RF-connector interface. However, it is assumed that only the fundamental

In Fig. 4.3 a ‘surface wave’ is indicated using green lines. Surface waves are transverse magnetic (TM) and transverse electric (TE) modes of the substrate and attenuate in the transverse direction. The phase velocity depends on the substrate height h_{PCB} and relative permittivity ϵ_r of the substrate. The TM_0 mode does not have a cutoff frequency. However, the higher TM_n and TE_n modes do have cutoff frequencies given by [122]⁷:

$$f_0 = \frac{nc_{air}}{4h_{PCB}\sqrt{\epsilon_r - 1}} \quad (4.1)$$

where c_{air} is the speed of light in air⁸, $n = 1, 3, 5, \dots$ for the TE_n modes and

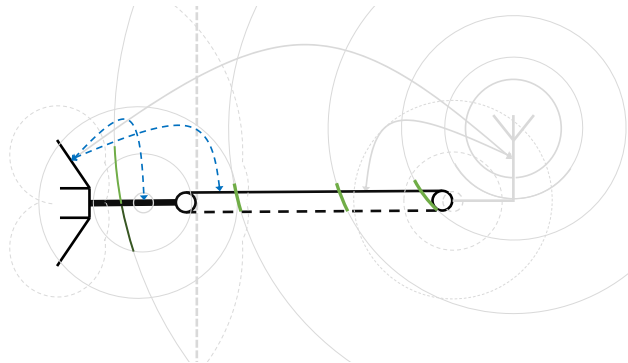


Figure 4.3: Illustration of surface waves in the substrate indicated by the green lines. The blue dashed lines with arrows indicate the indirect coupling between RF-connector and transmission line.

⁷This equation is only valid for a single layer PCB. Surrounded on both sides by air.

⁸The speed of light in air (c_{air}) is 299702547 m/s [146], where the speed of light in vacuum is 299792458 m/s.

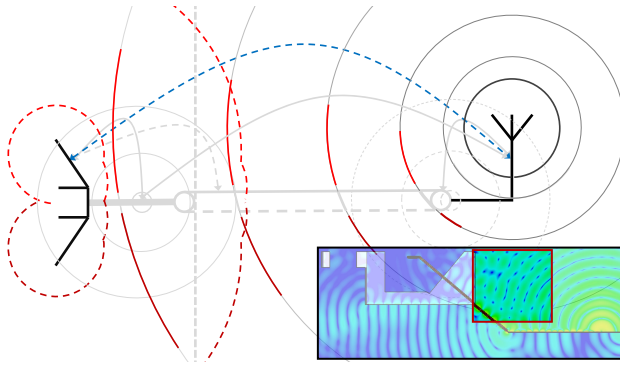


Figure 4.4: Illustration of the cause of reflection indicated by the red lines and the reflection indicated by the red dashed lines. The inset figure shows a contour plot of the E -field in dBV/m. Highlighted in the inset figure is an interference pattern caused by the reflection on the RF-probe housing. The blue dashed line with arrows indicates the indirect coupling between antenna and RF-probe housing.

Highlighted in the inset figure is an interference pattern caused by reflection of an electromagnetic wave, emitted from the antenna, on a surface on the metal housing of the top RF-probe. The influence of the reflected electromagnetic wave on the antenna characteristics depends on the size and position of the plane on which the reflection takes place. This means that if the plane on which reflection takes place is reduced or tilted sufficiently, the reflected wave will have minimal or even no influence on the antenna characteristics. There is an indirect coupling between the antenna and the surface on which the electromagnetic wave reflects. This is indicated by the dashed blue line with a double arrow.

mode propagates through the substrate. Therefore, limited effect on a well-designed antenna can typically be attributed to surface waves. Even if the TE_1 mode exists, due to limitations in the design of the thickness of the PCB, the distance to the edge or RF-connector is so far that effects on the antenna characteristics will not be noticed, as discussed in Appendix C.1. This physical phenomenon will therefore not be discussed further in this chapter.

In Fig. 4.4 ‘**reflection**’ of an electromagnetic wave is depicted by dashed red lines. The wave coming from the antenna and giving rise to reflection on, in this case, a top RF-probe, is depicted with solid red lines.

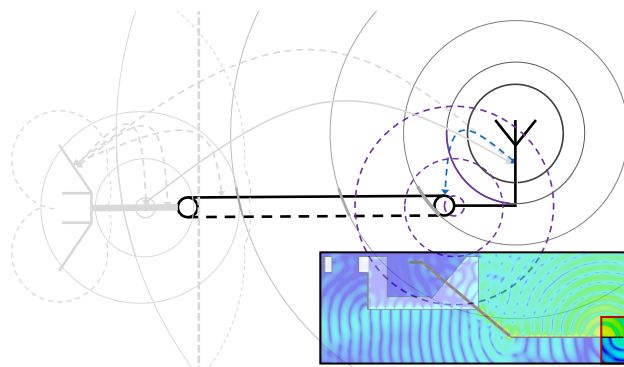


Figure 4.5: Illustration of diffraction indicated by the dashed purple circles initiated by antenna radiation indicated by the dark gray lines. The inset figure shows a contour plot of the E -field in dBV/m. Highlighted in the inset figure is the effect of diffraction on the edge of the PCB. The blue dashed line with arrows indicates the indirect coupling between antenna and diffraction on the edge of the PCB.

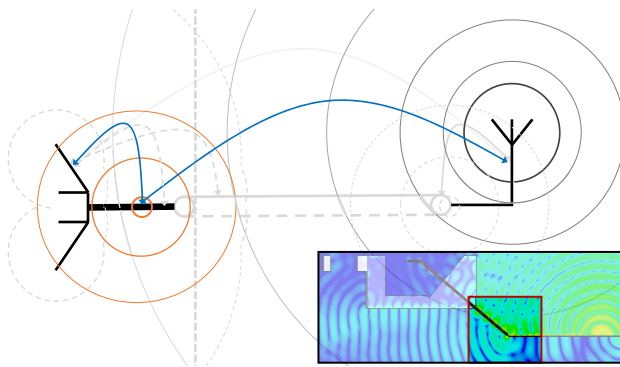


Figure 4.6: Illustration of unwanted radiation indicated by the orange circles. The inset figure shows a contour plot of the E -field in dBV/m. Highlighted in the inset figure is radiation from the RF-probe tip in two directions. The blue lines with arrows indicate the direct coupling between RF-probe tip and connector housing and between RF-probe tip and antenna.

indirect coupling with the antenna via the (virtual) source on the edge of the PCB. Indirect, because diffraction is caused by antenna radiation. The indirect link is indicated by the dashed blue line with a double arrow. Also visible in the inset figure is that the electromagnetic wave curves around the edge of the PCB to the opposite side of the antenna. An antenna holder could be placed on this opposite side. Because its material characteristics will be different from air, this holder can influence the behavior of the antenna. The diffraction-effect on the antenna can be remedied by either making the PCB sufficiently small or making the PCB sufficiently large. Making the PCB sufficiently small will enlarge the period of the disturbance such that it is no longer perceptible in the G_{rp} of the antenna. Making the PCB sufficiently large ensures that the losses in the substrate and the spherical spread will weaken the amplitude of the wave emitted at the edge to such a degree that the influence on the G_{rp} is no longer perceptible.

In Fig. 4.6 ‘**unwanted radiation**’⁹ is indicated using orange circles. Highlighted in the inset figure is unwanted radiation at the location where the RF-probe contacts the transmission line printed on the PCB. The electromagnetic wave from the RF-probe propagates in the direction of the antenna as well as in the opposite direction. The

In Fig. 4.5, ‘**diffraction**’ of an electromagnetic wave is indicated using dashed purple circles. The main source of the diffraction is the antenna radiation (dark gray circles). Highlighted in the inset figure is diffraction of an electromagnetic wave on the edge of the PCB coming from the antenna. On the edge of the PCB, the existence of a secondary (point) source is considered. Part of the electromagnetic wave will radiate towards the antenna and will interfere with the electromagnetic wave coming from the antenna. This constructive and destructive interference causes a ripple with a certain periodicity, on the radiation pattern of the antenna. Diffraction provides an in-

⁹We define ‘unwanted radiation’ as radiation from a different source as the antenna *inside* its frequency band. Sometimes this physical phenomenon is confused with the term spurious radiation. This is incorrect because spurious radiation is defined as: ‘Any emission from a radio transmitter at frequencies *outside* its frequency band. Also known as unwanted emission [147].’

unwanted radiation originates from the RF-probe tip. The cause of the unwanted radiation is the discontinuous transition from the coaxial cable to the transmission line on the PCB. This means that the propagating wave also undergoes a discontinuity creating higher order modes and unwanted radiation. Unwanted radiation creates a direct coupling between the RF-probe and the antenna indicated by the blue line and double arrow. Furthermore, the unwanted radiation also couples to the RF-probe housing, indicated by a blue line and double arrow.

The description of the four physical phenomena in the previous paragraphs provides insight into the correlation between these phenomena and their influence on the behavior of the antenna. Fig. 4.7 shows five plots of the simulated electric field in a snapshot for the various RF-connectors in combination with a rectangular inset-fed microstrip patch antenna. Fig. 4.7(a) shows the field for the top RF press-fit connector in top position, Fig. 4.7(b) for the bottom RF press-fit connector, Fig. 4.7(c) for the top RF-probe, Fig. 4.7(d) for the side RF-probe and in Fig. 4.7(e) for the waveguide-to-PCB connector. In all cases the same rectangular inset-fed microstrip patch antenna is taken and the same PCB size is used. The only difference is the RF-connector and the associated connector interface.

4.3.3 Illustrating the physical phenomena with help of contour plots

In all contour plots in Fig. 4.7 is the field intensity of the E -field of the **antenna radiation** (black arrow) is indicated by the color green for values <65 dBV/m and yellow for values <80 dBV/m. In the inset figures we see 3D simulation models of the patch antenna with a specific RF-connector and a yellow semi-transparent sphere¹⁰. This yellow semi-transparent sphere indicates the region of the reactive near field. It shows that in four [see Fig. 4.7(a) to Fig. 4.7(c) and Fig. 4.7(e)] out of five cases, the RF-connector is entirely or partly in the reactive near-field region.

The location where **reflection** takes place is indicated by a red arrow. In three of the five cases, shown in Fig. 4.7(a) to Fig. 4.7(c), interference patterns are visible. These interference patterns are caused by reflection of the electromagnetic wave coming from the antenna on the RF-connector housing. In the other two cases, shown in Fig. 4.7(d) and Fig. 4.7(e), no interference patterns are visible. This is due to the position of the RF-connector in relation to the antenna and the design of the RF-connector housing. For example, the surface of the housing on which the electromagnetic wave reflects is very small or is at an angle with respect to the antenna so that the wave propagates in a different direction than that from the antenna. Because there is reflection on the

¹⁰The size of the yellow sphere representing the reactive near-field is calculated with $\leq 0.62\sqrt{D_{rs}^3/\lambda}$ where D_{rs} is the diameter of the radiating surface and λ the wavelength of f_0 . Taking the whole PCB as a radiating surface the radius of the reactive near-field is ≈ 35 mm.

RF-connector housing, a part is also blocked. In another case, as can be seen in Fig. 4.7(b) and Fig. 4.7(c) the radiation deflects around the RF-connector housing. This is caused by diffraction.

The location where **diffraction** takes place is indicated with a purple arrow. As can be seen in all contour plots, an electromagnetic wave is created on the other side of the PCB opposite the antenna caused by diffraction. This area still belongs to the reactive near field as visualized with the semi-transparent sphere in the inset figure. Diffraction also takes place on the side where the RF-connector is located. However, in three out of five cases [see Fig. 4.7(a), Fig.4.7(b) and Fig. 4.7(e)] diffraction on the edge of the PCB is not possible because the RF-connector housing is mounted at that location. In the other two cases [see Fig. 4.7(c) and Fig. 4.7(d)], diffraction, both directly, and indirectly through reflection from the RF-probe housing, may affect the antenna behavior.

The location where **unwanted radiation** takes place is indicated with an orange arrow. unwanted radiation is more or less visible in every contour plot. This occurs in those locations where the electromagnetic wave, conducted by some transmission medium, experiences a discontinuity. For the RF-connector shown in Fig. 4.7(a) this is the location where the coaxial connector pin joins the microstrip line on the PCB. This also applies to the RF-connector shown in Fig. 4.7(b). Because the RF-connector is on the opposite side of the antenna, a passage (via) is made to connect the transmission line on the connector side to the transmission line on the antenna side. The via is a discontinuity for the electromagnetic wave and clearly causes unwanted radiation on both sides that is visible in the contour plot. The electromagnetic waves passing through the RF-probes shown in Fig. 4.7(c) and Fig. 4.7(d), both experience a discontinuity at the same location, i.e. where the RF-probe tip transitions to the transmission line on the PCB. In these cases as well, unwanted radiation propagating in both directions is clearly visible in the contour plot. Finally, we discuss the waveguide-to-PCB connector shown in Fig. 4.7(e). At the position where the PCB enters the waveguide, an air gap is present. Here as well the electromagnetic wave experiences a discontinuity, which causes unwanted radiation.

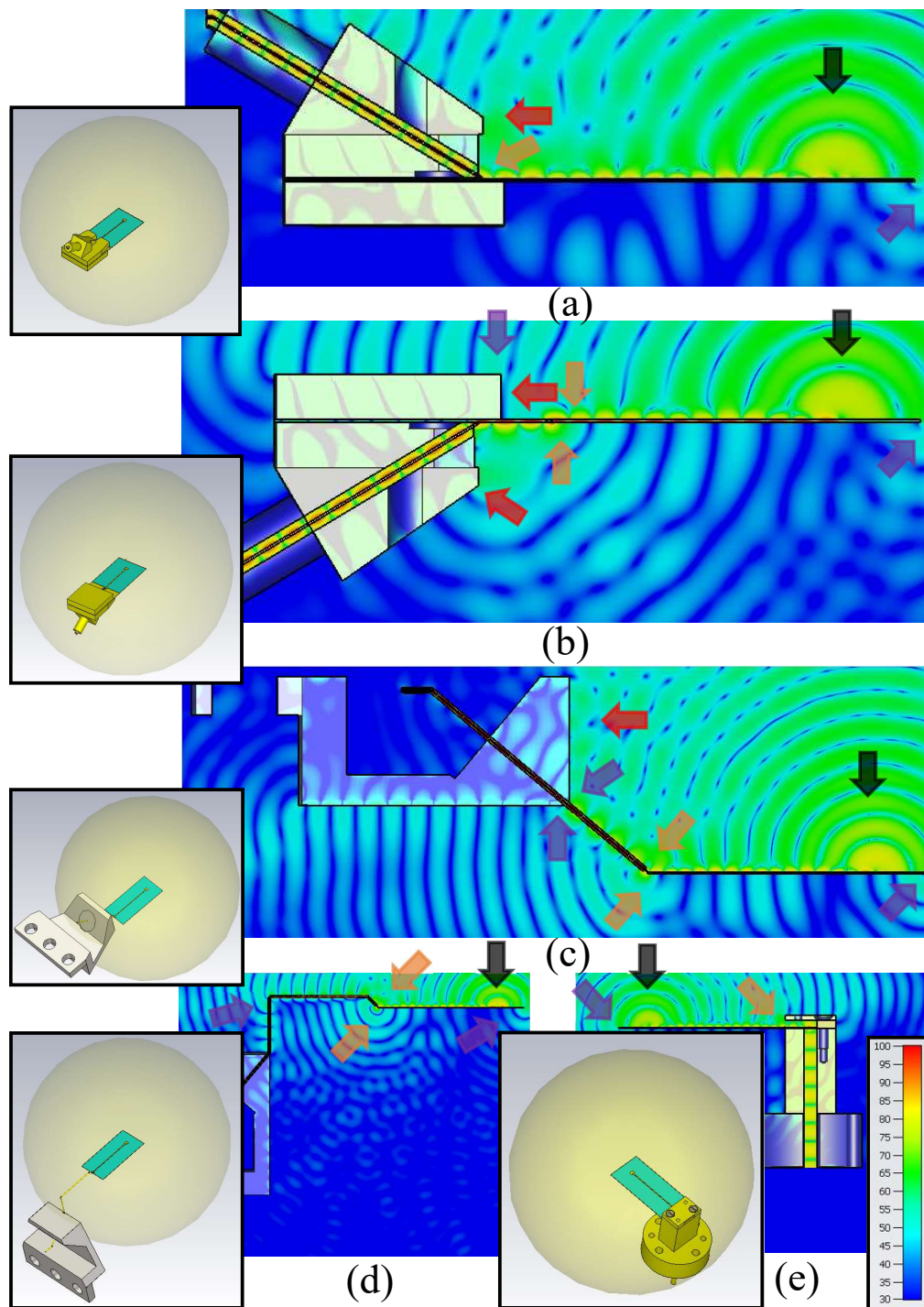


Figure 4.7: Contour plot of the E -field in dBV/m showing the cross section of (a) RF press-fit connector on the top side, (b) RF press-fit connector on the bottom side, (c) RF-probe on top, (d) RF-probe on the side and, (e) waveguide-to-PCB connector. The black arrows indicate the location of the rectangular inset-fed patch antenna, the red arrows point to locations of a reflection, the purple arrows where diffraction occurs, and the orange arrows where unwanted radiation occurs. The insets show the 3D models of the various connectors where the yellow sphere indicates the reactive near-field regions. For all simulation results $f_0 = 85$ GHz.

4.3.4 Effect of the RF-connector on the antenna characteristics

In Fig. 4.8 and Fig. 4.9 the obtained (simulated) antenna characteristics of the rectangular inset-fed microstrip patch antenna with and without RF-connector are found. In Fig. 4.8 the reflection coefficient as a function of frequency and in Fig. 4.9 the gain function in the E - and H -plane is shown. In the figures, a distinction is made for non-preferred RF-connectors (blue lines) and for preferred RF-connectors (green lines). The semi-transparent blue plane in Fig. 4.8 shows the required frequency bandwidth (see Chapter 3 section 3.4). Furthermore, the graph of a ‘reference’ antenna has been added to each figure (black line). This reference antenna (RA) is the antenna without RF-connector and without RF-connector interface. With the help of this RA it is made clear what and how large the effect of the RF-connector and RF-connector interface on the behavior of the antenna is. By analyzing the obtained antenna characteristics, we can find out which physical quantity causes a particular disturbance.

We start with the **antenna radiation**. In Fig. 4.8 and Fig. 4.9 it can be clearly seen that none of the simulation results for the antenna with RF-connector matches the result of the RA. If we look in Fig. 4.8 and Fig. 4.9 at the reflection coefficient and the gain function, it is noticeable that some RF-connectors have less influence on the behavior of the antenna than others. This has to do with the position of the RF-connector in relation to the antenna and the geometry of the RF-connector housing. Furthermore, four of the five RF-connectors are located in the near field of the antenna. The fifth RF-connector [see Fig. 4.7(d)] is located on the border between the reactive and radiating near-field. That the placement of the RF-connector in the near-field affects the behavior of the antenna is clearly seen in Fig. 4.8. In all RF-connector / antenna combinations the resonance frequency has shifted and in some cases another resonance appears. As for the gain functions in Fig. 4.9, a difference can clearly be seen between the E - and H -plane. The gain function in the E -plane is more affected by one of the phenomenon than the H -plane. This is because the RF-connector is in line with the E -plane of the rectangular inset-fed microstrip patch antenna.

In Fig 4.9(a) we see a disturbance of the gain function, possibly caused by **reflection** from the RF-connector housing. This disturbance is in the form of a ‘ripple’ with a certain periodicity. When we analyze the results of the gain functions, it is noticeable that the amplitude of the ‘ripple’ is larger for the non-preferred RF-connectors than for the preferred RF-connectors. This is because the housing of the non-preferred RF-connector is in the line of sight of the antenna. Depending on the specific antenna / RF-connector combination, we see in the associated gain functions in Fig. 4.9(a) constructive and destruction interference patterns.

Another phenomenon that can disturb the gain function is **diffraction**. Diffraction has the same effect on the gain function as reflection, namely causing a ripple with a certain period. The period of the ripple depends on the distance between the antenna and the

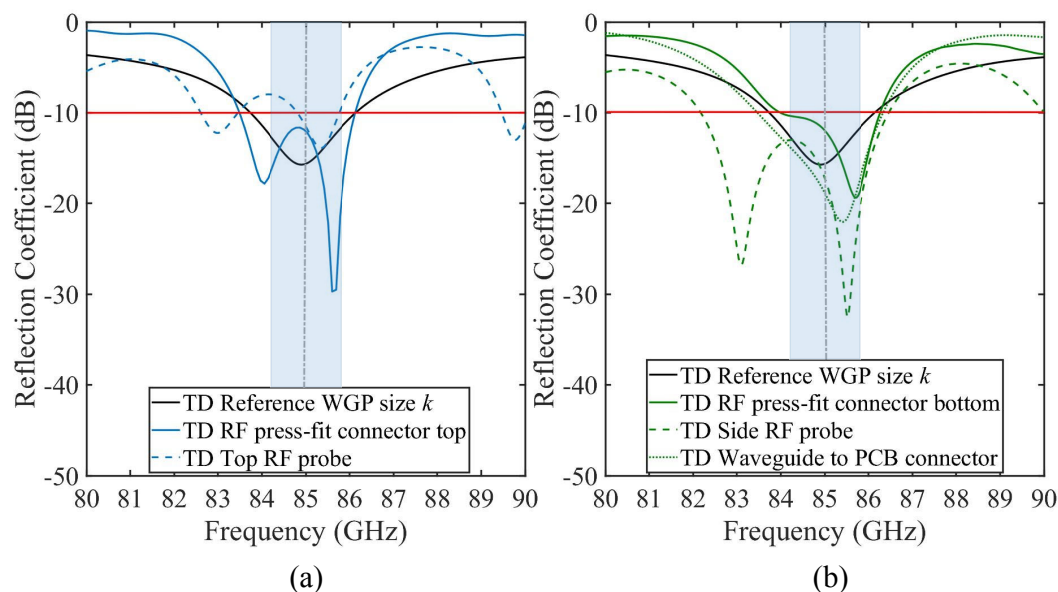
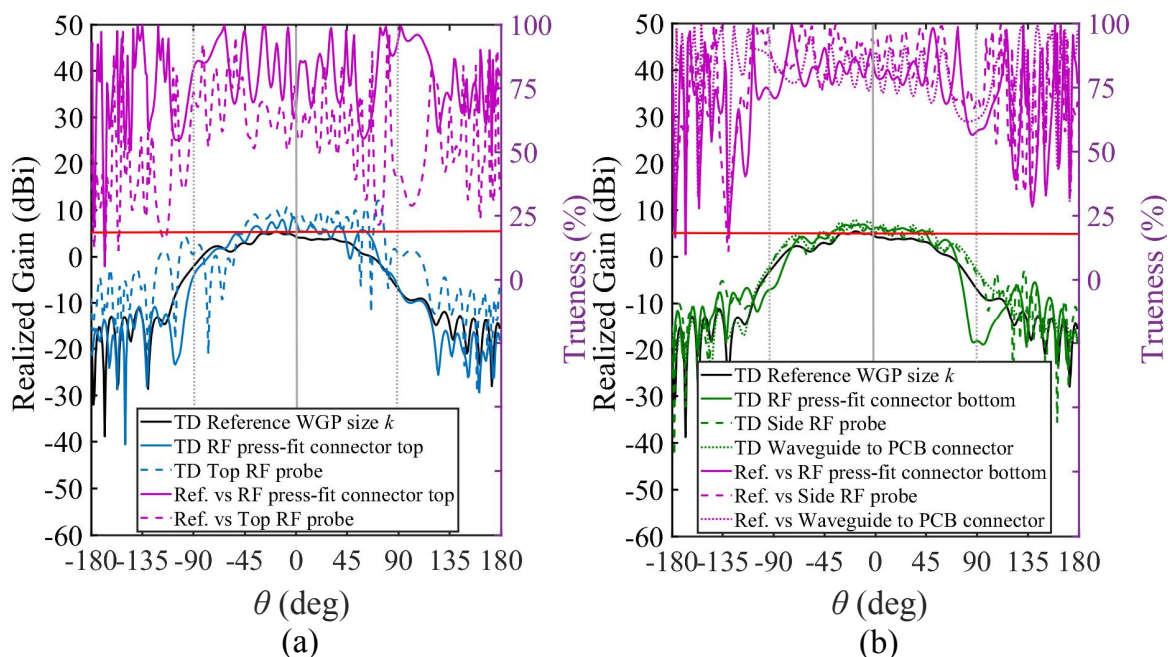


Figure 4.8: Reflection coefficient as a function of frequency for (a) non-preferred RF-connectors and, (b) preferred RF-connectors. The -10 dB threshold is indicated with the red solid line, the frequency bandwidth with the vertical blue area and the resonance frequency with the gray dotted line. ‘WGP k ’ stands for waveguide port where its dimensions are calculated with ‘port extension coefficient’ k [112] (see Chapter 3, Fig. 3.7).



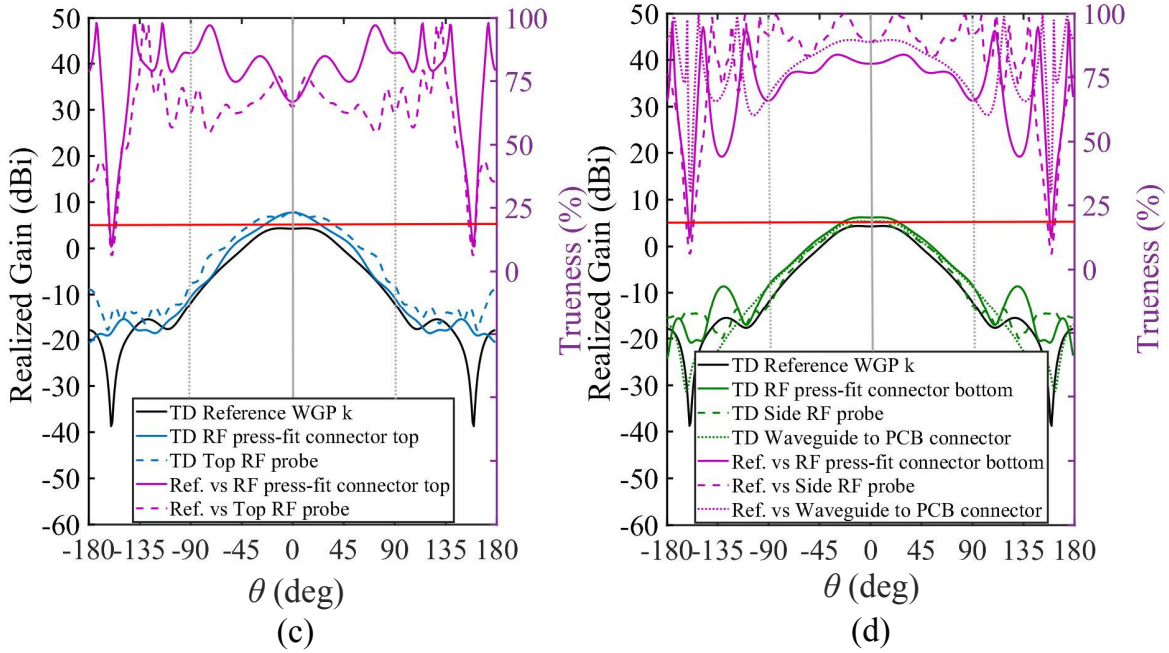


Figure 4.9: Realized gain pattern in the E -plane (a) less preferred RF-connector design, and, (b) preferred RF-connectors. The realized gain pattern in the H -plane for (c) non-preferred RF-connectors and, (d) preferred RF-connectors. In all cases the trueness, expressed in % is displayed on the right vertical axis. The 5 dBi realized gain is indicated with the red solid line, the gray dotted line indicates the 0° and $\pm 90^\circ$ angles. For all simulation results $f_0 = 85$ GHz.

source of the radiation, in this case, the edge of the PCB. This would mean that as the PCB gets bigger the periodicity of the ripple will increase. However, due to the greater distance between the edge of the PCB and the antenna and losses in the substrate, the amplitude of the ripple will decrease to a point that no disturbance is noticeable. The consequences of diffraction at the edges of the PCB on the behavior of the antenna are independent of the RF-connector and will therefore not be discussed further in this chapter.

Unwanted radiation is the last phenomenon we will discuss in this section. As with reflection and diffraction, unwanted radiation can affect the gain function. Unwanted radiation mainly originates from the probe to waveguide transition on the PCB (see Fig. 4.7, orange arrow). Both the effect of reflection and diffraction can be calculated or its origin based on the effect on the radiation pattern explained. However, not much is known about the effect of unwanted radiation on the antenna characteristics. Therefore, the influence of unwanted radiation and whether it can be reduced or even prevented will be examined in the next section.

In conclusion Fig. 4.9 shows the systematic error that is expressed as trueness (%) (see

Chapter 2, Section 2.6) and shown on the right vertical axis. In general, the trueness shows that the E -plane, [see Fig. 4.9(a) and 4.9(b)], is the most affected by the RF-connector compared to the H -plane, [see Fig. 4.9(c) and 4.9(d)]. For the preferred RF-connectors the trueness does not show a distinct difference.

4.4 Analysis of the cause of unwanted radiation

In the proceeding paragraphs we have analyzed a rectangular inset-fed microstrip patch antenna with different RF-connectors¹¹. Obviously, the influence of the RF-connector on the antenna characteristics depends mainly on the shape of the RF-connector housing and its position with respect to the antenna. By positioning the housing so that it is no longer in the line-of-sight of the antenna [see Fig. 4.7(d)], reflection on the housing can be prevented. Although it is possible to place the RF-connector out of the line-of-sight of the antenna, this is not enough to eliminate the disturbance of the antenna characteristics. As noted earlier, this may be caused by unwanted radiation. In Fig. 4.7 unwanted radiation is visible for all RF-connectors and is indicated by orange arrows. The cause and magnitude of the influence of unwanted radiation on the antenna characteristics will be discussed in the following sections.

4.4.1 Uncertainties caused by transmission line transitions

The mechanical connection between an antenna and a measuring instrument can consist of different types of waveguides as is illustrated in Fig. 4.10(a). In this example, the mechanical connection, between the rectangular inset-fed microstrip patch antenna and the VNA, consists of a coaxial cable going to a copper-backed coplanar waveguide (CBCPW) going to a microstrip line. Fig. 4.10(b) zooms in on the cross-section of a coaxial cable and the orientations of the E -field (blue) and the H -field (red) are illustrated with arrows. Fig. 4.10(c) zooms in on the cross-section of a CBCPW and Fig. 4.10(d) on the cross-section of a microstrip line. If we compare the field orientations between the three different waveguides from Fig. 4.10(b) to Fig. 4.10(d) with each other, we notice that at the transitions of the waveguides a change in orientation of the field lines occurs. This is especially true for the orientation of the E -field [148], [149].

A phenomenon that occurs in the transition from a coaxial cable to a coplanar waveguide are fringe fields as illustrated with yellow arrows in Fig. 4.10(e). The fringe fields (E -field) bend out, from the inner conductor, to the shield of the coaxial cable (left figure)

¹¹The combination of antenna with RF-connector is referred to as the “measurable” antenna in Chapter 1, section 1.6. The measurable antenna fits the functional model presented in Chapter 3 Fig. 3.2 and Chapter 4 section 4.3.

and, in this case, to the ground plane on the PCB (right figure). The deflection of the E -field towards, for example, the shield of the coaxial cable results in currents on the outside of the coaxial shield. These currents can cause radiation that could interfere with the antenna characteristics. The presence of fringe fields also makes the position where the RF-probe is placed on the connector interface important. In Fig. 4.10(e), the right figure shows the RF-probe in a different location on the connector interface than in the left figure. In the right figure, the fringe fields not only pass through air but also through a part of the substrate (PCB). Since the substrate has a different relative permittivity than that of air, this will affect the impedance at the position where the RF-probe transitions to the connector interface. This position dependence also occurs when the RF-probe is calibrated with a so-called commercially available calibration substrate [150]. This would mean that the results and reproducibility of the calibration performed is unreliable. Furthermore, the calibration substrate has a different relative permittivity (10.9)¹² than that of the substrate used for the inset-fed microstrip patch antenna (3.16). Due to the presence of the fringe field, the calibration standard consists not only of a load, but of a load, air and dielectric material. Here, the ratio of air to dielectric material can vary depending on the position of the RF-probe on the connector interface of the antenna design or the calibration substrate.

Furthermore, in Fig. 4.10(e), at the location where the RF-probe connects to the PCB, electromagnetic waves are indicated with orange colored curved lines. Not only does a change of orientation of the E -field takes place here. Also, the RF-probe waveguide is not physically aligned with the waveguide on the PCB but is angled, causing unwanted radiation.

An illustration of an RF press-fit connector can be found in Fig. 4.10(f). The transition between the waveguide of the RF press-fit connector and the waveguide on the PCB experiences the same uncertainties as that of the RF-probe. This is because it is essentially the same composition of waveguides. The difference between the RF-probe and the RF press-fit connector is the housing. The housing of the RF press-fit connector is designed in such a way that it can be fixed to the PCB with screws. Again, fringe fields are created where the coaxial cable ends and unwanted radiation at the location where the RF-connector transitions to the RF-connector interface on the PCB.

In the right picture of Fig. 4.10(f) we see an illustration of an RF press-fit connector placed on the side where the antenna is located (top). Another option is to place the RF press-fit connector on the back of the PCB as illustrated in the left picture in Fig. 4.10(f). This makes it necessary to connect the transmission line on the back of the PCB to the transmission line on the top of the PCB using a metallization (via). The use of vias is often not desirable because it is a discontinuous transition, which could

¹²The relative permittivity of the calibration substrate is 10.9, which corresponds to the relative permittivity of some of the IC materials used.

cause unwanted radiation [see Fig. 4.7(b)].

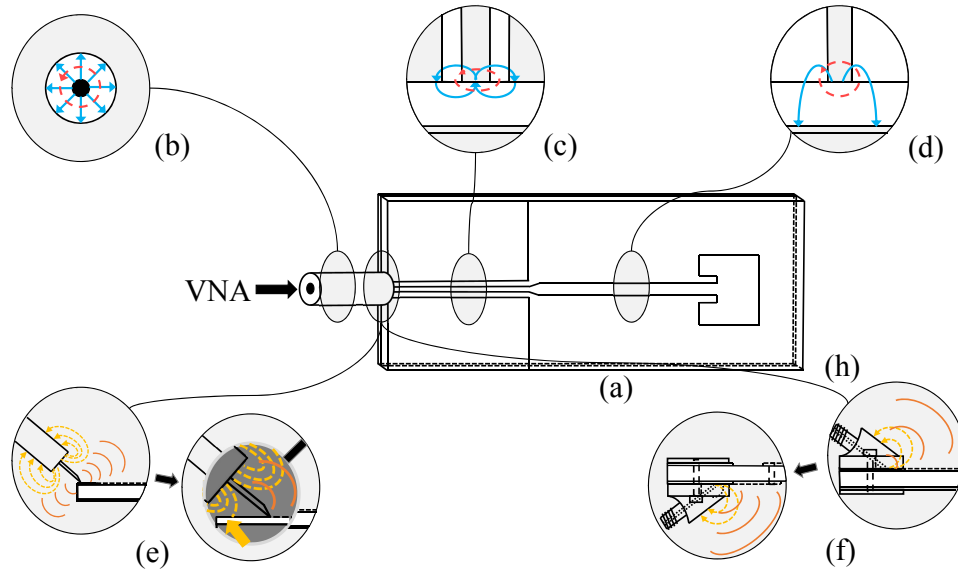


Figure 4.10: (a) From left to right illustration of a coaxial cable, copper-backed coplanar waveguide and microstrip line, respectively. Electric (light blue arrows) and magnetic field (light red dashed ellipse) field lines (b) coaxial cable, (c) copper-backed coplanar waveguide and, (d) microstrip line. (e) RF-probe and, (f) RF press-fit connector. The unwanted radiation is indicated with orange lines and the fringe fields with yellow dotted arrows.

4.4.2 Determining the effect of the unwanted radiation on the antenna characteristics

To be able to illustrate the effect of the transmission line transitions, as discussed in the preceding section, a simulation model is made as shown in Fig. 4.11(a). This figure shows the simulation model consisting of three different kinds of transmission line. From left to right these are: a coaxial cable (Coax), a CBCPW and a microstrip line (μ SL). In Fig. 4.11(b) to Fig. 4.11(d) the simulation results are shown in contour plots of the E -field in dBV/m. The locations where unwanted radiation takes place are indicated by orange arrows. In Fig. 4.11(c) the edge fields are indicated with a yellow arrow. In Fig. 4.11(b) and Fig. 4.11(d), diffraction is present at the longitudinal edges of the PCB that is caused by the transmission line in combination with the finite ground plane. The diffraction is indicated by purple arrows.

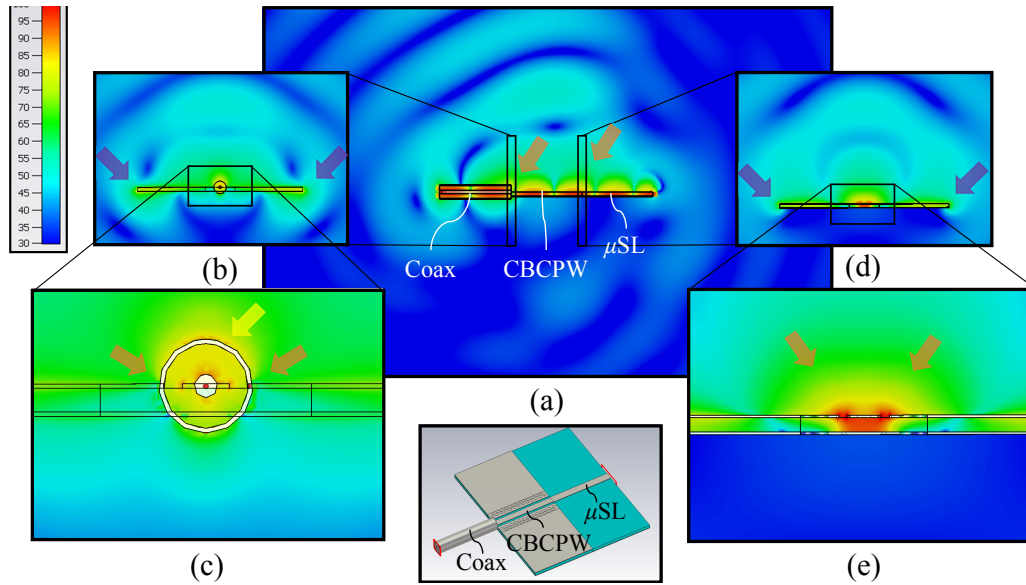


Figure 4.11: Contour plot of the E -field in dBV/m of (a) coaxial cable to CBCPW to μ SL simulation model (bottom). (b) Orthogonal plane at the coaxial cable to CBCPW transition and, (c) zoomed-in. (d) Orthogonal plane at the CBCPW to μ SL transition and, (e) zoomed-in. The yellow arrow indicates the location of the fringe fields, the orange arrows the location of the unwanted radiation and the purple arrows the location where diffraction occurs.

In Fig. 4.12 the simulation results are shown, in the form of the reflection coefficient and realized gain function, of the transmission line model [see Fig. 4.11(a)]. In Fig. 4.12(a) the level of the reflection coefficient for the different kind of transmission lines and a combination thereof is below -20 dB. This means that in all cases 99% of the power is accepted by port one, regardless of the transmission line composition. It should be noted that the size of the WGP port and its impedance are ideally matched to the area of the fringe fields and to the impedance of the transmission line, respectively.

To determine whether the non-ideal transmission lines and the combination of transmission lines radiate, the gain function has also been plotted. In Fig. 4.12(b) the results are shown for the E -plane and in Fig. 4.12(c) the results for the H -plane. It is noticeable that the level of the gain function for the individual transmission lines is lower than the level of the gain function for the combination of transmission lines. This is especially true for the CBCPW compared to the results of the microstrip line. What is shown with the results of the combination of transmission lines is that the transitions between the different waveguides make a significant contribution to the unwanted radiation. For certain angles, this contribution increases by almost 20 dB compared to the results of the individual waveguide.

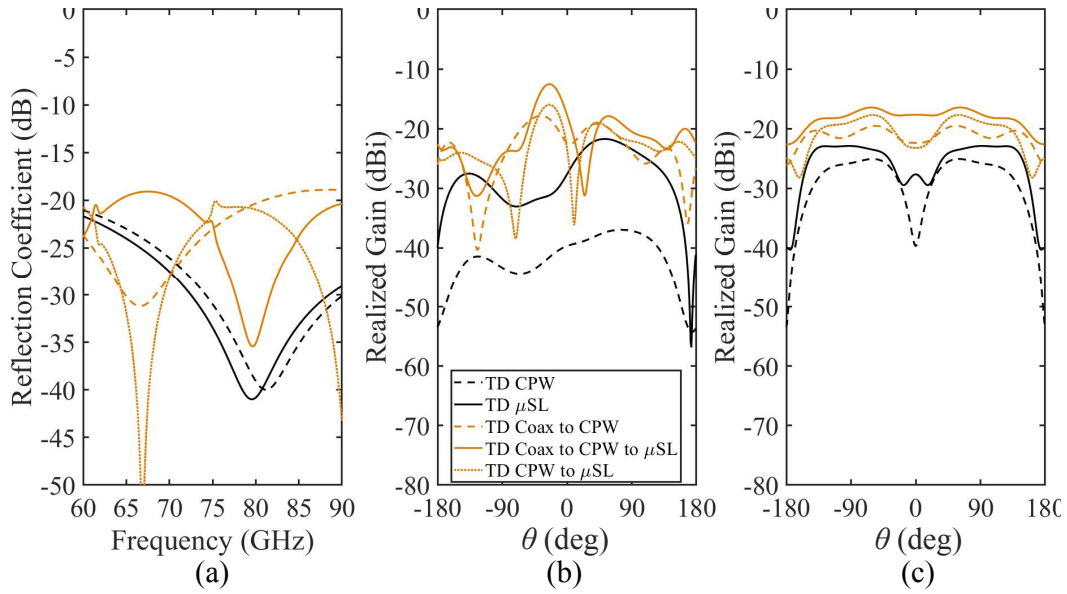


Figure 4.12: The (a) Reflection coefficient, (b) realized gain pattern in the E -plane and, (c) realized gain pattern of the H -plane in the co-planar waveguide (CPW), microstrip line (μ SL) and a combination of both. The simulations are performed in the time domain (TD). For all simulation results $f_0 = 85$ GHz.

4.4.3 Antenna radiation versus unwanted radiation

Now that it is known that the transitions radiate, the ‘antenna model’ is modified as illustrated in Figure 4.13(a). The modification consists of omitting the antenna from the design, leaving the connector and microstrip line, as shown in Fig. 4.13(b). The antenna has been replaced by a load whose impedance matches that of the antenna. The design of the load¹³ is shown in more detail in Figure 4.13(c).

¹³Possible radiation coming from the waveguide port as discussed in Chapter 3 is not included in this analysis.

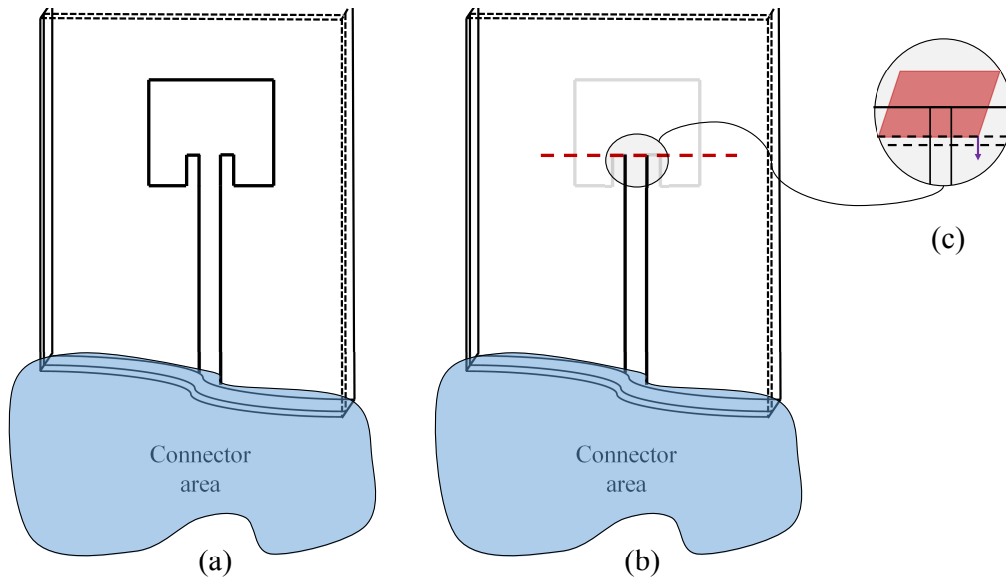


Figure 4.13: (a) Illustration of a rectangular inset-fed microstrip patch antenna i.e. the antenna model. (b) Illustration of the design where the patch antenna is omitted and replaced by a waveguide port acting as a load. The location of the waveguide port is indicated with the red dashed line. (c) Shows the design of the waveguide port. The blue area is where a certain RF-connector is located.

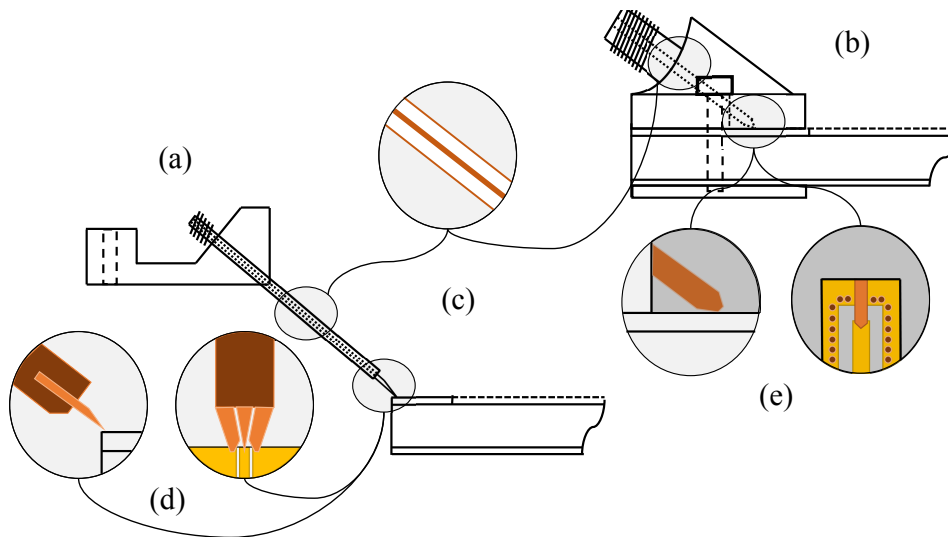


Figure 4.14: (a) Illustration of a top RF-probe and, (b) an RF press-fit connector, (c) a section of a rigid coaxial cable, (d) RF-probe tip with ground-signal-ground pins and, (e) an RF press-fit connector tip with pin (signal) and housing (ground).

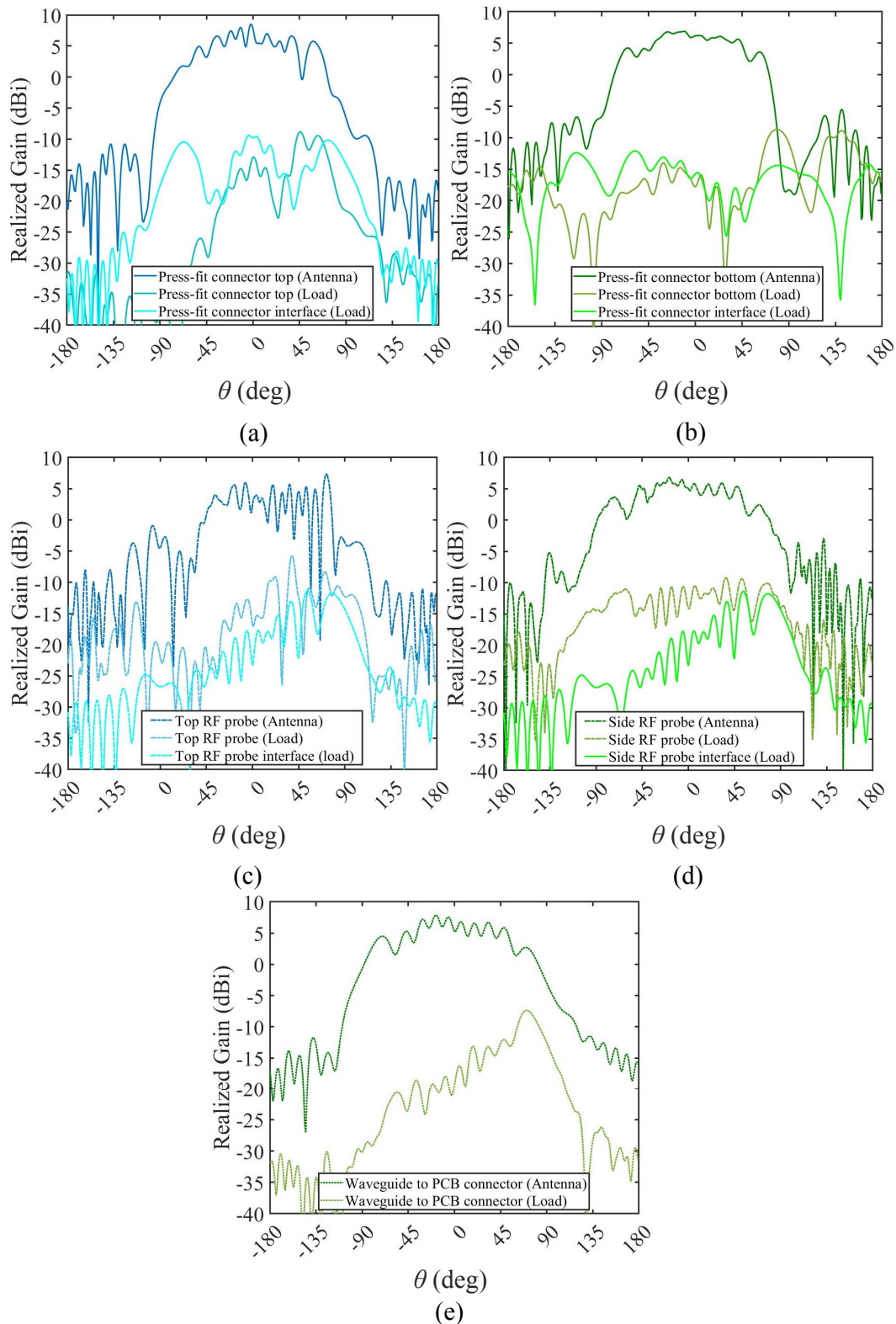


Figure 4.15: Realized gain pattern of the E -plane of the (a) less preferred RF-connector design, (b) preferred RF-connectors, (c) less preferred RF-probe design, (d) preferred RF-probe design, and (e) preferred waveguide to PCB design. For all simulation results $f_0 = 85$ GHz.

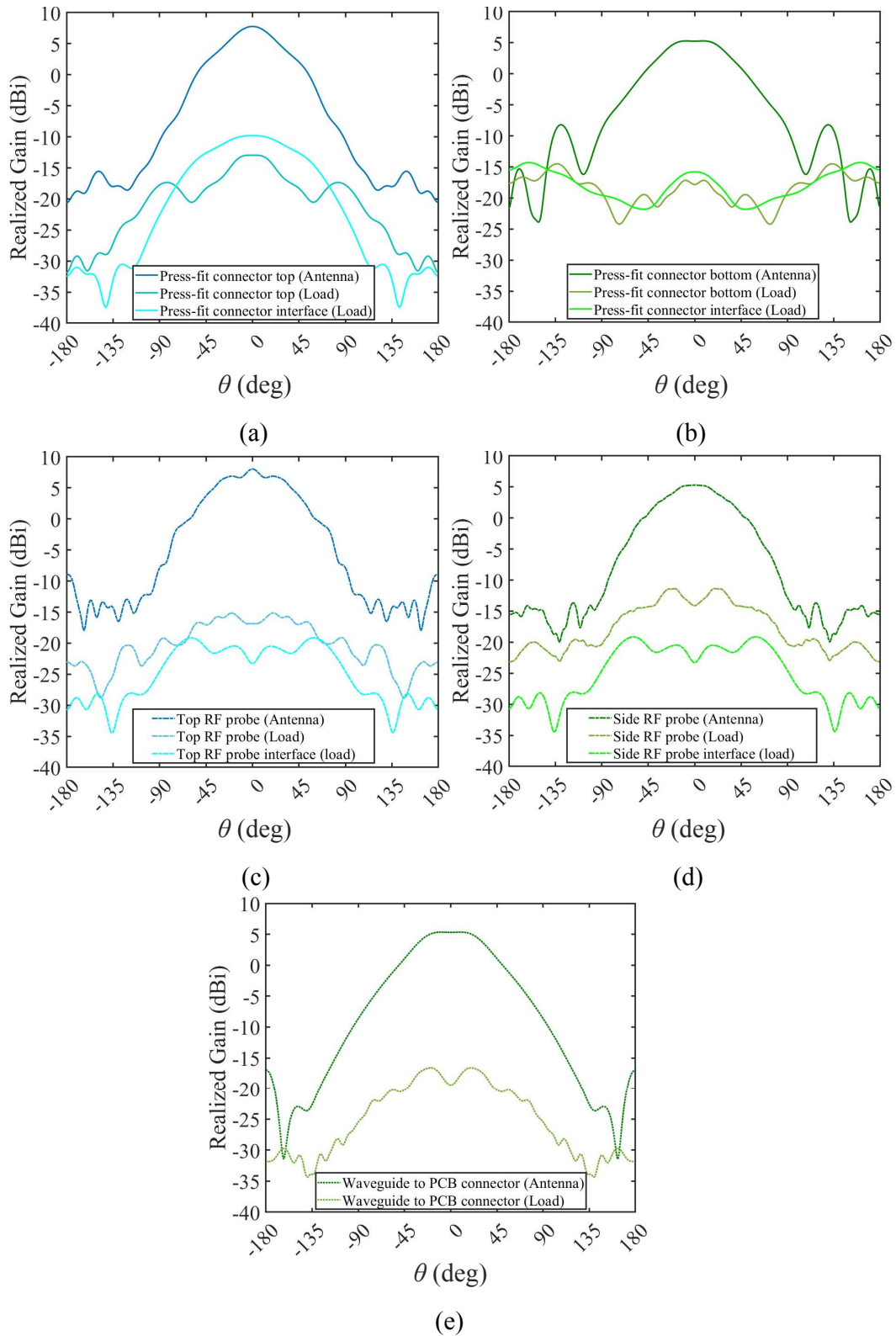


Figure 4.16: Realized gain pattern of the H -plane of the (a) less preferred RF-connector design, (b) preferred RF-connectors, (c) less preferred RF-probe design, (d) preferred RF-probe design, and (e) preferred waveguide to PCB design. For all simulation results $f_0 = 85$ GHz.

The results of the realized gain pattern G_{rp} in Fig. 4.15 for the E -plan and Fig. 4.16 for the H -plan show the comparison between an RF-connector type with antenna (dark colored solid line), RF-connector without antenna (lighter colored solid line), and RF-connector interface¹⁴ without antenna (lightest colored solid line). It becomes clear that the magnitude of the unwanted radiation for the E -plane has become very close to the lowest magnitude of the G_{rp} . Fig. 4.15(b), 4.15(c) and, 4.15(d) show that the magnitude of the unwanted radiation is even higher at some angles than the magnitude of the G_{rp} . For the H -plane just in two cases the magnitude of the unwanted radiation is higher than the magnitude of G_{rp} shown in Fig. 4.16 and Fig. 4.16. The fact that the magnitude of the unwanted radiation exceeds the magnitude of the G_{rp} is because the radiation from the antenna is missing [see Fig. 4.14(b)].

Interestingly, the top press-fit connector shows the best ratio between unwanted radiation and G_{rp} . This is due to the shape of the connector housing. It does not mean that this connector-type does not radiate, but that the housing reflects the radiation in a different direction so that it does not interfere with the radiation coming from the RA.

Because each connector makes a transition to a μ SL, unwanted radiation is inevitable. Although the side probe seems to give the best overall performance a major disadvantage is that it is fragile. The probe tip could easily be damaged without noticing it visually. It is difficult to judge that the RF-probe is broken based on the calibration results or the measured results alone. Simulation results in which the RF-probe is included could offer a solution to compare the measurement results with. Major differences could indicate that the RF-probe is broken. Possible damage to the RF-probe could be simulated as a verification of the hypothesis.

4.5 New RF probe design

From the preceding section it can be concluded that unwanted radiation is caused by the transition from one type of transmission line to another. Furthermore, in some cases the RF-connector housing forms a complete or partial obstruction affecting the radiation pattern of the AUT. In this section a new RF-probe design is described where the goal is that both the unwanted radiation and the effect of the presence of the RF-probe on the behavior of the AUT are minimized.

The electrical requirements are:

- to avoid a CBCPW interface design on the PCB,
- the dielectric materials of the RF-probe are equal or close to that of the substrate

¹⁴The RF-connector interface is not present for the waveguide to PCB connector.

of the AUT.

The mechanical requirements are:

- to avoid discontinuity between the various transmission media as much as possible,
- the size of the RF-probe should be as small as possible,
- the probe contact should be designed such that no or a minimum air gap exists,
- the RF-probe should be placed out of the field of view of the antenna.

The new RF-probe connected to the AUT [see Fig. 4.17(a)] consists of a semi-rigid coaxial cable that transits gradually to a semi co-planar microstrip line, as illustrated in Fig. 4.17 (b). The two metal bars on the side of the coaxial cable, transitioning to the PCB, prevent unwanted radiation by creating a semi-coplanar waveguide, which in turn prevents fringe fields. Fig. 4.17(c) to 4.17(e) show the mode transition from the coaxial cable to the microstrip line on the PCB, respectively.

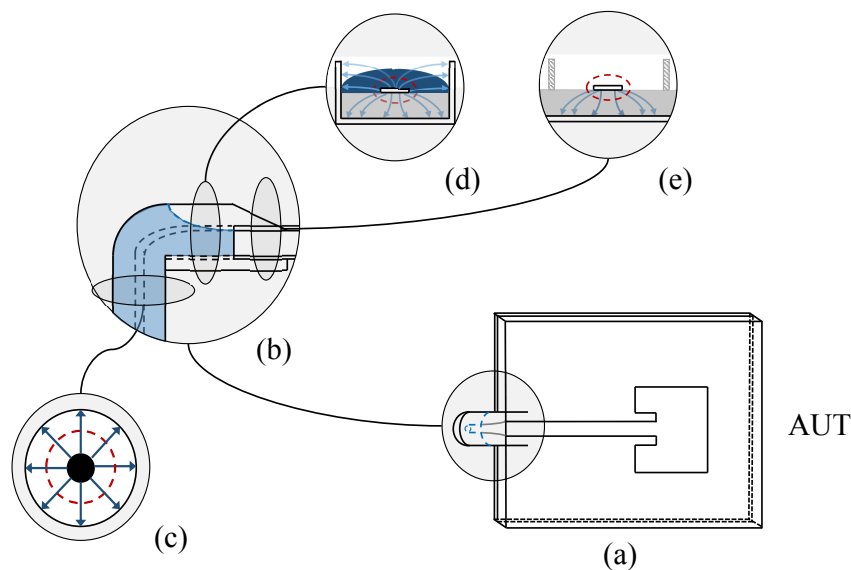


Figure 4.17: Illustration of (a) the new RF-probe with a patch antenna, (b) side view of the RF-probe, (c) coaxial mode, (d) semi-coplanar waveguide mode and, (e) microstrip line mode.

Fig. 4.18(a) and Fig 4.18(b) show the contour plot of an E -field in dBV/m for the side RF-probe and new RF-probe, respectively. The red ellipses indicate the area where

interference can be observed. The interference pattern is more distinct in the presence of the side RF-probe with antenna combination than in the presence of the new RF-probe. The way the new RF-probe is attached to the antenna is illustrated in Fig. 4.18(c), which shows that all the mechanical requirements presented in this section are met.

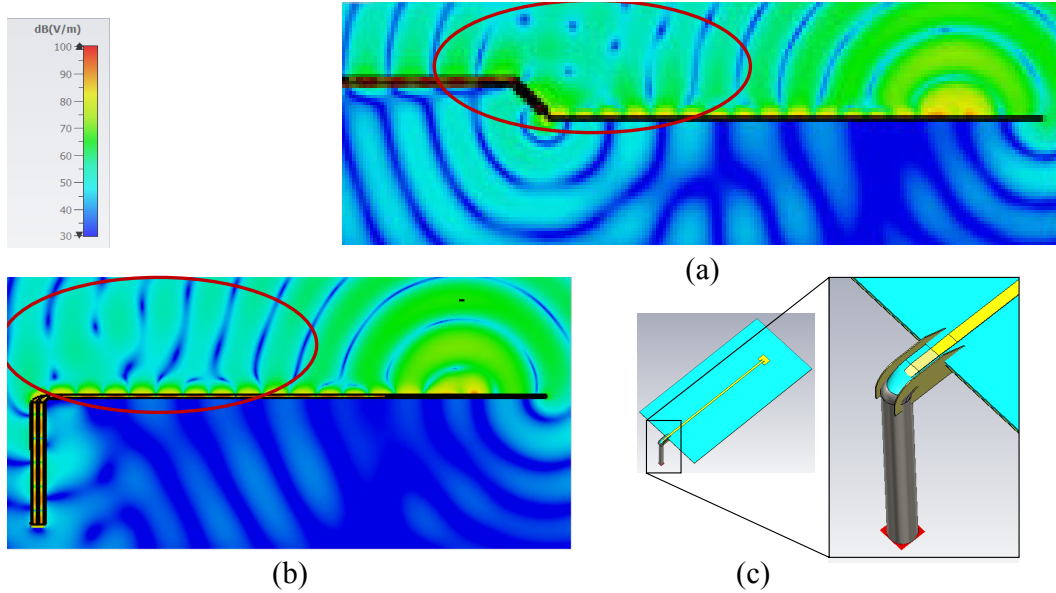


Figure 4.18: Contour plot of the E -field in dBV/m, (a) side RF-probe and, (b) new RF-probe. In (c) a perspective view of the new RF-probe and zoomed in. The red ellipses indicate the area where interference occurs caused by the RF-probe.

The simulation results of the realized gain pattern in the E -plane are shown in Fig. 4.19(b) and in the H -plane in Fig. 4.19(c). The results consist of the new RF-probe with inset fed patch antenna and the new RF-probe with load are compared. Also added are the results of the best option for the RF-connector as presented in the previous section, namely the side RF-probe.

The results in Fig. 4.19(a) show that the reflection coefficient is less affected by the new RF-probe than by the side RF-probe. On the other hand at $f_0 = 85$ GHz the reflection coefficient is lower for the side RF-probe, thus affecting the realized gain as illustrated by the trueness.

Fig. 4.19(b) and Fig. 4.19(c) show, for the E and H -plane, respectively, that the new RF-probe has much less unwanted radiation compared to the results of the side RF-probe (at $\theta = 0^\circ \approx 20$ dB). Furthermore, the rectangular inset-fed microstrip patch antenna, with new RF-probe, shows less distortion on the realized gain pattern for both E - and H -plane compared to the rectangular inset-fed microstrip patch antenna with side RF-probe.

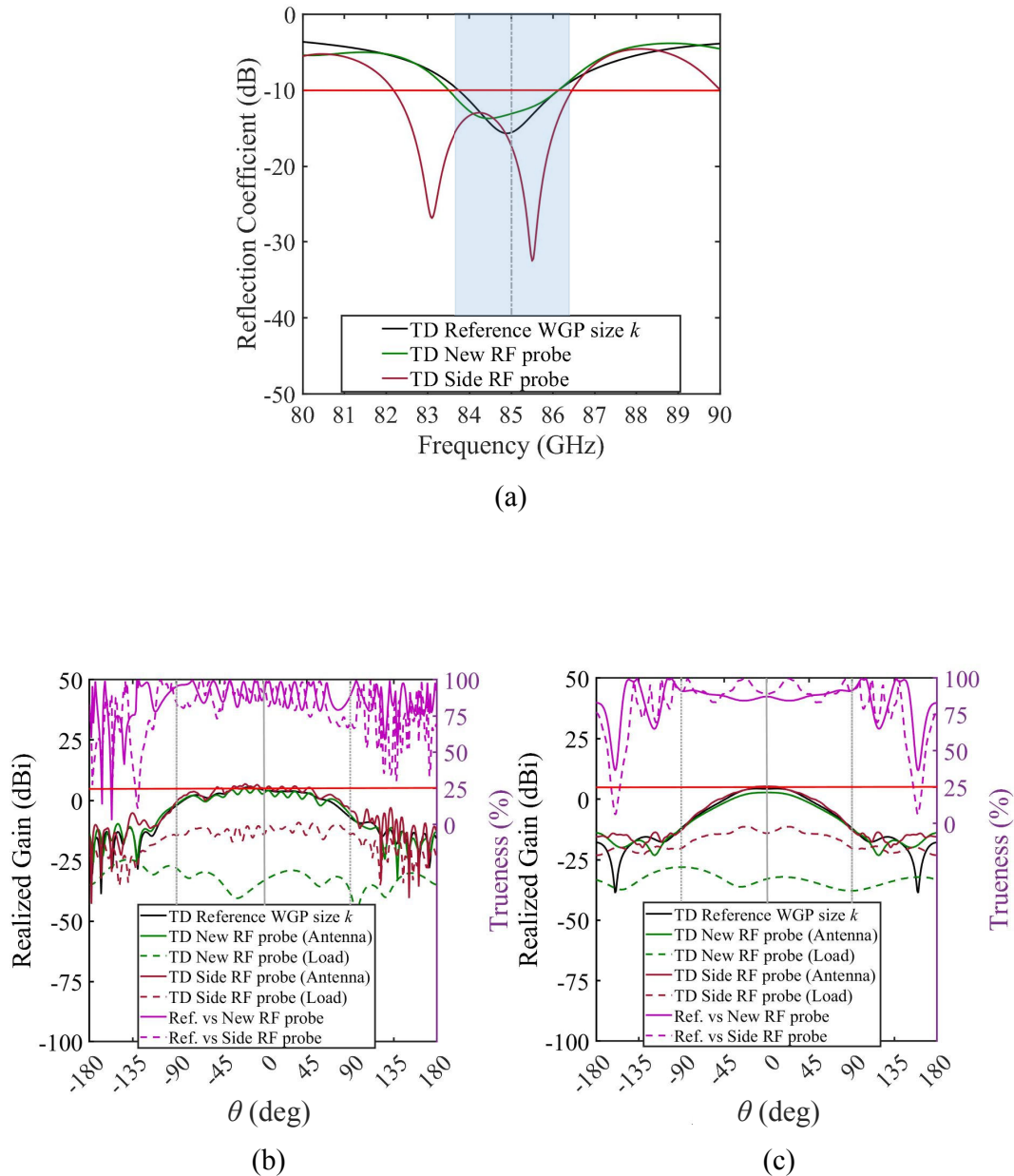


Figure 4.19: (a) Reflection coefficient as function of frequency for a new RF-probe versus side RF-probe (preferred RF-connectors). Gain pattern of the new RF-probe versus the side RF-probe, (b) E -plane and, (c) H -plane. The -10 dB threshold for the reflection coefficient is indicated with the red solid line, the frequency bandwidth with the vertical blue area and the resonance frequency with the gray dotted line. For the realized gain the trueness, expressed in % is displayed on the right vertical axis. The 5 dBi threshold of the realized gain is indicated with the red solid line, the gray dotted line indicates the 0° and $\pm 90^\circ$ angles. For all simulation results in (b) and (c) $f_0 = 85$ GHz.

The difference in gain patterns [see Fig. 4.19(b)] between the two RF-probes is mainly due to the fact that the new RF-probe is located on the side of the PCB where the side RF-probe is partially located on top of the PCB. This allows the wave emanating from the antenna propagating towards the side RF-probe to reflect off the coaxial cable, causing constructive and destructive interference on the realized gain pattern [see Fig. 4.7(d)].

4.6 Contactless antenna measurement

Published in [151]

As discussed in the previous sections the contacted measurement will always have, to some extent, effect on the antenna results (observer effect). Therefore, performing a reflection coefficient or G_{rp} measurement without any mechanical connection to a measurement system, i.e. contactless, could be an improvement or not.

Such a contactless antenna measurement is introduced in [152] and its principle is illustrated in Fig. 4.20(a) [151]. The setup consists of a RA (horn) attached to a VNA

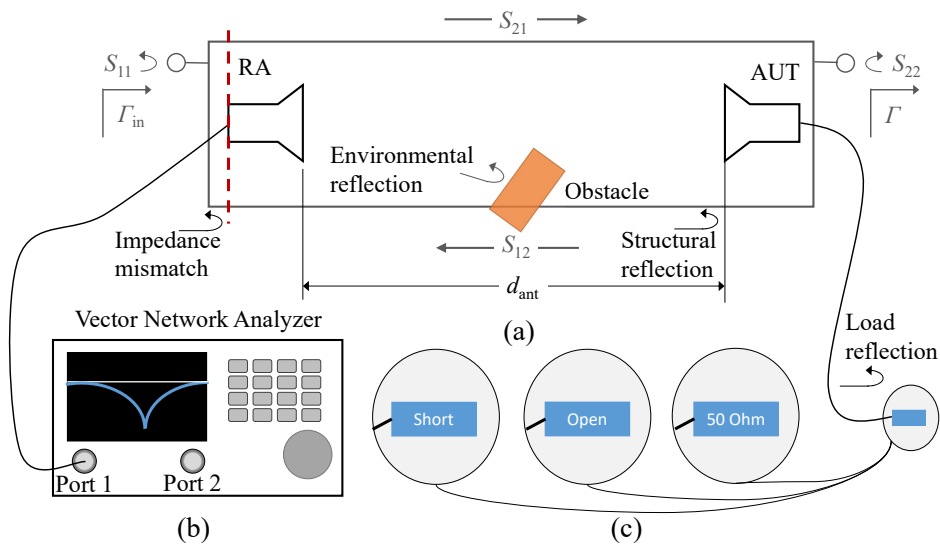


Figure 4.20: (a) Schematic illustration of a contactless antenna measurement setup with d_{ant} the distance between the two antennas. In light gray the two-port model of the contactless measurement method. The orange rectangle represents objects in the vicinity of the AUT that causes environmental reflections. The RA (horn) is connected to (b) a vector network analyzer (port 1) and the antenna under test is connected to (c) one of the three loads, open, short or 50 Ω .

[see Fig. 4.20(b)], and an AUT attached to one of three loads [see Fig. 4.20(c)]. By

obtaining the measurement results of all three loads by performing a reflection (S_{11}) or transmission (S_{21}) measurement, both the impedance and G_r function can be derived.

The key aspect of this method is that the environment including the AUT is static during the reflection coefficient measurement. The only aspect that changes is the load connected to the AUT, as illustrated in Fig. 4.20(c). For the G_{rp} measurement the AUT has to be rotated once to obtain the H -plane.

4.6.1 Determining the input impedance

The contactless setup is modeled as a two-port network. This is illustrated in light gray in Fig. 4.20(a). The VNA is connected to port 1 and a known load with reflection coefficient Γ to port 2. The reflection coefficient at the RA, Γ_{in} is calculated as:

$$\Gamma_{in} = S_{11} + \frac{S_{12}S_{21}\Gamma}{1 - S_{22}\Gamma}. \quad (4.2)$$

To be able to find the three unknowns S_{11} , S_{22} , and the product of $S_{12}S_{21}$ shown in Equation (4.2), three sequential measurements have to be performed. During these three measurements, nothing can change in the measurement setup except the load to be attached to the AUT. With the obtained three data sets the following solution for the three unknowns is found [153]-[155]:

$$\begin{pmatrix} S_{11} \\ S_{22} \\ S_{12}S_{21} - S_{11}S_{22} \end{pmatrix} = \begin{pmatrix} 1 & \Gamma_{Z_1-in}\Gamma_{Z_1} & \Gamma_{Z_1} \\ 1 & \Gamma_{Z_2-in}\Gamma_{Z_2} & \Gamma_{Z_2} \\ 1 & \Gamma_{Z_3-in}\Gamma_{Z_3} & \Gamma_{Z_3} \end{pmatrix}^{-1} \begin{pmatrix} \Gamma_{Z_1-in} \\ \Gamma_{Z_2-in} \\ \Gamma_{Z_3-in} \end{pmatrix}, \quad (4.3)$$

where Γ_{Z_1-in} , Γ_{Z_2-in} , and Γ_{Z_3-in} represent the measured reflection coefficient at port 1 (see Fig. 4.20) while port 2 is terminated with known loads having reflection coefficients Γ_{Z_1} , Γ_{Z_2} and Γ_{Z_3} , respectively.

4.6.2 Determining the realized gain pattern

The two-port network illustrated in Fig. 4.20 is similar to that of a G_r measurement. Based on the Friis equation the unknown gain of the AUT can be derived if the gain of the RA is known. The Friis equation, based on the G_r , can be written as follows:

$$|S_{21}|^2 = G_{RA_r} G_{AUT_r} \left(\frac{\lambda_0}{4\pi d_{ant}} \right)^2. \quad (4.4)$$

where λ_0 is the wavelength in free-space, d_{ant} is the distance¹⁵ between the antennas, G_{RA_r} the gain of the RA and G_{AUT_r} the gain of the AUT. When both the RA and AUT are connected to a VNA and the G_r of the RA is known, a measurement of S_{21} will reveal the G_r of the AUT. To be able to apply this method, the VNA [see Fig. 4.20(a)] has to be calibrated up to antenna port 1 [see Fig. 4.20(a) red dashed line]. Antenna port 2 has to be connected to the known loads [see Fig. 4.20(c)]. By performing three measurements, each with a different load, Equation (4.3) can be used to derive the realized antenna gain¹⁶ [151].

4.6.3 Uncertainties and usability of this method

The contactless method was tested at lower frequencies (30 GHz), where results are published in [155], [151]. For this research we use the same contactless method but now for frequencies between 80 GHz and 90 GHz. A standard gain horn has been used as a RA and a rectangular inset-fed microstrip patch antenna with a center frequency of 85 GHz as the AUT.

For this contactless measurement setup we investigated various uncertainties such as:

- displacement errors,
- tolerance on the load value.

An uncertainty that still needs to be investigated is:

- impact of noise and drift.

To assess the influence of these uncertainties a sensitivity analysis is performed. However, before we go into detail concerning the sensitivity analysis, first the system and the associated signals need to be analyzed. Starting with the reflection at the AUT named load reflection [see Fig. 4.20(a)], which will be referred to as the reflected signal of interest (RSI). The Γ_{in} consists of the RSI and signals coming from static objects present in the measurement environment like an antenna holder. The RSI cannot be distinguished by the VNA from the other (static) reflections. In Fig. 4.21 the relationship between the RSI, measured reflection coefficient Γ^{in} , and static reflections $\Sigma\Gamma^{\text{s}}$ is illustrated. If the environment remains static, the difference between Γ^{in} and Γ^{RSI} is independent of the reflection coefficient of the load Γ . Therefore, the static reflections will only contribute to the S_{11} [see Fig. 4.20(a)] and leave the S_{21} , S_{12} and S_{22} not

¹⁵Fraunhofer.

¹⁶It is assumed that $S_{21} = S_{12}$.

affected by these static reflections because their values are the only one changed by applying different loads.

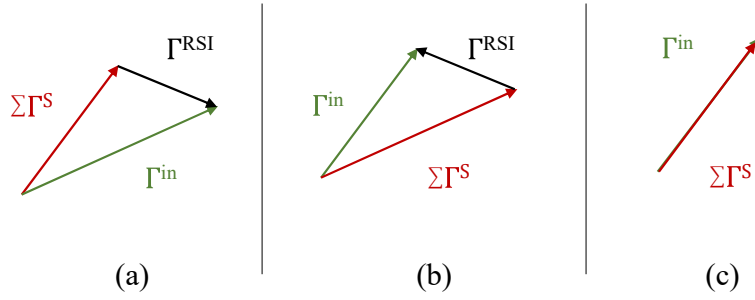


Figure 4.21: Illustration of the relationship between the measured reflection coefficient Γ^{in} , static reflections $\Sigma\Gamma^s$, and the reflected signal of interest Γ^{RSI} when a perfect (a) short, (b) open, and (c) load is connected [151].

In other words, all the required information to determine the input impedance and the realized gain are present in the RSI.

Therefore, the sensitivity of the system can be determined, in first order¹⁷, with the following equation:

$$\Gamma_{RSI} = (S_{21-c})^2 G_{RA-r} \left(\frac{\lambda_0}{4\pi d_{ant}} \right)^2 e^{-j2k_0 d_{ant}} G_{AUT-r} \frac{\Gamma}{1 - S_{22}\Gamma}. \quad (4.5)$$

S_{21-c} is the transmission through the cable connecting the VNA with the RA and are normally known values, k_0 is the wavenumber in vacuum and Γ is the reflection coefficient of the load. In this setup a horn antenna is used from which the gain G_{RA-r} is provided by the supplier. This leaves us with two unknowns, the G_r and complex impedance of the AUT (G_{AUT-r} and S_{22} , respectively). Both values can be obtained with help of simulation results such that the RSI could be determined. As for the results in Fig. 4.22, both the complex impedance and G_r are supplied by the simulation software and are used as references for the real part and imaginary part of the impedance and the G_r , respectively.

¹⁷Like in the Friis equation, multipath reflections or standing waves are taken into account in (4.5).

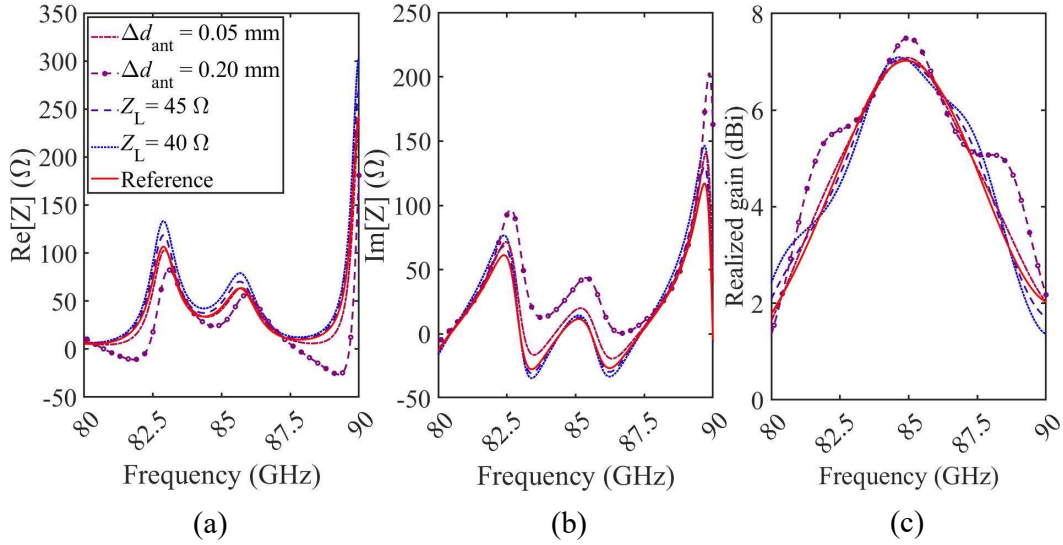


Figure 4.22: Various uncertainties are introduced and compared with a reference value for in (a) the real-part and in (b) the imaginary part of the complex impedance. An in (c) for the G_r . The uncertainties are the variation in distance between the antennas Δd_{ant} and the variation in load impedance Z_L .

The largest deviation in Fig. 4.22 is caused by the variation in the distance Δd_{ant} between the RA and AUT. The displacement error is approximately $\lambda_0/8$. In reality, this 0.2 mm displacement error would be easy to make. However, while obtaining the measurement results of the three loads the antenna is not touched. The load will be attached to the connector of the side RF probe [see Fig. 4.1(b)] and then the probe is placed on the antenna. When the probe is connected to the AUT, a S_{11} measurement will be performed. This procedure of lifting the side RF probe connecting a different load and replacing the probe on the antenna is repeated twice.

What is more of a problem is that the Friis equation has to be solved twice due to the S_{22} measurement. Once because of the transmission between RA and AUT and once because of the transmission between AUT and RA. This means that the spherical spreading losses and cable losses should be counted twice. In Table 4.2 the losses and gain are summarized. It shows that the expected RSI can be measured assuming a noise floor of -120 dBm or lower with an IF BW of 100 Hz depending on the type of VNA¹⁸ used for this measurement.

¹⁸For this research we used a A5225E VNA [156].

Table 4.2: The input parameters for determining the dynamic range of the antenna measurement system for frequencies between 60 GHz and 90 GHz.

| # | Sources | Values @ 60 GHz | Values @ 90 GHz |
|-----|---|--------------------|--------------------|
| 4.5 | Cable losses (<i>TCF119XY500S2P, TOTOKU</i>) | -9.0 dB | -14.2 dB |
| 4.6 | RF Probe (<i>Model 110H RVP-style, PicoProbe</i>) | -1.0 dB | -1.3 dB |
| 4.7 | SSF | -108.0 dB | -124.0 dB |
| 4.8 | Reference antenna | 34.0 dBi | 46.0 dBi |
| 4.9 | Antenna under test (<i>rectangular inset-fed microstrip patch antenna</i>) | 8.0 dBi | 10.0 dBi |
| | Maximum measured power | -76.0 dB | -83.5 dB |
| | Noise floor @ 10 Hz IFBW | -120 dBm | -120 dBm |
| | Dynamic range | 44.0 dB | 36.5 dB dB |

A possible candidate we had in mind for this method is an AoC. When the AoC is part of a system, the possibility exists to incorporate the three loads into the design. By simply switching between the loads the necessary data can be obtained. This would be very convenient during production testing, where both the reflection coefficient and gain could be obtained and validated with respect to the research requirements published in the data sheet of the system. For an apparently perfect solution, there is an important uncertainty. For this contactless method it is necessary that the values of the three loads are known (see Fig. 4.22). This is not simply the case with the values of the loads that are integrated on a realized IC which are subject to tolerances. The exact value of the loads can only be obtained by a contact method of measurement. If it is necessary to make contact with the IC, in this case to measure the loads, it is as well to contact the antenna directly and measure. With this in mind, it is better to put effort into a modified RF probe that will affect the antenna-on-chip or in-package as little as possible.

4.7 Conclusions and recommendations

This chapter investigated the effect of the connector on the behavior of the AUT. The most complex part of this research is to be able to differentiate between the different causes of uncertainty. This is mainly caused by the coupling between antenna transmission line and connector, which is less or not present when individually analyzed. With regard to the antenna characteristics, the impedance is least affected, in any case it still meets the research requirements. This cannot be said of the realized gain pattern

and the realized gain (dBi). The realized gain patterns in the E -plane and to a lesser extent the H -plane are indeed affected depending on the connector. Ultimately, the side RF-probe comes out best from the existing connectors. Based on the knowledge gained, an attempt has been made to design a new RF-probe. By applying the knowledge using existing technology, a new design has been analyzed. The reflection coefficient is less affected where the results of the new RF-probe are closer to the reference than the results of the side RF-probe. The trueness is almost equal to that of the side RF-probe. However, the distortion on the realized gain in both planes is much less when the new RF-probe is connected to the AUT.

The contactless method, i.e. no mechanical contact between the AUT and measurement equipment, has been investigated. Because the principle is based on applying three different loads, several uncertainties are introduced and discussed. The largest effect on the obtained results is the change in distance between the AUT and the reference antenna. Since in reality the antenna is not touched during the collection of the measurement data of the three loads, there will be no displacement error. However, because the Friis equation has to be applied twice the spherical spreading losses will be significant such that dynamic range is limited to approximately 20 dB @ 60 GHz and approximately 12 dB @ 90 GHz. The values are obtained assuming that the antennas are in the far field. Moving the antennas half the distance closer, an additional 12 dB can be gained. This method could be useful for testing the behavior of an antenna-on-chip or in-package where the possibility exists to incorporate the loads on-chip.

Uncertainties in the measured dielectric properties of solid materials with help of a Fabry-Pérot open-cavity resonator

“In the material sciences these are and have been, and are most surely likely to continue to be heroic days.”

(Julius Robert Oppenheimer 1904 - 1967)

5.1 Introduction

Integrated millimeter-wave antennas are often realized on and/or surrounded by dielectric materials. To achieve the required accuracy for such an antenna design (see Chapter 3), it is therefore necessary to know the relative permittivity ϵ_r and loss tangent $\tan\delta$ of the dielectric materials up to a certain significance. At millimeter-wave frequencies, the ϵ_r and $\tan\delta$ are often not known or, if these values are known, not accurate enough. In this chapter some material characterization methods will be described. It is argued why the Fabry-Pérot open-cavity resonator is the most suitable option for this research. In the description of the Fabry-Pérot open-cavity resonator attention will be paid to the stability criterion, the use of the different focal distances with the same system, the mechanical design and the post-processing algorithm that is applied to the measurement data. The second part of this chapter describes the results of a probabilistic sensitivity analysis using Monte Carlo simulation to find out which parameter has the highest influence on the accuracy of the measured ϵ_r and $\tan\delta$. This analysis will give insight how accurate and with which significance, less than one-hundredth for the ϵ_r and less than ten times the measured $\tan\delta$, the dielectric material can be measured. In order to be able to assess the system for measurement accuracy, the permittivity of air is measured with the Fabry-Pérot open-cavity resonator. In one of the last sections,

two materials, PTFE (polytetrafluoroethylene), also known as Teflon and often used as a dielectric material reference, and FR-4, is measured between 60 GHz to 70 GHz, whereby the accuracy of the measurements will be expressed in terms of an expanded uncertainty U [see Chapter 2, Subsection 2.8.3, Equation (2.32)].

5.2 Overview of methods for characterizing dielectric materials

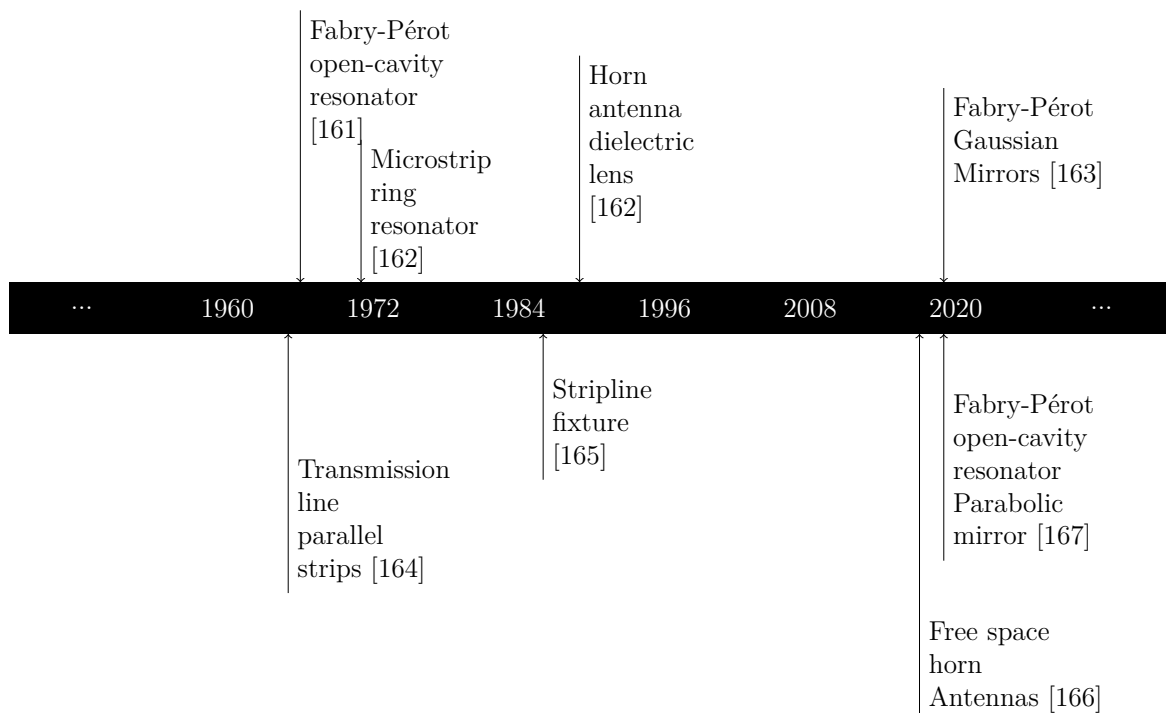
Over the years, various methods to characterize dielectric materials have been developed and investigated. Some of these material characterization methods are summarized in Table 5.1. The characterization methods can be divided according to the following two properties, namely, resonant [(# 5.1), (# 5.2)] and non-resonant [(# 5.3), (# 5.4)]. Another distinction that can be made between the different material characterization methods is that in case of (# 5.2), the technique is destructive to the dielectric material to be measured¹. In contrast, the methods described in (# 5.1), (# 5.3) and (# 5.4) are non-destructive to the dielectric material to be measured. For the destructive method, a transmissionline structure is printed on the dielectric material whose ϵ_r and $\tan\delta$ is to be determined. This means that the ϵ_r and $\tan\delta$ of only that one piece of material are accurately known. The rest of the material that comes from the same production batch and whose ϵ_r and $\tan\delta$ might deviate from that characterized piece of material will have an undefined inaccuracy. As for the non-destructive method, the ϵ_r and $\tan\delta$ of the material are obtained in a contactless manner. This means that all material from the same batch can be measured individually and be reused for the intended application. This way, the ϵ_r and $\tan\delta$ are determined as accurate as possible for each sample. In this case, it is even possible to determine the accuracy of the production process itself, both within a batch or between batches. Finally, local variations of the ϵ_r and $\tan\delta$ over the substrate surface can be measured and analyzed. In this way, the homogeneity and isotropic properties can be determined (See Appendix *D.1*).

¹In this case destructive means that the material cannot be reused for the intended application. In another case the material characterization method may require the material to be sized to fit in the material characterization system.

Table 5.1: Material characterization techniques for millimeter-wave frequencies.

| # | Measurement technique | Frequency range (GHz) | Advantage | Disadvantage | Ref. |
|-----|-----------------------------------|-----------------------|---|---|-------|
| 5.1 | Fabry-Pérot open-cavity resonator | 20 - 300 | ϵ_r , $\tan\delta$, thin dielectric $< 100\mu\text{m}$, non-contact. | Limited accuracy for high loss mat., complex algorithm. | [157] |
| 5.2 | Ring resonator | 0.5 - 60 | ϵ_r , simple algorithm. | difficult to obtain $\tan\delta$. | [158] |
| 5.3 | Free space (TL) | 1 - 100 | ϵ_r , non-contact. | Air-gap causes large errors. | [159] |
| 5.4 | Radar (FMCW ²) | > 50 | ϵ_r , $\tan\delta$, non-contact. | Needs a dielectric lens. | [160] |

Fig 5.1 shows a time-line of the development of various material characterization methods over the years.

**Figure 5.1:** Time-line of the evolvement of material characterization methods for determining the relative permittivity and loss tangent.

²Frequency modulated continuous wave.

In summary, from the material characterization methods addressed in Table 5.1 two methods stand out, namely the Fabry-Pérot open-cavity resonator³ and the FMCW radar. Both methods are contactless, non-destructive for the dielectric material and its measurement is relative⁴ which makes this a robust measurement principle. However, the system design of the Fabry-Pérot open-cavity resonator is much simpler compared to that of the radar system. The Fabry-Pérot open-cavity resonator consists only of two mirrors compared to two horn antennas and two lenses that need to be accurately aligned. Additionally, the arrangement of two spherical mirrors placed on two motor stages lends itself also to introduce uncertainties by allowing the misplacement of both the mirrors and the dielectric material to be able to investigate the impact on the obtained dielectric properties.

With the Fabry-Pérot open-cavity resonator it is possible to create an air-based reference with which the measurement accuracy in a specific frequency range, in this case 60 GHz to 90 GHz, can be determined. The method, which uses air as a reference material for determining the measurement accuracy, will be described later in this chapter.

5.3 Principle of the Fabry-Pérot open-cavity resonator

The principle of the Fabry-Pérot open-cavity resonator stems from the Fabry-Pérot interferometer [157]. The Fabry-Pérot interferometer is traditionally associated with optical resonators or etalons and consists of two parallel, partially reflective mirrors as illustrated in Fig. 5.2(a). When light is coupled into the cavity through the partially reflecting mirrors, reflections on the mirrors create a series of resonating modes. The resonance frequencies of these modes depend on the number of half wavelengths that the mirrors are separated from each other. It is important that the resonating modes have the highest possible quality factor⁵, also known as the Q -factor. The Q -factor for an unloaded optical cavity Q_{ucav} ⁶ of a Fabry-Pérot resonator defined as ‘energy storage’ can be written as [168]:

$$Q_{\text{ucav}} = 2\pi \left(\frac{\text{Total energy stored in the cavity}}{\text{Energy lost in one cycle of oscillation}} \right). \quad (5.1)$$

³The basis for the design of this material characterization method was invented by Charles Fabry and Alfred Pérot in 1897.

⁴By a relative measurement is meant that the permittivity and $\tan\delta$ are determined by two successive transmission measurements, with help of a VNA, that are related to each other. It is assumed that nothing changes during the measurement other than whether a dielectric material has been placed.

⁵The quality factor was first introduced in 1914 by K. S. Johnson [168].

⁶The Q -factor for a millimeter-wave Fabry-Pérot open-cavity resonator will be described later in this chapter.

It should be noted that for an optical or microwave resonator, ‘one oscillation cycle’ is understood as corresponding to the field oscillation (time) period, not the round-trip period [169].

The Q -factor can also be expressed in terms of the ‘resonance bandwidth’ as:

$$Q_{\text{ucav}} = \frac{f_i}{BW_{-3\text{dB}}}, \quad (5.2)$$

where f_i is the i^{th} resonance frequency and $BW_{-3\text{dB}}$ the frequency bandwidth at the -3 dB points of the frequency response of the resonator. Both definitions are equivalent only in the limit for high Q -values (> 10000) [169].

This concept of a Fabry-Pérot interferometer remains almost intact for the millimeter-wave region [see Fig. 5.2(b)] [157]. An important difference is the way in which the electromagnetic wave, or light in the case of the interferometer, is coupled in to the cavity. For the Fabry-Pérot interferometer this is done with the aid of partially reflecting mirrors [see Fig. 5.2(a)]. A similar concept is described in [170] for the millimeter-wave Fabry-Pérot open-cavity resonator, but now the partially reflective mirrors are replaced by planar metal plates with small holes e.g. coupling apertures or irises in it, as illustrated in Fig. 5.2(b). By means of a horn antenna, the electromagnetic wave is coupled via these irises (see Appendix D.2) in to the open cavity. However, this concept has two drawbacks. First, diffraction at the edges of the planar mirrors [see Fig. 5.2(b)] increases the losses and complicates an accurate modeling of the field distribution and secondly, there is a stringent requirement for the precise alignment of the mirrors [157]. Both drawbacks can easily be solved by replacing the plane mirrors by spherical mirrors. With spherical mirrors the field is focused in a smaller area and the impact of diffraction is negligible if the mirrors are large enough [170] (see Appendix D.3). Also, the excitation of the spherical configuration is simpler compared to that of the plane mirrors. Via a waveguide and by means of only one iris the electromagnetic wave is coupled in to the open cavity where through the spherical mirrors a Gaussian beam (see Appendix D.3) is created as illustrated in Fig. 5.2(c). The design and dimensions of the spherical mirrors are described later in this chapter.

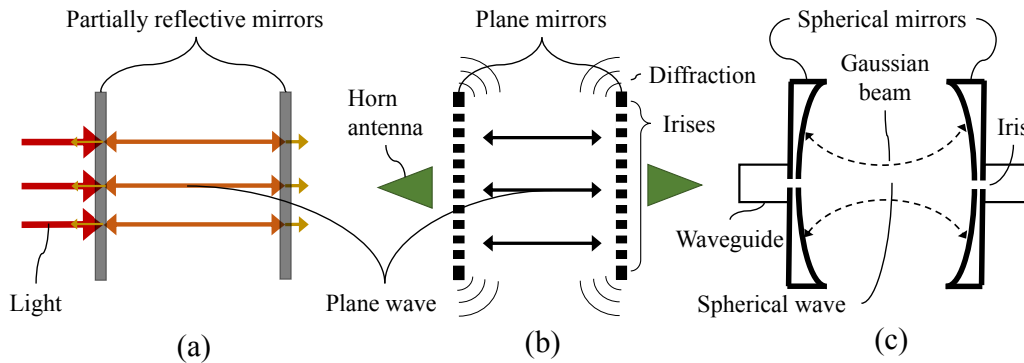


Figure 5.2: Principle of the open cavity resonator. (a) Light couples into the cavity via a partially-reflective mirror. A plane wave is illustrated by the red/orange/yellow arrows. (b) A horn antenna excites an electromagnetic wave through small coupling holes (irises) in a plane mirror into the cavity. A plane wave is illustrated by the black arrows. Diffraction is indicated by black arches on the edge of the plane mirrors [170]. (c) Via a waveguide and an iris located in the middle of the spherical mirror the electromagnetic wave is coupled into the cavity creating a Gaussian beam with a spherical wave.

5.3.1 Condition for a stable Fabry-Pérot open-cavity resonator

An important setting for the Fabry-Pérot open-cavity resonator is the optimal distance between the spherical mirrors depending on the focal distance. The term, which defines the optimal distance between the spherical mirrors, is stability⁷, which is defined as [172]:

“The range of the distance between mirrors within which a resonator is stable is determined by the condition that an electromagnetic wave excited within the resonator parallel to the mirror axis remains within the resonator after an infinite number of reflections.”

Ideally, the definition states that if we assume a Gaussian beam between two identical spherical mirrors, then stability means that after a reflection on a large enough mirror (see Appendix D.3) the Gaussian beam reflects exactly back on itself, with exactly reversed wavefront curvature and direction [171]. Under these conditions the energy stays within the open cavity. The definition states also that the distance between the spherical mirrors D is limited to be able to achieve a stable arrangement. The stability of a mirror arrangement can be derived from the stability diagram, also called a g -diagram

⁷A more detailed explanation about stability of a Fabry-Pérot open-cavity resonator can be found in [171].

illustrated in Fig. 5.3(a).

It should be noted that the stability diagram is used for resonators in the optical spectrum, like the Fabry-Pérot interferometer [173]. However, in [172] and [174] the stability diagram is applied to a millimeter-wave Fabry-Pérot open-cavity resonator for which the same conditions apply to define a stable system.

For a setup with two mirrors with a radii of curvature R_0 and R_1 that are at a distance D from each other, we find for the g -parameters [see Fig. 5.3(a)] that [172]:

$$g_j = 1 - \frac{D}{R_j} \quad j = 0, 1, \quad (5.3)$$

then the condition for a stable mirror arrangement [172] becomes:

$$0 \leq g_0 g_1 \leq 1. \quad (5.4)$$

In combination with Equation (5.3) and Equation (5.4), the stability diagram in Fig. 5.3(a) gives immediately insight whether the mirror setup meets the stability criterion. The blue colored area is limited by the coordinate axes g_0 and g_1 and the hyperbolas for which $g_0 g_1 = 1$. When the calculated g -parameters [see Equation (5.3)] are on the edge or inside the blue colored area the mirror arrangement is stable, meaning that the Q -factor is not affected. It should be noted that when the g -parameter of a certain setup is on the edge of the stability diagram (see Fig. 5.3, black colored dot 1, 3 and 4) it is prone to instability making the placement of the mirrors at a certain distance D very critical [172]. When outside this blue-colored area, the mirror arrangement is unstable, i.e. energy will be lost, such that the Q -factor deteriorates making the setup unusable to accurately determine the ϵ_r and $\tan\delta$ of a dielectric material [172], [174]. The following g -parameters have been derived for the various mirror arrangements (see Fig. 5.3) [172], [171]:

| | | | |
|-----------------------|----------------|---------------|------------------------------------|
| • Planar ⁸ | $g_0 = 1.00,$ | $g_1 = 1.00$ | [Black dot no. 1] |
| • Hemispherical | $g_0 = 1.00,$ | $g_1 = 0.00$ | [Black dot no. 5, see Fig. 5.3(b)] |
| • Focal | $g_0 = 0.50,$ | $g_1 = 0.50$ | [White dot no. 2, see Fig. 5.3(c)] |
| • Near-focal | $g_0 = 0.56,$ | $g_1 = 0.56$ | [Purple dot] |
| • Confocal | $g_0 = 0.00,$ | $g_1 = 0.00$ | [Black dot no. 3, see Fig. 5.3(d)] |
| • Near-confocal | $g_0 = 0.13,$ | $g_1 = 0.13$ | [Orange dot] |
| • concentric | $g_0 = -1.00,$ | $g_1 = -1.00$ | [Black dot no. 4, see Fig. 5.3(e)] |
| • Near-concentric | $g_0 = -0.75,$ | $g_1 = -0.75$ | [Red dot] |

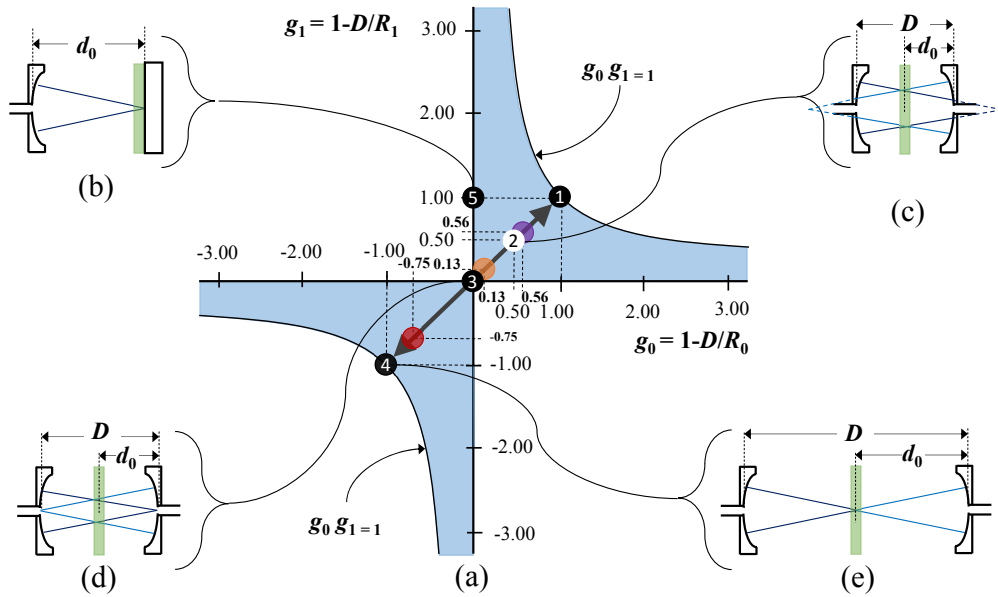


Figure 5.3: (a) Stability or g -diagram. (b) A hemispherical setup with one spherical and one planar mirror, (c) two spherical mirrors in a near-focal setup, (d) two spherical mirrors in a near-confocal setup and (e) two spherical mirrors in a near-concentric setup. The distance between two spherical mirrors is indicated by D and the distance between a spherical and planar mirror is indicated by $d_0 = D/2$. The green transparent rectangle represents the dielectric material. The red, orange, and purple dots indicate a near-focal distance with one and the same system. Black dot 1 and 3 to 5 are the planar, confocal, concentric and hemispherical setup on the edge of the stability diagram, and white dot 2 is in the stability area (blue). The dots located on the gray arrow (45°) have identical mirrors.

5.3.2 Different focal distances that meet the stability criterion

As described in the former section, the two spherical mirrors of the Fabry-Pérot open-cavity resonator can be arranged according to the g -parameter diagram [see Fig. 5.3(a)] for different focal distances, and still be stable. In the case of the Fabry-Pérot open-cavity resonator the spherical mirrors can be placed at three different focal distances

⁸An important condition for a planar or hemispherical setup is that the flat plate mirror satisfies the effective Fresnel number $N_{\text{eff}} = a^2/\lambda D$ [see Fig. 5.3(b)]. Where a is the radius of the flat mirror, λ the wavelength of the frequency of interest and N_{fres} the Fresnel number. N_{fres} must be at least 10 to speak of a stable resonator with a sufficient Q -factor [157].

and in the hemispherical setup at one focal distance⁹. The focal distances are derived as follows:

- Focal $D = R_j/2$ [see Fig. 5.3(c), White dot no. 2]
- Confocal $D = R_j$ [see Fig. 5.3(d), Black dot no. 3]
- Concentric $D = 2R_j$ [see Fig. 5.3(e), Black dot no. 4]
- Hemispherical $D = R_j$ [see Fig. 5.3(b), Black dot no. 5]

The first three focal distances are derived from R_j and the last focal distance from the focal point f_p of the spherical mirror. This focal point f_p of a spherical mirror is at half of R_j [see Fig. 5.4(a)]. A planar mirror can be placed in the center R_j of the same arrangement. In this way a hemispherical setup is created [see Fig. 5.3(b)]. This means that basically with the same setup two different mirror configurations can be made with three different focal distances. Each mirror arrangement and each focal distance has its own advantages, disadvantages and uncertainties on determining the ϵ_r and $\tan\delta$, which will be described later in this chapter.

5.3.3 Development of various Fabry-Pérot open cavity resonator configurations

The millimeter-wave Fabry-Pérot open-cavity resonator with two movable spherical mirrors was first described in 1966 in [161]. In this setup, the dielectric material is placed at an angle φ_{dm} with respect to the axis of the resonator [see Fig. 5.4(a)]. The reason for this tilt is that then no more reflections would occur in the cavity. This simplifies the theory to derive the ϵ_r from this measurement. Experiments have been carried out with different φ_{dm} -angles (from $\varphi_{dm} = 3$ to $\varphi_{dm} = 7$ degrees with steps of one degree). The ϵ_r changed with an unacceptable range for the millimeter-wave frequencies, of 15% over these φ_{dm} -angles. To correct this error, the theory would be more complex than compared to the theory assuming there are reflections in the cavity. The Q -factor decreases depending on the φ_{dm} -angle until it can no longer be detected at eight degrees or more [161].

A similar setup is described in 1967 in [175], but now the dielectric material is placed at the Brewster-angle¹⁰ φ_B [see Fig. 5.4(b)]. However, the principle of the Brewster-angle, i.e. change of polarization of the electromagnetic wave, only works if the material has

⁹It should be noted that the focal distance of the confocal is the same as for the hemispherical setup.

¹⁰In optics, the Brewster-angle or polarization angle is understood to be the angle of incidence at which full polarization occurs.

very few losses. Another disadvantage of this method is that the Brewster-angle is only known if the ϵ_r is known. Furthermore, experiments have shown that no reflections are observed in the measurement results on a material with a $\tan\delta$ of 0.1 and smaller [175]. This means that placing the material parallel to the spherical mirrors [see Fig. 5.4(c)] is ‘good enough’ [175] to be able to perform accurate measurements in order to derive the ϵ_r and $\tan\delta$ [175].

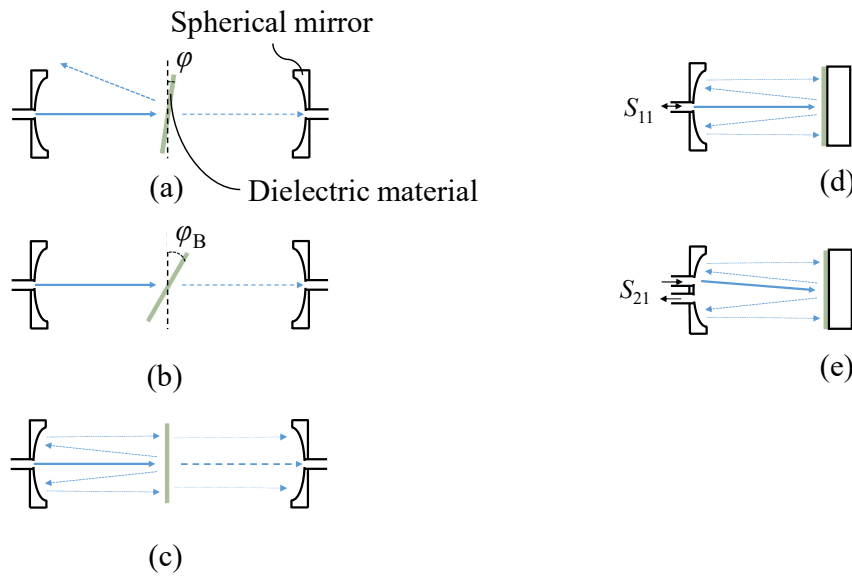


Figure 5.4: Different configurations of the Fabry-Pérot open-cavity resonator in transmission mode (S_{21}) with two spherical mirrors (a) with a dielectric material, represented by a green rectangle, at an angle φ_{dm} , (b) a dielectric material at the Brewster angle φ_B and (c) a dielectric material parallel to the spherical mirrors. (d) The Fabry-Pérot open-cavity resonator with a spherical and planar mirror in reflection mode (S_{11}) and (e) the Fabry-Pérot open-cavity resonator with a spherical and planar mirror in transmission mode (S_{21}). In all illustrations in this figure the blue arrows with decreasing thickness represents decreasing electric field strength.

The last configuration of the Fabry-Pérot open-cavity resonator described here was introduced in [176] in 1978. This setup consists of one movable spherical mirror and one non-movable planar mirror in a hemispherical configuration [see Fig. 5.4(d) and Fig. 5.4(e)]. Since only one mirror needs to be moved, this is a much simpler setup from a mechanical point of view compared to the previously described setup with two spherical mirrors. The electromagnetic wave can be excited in the cavity in two ways. With one waveguide [see Fig. 5.4(d)] in which a reflection measurement (S_{11}) [177] is performed and with two waveguides [see Fig 5.4(e)] in which a transmission measurement (S_{21}) [178], [179] is performed. An advantage of this setup is that not only solids but also

fluids can be measured [176]. A disadvantage of such a hemi-spherical setup is that an air gap between the dielectric material placed on the planar mirror should be avoided. This results in stringent requirements for the flatness of the dielectric material, which can be a challenge depending on the type of material.

5.4 Design of the Fabry-Pérot open-cavity resonator with spherical mirrors

The design of the Fabry-Pérot open-cavity resonator, together with the dimensions (see Table 5.2), are illustrated in Fig. 5.5. The hemispherical setup consisting of a spherical and a planar mirror is shown in Fig. 5.5(a) [177] - [180]. The setup consisting of two spherical mirrors is illustrated in Fig. 5.5(b) [181]. The dielectric material (green semi-transparent rectangle) is located at the center of the cavity at distance d from the mirror. The thickness of the dielectric material is expressed with $2t = d - d_0$ [see Fig. 5.5(a)].

Fig. 5.5(c) shows a cross-section of a waveguide (dashed rectangle) and a circular coupling aperture (dark gray circle) through the mirror (gray colored background) e.g. iris. The iris connects a rectangular waveguide to the cavity via the mirror. A second purpose of the round iris is to create a Gaussian beam at the surface of the mirror that is symmetrical in the radial (ρ_p) direction [see Fig. 5.5(d)]. The subscripts p, l, q, are the indices of the radial (ρ_p), angular (φ_l), and axial (z_q) mode from a Laplacian in cylindrical coordinates [181] [see Fig. 5.5(d)]. Concerning unwanted-modes, these are not detected when the mirrors are at the near-concentric distance. However, when the mirrors are positioned at a near-confocal and near-focal distance unwanted-modes arise, as will be described later in this chapter.

For the setup with two spherical mirrors the resonance frequency f_0 of the unloaded cavity is given by [181]:

$$f_0 = \frac{c_{\text{air}}}{2D} \left[q + 1 + \frac{1}{\pi} \cos^{-1} \left(1 - \frac{D}{R_0} \right) \right], \quad (5.5)$$

where D is the distance between the mirrors and c_{air} is the speed of light in air¹¹.

For the hemispherical setup the resonance frequency is given by [178]:

$$f_0 = \frac{c_{\text{air}}}{2D} \left[q + 1 + \frac{1}{\pi} \tan^{-1} \left(\frac{D}{R_0 - D} \right) \right]. \quad (5.6)$$

¹¹The speed of light in air c_{air} is 299702547 m/s [146] and will be used in this chapter from now on (see Section 5.6).

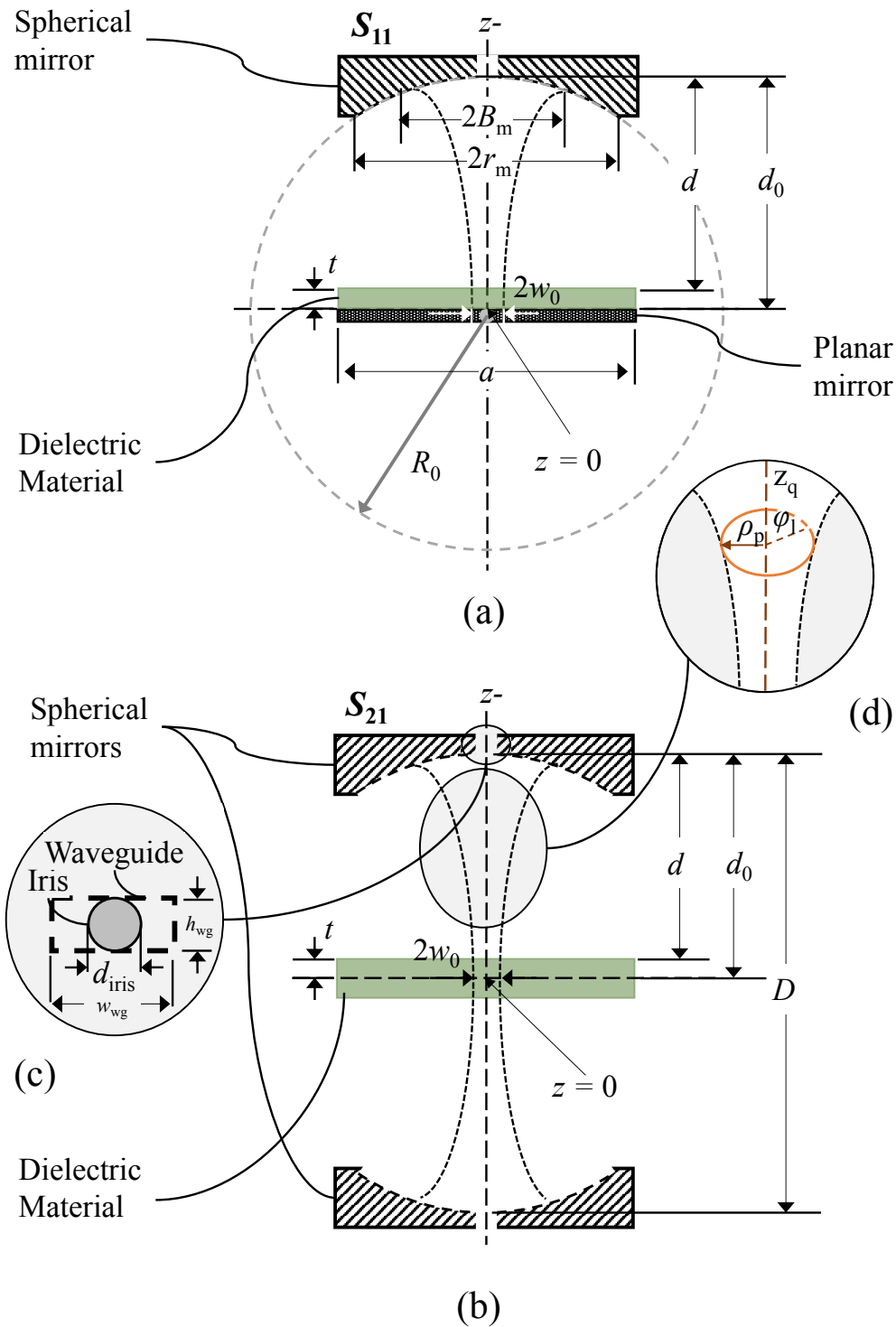


Figure 5.5: (a) Hemispherical mirror arrangement and (b), depending on the focal distance, a spherical concave or a near-concentric mirror arrangement. (c) An illustration of a cross section of a waveguide and hole transition in the mirror, i.e. iris, through which the electromagnetic wave is excited into the cavity. (d) Shows the cylindrical coordinate system with respect to the Gaussian beam with ρ_p the radial distance, φ_L the angular distance and z_q the axial distance. The dashed line defining the middle of the setup is the optical axis and the dotted curved line illustrates a Gaussian beam.

5.4.1 Design parameters of the Fabry-Pérot open-cavity resonator

The design of the concave spherical mirror consists of determining the expected beam waist and radius of the beam on the spherical mirror. Important design parameters are the radius or curvature R_0 and the distance between the mirrors D . With these parameters the radius of the beam waist w_0 can be determined with [182]:

$$w_0 = \sqrt{\frac{\lambda \sqrt{D(2R_0 - D)}}{\pi}}. \quad (5.7)$$

The radius B_m of the beam on the mirror can be determined with [182]:

$$B_m = w_0 \sqrt{\left(1 + \frac{2D}{k_w w_0^2}\right)^2}, \quad (5.8)$$

where k_w is the wave number in air:

$$k_w = \frac{2\pi f}{c_{\text{air}}}. \quad (5.9)$$

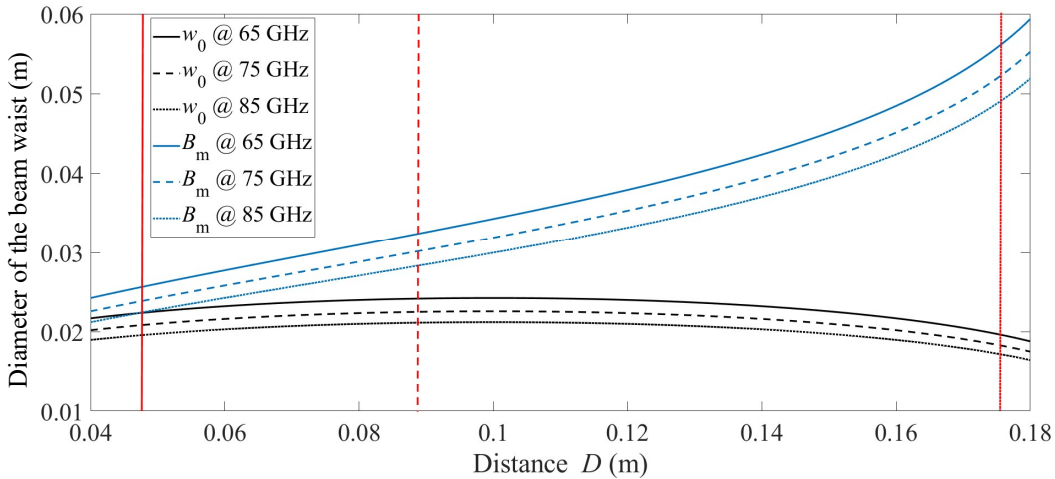


Figure 5.6: Diameter of the beam waist $2B_m$ on the surface of the spherical mirror (blue lines) and the diameter of the beam waist $2w_0$ (black lines) in the middle of spherical mirror arrangement at near-focal (solid red line), near-confocal (dashed red line) and near-concentric (dotted red line) distance D for several frequencies.

Fig. 5.6 shows the results of the beam waist $2w_0$ in the middle of the spherical mirror arrangement and beam waist $2B_m$ on the surface of the spherical mirror versus various distances D per frequency. The radius of curvature R_0 of the spherical mirrors used during this reserach is 0.1 m (see Table 5.2). The solid red line is located at the near-focal distance of 46.1 mm [$q = 10$, see Equation (5.5) and (5.5)], the dashed red line at the near-confocal distance of 87.6 mm ($q = 19$) and the dotted red line at the near-concentric distance of 175.2 mm ($q = 38$) (see Subsection 5.3.1).

5.4.2 Quality-factor of the unloaded cavity

For a resonant system, like the Fabry-Pérot open-cavity resonator, the Q -factor is the most important parameter, as described in Section 5.3. The higher the Q -factor the more accurate the resonance frequency f_0 of the unloaded open-cavity can be determined. Furthermore, the higher the Q -factor the higher the peak value and thus an increased dynamic range, allowing dielectric material with greater $\tan\delta$ to be measured. The Q -factor of an unloaded cavity can be determined with [181]:

$$Q = 1 / \left[1 / \left(\frac{D}{2\delta_s} \frac{1}{\left(1 - 1 / \left(k_w \sqrt{D(2R_0 - D)} \right) \right)} \right) + 1 / \left(\frac{2\pi D}{\lambda_0 \alpha_d} \frac{1}{\left(1 - (2p + l + 1) / \left(k_w \sqrt{D(2R_0 - D)} \right) \right)} \right) \right]. \quad (5.10)$$

The p - and l are the indicies of the radial and angular mode from a Laplacian in cylindrical coordinates, respectively [see Fig. 5.5(d)]. Further, the skin depth δ_s can be calculated with [181]:

$$\delta_s = \sqrt{\frac{\rho_r}{\pi f \mu}}, \quad (5.11)$$

where ρ_r is the resistivity of the mirror material, in this case aluminum with $\rho_r = 2.65 \times 10^{-8} \Omega\text{m}$ ¹². The absolute magnetic permeability of the conductor $\mu_a = \mu_0 \mu_r$, where $\mu_0 = 4\pi \times 10^7 \text{ H/m}$ and $\mu_r = 1.000022$ for aluminum. The skin depth¹³ for aluminum is 0.3348 μm at 60 GHz and 0.2733 μm at 90 GHz.

¹²The resistivity for gold is $2.2 \times 10^{-6} \Omega\text{m}$, for copper $1.78 \times 10^{-8} \Omega\text{m}$ and for silver $1.59 \times 10^{-8} \Omega\text{m}$.

¹³The skin depth for gold, copper and silver is 0.3075 μm , 0.2662 μm and 0.2588 μm , respectively. The corresponding Q -factor are 143510, 165770 and 170510.

The factor α_d in Equation (5.10) is the fractional power loss per reflection. It represents a sum of diffractive and reflective losses. The diffractive losses depend on the size of the mirror r_m (see Appendix D.3) and the reflective losses depend on the area illuminated by the Gaussian beam B_m on the surface of the mirror (see Fig. 5.6) in combination with the type of material, in this case aluminium. Because the spherical mirror is relatively large (ratio of 1.44, i.e. 98%, see Appendix D.3) compared to B_m (see Fig. 5.6), the diffractive losses can be neglected and then α_d can be expressed as [181]:

$$\alpha_d = \exp\left(\frac{-2r_m}{B_m^2}\right). \quad (5.12)$$

If we assume that the p- and l-modes are zero, which is the case when the spherical mirrors are placed at the near-concentric distance, only the first term of (5.10) is taken into account. The calculated Q -factor of the Fabry-Pérot open-cavity resonator becomes then for the near-focal distance at 65 GHz ≈ 33319 , for the near-confocal distance at 65 GHz ≈ 63222 and for the near-concentric distance at 65 GHz ≈ 126922 (see Appendix D.4 for the obtained Q -factor per frequency band).

5.5 Derivation of the relative permittivity and loss tangent

As described in Section 5.4, the resonance frequency for the unloaded cavity can be derived from (5.5) or (5.6). The distance D between the two spherical mirrors is determined for a specific resonant frequency f_0 with a number of half wavelengths q that fit into the open cavity [see Fig. 5.7(b) to Fig. 5.7(d)]. By varying the distance with steps of q , the spectrum is found as shown in Fig. 5.7(a)¹⁴. For the near-concentric distance the optimal number q , per resonance frequency, is determined by looking at the maximum measured Q -factor associated with a particular number q . The maximum q per frequency in the 60 GHz to 90 GHz frequency band is summarized in Table D.2 (see Appendix D.4).

The successive resonant frequencies $f_0, f_1 \cdots f_i \cdots f_{i,\max}$ consist of so-called odd or quarter or even modes as shown in Fig. 5.7(b) to Fig. 5.7(d), respectively. Terms that are also used for the odd mode are half-node (anti-node) or symmetrical mode. When a dielectric material is inserted into the Fabry-Pérot open-cavity resonator the odd mode gives a smaller shift in resonance frequency as compared to the even mode. Based on a frequency range of 60 GHz to 90 GHz the odd mode can be used for dielectric sheets

¹⁴This resonant frequency spectrum is based on the mirrors being at a near-concentric distance (see Fig. 5.3).

with a thickness $> 1500\mu\text{m}$ [181]. The even mode, also known as node or anti-symmetric mode gives a larger shift δf_{sa} in the resonance frequency [see Fig. 5.7(a) for example f_0 versus f_{s0} and f_2 versus f_{s2}] compared to the odd mode. Based on a frequency range of 60 GHz to 90 GHz the even mode can be used for dielectric materials that have a thickness $< 1500\mu\text{m}$ [181].

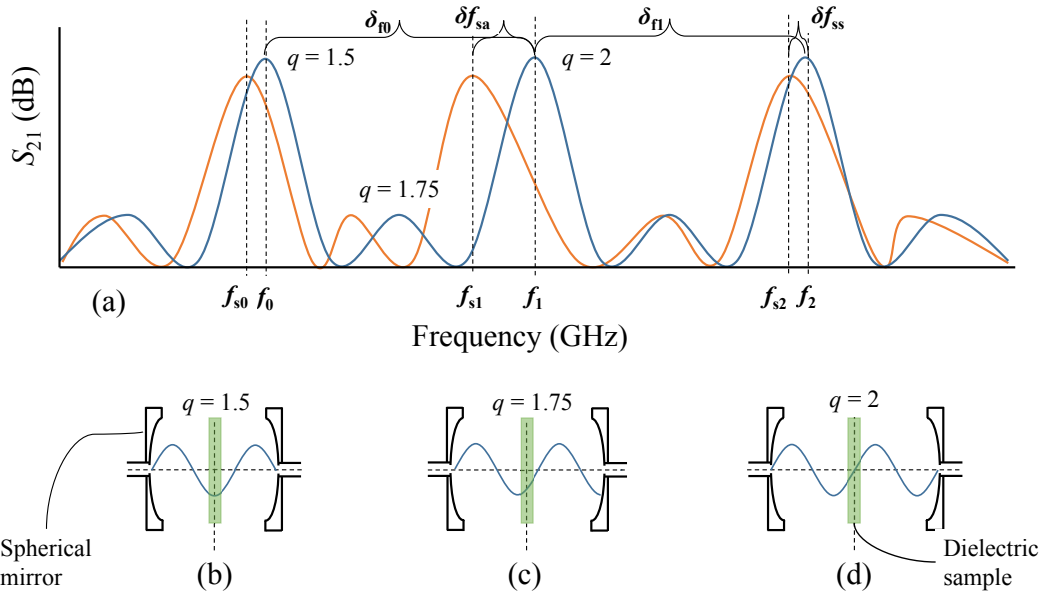


Figure 5.7: (a) Example of a frequency spectrum of an unloaded cavity (blue) with successive resonance frequencies f_0 to f_2 and filled cavity (orange) with resonance frequency f_{s0} to f_{s2} . δf_0 and δf_1 are the frequency differences between the different resonance frequencies and δf_{sa} and δf_{ss} the difference between the resonance frequency and the odd and even shift caused by a dielectric material. (b) The illustration of an odd number of q or a half-node 90° or symmetric (cosine) mode, (c) the illustration of a quarter-node 45° or asymmetric mode and (d) the illustration of an even number of q or full node 0° or anti-symmetric (sinu) mode. A dielectric material is illustrated by the green rectangle.

5.5.1 Determination of the relative permittivity

Placing a dielectric material in an open-cavity¹⁵ with an ϵ_r greater than that of air, will give a shift δf_s and results in a resonance frequency f_{s1} as illustrated in Fig. 5.7(a). The perturbation caused by the dielectric material and the associated frequency shift δf_s is related to the ϵ_r . The equations that will be described in this section are derived

¹⁵When the dielectric material, with a certain thickness t , is placed in the open-cavity the influence of the dielectric material holder on the measurement results is assumed to be negligible. The dielectric material should be placed in a reproducible manner where its surface is flat and perpendicular to the mirrors.

from the Gaussian-beam theory [181]. The equations assume that the surface of the dielectric material is spherical corresponding to the Gaussian beam which equiphase plane is spherical. Since the dielectric materials are flat, it will introduce an error in the obtained resonance frequency. However, because the radius of curvature of the Gaussian beam is very large close to the center of the resonator, it is reasonable to assume that the wave is nearly planar. According to [181], the error is less than 0.1% for the ϵ_r and 0.5% for the $\tan\delta$.

For the symmetrical mode i.e. odd mode with an anti-node of the electric field in the center of the open cavity [see Fig. 5.7(b)], the following equation applies [181]:

$$\frac{1}{n_r} \cot(n_r k_w t - \Phi_t) = \tan(k_w d - \Phi_d), \quad (5.13)$$

where n_r ¹⁶ is the refractive index, $2t$ the thickness of the dielectric material and d the distance from the mirror to the edge of the dielectric material (see Fig. 5.5). Here k_w is the wave number [see Equation (5.9)] based on an i^{th} resonance frequency f_{si} of the loaded cavity.

For the anti-symmetric mode i.e. even mode with a node of the electric field in the center of the cavity [see Fig. 5.7(d)] the following equation applies [181]:

$$\frac{1}{n_r} \tan(n_r k_w t - \Phi_t) = -\tan(k_w d - \Phi_d), \quad (5.14)$$

In these formulae,

$$\begin{aligned} \Phi_t &= \arctan\left(\frac{2t}{n_r k_{\text{ws}} w_0^2}\right), \\ \Phi_d &= \arctan\left\{\frac{2}{k_{\text{ws}} w_0^2} \left(d + \frac{t}{n_r^2}\right)\right\} - \arctan\left(\frac{2t}{n_r^2 k_{\text{ws}} w_0^2}\right), \end{aligned} \quad (5.15)$$

where,

$$k_{\text{ws}} w_0^2 = 2\sqrt{\left\{\left(d + \frac{t}{n_r^2}\right) \left(R_0 - d - \frac{t}{n_r^2}\right)\right\}}, \quad (5.16)$$

and w_0 is the radius of the Gaussian beam in the middle of the cavity (5.7). The rest of the parameters are indicated in Fig. 5.5.

¹⁶The refractive index is assumed real for now.

The distance D between the mirrors can be calculated by experimentally obtaining δ_{f_0} or δ_{f_1} , for example [see Fig. 5.7(a)] [181]:

$$D = \frac{c_{\text{air}}}{\delta_{f_1}/2}. \quad (5.17)$$

For a given thickness $2t$ and with $d = (D/2) - t$ [see Fig. 5.5(b)] we can determine the n_r of the dielectric material by using (5.13) or (5.14). Both equations can be written in the form of a transcendental equation $F(n_r) = 0$, and solved numerically [181].

5.5.2 Determination of the loss tangent

To be able to determine the $\tan\delta$, the quality factor from the unloaded cavity Q_{ucav} and the quality factor from the loaded cavity Q_L , filled with a dielectric material, need to be obtained. By placing the dielectric material in the cavity, the energy stored in the cavity will be affected and will cause an additional power loss proportional to its $\tan\delta$. Thus Q_e is defined as follows [181]:

$$\frac{1}{Q_e} = \frac{1}{Q_L} - \frac{1}{Q_{\text{ucav}}}, \quad (5.18)$$

the $\tan\delta$ can be expressed in terms of Q_e as follows [181]:

$$\tan \delta = \frac{1}{Q_e} \frac{\Delta t + d}{\Delta t + (1/(2k_w)) \sin(2(k_w d - \Phi_d))}, \quad (5.19)$$

where $1 < \Delta < \epsilon_r$ and Δ can be written for symmetric-modes as Δ_s and for anti-symmetric-modes as Δ_a , according to the following equations [181]:

$$\begin{aligned} \Delta_s &= \frac{n_r^2}{n_r^2 \sin^2(n_r k_w t - \Phi_t) + \cos^2(n_r k_w t - \Phi_t)}, \\ \Delta_a &= \frac{n_r^2}{n_r^2 \cos^2(n_r k_w t - \Phi_t) + \sin^2(n_r k_w t - \Phi_t)}. \end{aligned} \quad (5.20)$$

5.6 Realized Fabry-Pérot open-cavity resonator

Based on Equations (5.5) to (5.9) the Fabry-Pérot open-cavity resonator has been designed and realized as shown in Fig. 5.8(a). Equations (5.5) to (5.9) provide the values

for the geometry of the spherical mirrors¹⁷ like the R_0 and r_m and also the dimensions of the Gaussian beam width w_0 and B_m (see Fig. 5.6) and the maximum distance D between the spherical concave mirrors.

The spherical concave mirrors are placed on two different motor stages¹⁸ [see Fig. 5.8(a)], making it possible to displace the mirrors individually with a resolution of $0.2\mu\text{m}$. Moving the spherical concave mirrors individually has the advantage that the distance with respect to the dielectric material can be optimized such that both mirrors have the same distance (error less than $\pm 0.2\mu\text{m}$).

The dielectric material holder shown in Fig. 5.8(b) is made from Rohacell [184], which has a very low ϵ_r of 1.05, which is close to air. The choice for Rohacell, instead of aluminum, which is mechanically more rigid, is that the influence of Rohacell on the measured result can be neglected, whereas metal structures tend to cause unwanted interference. In the middle of the holder there is a round cutout with a size of 40 mm

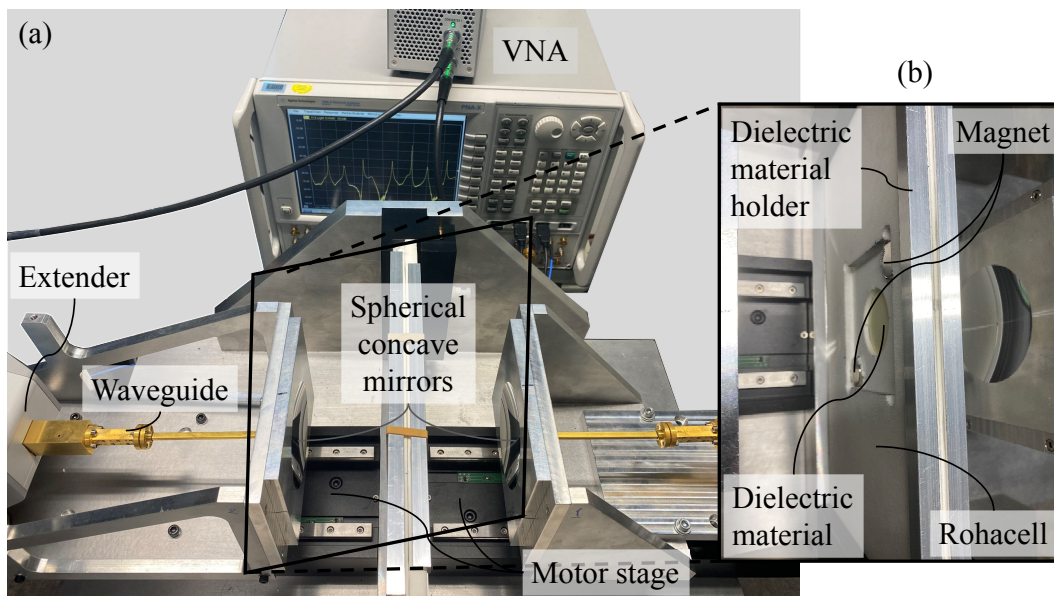


Figure 5.8: (a) Perspective view of the realized Fabry-Pérot open-cavity resonator with VNA and frequency extenders (60 GHz to 90 GHz), and (b) perspective view of the dielectric material holder with dielectric material located in the middle of the holder.

[see Fig. 5.8(b)], which is large enough such that the Gaussian beam, which beam waist diameter at the center of the cavity is maximum 22 mm (see Fig. 5.6), does

¹⁷The spherical mirrors are realized by the Equipment & Prototype Center (EPC) from Eindhoven University of Technology.

¹⁸Motor stages 413.32S and motor controllers C-663 are both from PI [183].

not experience direct interaction with the Rohacell holder. The dielectric material is clamped between two pieces of Rohacell and held in place by magnets [see Fig. 5.8(b)]. The dimensions of the Fabry-Pérot open-cavity resonator are summarized in Table 5.2 with the corresponding uncertainties and evaluation type¹⁹.

Table 5.2: Dimensions of the Fabry-Pérot open-cavity resonator with two spherical concave mirrors (see Fig. 5.5).

| # | Variable | size (mm) | Uncertainty (μm) | Evaluation type |
|------|-----------------------|-----------------|----------------------------------|--------------------|
| 5.5 | B_m | See Fig. 5.6 | | B |
| 5.6 | w_0 | See Fig. 5.6 | | B |
| 5.7 | r_m | 40.0 | 100.0 | B |
| 5.8 | R_0 | 100.0 | 0.3 | B |
| 5.9 | D (near-concentric) | 175.2 | 0.2 | A |
| 5.10 | D (near-confocal) | 87.6 | 0.2 | A |
| 5.11 | D (near-focal) | 46.1 | 0.2 | A |
| 5.12 | d_{iris} | 1.5494 | 10.0 | A |
| 5.13 | WR-12 | 1.5494 x 3.0988 | ± 5.0 | B |

5.7 Probabilistic sensitivity analysis

This section provides insight into which variable from Equation (5.13) to (5.18) has the largest influence on the accuracy²⁰ of the ϵ_r and $\tan\delta$ (see Table 5.3 to Table 5.5). This process is called a probabilistic sensitivity analysis (PSA) simulation (see Chapter 2, Subsection 2.6.1). The PSA consists of a probabilistic input variable, a mathematical model and an output variable. In Table 5.3 to Table 5.5 these probabilistic variables, obtained from the relevant equations, are called ‘input variables’ [see (#5.14) to (#5.29)] and follow a Gaussian distribution [see Chapter 2, Subsection 2.6.1, Fig. 2.7)]. The mathematical model consists of a set of equations [see (5.13) to (5.18)] and the output value is related to either the ϵ_r or to the $\tan\delta$ and expressed as a standard deviation of $\pm 2s$.

The truncation (see Chapter 2, Subsection 2.6.1) of the distribution function, used for the input variables, originate from production tolerances (see Chapter 2, Section 2.6.1)

¹⁹The evaluation type tells us where the information is coming from, defining the uncertainty. Type A evaluation is obtained via self-performed measurements and type B evaluation by other sources like data-sheets (see Chapter 2, Section 2.7.1).

²⁰The ‘condition for the significance’ of the ϵ_r is smaller than one hundredth and, the ‘condition for the accuracy’ of the ϵ_r is smaller than one thousandth and ten times smaller than the obtained $\tan\delta$.

or from deviations related to, for instance, measuring the thickness of a dielectric material. The simulation is performed based on a measured value of either the ϵ_r or the $\tan\delta$ of a certain material²¹. The PSA simulation, which is an in-house developed algorithm in Matlab [185], is iterated one million times per probabilistic input variable²² (see Table 5.3, second column). To be able to distinguish between the same input variable with a different tolerance a subscript, with a description of the applied tolerance, is added.

Table 5.3: In- and output variables, tolerances and outcome of the probabilistic sensitivity analysis for the relative permittivity at 65 GHz (≈ 2.028) with an expanded uncertainty of (± 0.005) and for the loss tangent (≈ 0.0003) with an expanded uncertainty of (± 0.0001) for PTFE with a thickness of $264\mu\text{m} \pm 2.6\mu\text{m}$.

| # | Input variable | Tolerance / uncertainty (%) | Input ($\pm 2s$) | Output ϵ_r ($\pm 2s$) | Equation |
|------|----------------------------|-----------------------------|----------------------|----------------------------------|------------------|
| 5.14 | δR_0 | 0.005 | 4.996 μm | 0.0003 | (5.13) .. (5.16) |
| 5.15 | $\delta_{\text{fx}0020}$ | 0.002 | 17110 Hz | 0.0142 | (5.17) |
| 5.16 | $\delta_{\text{fx}0002}$ | 0.0002 | 1710 Hz | 0.0014 | (5.17) |
| 5.17 | δ_{fs} | 0.000075 | 49826 Hz | 0.0005 | (5.17) |
| 5.18 | δt_{05} | 0.5 | 1.3191 μm | 0.0047 | (5.13) .. (5.16) |
| 5.19 | δc_{air} | 0.015 | 44938 m/s | 0.0013 | (5.13) .. (5.16) |
| # | Input variable | Tolerance / uncertainty (%) | Input ($\pm 2s$) | Output $\tan\delta$ ($\pm 2s$) | Equation |
| 5.20 | δR_0 | 0.005 | 4.996 μm | $1.4097e^{-8}$ | (5.13) .. (5.16) |
| 5.21 | $\delta_{\text{fx}0020}$ | 0.002 | 17110 Hz | $5.0273e^{-7}$ | (5.17) |
| 5.22 | $\delta_{\text{fx}0002}$ | 0.0002 | 1710 Hz | $5.0239e^{-8}$ | (5.17) |
| 5.23 | δ_{fs} | 0.000075 | 49826 Hz | $1.9027e^{-8}$ | (5.17) |
| 5.24 | δt_{05} | 0.5 | 1.3191 μm | $2.4082e^{-7}$ | (5.13) .. (5.16) |
| 5.25 | $\delta Q_{\text{ucav}10}$ | 10 | 10559 | $1.4826e^{-4}$ | (5.18) |
| 5.26 | $\delta Q_{\text{ucav}5}$ | 5 | 5381 | $7.3607e^{-5}$ | (5.18) |
| 5.27 | $\delta Q_{\text{L}10}$ | 10 | 8611 | $1.8163e^{-4}$ | (5.18) |
| 5.28 | $\delta Q_{\text{L}05}$ | 5 | 4309 | $9.0178e^{-5}$ | (5.18) |
| 5.29 | δc_{air} | 0.015 | 44917 m/s | $3.5079e^{-8}$ | (5.18) |

Analyzing Table 5.3 to Table 5.5 the following is concluded:

- The uncertainty δR_0 represents the variation on the radius of curvature R_0 (see Fig. 5.5). In none of the three cases is the ϵ_r and $\tan\delta$ affected by the

²¹The used measured data for the ϵ_r and $\tan\delta$ are from two samples of PTFE with a thickness of $264\mu\text{m}$ and $1018\mu\text{m}$ (see Tables 5.3 and 5.4) and FR-4 with a thickness of $130\mu\text{m}$ (see Table 5.5).

²² $n = 1,000,000$ is chosen because then the probabilistic input reaches a Gaussian distribution.

proposed maximum tolerance [see for instance (#5.14) and (#5.20)]. Therefore, for this uncertainty the condition for the accuracy is met. The $\tan\delta$ is not sensitive for this uncertainty.

- The uncertainty $\delta_{f_{x00xx}}$ ²³ represents the variation on the δ_f (see Fig. 5.7). The $\delta_{f_{x00xx}}$ plays only a role for the thinner materials as shown in Table 5.3 and Table 5.5. The proposed tolerance in (#5.15), and (#5.21) for instance, is too large and therefore affects the ϵ_r such that the condition for the accuracy is not met. When the tolerance is reduced by a factor of ten, as shown in (#5.16) and (#5.22), then the condition for the accuracy is met. The $\tan\delta$ is not sensitive for this uncertainty.
- The uncertainty δ_{f_s} represents the variation in the frequency difference δf_{sa} or δf_{ss} (see Fig. 5.7). In none of the three cases is the ϵ_r and $\tan\delta$ affected by the proposed tolerance [see for instance (#5.17) and (#5.23)]. The condition for the accuracy is met.
- The uncertainty δt is the variation on the measured thickness of the dielectric material, where t is half the thickness of the dielectric material (see Fig. 5.5). The δt plays only a role for the thinnest dielectric material used for this research as shown in Table 5.5 [see (#5.50) and (#5.57)]. In this case the condition for the accuracy is not met. Therefore, a micrometer²⁴ with an resolution of $\pm 1\mu\text{m}$ is used. As shown in (#5.51) and (#5.58) the accuracy is met when the thickness of the dielectric material is determined with $\pm 1\mu\text{m}$ resolution.
- The uncertainty δc_{air} is the variation on the speed of light in air c_{air} (see Section 5.8). In none of the three cases is the ϵ_r and $\tan\delta$ affected by the proposed tolerance [see for instance (#5.14) and (#5.20)]. The condition for the accuracy is met.

²³The ‘x’ represents a particular tolerance value used as input to the PSA simulation.

²⁴Type Micromaster system, 0 – 30 mm.

Table 5.4: In- and output variables, tolerances and outcome of the probabilistic sensitivity analysis for the relative permittivity at 65 GHz (≈ 2.081) with an expanded uncertainty of (± 0.002) and for the loss tangent (≈ 0.0007) with an expanded uncertainty of (± 0.0001) for PTFE with a thickness of $1018\mu\text{m} \pm 11\mu\text{m}$.

| # | Input variable | Tolerance / uncertainty (%) | Input ($\pm 2s$) | Output ϵ_r ($\pm 2s$) | Equation |
|------|----------------------------|-----------------------------|----------------------|----------------------------------|------------------|
| 5.30 | δR_0 | 0.005 | 4.999 μm | 0.0002 | (5.13) .. (5.16) |
| 5.31 | $\delta_{\text{fx}0020}$ | 0.002 | 17117 Hz | 0.0082 | (5.17) |
| 5.32 | $\delta_{\text{fx}0002}$ | 0.0002 | 1710 Hz | 0.0008 | (5.17) |
| 5.33 | δ_{fs} | 0.000075 | 49741 Hz | 0.0003 | (5.17) |
| 5.34 | δt_{05} | 0.5 | 0.5089 μm | 0.0019 | (5.13) .. (5.16) |
| 5.35 | δc_{air} | 0.015 | 44941 m/s | 0.0008 | (5.13) .. (5.16) |
| # | Input variable | Tolerance / uncertainty (%) | Input ($\pm 2s$) | Output $\tan\delta$ ($\pm 2s$) | Equation |
| 5.36 | δR_0 | 0.005 | 4.999 μm | $2.7693e^{-8}$ | (5.13) .. (5.16) |
| 5.37 | $\delta_{\text{fx}0020}$ | 0.002 | 17117 Hz | $1.0301e^{-6}$ | (5.17) |
| 5.38 | $\delta_{\text{fx}0002}$ | 0.0002 | 1710 Hz | $1.0290e^{-7}$ | (5.17) |
| 5.39 | δ_{fs} | 0.000075 | 49741 Hz | $3.9126e^{-8}$ | (5.17) |
| 5.40 | δt_{05} | 0.5 | 0.5089 μm | $5.1406e^{-7}$ | (5.13) .. (5.16) |
| 5.41 | $\delta Q_{\text{ucav}10}$ | 10 | 10544 | $1.2735e^{-4}$ | (5.18) |
| 5.42 | $\delta Q_{\text{ucav}5}$ | 5 | 52764 | $6.3247e^{-5}$ | (5.18) |
| 5.43 | $\delta Q_{\text{L}10}$ | 10 | 66888 | $2.0108e^{-4}$ | (5.18) |
| 5.44 | $\delta Q_{\text{L}05}$ | 5 | 33437 | $9.9767e^{-5}$ | (5.18) |
| 5.45 | δc_{air} | 0.015 | 44941 m/s | $9.8471e^{-8}$ | (5.18) |

Concerning the Q -factor, which is only used to determine the $\tan\delta$, the following is concluded:

- The uncertainty δQ_{ucavxx} is the variation in the Q -factor of the unloaded cavity Q_{ucavxx} . As shown in (#5.26), (#5.42) and (#5.60) the condition for the accuracy is met when the tolerance is not larger than 5%.
- The uncertainty δQ_{Lxx} is the variation on the Q -factor of the loaded cavity Q_{L} . As shown in (#5.26), and (#5.60) the condition for the accuracy is met when the tolerance is not larger than 5%. Even for the thinnest material [see (#5.61)], where the uncertainty is a hundred times higher than in the other two cases, the condition for the accuracy is met. This is because the $\tan\delta = 0.01$ is relatively high. To be able to achieve the same uncertainty as in (#5.26), and (#5.60) the tolerance has to be reduced to 0.1% [see (#5.62)].

Table 5.5: In- and output variables, tolerances and outcome of the probabilistic sensitivity analysis for the relative permittivity at 65 GHz (≈ 3.999) with an expanded uncertainty of (± 0.009) and for the loss tangent (≈ 0.0101) with an expanded uncertainty of (± 0.0001) for FR-4 with a thickness $130\mu\text{m} \pm 1.3\mu\text{m}$.

| # | Input variable | Tolerance / uncertainty (%) | Input ($\pm 2s$) | Output ϵ_r ($\pm 2s$) | Equation |
|------|----------------------------|-----------------------------|----------------------|----------------------------------|------------------|
| 5.46 | δR_0 | 0.005 | 4.999 μm | 0.0008 | (5.13) .. (5.16) |
| 5.47 | $\delta_{\text{fx}0020}$ | 0.002 | 17102 Hz | 0.0295 | (5.17) |
| 5.48 | $\delta_{\text{fx}0002}$ | 0.0002 | 1709 Hz | 0.0029 | (5.17) |
| 5.49 | δ_{fs} | 0.000075 | 49789 Hz | 0.0011 | (5.17) |
| 5.50 | δt_{075} | 0.75 | 0.9745 μm | 0.0218 | (5.13) .. (5.16) |
| 5.51 | δt_{025} | 0.25 | 0.3252 μm | 0.0073 | (5.13) .. (5.16) |
| 5.52 | δc_{air} | 0.015 | 44975 m/s | 0.0029 | (5.13) .. (5.16) |
| # | Input variable | Tolerance / uncertainty (%) | Input ($\pm 2s$) | Output $\tan\delta$ ($\pm 2s$) | Equation |
| 5.53 | δR_0 | 0.005 | 4.999 μm | $4.1923e^{-7}$ | (5.13) .. (5.16) |
| 5.54 | $\delta_{\text{fx}0020}$ | 0.002 | 17102 Hz | $1.5230e^{-5}$ | (5.17) |
| 5.55 | $\delta_{\text{fx}0002}$ | 0.0002 | 1709 Hz | $1.5218e^{-6}$ | (5.17) |
| 5.56 | δ_{fs} | 0.000075 | 49789 Hz | $5.7710e^{-7}$ | (5.17) |
| 5.57 | δt_{075} | 0.75 | 0.9745 μm | $5.2334e^{-6}$ | (5.13) .. (5.16) |
| 5.58 | δt_{025} | 0.25 | 0.3252 μm | $1.7467e^{-6}$ | (5.13) .. (5.16) |
| 5.59 | $\delta Q_{\text{ucav}10}$ | 10 | 10661 | $1.4977e^{-4}$ | (5.18) |
| 5.60 | $\delta Q_{\text{ucav}05}$ | 5 | 5310 | $7.4337e^{-5}$ | (5.18) |
| 5.61 | $Q_{\text{L}10}$ | 10 | 1366 | $1.1695e^{-3}$ | (5.18) |
| 5.62 | $\delta Q_{\text{L}001}$ | 0.1 | 13.66 | $1.1580e^{-5}$ | (5.18) |
| 5.63 | δc_{air} | 0.015 | 44975 m/s | $1.1539e^{-6}$ | (5.18) |

In each header of Table 5.3 to Table 5.5 the expanded uncertainty U can be found for both ϵ_r and $\tan\delta$. Concerning the expanded uncertainty of the ϵ_r , the condition for the accuracy is met for both PTFE materials and FR-4. Concerning the $\tan\delta$ the condition of the accuracy is only met for the FR-4 material. This is because the $\tan\delta$ is relatively high, i.e. around 0.01.

5.8 Measuring the relative permittivity of air for assessing the measurement significance and accuracy

The measurement and obtained values of the permittivity of air have been described in detail in [146]. The interesting thing about the permittivity of air is that its value is determined with a significance to the nearest ten-thousandth. Measuring the ϵ_r of air with the Fabry-Pérot open-cavity resonator will give insight with which significance

and with which accuracy the measurement system can measure²⁵. Based on the earlier mentioned article the ϵ_r has been determined for a frequency range from 0.009 MHz to 24000 MHz with an ϵ_r from 1.000567 [186] to 1.000576 [187], respectively. As shown, for example in Table 5.5 [#5.52], it introduces an uncertainty. Therefore it is important to measure the ϵ_r of air at the same frequencies at which the dielectric material is measured, in this case from 60 GHz to 90 GHz. Since the ϵ_r of air is affected by the ambient temperature, humidity and air pressure, these quantities are monitored during the measurement. An additional advantage is that the ϵ_r of air can be used to determine the speed of light c_{air} in the cavity. Subsequently, c_{air} is used as input parameter for the PSA (see Section 5.7) for obtaining the uncertainty of the ϵ_r and $\tan\delta$ of a dielectric material.

Initially, the Fabry-Pérot open-cavity resonator does not seem suitable for determining the ϵ_r of air. The reason for this is that the principle of the Fabry-Pérot open-cavity resonator is based on perturbation by a dielectric material placed in the cavity with an ϵ_r greater than air. This means that the resonator is used in a way it was not intended for to be able to determine the ϵ_r of air. To accommodate this, we have modified the procedure with the following steps:

Firstly, the spherical concave mirrors are placed at a certain distance D that corresponds to a certain frequency, at which the ϵ_r of air will be determined with the highest Q -factor. The q (see Section 5.5) is then derived from this distance D (see Appendix D.3). After the spherical concave mirrors are placed at the desired distance the difference between resonance frequencies f_0 and f_1 , i.e. δf_0 (see Fig. 5.9) are obtained via measurement. With the value for resonance frequencies f_0 and f_1 the $f_{\delta f}$ can be determined with:

$$f_{\delta f} = [(f_1 - f_0) (2q)], \quad (5.21)$$

Secondly, the wavelength in the cavity λ_{cav} is obtained by moving one spherical concave mirror over a distance d_{mirror} , which corresponds to a quarter-wavelength obtained from resonance frequency f_1 , towards the other spherical concave mirror. The moving resonance frequency (dotted green line) is illustrated in Fig. 5.9 by resonance frequency f'_0 and moves from resonance frequency f_0 to resonance frequency f_1 . The direction of movement is indicated by the green arrow (see Fig. 5.9). If the speed of light in the cavity is the same as the speed of light that is used to determine the quarter-wavelength

²⁵With the measurement of the ϵ_r of air the uncertainties of the Fabry-Pérot open cavity resonator including motors for positioning the mirrors, vector network analyzer, extenders and cables are taken into account, but excludes the tolerance of the placement of the dielectric material. The reason for this is that the placement of the dielectric material and dielectric material holder is not part of the measurement of the ϵ_r of air.

of resonance frequency f_1 , then resonance frequency f'_0 must be exactly at resonance frequency f_1 . If this is not the case, then the speed of light in the cavity is different from the speed of light used to determine the quarter-wavelength over which distance the spherical concave mirror has traveled. Based on the ratio between resonance frequency f_1 and f'_0 and the distance d_{mirror} the λ_{cav} in the cavity can be obtained with:

$$\lambda_{\text{cav}} = 2 \left[\left(\frac{f_1}{f'_0} \right) d_{\text{mirror}} \right], \quad (5.22)$$

Thirdly, now that both $f_{\delta f}$ and λ_{cav} have been obtained the speed of light in the cavity c_{cav} can be calculated with:

$$c_{\text{cav}} = \lambda_{\text{cav}} f_{\delta f}, \quad (5.23)$$

Fourthly, with the obtained speed of light in the cavity c_{cav} together with the speed of light in vacuum c_0 (299792458 m/s) the ϵ_r of air $\epsilon_{r,\text{air}}$ can be calculated with:

$$\epsilon_{r,\text{air}} = \left(\frac{c_0}{c_{\text{cav}}} \right)^2. \quad (5.24)$$

The measured $\epsilon_{r,\text{air}}$ and c_{air} using the Fabry-Pérot open-cavity resonator can be found in Table 5.6. The expanded uncertainty ($k = 2$, see Chapter 2, Subsection 2.8.3) expressed as a standard deviation comes from the limited resolution from the motor stages d_{mirror} ($0.2\mu\text{m}$), and possible frequency drift (≈ 1700 Hz) illustrated in Fig. 5.9 by the red arrows. The obtained values of the $\epsilon_{r,\text{air}}$ are comparable with the results in literature. The spread in the value of the $\epsilon_{r,\text{air}}$ is mainly caused by the limited positioning resolution of the mirrors.

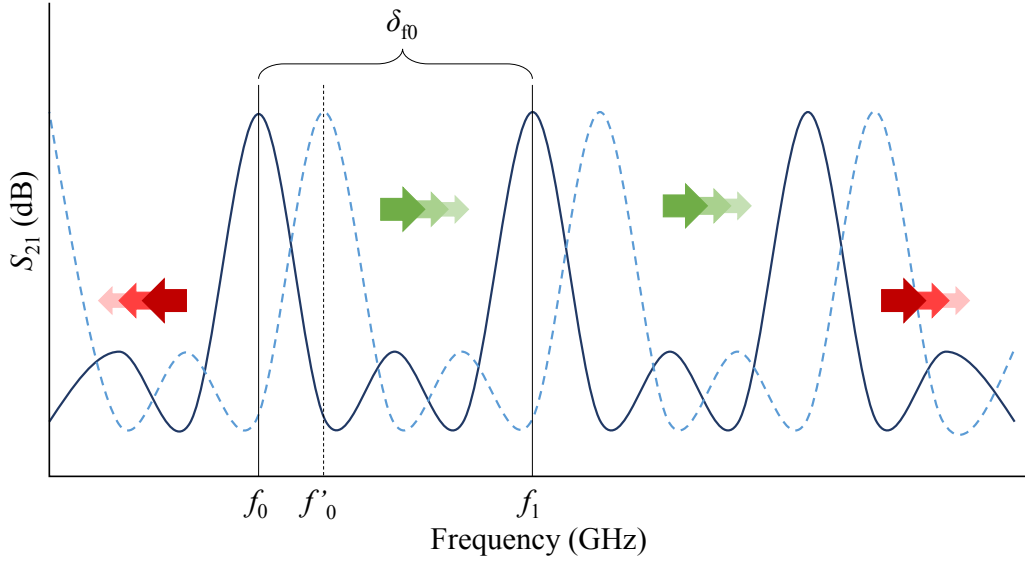


Figure 5.9: Shift in resonance frequency f_0 by moving the spherical mirrors. The movement of the spherical mirror is illustrated by the moving resonance peak f'_0 starting from f_0 and moves towards f_1 . The green arrows indicate the movement of the resonance peak caused by moving one spherical mirror. The red arrows indicate the possible direction of the frequency drift.

Table 5.6: The results of the measured relative permittivity of air $\epsilon_{r'air}$ and the speed of light c_{air} in the cavity of the Fabry-Pérot resonator. The measurement uncertainty is expressed as a standard deviation of $\pm 2s$. During the actual measurements the environmental condition was 22.5°C with a humidity of 54.6%, and an air-pressure of 1016 hPa. (The speed of light in vacuum is 299792458 m/s and the speed of light in air at 900 kHz is 299702547 m/s.)

| # | Frequency (GHz) | q | $\lambda/2$ (μm) | c_{air} (m/s) | $\epsilon_{r'air}$ Mean | Standard deviation ($\pm 2s$) |
|------|-----------------|-----|-------------------------------|-----------------|-------------------------|---------------------------------|
| 5.64 | 60 | 33 | 2497.5 | 299733582 | 1.000405 | 0.000162 |
| 5.65 | 65 | 38 | 2305.4 | 299743369 | 1.000343 | 0.000174 |
| 5.66 | 70 | 42 | 2140.7 | 299744020 | 1.000603 | 0.000184 |
| 5.67 | 75 | 45 | 1998.0 | 299733893 | 1.000595 | 0.000200 |
| 5.68 | 80 | 49 | 1873.0 | 299745775 | 1.000414 | 0.000220 |
| 5.69 | 85 | 52 | 1763.0 | 299755364 | 1.000306 | 0.000219 |
| 5.70 | 90 | 54 | 1665.0 | 299742835 | 1.000375 | 0.000262 |

5.9 Causes of uncertainty in characterizing dielectric materials

From the preceding sections it is concluded that there are two important parameters that have a significant effect on the accuracy of determining the permittivity and $\tan\delta$, namely, the uncertainty in δ_{fi} and the Q -factor of both the unloaded Q_{ucav} and loaded Q_{L} cavity. In this section the causes that affect δ_{fi} , Q_{ucav} and Q_{L} and possible solutions are described.

5.9.1 Measurement stability

A Fabry-Pérot open-cavity resonator, used during this research, is connected to a VNA and frequency extenders²⁶ to perform a transmission measurement (S_{21} or S_{12}) and retrieve the measured data. Settings of the VNA²⁷ that can be used and adjusted to obtain a frequency spectrum as shown in Fig. 5.7(a) are:

- a *single* frequency sweep with a certain *sweep-time* (< 60 sec.) to obtain a data-set,
- a given *frequency bandwidth*, which changes depending on the focal distance which can be:
 1. Near-focal distance with a frequency bandwidth of 8.0 GHz.
 2. Near-confocal distance with a frequency bandwidth of 4.5 GHz.
 3. Near-concentric distance with a frequency bandwidth of 3.5 GHz.
- a certain number of *frequency points*, which is limited by the type of VNA, in this case 32001 points,
- and a certain *IF bandwidth* (IF-BW). The choice of the IF-BW is a trade-off between signal-to-noise ratio and sweep-time and set to a maximum of a 1000 Hz, which still satisfies the sweep-time criteria (see first bullet).

The δ_{fi} is derived from measuring two successive resonance frequencies sequentially. Obtaining these two resonance frequencies will take time. During this measurement time, obtaining both resonance frequencies, the setup is to be expected stable i.e. that a minimum frequency drift occurs according the specifications of the VNA [156]. In Table 5.3 to Table 5.5 it is shown that a frequency drift of 1.7 kHz is conform the

²⁶E8361C from the company Keysight and frequency extenders from the company VDI [188].

²⁷The actual VNA settings are in italic in the text.

condition for accuracy [see (#5.24), (#5.40) and (#5.56)]. The question is whether we can guarantee this maximum allowable frequency drift when environmental conditions such as temperature and humidity change to a certain extent.

With the designed and realized setup illustrated in Fig. 5.10 it is possible to monitor the temperature and humidity with respect to a resonance frequency. Two temperature / humidity sensors²⁸ are placed close to the open cavity [see Fig. 5.10(c)]. To exclude that the accuracy of the local oscillator of the VNA plays a role, a frequency counter²⁹ [see Fig. 5.10(a)], has been added³⁰. The data is obtained, over a period of nine days, via an AD converter and logged with a computer³¹ [see Fig. 5.10(b)]. From these measurement results (see Appendix D.4, Fig. D.6) the following conclusions can be drawn:

- A temperature change in the cavity and in the RF-cables of $\approx 2^\circ\text{C}$ results in an inverse variation of frequency drift up to 4 MHz that follows the temperature variation (see Appendix D.4, Fig. D.6).
- The climate control of the building has an overall effect on the steepness and amplitude of the slope of the temperature and humidity. This becomes apparent during nights and weekends when the climate control is turned off (see Appendix D.4).

From additional tests with a heater the main cause of the frequency drift is determined. It turns out that the heat flow through the cavity is the dominant factor. Based on this investigation all material characterization measurements are performed in a more temperature stable room with a 4-port VNA³² and transceiver extenders³³. A combination of factors such as a more temperature-stable room together with a new VNA and extenders has led to a more stable measurement environment. The frequency drift over one day has been brought back to ≈ 2 MHz instead of ≈ 4 MHz.

²⁸T9602 – 5–A from the company Amphenol.

²⁹HP53131A Universal counter from Keysight.

³⁰The maximum frequency provided by the VNA as input for the frequency extenders is 15 GHz [188]. At 15 GHz, the frequency drift, due to temperature stability, is 750 Hz without frequency counter and 32.5 Hz with a frequency counter [156].

³¹16 bits ADC U6 Pro from the company Labjack.

³²PNA N5227B from Keysight [156].

³³ZC90 from Rohde and Schwarz [189].

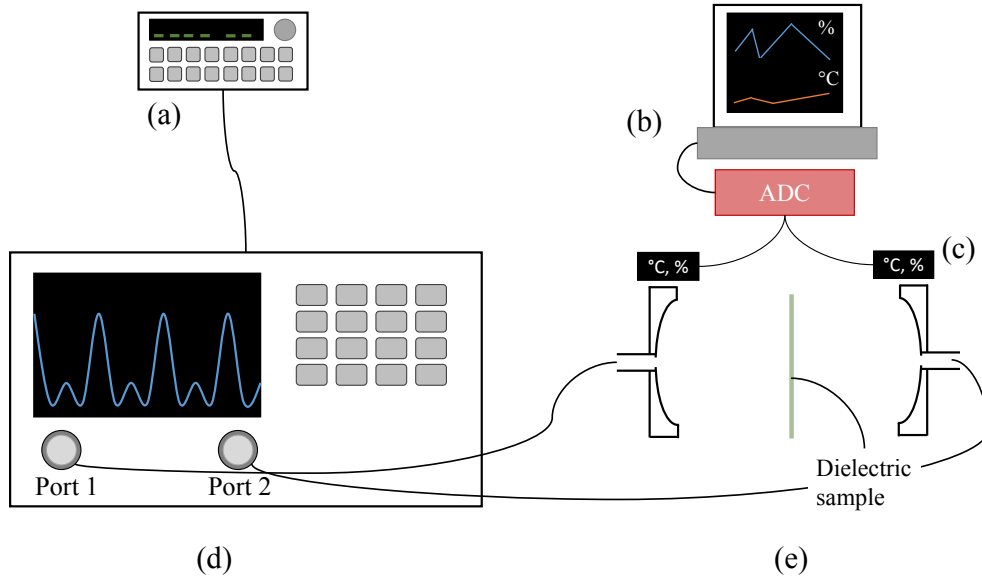


Figure 5.10: Measurement setup for sampling temperature, humidity and a resonance frequency over time. (a) Frequency counter, (b) PC with analogue / digital converter, (c) temperature and humidity sensors, (d) vector network analyzer, and (e) the Fabry-Pérot open-cavity resonator.

5.9.2 Post-processing the resonance peak in case of a limited number of frequency points

As described in the preceding subsection, to minimize the effect of frequency drift, the measured data without and with dielectric material must be obtained in less than five minutes. An important condition is that the data set contains at least three resonance frequencies [see Fig. 5.7(a)]. This means that the obtained data has a limited number of frequency points³⁴ for reconstructing the resonance peak. To be able to determine both the resonance frequency and the frequency bandwidth at -3 dB the resonance peak needs to be reconstructed. This is done by a process that is described via a flow chart in Fig. 5.11(a).

The post-processing of the resonance frequencies $f_{i-\text{ulcav}}$ of the unloaded cavity relies on the convergence of the difference between the resonance frequencies δ_{f_0} and δ_{f_1} . The difference between the resonance frequencies is assumed to be equal. However, due to the deformation of the resonance peak caused by the limited number of frequency points the difference between, in this case δ_{f_0} and δ_{f_1} , will differ. By finding the actual f_i for all three resonance frequencies the difference between δ_{f_0} and δ_{f_1} should become zero. The convergence is tested by obtaining the standard deviation of both δ_{f_0} and δ_{f_1} , which

³⁴The number of frequency points changes when a different focal distance is chosen (see Subsection 5.3.2 and Subsection 5.9.1).

must approach zero.

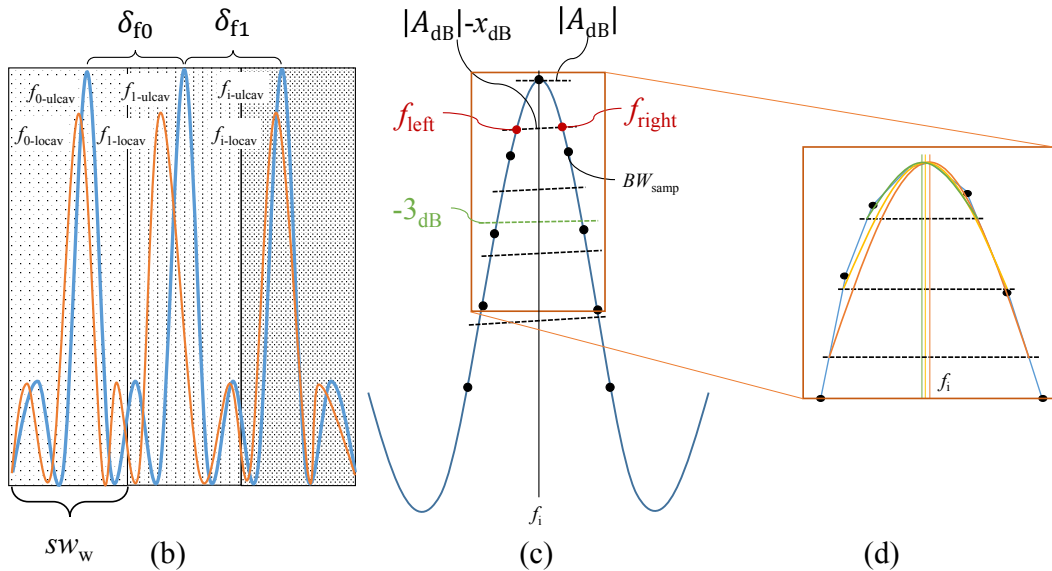
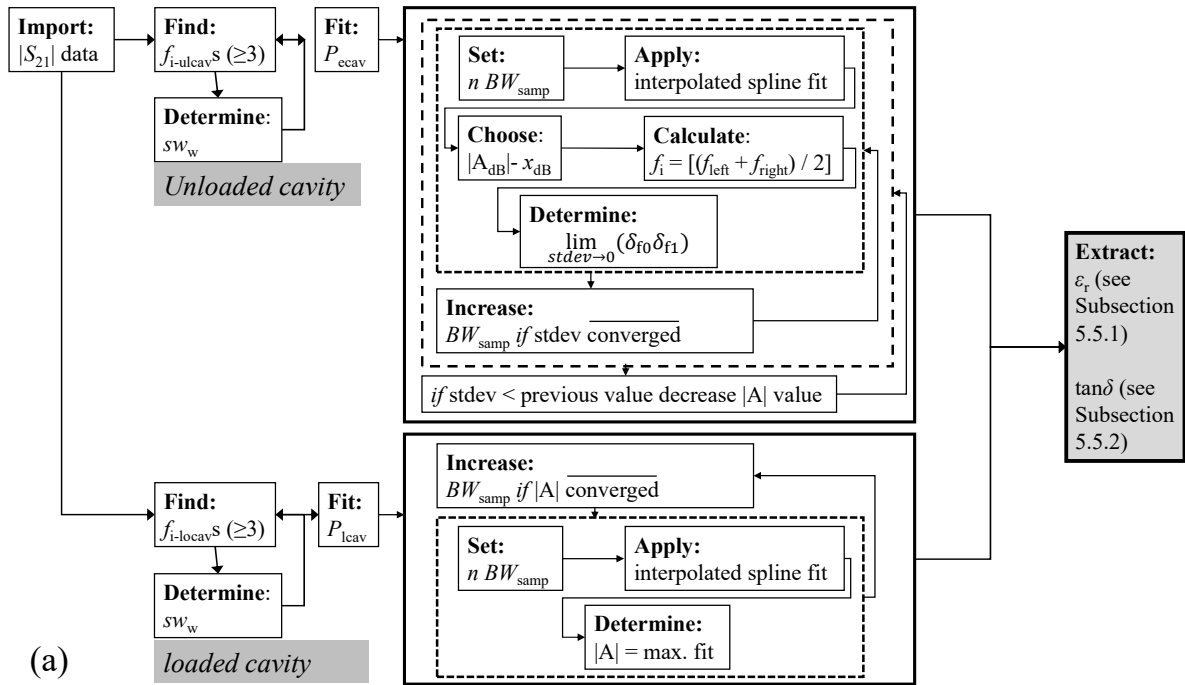


Figure 5.11: (a) Post-processing flow chart, (b) frequency spectrum with resonance frequencies from both unloaded (blue) and loaded (orange) cavity and rectangular sliding window, (c) resonance peak with frequency points (black) and (d) the top of a resonance peak curve fitted based on different values for $|A_{dB}| - x_{dB}$.

The resonance frequencies are obtained by using a sliding window sw_w [see Fig. 5.11(b)]. The sliding window is used to retrieve the resonance frequencies of the unloaded cavity as well as those of the loaded cavity. The width sw_w of the sliding window is iteratively adjusted so that there is only one resonance frequency in the window. Fig. 5.11(c) shows a resonance peak with the different variables used to reconstruct f_0 and the Q -factor for both the results of the unloaded and loaded cavity.

A minimum number of BW_{samp} [see Fig. 5.11(c)] is taken to reconstruct the resonance peak and apply an interpolated spline curve [see Fig. 5.11(d), green line]. Then, at for instance $|A_{\text{dB}}|-1$ dB, a line is drawn [see Fig. 5.11(b), horizontal black dashed lines] where at the crossing with the curve f_{left} and f_{right} are obtained. The resonance frequency is now determined by $f_i = [(f_{\text{left}} + f_{\text{right}})/2]$. These steps [see Fig. 5.11(a)] are repeated for the unloaded cavity until the standard deviation of δ_{f_0} and δ_{f_1} are converged. For the loaded cavity these steps are repeated until the value of f_i has converged. At the end the f_i is obtained at a minimum of $|A_{\text{dB}}|-4$ dB such that the Q -factor can be determined at -3 dB [see Fig. 5.11(c), green dashed line].

For the in this section described fitting technique, it is assumed that the resonance peak is symmetrical as illustrated Fig. 5.11(c) and Fig. 5.11(d). However, in some cases, depending on the ϵ_r and $\tan\delta$ of the dielectric material to be measured (see Sub-section 5.3.3), an asymmetric resonance peak, also called a ‘Fano’ or skewed resonance³⁵, can occur. Research into curve fitting techniques for these asymmetric resonance peaks is described in [191]. One of the recommendations is to use a Lorentzian curve fit with the addition of a cross-coupling perturbation term. The implementation of a suitable or adaptive curve fitting technique is recommended for future work.

5.10 Measured permittivity and loss tangent of PTFE and FR-4 including the combined standard expanded uncertainty

Two different dielectric materials have been measured with the realized Fabry-Pérot open-cavity resonator (see Section 5.6, Fig. 5.8). The measured ϵ_r and $\tan\delta$ for one sample of PTFE with a thickness of $\approx 264\mu\text{m}$ is provided in Table 5.7 and for a dielectric sample of FR-4 with a thickness of $\approx 130\mu\text{m}$ the results are shown in Table 5.8. Both tables include both results obtained directly from the measured raw data as well as from the curve-fitted data.

³⁵In physics, a ‘Fano’ resonance is a type of resonant scattering phenomenon that gives rise to an asymmetric curve. Interference between a background and a resonant scattering process produces the asymmetric line-shape [190].

Table 5.7: The measured relative permittivity and loss tangent of PTFE (264 μm) material.

| # | Frequency band (GHz) | ϵ_r Raw data | ϵ_r Curve fit | Diff. |
|------|----------------------|-----------------------|------------------------|-----------|
| 5.71 | 58 .. 61 | 2.049 | 2.082 | 0.033 |
| 5.72 | 61 .. 64 | 2.137 | 2.072 | -0.065 |
| 5.73 | 64 .. 67 | 2.017 | 2.021 | 0.004 |
| 5.74 | 67 .. 70 | 2.064 | 2.088 | 0.024 |
| # | Frequency band (GHz) | $\tan\delta$ Raw data | $\tan\delta$ Curve fit | Diff. |
| 5.75 | 58 .. 61 | NR ³⁶ | NR | NR |
| 5.76 | 61 .. 64 | 0.000469 | 0.000373 | -0.000096 |
| 5.77 | 64 .. 67 | 0.000936 | 0.000376 | -0.000560 |
| 5.78 | 67 .. 70 | 0.000463 | 0.000362 | -0.000101 |

Table 5.8: The measured relative permittivity and loss tangent of FR-4 (130 μm) material.

| # | Frequency band (GHz) | ϵ_r Raw data | ϵ_r Curve fit | Diff. |
|------|----------------------|-----------------------|------------------------|---------|
| 5.79 | 58 .. 61 | 4.114 | 4.040 | -0.074 |
| 5.80 | 61 .. 64 | 4.104 | 4.047 | -0.057 |
| 5.81 | 64 .. 67 | 4.100 | 4.003 | -0.097 |
| 5.82 | 67 .. 70 | 4.097 | 4.009 | -0.088 |
| # | Frequency band (GHz) | $\tan\delta$ Raw data | $\tan\delta$ Curve fit | Diff. |
| 5.83 | 58 .. 61 | NR | NR | NR |
| 5.84 | 61 .. 64 | 0.0090 | 0.0096 | 0.0006 |
| 5.85 | 64 .. 67 | 0.0107 | 0.0102 | -0.0005 |
| 5.86 | 67 .. 70 | 0.0102 | 0.0114 | 0.012 |

The difference between the ϵ_r obtained from the raw data and the ϵ_r after post-processing is in all cases not smaller than 0.05 for FR-4. This means that the deviation caused by the limited number of frequency points is larger than the condition for accuracy for the ϵ_r . Therefore, post-processing is necessary to be able to obtain the permittivity according the condition for accuracy.

³⁶NR = no result. The reason that no results could be obtained for this frequency band is unknown.

For sake of completeness, a repeatability measurement is performed³⁷, which resulted in a mean, standard deviation, standard deviation corrected³⁸ and a standard deviation based on a combined expanded uncertainty u_c ($k = 2.57$) for the two measured samples, where the results are combined in Table 5.9.

Table 5.9: The relative permittivity and loss tangent of FR-4 (130 μm) and PTFE (264 μm and 1018 μm) material obtained via a repeatability (5 times) measurement for a frequency range of 64 GHz to 67 GHz with different uncertainties expressed as a standard deviation of 2s, a corrected standard deviation with $k_p = 2.87$ (T-table, see Appendix A.5.) and an expanded uncertainty U .

| # | Material | ϵ_r Mean | Standard uncertainty $\pm 2s$ | Standard uncertainty Corrected $\pm 2s$ | Expanded uncertainty $k_p = 2.87$ |
|------|----------------------------|----------------------|-------------------------------------|---|---|
| 5.87 | FR-4 (130 μm) | 4.0019 | 0.0136 | 0.0195 | 0.0244 |
| 5.88 | PTFE (264 μm) | 2.0654 | 0.0103 | 0.0148 | 0.0146 |
| 5.89 | PTFE (1018 μm) | 2.0965 | 0.0039 | 0.0056 | 0.0063 |
| # | Material | $\tan\delta$ Mean | Standard uncertainty $\pm 2s$ | Standard uncertainty Corrected $\pm 2s$ | Expanded uncertainty $k_p = 2.57$ |
| 5.90 | FR-4 (130 μm) | 0.01007 | 0.00013 | 0.00019 | 0.00017 |
| 5.91 | PTFE (264 μm) | 0.00019 | 0.00002 | 0.00002 | 0.00012 |
| 5.92 | PTFE (1018 μm) | 0.00080 | 0.00009 | 0.00012 | 0.00013 |

By comparing the results in Table 5.3 to Table 5.5 we can observe that the setup itself should be able to achieve the desired accuracy (see last column of Table 5.9). However, when the measurements must be repeated the uncertainty becomes too large (see Table 5.9, column with corrected results), for dielectric materials with a certain thickness (#5.87) and (#5.88), up to one-hundredth. In case of (#5.87) this is caused by the fact that the thickness of the dielectric material cannot be determined accurately and that the dielectric material is not placed at the exact location. FR-4 is considered in-homogeneous. However, when observing the results of the thicker PTFE material (#5.89) then in all cases the standard deviation does not exceed one-thousandth, making even repeated measurements accurate. This does not hold for the thinner PTFE material (#5.88).

³⁷By repeatability is meant that five times the material holder and dielectric material are removed from the Fabry-Pérot open-cavity resonator and put back in place. After replacing the material holder, the measurement is repeated and the ϵ_r is determined.

³⁸The measurements are repeated five times where the obtained measurement data is corrected, with help of a T-table (see Appendix A.1, Section A.5, Table A.3), to be able to obtain the standard deviation.

A possible reason for this is that the dielectric material used for this measurement is relatively small. The dielectric material holder is designed to be able to stretch the dielectric material such that it becomes flat at the area where it is illuminated. However, when the material is relatively small and has a certain thickness it becomes difficult to achieve a certain flatness. Even more, small deviations in placing the dielectric material in the holder could cause large deviations in obtaining the ϵ_r . Concerning the standard deviation and u_c of the $\tan\delta$ the placement of the dielectric material has less effect [see (#5.90) to (#5.92)].

5.11 The advantages and disadvantages of using different focal distances to determine relative permittivity and loss tangent

As described in Subsection 5.3.2 and based on the stability criterium [see Fig. 5.3(a)], it is possible to determine the ϵ_r and $\tan\delta$ in the same setup with three different focus distances. In this subsection we discuss the advantages and disadvantages per focus distance.

The frequency spectrum for the near-concentric distance is illustrated in Fig. 5.7(a) and consist of a distinct pattern of consecutive resonance frequencies. This is less apparent for the other two distances, the near-confocal and the near-focal distance, where multiple resonance frequencies (to illustrate four) become visible caused by multiple p-modes (see Section 5.4) as shown by the black solid line in Fig. 5.12(a). With this type of frequency spectrum, it is impossible to determine from which resonance frequencies (f_0 , f_1 , f_2 , or f_3) the ϵ_r can be derived. Therefore, the dielectric material-holder (see Section 5.6) is altered such that an electromagnetic absorber can be added, as illustrated in Fig. 5.12(b). By using electromagnetic absorbers surrounding the diaphragm the p-modes are suppressed, thus creating a frequency spectrum as shown in Fig. 5.12(a) orange line with one distinct resonance frequency.

The beam pattern for the three different focal distances are shown in Fig. 5.12(c) for the near-focal distance, Fig. 5.12(d) for the near-confocal distance and Fig. 5.12(e) for the near-concentric distance. The mirrors and the beam shape are proportional and the sizes are taken from Fig. 5.6.

Two important conclusions are:

- At near-concentric focal distance the highest Q -factor is achieved. This means that the $\tan\delta$ is most accurately determined.
- The size of the beam waist w_0 changes slidely with varying focal distances where the size of the beam waist B_m changes significantly [see Fig. 5.12(c) to 5.12(e)].

This places requirements on the size of the mirror, which must be clearly based on the size of the beam waist B_m at the concentric distance (see Fig. 5.6 and Appendix D.3).

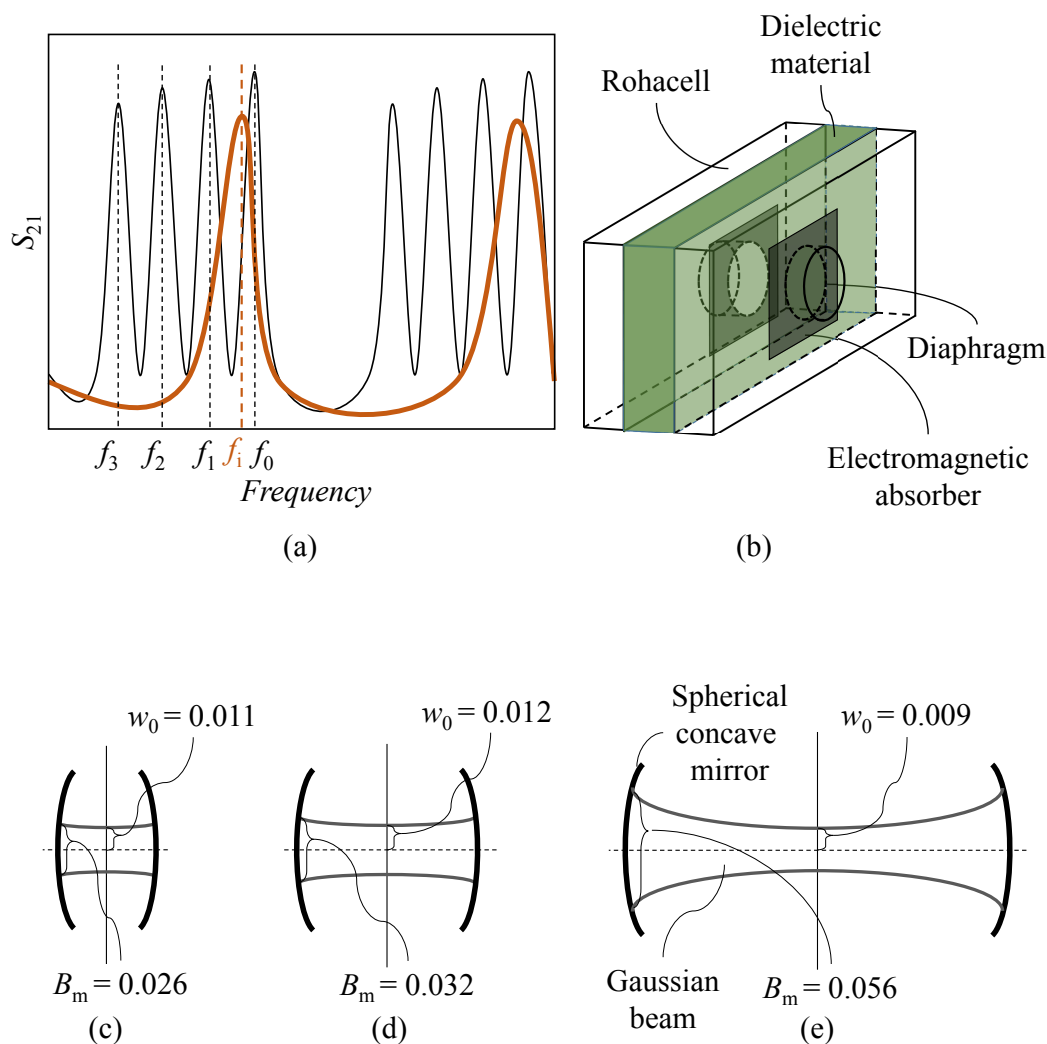


Figure 5.12: (a) Illustration of a sequence of four resonance frequencies f_3 to f_0 (black solid line) and a single resonance frequency f_i (orange line). (b) Illustration of a dielectric material holder made from Rohacell (white) with an electromagnetic absorber (black) and dielectric material (green). The different sizes of the Gaussian beam in the middle of the cavity w_0 and on the spherical mirror B_m are shown in (c) at near-focal distance, (d) at near-confocal distance, and (e) at near-concentric distance.

5.12 Conclusions

By investigating different material characterization methods, the advantages of the Fabry-Pérot open-cavity resonator became apparent. In summary, it is possible to measure, without contact, materials with a large variation in both thickness and size can be easily placed in the measuring system and the set-up is relatively simple to realize. Based on the stability diagram it has become clear that it is possible to measure at three different distances with the same system, each distance having its own advantages and disadvantages. Two striking advantages are that the $\tan\delta$ can be measured accurately at the near-concentric distance and the permittivity at the near-focal distance. Furthermore, we have derived from this theory an optimized distance with the highest Q -factor, which is summarized in a so-called qQ -Table (see Appendix D.4).

The measurement accuracy of the Fabry-Pérot open-cavity resonator has been determined by measuring the permittivity of air with this system. As far as we know, this has never been done before. The measurement accuracy of this Fabry-Pérot open-cavity resonator for the ϵ_r is therefore determined to be at least one ten-thousandth in the frequency range from 60 GHz to 90 GHz. Furthermore, from this measurement, the speed of light c_{air} observed in the cavity has been derived. This is used in the equations from which the ϵ_r and $\tan\delta$ are calculated, thereby improving the accuracy.

With the use of the probability sensitivity analysis, it has become clear which parameters are responsible for the inaccuracy in the ϵ_r and $\tan\delta$ and whether it is possible to improve it. For the relatively low-loss dielectric materials (PTFE), with a thickness of $264\mu\text{m}$ and $1018\mu\text{m}$, this is caused by the δ_f and the Q -factor. For the higher loss sample, with a thickness of $130\mu\text{m}$, this is mainly caused by determining the thickness t of the dielectric material. This must be determined with an accuracy of 1% with regard to the thickness of the dielectric material to satisfy the desired accuracy.

Finally, two causes have been found that affect the accuracy of the system. One cause is the ambient temperature and humidity, the influence of which can be limited by measuring in a shorter period of time (<5 min). The other cause is the limited number of measuring points, which creates an inaccuracy in determining both the f_0 and the Q -factor. This is solved by applying a curve fitting technique. Both solutions have been implemented and the measurement results of both PTFE and FR-4 are summarized with a combined standard uncertainty.

Conclusions and recommendations

6.1 Conclusions

In recent years, wireless technology has become increasingly popular with emerging applications such as 5G and 6G wireless communications and automotive radar sensing. These applications use higher frequencies (millimeter waves), which enables to integrate the so-called millimeter-wave antennas, either as single element or as an array, into a complete active wireless device. This has created challenges in design, integration and characterization through antenna modeling and measurements. So, uncertainty, of which Frank Knight, who was an American economist, said: “*you cannot be certain about uncertainty*”[192], is the keyword during this research. The goal of this research is to become more certain about the uncertainties concerning modeling, integration and measurement of a millimeter-wave antenna. Not only the uncertainties are described, but also the usefulness of validating the outcome of the simulation with the measurements of a millimeter-wave antenna.

It is important to explore the main causes of uncertainty in the design and characterization process of millimeter-wave antennas. Given the design complexity of a millimeter-wave antenna, we cannot just rely on our experience or intuition. There can be various causes, and not all of them have the same impact on the behavior of the antenna. About a hundred years ago it was already noted that measurement results will always be influenced by the measuring instrument, the so-called ‘observer effect’. The measurement setup is robust if these so-called ‘measuring instrument’ influences are minimal, as it was not noticed in the behavior of the object to be measured i.e. are not ‘observed’ in the measurement results.

This means that before starting with the design of a millimeter-wave antenna, the possible uncertainties must be mapped out. With the help of four Euler diagrams i.e.

worlds, the different stages of the development of an antenna are indicated. For example, there is an overlapping world called the ‘world of influence’. This is the world where the other three Euler diagrams fall in and describes the extrinsic uncertainties. The other three Euler diagrams are the ‘design world’, where the choice is made in which configuration stage the antenna design is in, the ‘symbolical world’ where the design parameters e.g. geometry of the antenna, are obtained via analytical or numerical simulation, and the ‘empirical world’ where the antenna is measured to determine the various characteristics. Between the last two worlds a validation takes place. To be able to perform a validation, one of these worlds should be considered as a reference. This is often an iterative process. In those four Euler diagrams e.g. the ‘antenna design process’, the uncertainties are subdivided into groups and in those groups the actual uncertainties are pin-pointed. The antenna design process maps all possible uncertainties.

After the antenna design process has been drawn up and most of the uncertainties have been identified, it is necessary to define useful statistical measures. However, applying the correct statistical techniques is not trivial. Therefore, during this research it has been investigated which statistical measures can be used for both simulated and measured data of millimeter-wave antennas, where the terms and conditions for applying statistical measures are thoroughly described. The main conclusion of this study into statistical measures is that specific statistical tools are needed that already consider the limited available data. Student’s t -distribution forms the basis to be able to analyze limited data, supplying a correction table for the standard deviation e.g. the T-table. In addition to these measures, attention is paid to the various distribution functions. Given some uncertainties are caused by tolerances, a truncated Gaussian distribution has been described, just to mention one. Another conclusion is that we must describe in detail how data is obtained, what the circumstances are and how the statistical measures are applied. Based on this study, the Euler diagrams related to the simulation and measurement of millimeter-wave antennas have been extended with statistical terms and measures.

Based on the antenna design process, extended with statistical terms and measures, an uncertainty model of a specific antenna is created. This uncertainty model can be used to predict the main causes affecting the behavior of the millimeter-wave antenna. With help of this uncertainty model the behavior of the antenna including the uncertainties are described, thus creating a reference to compare and quantify the measurement results to as well. This uncertainty model is applied to two case studies. The first case study concerns a linearly polarized millimeter-wave inset-fed patch antenna. A probabilistic sensitivity analysis is applied to investigate which tolerance in the antenna production process has the largest influence on its behavior. The effect of the tolerances and the possible correlation is presented in a correlation diagram in which the magnitude of correlations is explained and quantified. From this analysis it can be concluded that a

10% tolerance in the production of this PCB antenna is enough to achieve the desired accuracy of the antenna characteristics like the antenna gain etc..

The second case study uses a circularly polarized millimeter-wave rod antenna. Here, the tolerances are introduced as minimum and maximum values and are used as input values for the simulation model of the millimeter-wave rod antenna. From the analysis of this antenna we concluded that it is necessary to know the relative permittivity as accurately as 0.001 and that the tolerance in the layer registration of the PCB provides the largest deviation. Furthermore, the influence of specific settings and choices in the numerical simulation software (the number of mesh cells, and port excitation) was investigated. Especially the type of excitation influences the outcome of the antenna's behavior, which is mainly caused by its size and geometry, which may cause obstruction. The main conclusion is that the excitation port should represent reality as accurate as possible. The research antenna is meant as a reference, to make the effects from for instance the RF-connector, antenna-holder, etc. insightful. If the simulation model of the antenna should represent reality, i.e. a 'measurable' antenna, it is recommended to integrate the entire RF-connector in the simulation model. From experiments, we found that the most detailed simulation model, including the RF-connector, matches the closest to the measurement results, that falls within the minimum and maximum value of an antenna characteristic predicted by the simulation model.

The effect of the RF connector on the behavior of the AUT has been investigated. The uncertainty model shows that much of the interference comes from the RF-connector and the RF-connector interface. This is not only caused by blockage of the RF-connector housing, but also by unwanted radiation from transitions. Therefore, three different RF connectors have been investigated, namely a press-fit connector, an RF probe and a waveguide-to-PCB connector, to analyze the various effects that affect the behavior of the antenna. It becomes apparent that each RF connector radiates, and that this radiation limits the dynamic range of the measurement. We also found that the RF side probe together with the waveguide-to-PCB connector gives the lowest amount of interference, blockage and unwanted radiation. The contactless method is briefly explained. However, the usefulness of the contactless method needs further investigation.

A millimeter-wave antenna is typically realized on dielectric materials for which most of the time the relative permittivity and loss tangent are not accurately known. The Fabry-Perot open-cavity resonator is presented in Chapter 5 and is the preferred material characterization method in our case, because the material can be easily placed and removed from the setup without modifying the material. This contactless characterization system also allows to investigate the homogeneity of the dielectric material. The system has been characterized in various ways. For instance, the system accuracy, for measuring the relative permittivity, has been determined up to one ten-thousandth. This is done by measuring the relative permittivity of air.

In addition, a probabilistic sensitivity analysis has been applied. Two different dielectric materials are used, which act as a reference, to check whether it is at all possible to obtain the required accuracy for the relative permittivity of 1.001 and for the loss tangent ten times smaller than the measured value. These two different dielectric materials are PTFE with a thickness of $264\mu\text{m}$ and $1018\mu\text{m}$ and FR-4 with a thickness of $130\mu\text{m}$. From the outcome of the probabilistic analysis it can be concluded that the thickness of the dielectric material needs to be known within 1% to be able to obtain an accuracy for the relative permittivity up to one thousandth. Measuring the thickness with an accuracy of less than $1\mu\text{m}$ was not possible during this research. The analysis of the measurement accuracy has been complemented by a repeatability measurement, which shows that only for the PTFE material with a thickness of $1018\mu\text{m}$ the desired accuracy of one thousandth is achieved.

6.2 Recommendations

This research has attempted to establish a foundation to quantify and understand uncertainties in millimeter-wave antenna measurements, but this work is far from complete. In this thesis various aspects related to uncertainty in antenna modeling and measurement are investigated. In most of the cases various statistical measures are applied to quantify the uncertainty and its impact on the modeling and measurement results. Advances in insight into these topics have led to various recommendations and future work, which include:

- **Antenna design process:** The combination of Euler diagrams i.e. worlds, have proven to be very useful in identifying and visualizing uncertainties in the various stages of the design process of for example an antenna. However, adding a weight to each uncertainty predicting which uncertainty will have the greatest impact is of great value. This forces one to investigate every uncertainty and thus verify whether the assessment is correct. Afterwards one can then reflect on whether the prior knowledge was enough and whether one was not guided by the observer bias. Another important factor that needs to be investigated is the interaction between the various uncertainties identified in the different Euler diagrams e.g. the interaction between the uncertainties.
- **Modeling a reference:** During this research it was suggested to use the simulation model as a reference to compare the measurement results. An attempt has been made to describe a reference model that is as complete as possible by explaining the uncertainties arising from the simulation. However, the simulation model as a reference remains a topic of discussion. The reason for this is that it must be determined which standards an antenna reference must meet. Is a

description as complete as possible of the behavior of the antenna, by means of simulation results, including the effects of uncertainties, sufficient? This description of a reference antenna must be further investigated, whereby other sciences, like chemistry and physics, can be used as an example.

- **Interfacing the antenna:** It has proven to be a challenge to interface a millimeter-wave antenna with a commonly known RF-connector or RF-probe. The verification of the RF-probe has been done in the past. However, a more extensive analysis by measurement, making the same comparison as has been done during this research with help of simulation models, is advised. This is seen as future work because the anechoic measurement chamber with which it should be possible to characterize the RF-connector models was not finished and fully characterized when this research was completed.
- **The limits of material characterization system:** The probabilistic sensitivity analysis simulation is used several times in this study. This means that different variables both in the antenna design and in the material characterization system are individually analyzed with a certain distribution function. However, for the completeness of the probabilistic analysis, it is necessary to analyze all variables of an antenna design simultaneously. This means that it is advised to use a brute-force method by performing for instance a Monte Carlo simulation. In this way it becomes clear what the mutual influences are between the variables.

Furthermore, it has been observed that at the near-confocal and near-focal distance the p and l modes start propagating. The presence of the p and l modes becomes visible in the frequency spectrum because additional resonance frequencies appear. A way to suppress these modes is to change the diameter of the iris. A simulation model must be designed to optimize the diameter of the iris. The outcome of the simulation needs to be verified by measurement by implementing new mirrors with the new iris design.

Due to the limited number of frequency points available, the resonance peak is distorted. This makes it impossible to find accurately the f_0 and the -3dB frequencies. These frequency and amplitude parameters are needed as inputs to determine both the relative permittivity and loss tangent. A curve fitting technique has been applied that only assumes a symmetrical resonance peak. However, with certain dielectric materials, a so-called Fano or asymmetric peak can also arise. Therefore, it is advised to apply an adaptive curve fitting technique that considers the symmetry of the resonance peak.

An extensive measurement of various dielectric materials with different thicknesses, relative permittivity, and loss tangent at different focal distances is proposed. With this extensive measurement campaign it is possible to determine with what distance which type of dielectric material can be measured and what in

the end the measurement range of the Fabry-Perot open-cavity resonator is with which the relative permittivity and loss tangent can be determined.

A.1 Metrological terms used in this thesis [1], [2]

- A.1.1 accuracy:** The closeness of the agreement between the result of a measurement and a true value of the measurand. 'Accuracy' is a qualitative concept.
- A.1.2 arithmetic mean (average):** The sum of *values* **A.1.60** divided by the number of values.
- A.1.3 bias:** The difference between the expectation of the test results and an accepted reference value.
- A.1.4 characteristic:** A property which helps to identify or differentiate between items of a given *population* (**A.1.38**).
- A.1.5 confidence coefficient (confidence level):** The value $(1 - \alpha)$ of the *probability* (**A.1.40**) associated with a confidence interval or a *statistical coverage interval* (**A.1.58**).
- A.1.6 confidence interval, one sided:** When T_1 and T_2 are two functions of the observed values such that, θ_p being a *population* (**A.1.38** parameter to be *estimated* (**A.1.21**), the *probability* (**A.1.40**) $\mathbb{P}(T_1 \leq \theta_p \leq T_2)$ is at least equal to $(1 - \alpha)$ [where $(1 - \alpha)$ is a fixed number, positive and less than 1], the interval between T_1 and T_2 is a two-sided $(1 - \alpha)$ confidence interval for θ_p .
- A.1.7 confidence interval, two sided:** When T is a function of the observed values such that, θ_p being a *population* (**A.1.38** parameter to be *estimated* (**A.1.21**), the *probability* (**A.1.40**) $\mathbb{P}(T \leq \theta_p)$ [or the probability $\mathbb{P}(T \leq \theta_p)$] is at least equal to $(1 - \alpha)$ [where $(1 - \alpha)$ is a fixed number, positive and less than 1], the interval from the smallest possible value of θ_p up to T (or the interval from T up to the largest possible value of θ_p) is a one-sided $(1 - \alpha)$ confidence interval for θ_p .

A.1.8 correction: value added algebraically to the *uncorrected* (A.1.50) result of a measurement (A.1.35) to compensate for *systematic error* (A.1.19).

A.1.9 correction factor: Numerical factor by which the *uncorrected* (A.1.50) result of a measurement (A.1.35) is multiplied to compensate for *systematic error* (A.1.19).

A.1.10 correlation: The relationship between two or several random variables within a distribution of two or more random variables.

A.1.11 covariance: The covariance of two random variables is a measure of their mutual dependence.

A.1.12 coverage factor: Numerical factor used as a multiplier of the combined standard uncertainty in order to obtain an expanded uncertainty.

A.1.13 degrees of freedom: In general, the number of terms in a sum minus the number of constraints on the terms of the sum.

A.1.14 distribution function: A function giving, for every value x , the probability that the random variable X be less than or equal to x :

$$F(x) = \mathbb{P}(X \leq x). \quad (\text{A.1})$$

A.1.15 distribution, normal (Laplace-Gauss distribution): The probability distribution of a continuous random variable x .

A.1.16 error (of measurement): Result of a measurement minus a true value of the measurand.

A.1.17 error, random: Result of a measurement minus the mean that would result from an infinite number of measurements of the same measurand carried out under repeatability conditions.

A.1.18 error, relative: Error of measurement divided by a true value of the measurand.

A.1.19 error, systematic: Mean that would result from an infinite number of measurements of the same measurand carried out under repeatability conditions minus a true value of the measurand.

A.1.20 error, total: Both systematic and random errors, when combined, results in the total error.

A.1.21 estimate: The value of an estimator obtained as a result of an estimation.

A.1.22 estimation: The operation of assigning, from the observations in a sample, numerical values to the parameters of a distribution chosen as the statistical model of the population from which this sample is taken.

A.1.23 estimator: A statistic used to estimate a population parameter.

A.1.24 expectation (of a random variable or of a probability distribution), expected value, mean: 1) For a discrete random variable X taking the values x_n with the probabilities p_n , the expectation, if it exists, is:

$$\mu_e = E(X) = \sum p_n x_n, \quad (\text{A.2})$$

the sum being extended over all the values x_n which can be taken by X .

2) For a continuous random variable X having the probability density function $f(x)$, the expectation, if it exists, is:

$$\mu_e = E(X) = \int x f(x) dx. \quad (\text{A.3})$$

the integral being extended over the interval (s) of variation of X .

A.1.25 fixture: The calibration system that includes both hardware and software necessary to perform the calibration under stable, repeatable conditions.

A.1.26 frequency: The number of occurrences of a given type of event or the number of observations falling into a specified class.

A.1.27 frequency distribution: The empirical relationship between the values of a characteristic and their frequencies or their relative frequencies.

A.1.28 independence: Two random variables are statistically independent if their joint probability distribution is the product of their individual probability distributions.

A.1.29 measurand: Particular quantity subject to measurement.

A.1.30 measurement: Set of operations having the object of determining a value (**A.1.60**) of a quantity (**A.1.44**).

A.1.31 measurement, accuracy of: Closeness of the agreement between the result of a measurement and a true value of the measurand.

A.1.32 measurement, method of: Logical sequence of operations, described generically, used in the performance of measurements.

A.1.33 measurement, principle of: Scientific basis of a measurement.

A.1.34 measurement procedure: Set of operations, described specifically, used in the performance of particular measurements according to a given method.

- A.1.35 measurement, result of a:** Value attributed to a measurand, obtained by measurement.
- A.1.36 measuring system:** Set of one or more measuring instruments and often other devices, including any reagent and supply, assembled and adapted to give information used to generate measured quantity values within specified intervals for quantities of specified kinds.
- A.1.37 parameter:** A quantity used in describing the probability distribution of a random variable.
- A.1.38 population:** The totality of items under consideration.
- A.1.39 precision:** Closeness of agreement between results obtained by replicate measurements on the same object under specified conditions.
- A.1.40 probability:** A real number in the scale 0 to 1 attached to a random event.
- A.1.41 probability distribution (of a random variable):** A function giving the probability that a random variable takes any given value or belongs to a given set of values.
- A.1.42 probability density function:** The derivative (when it exists) of the distribution function:
- $$f(x) = dF(x)/dx. \quad (\text{A.4})$$
- A.1.1 probability mass function:** A function giving, for each value x_n of a discrete random variable X , the probability p_n that the random variable equals x_n :
- $$p_n = \mathbb{P}(X = x_n). \quad (\text{A.5})$$
- A.1.43 quantity, influence:** Quantity that is not the measurand but that affects the result of the measurement.
- A.1.44 quantity (Measurable):** Attribute of a phenomenon, body or substance that may be distinguished qualitatively and determined quantitatively.
- A.1.45 random variable:** A variable that may take any of the values of a specified set of values and with which is associated a probability distribution.
- A.1.46 random variable, centred:** A random variable the expectation of which equals zero.
- A.1.47 repeatability (of results of measurement):** Closeness of the agreement between the results of successive measurements of the same measurand carried out under the same conditions of measurement.

- A.1.48 reproducibility (of results of measurement):** Closeness of the agreement between the results of measurements of the same measurand carried out under changed conditions of measurement.
- A.1.49 result, corrected:** Result of a measurement after correction for systematic error.
- A.1.50 result, uncorrected:** Result of a measurement before correction for systematic error.
- A.1.51 true value (of a quantity):** Value consistent with the definition of a given particular quantity.
- A.1.52 true value 'conventional'(of a quantity):** Value attributed to a particular quantity and accepted, sometimes by convention, as having an uncertainty appropriate for a given purpose.
- A.1.53 trueness:** The closeness of agreement between the average of an infinite number of replicate measured quantity values and a reference quantity value.
- A.1.54 standard deviation:** The positive square root of the *variance* **A.1.61**.
- A.1.55 standard deviation (of a random variable or of a probability distribution):** the positive square root of the *variance* **A.1.61**
- A.1.56 standard deviation, experimental:** For a series of n measurements of the same measurand, the quantity $s(qk)$ characterizing the dispersion of the results.
- A.1.57 statistic:** The positive square root of the *variance* **A.1.61**.
- A.1.58 statistical coverage interval:** An interval for which it can be stated with a given level of confidence that it contains at least a specified proportion of the population.
- A.1.59 uncertainty (of measurement):** Parameter, associated with the result of a measurement, that characterizes the dispersion of the values that could reasonably be attributed to the measurand.
- A.1.60 value (of a quantity):** Magnitude of a particular quantity generally expressed as a unit of measurement multiplied by a number.
- A.1.61 variance:** A measure of dispersion, which is the sum of the squared deviations of observations from their average divided by one less than the number of observations.
- A.1.62 variance (of a random variable or of a probability distribution):** The expectation of the square of the *centred random variable* **A.1.46**.

A.2 Skewness and kurtosis

In Chapter 2 Fig. 2.3 trying to determine visually if the data is normal distributed can be misleading i.e., the observer effect (Chapter 1, Section 1.5). There is another way of determining if the data is normal distributed namely via ‘testing for normality.’ The first two tests that can be applied are those of higher order moments namely ‘skewness’ S and ‘kurtosis’ C . The sample skewness can be expressed with [185]:

$$S = \frac{\frac{1}{n} \sum_{n=1}^N (x_n - \bar{x})^3}{\left(\sqrt{\frac{1}{n-1} \sum_{n=1}^N (x_n - \bar{x})^2} \right)^3}. \quad (\text{A.6})$$

The equation shows that a minimum of three observations x is needed to be able to conclude. A positive number represents a right-skewed distribution and a negative number a left-skewed distribution. A rule of thumb [193] is that values between ± 0.5 or in other words close to zero are an indication of a ‘good’ normal distribution. Values between ± 1 are an indication of a ‘moderate’ normal distribution and larger than ± 1 of a ‘not’ normal distribution. The results are shown in Table A.1.

Kurtosis means ‘curved’ or ‘arched’ and is a measure of tailedness and tells if the top of the normal distribution is flat or has a peek. The kurtosis is a descriptor of the shape of the function like the skewness. The sample kurtosis can be calculated with [185]:

$$C = \frac{\frac{1}{n} \sum_{n=1}^N (x_n - \bar{x})^4}{\left(\frac{1}{n-1} \sum_{n=1}^N (x_n - \bar{x})^2 \right)^2} - 3. \quad (\text{A.7})$$

When the value is zero, the distribution is normal. It should be noted that the positive value could go to infinity. However, when the value is -3 the shape of the distribution is flat.

Table A.1: Skewness and Kurtosis expressed for 20 and 1000 observations of a S_{21} measurement with two identical standard gain horns, at a fixed position, at a frequency of 85 GHz, respectively.

| # | Observations | Skewness S ($-0.5 \dots 0.5$) | Kurtosis C ($-3 \dots 0$) |
|-----|--------------|--------------------------------------|----------------------------------|
| 2.7 | 20 | 0.2738 | 0.0267 |
| 2.8 | 1000 | 0.0585 | -0.2484 |

To conclude, kurtosis tells us something about the situation that the distribution is normal but does not influence the use of statistical tools. This is different from the value related to the skewness which tells us that the distribution is not normal.

A.3 Transformations for skewed data

After the probability distribution function of the data has been analyzed, the possibility exist to transform the skewed data [194] to normality. A useful tool is the ‘ladder of powers’ [195] $x' = x^\zeta$ where x' is the data transformed of x . In Table A.2 the different powers are summarized.

Table A.2: The ‘ladder of powers’ to transform different types of skewness to normality

| # | transformation | ζ | x' | Skewness S |
|---|-------------------|---------|--------------|--------------|
| | Cube | 3 | x^3 | Left |
| | Square | 2 | x^2 | Left |
| | Identity | 1 | x^1 | No transform |
| | Square root | 1/2 | $x^{1/2}$ | Left & Right |
| | Cube root | 1/3 | $x^{1/3}$ | Left & Right |
| | Logarithmic | 0 | $\log(x)$ | Right |
| | Reciprocal root | -1/2 | $-1/x^{1/2}$ | Right |
| | Reciprocal | -1 | $-1/x^1$ | Right |
| | Reciprocal square | -2 | $-1/x^2$ | Right |

If one of the powers is used to transform the data to normality then the same power should be used for other data related to the same research topic to secure a fair comparison. Although addressed here for sake of completeness it will not be used in this research.

A.4 Kernel density estimation

In Chapter 2, Fig. 2.3(a) to Fig. 2.3(c), the outcome illustrates that with minimum amount of observations or samples are far from normally distributed. Although the histogram shows the probability, it has round off errors due to the bin width. Closely related to the histogram is the kernel density estimation (KDE) [196], [197]. The shape of the KDE \hat{f}_h is estimated with [185]:

$$\hat{f}_{h_s}(x) = \frac{1}{N h_s} \sum_{n=1}^N K\left(\frac{x - x_n}{h_s}\right), \quad (\text{A.8})$$

where K is the kernel, a non-negative function that integrates to one, $h_s > 0$ is a smoothing parameter called the bandwidth. The smoothing parameter h_s is of main influence on the shape of the distribution function and should be chosen carefully. This is illustrated in Fig. A.1 based on 20 random variables from a data set obtained via a S_{21} measurement between two standard gain horn antennas, at a fixed position, at 85 GHz.

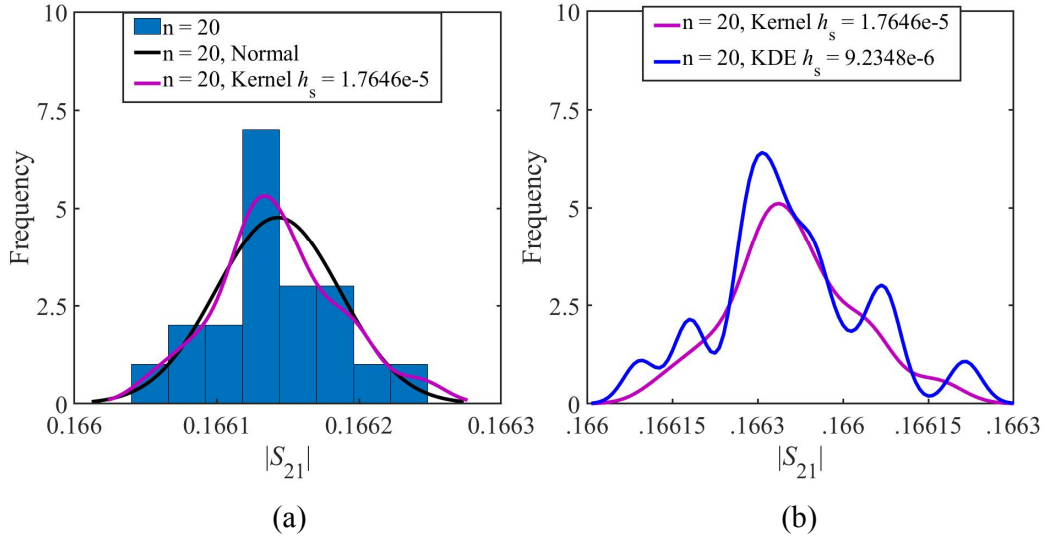


Figure A.1: The kernel density estimation on a data set of 20 observations (a) comparing the histogram with a normal distribution and a kernel and, (b) with a different smoothing factor h_s .

Finding the correct setting for h_s is a research topic on itself. Normally the mean integrated square error is used to determine h_s . However, because the real density function is unknown a variety of automated data-based methods has been developed to be able to select the correct h_s . A rule of thumb bandwidth estimator (A.1.23) that can be used for univariate data is expressed as follows [185]:

$$h = \left(\frac{4s^5}{3n}\right) = 1.06sn^{-\frac{1}{5}}, \quad (\text{A.9})$$

where s is the standard deviation of a sample. This formula becomes more accurate when the obtained data tends to a normal distribution. This is illustrated in Fig. A.1(b)

where there is a distinct difference between the calculated estimated bandwidth and the by Matlab estimated bandwidth. Because a full analysis of the different distribution function is out of scope of this thesis the software tool Matlab [185] is used to determine the h_s parameter. This means that for each fitting of an applied distribution these details are mentioned accordingly as shown in Fig. A.1. When data is presented in a histogram the KDE will be used to approximate the distribution function.

A.5 Coverage factor k_p with a certain level of confidence p for a limited amount of degrees of freedom v

Table A.3: Value of $t_p(v)$ from the t -distribution for degrees of freedom v that defines an interval $-t_p(v)$ to $+t_p(v)$ that encompasses the fraction p of the distribution [1]. For example, the coverage factor k_p for $v = 20$ with a confidence level $\mathbb{P} = 68.27\%$ is 1.03.

| Degrees of freedom v | Fraction \mathbb{P} in percent | | | | | |
|---------------------------|----------------------------------|-------------|-------------|-------------|-------------|-------------|
| | 68.27 | 90.00 | 95.00 | 95.45 | 99.00 | 99.73 |
| 1 | 1.84 | 6.31 | 12.71 | 13.97 | 63.66 | 235.80 |
| 2 | 1.32 | 2.92 | 4.30 | 4.53 | 9.92 | 19.21 |
| 3 | 1.20 | 2.35 | 3.18 | 3.31 | 5.84 | 9.22 |
| 4 | 1.14 | 2.13 | 2.78 | 2.87 | 4.60 | 6.62 |
| 5 | 1.11 | 2.02 | 2.57 | 2.65 | 4.03 | 5.51 |
| 6 | 1.09 | 1.94 | 2.45 | 2.52 | 3.71 | 4.90 |
| 7 | 1.08 | 1.89 | 2.36 | 2.43 | 3.50 | 4.53 |
| 8 | 1.07 | 1.86 | 2.31 | 2.37 | 3.36 | 4.28 |
| 9 | 1.06 | 1.83 | 2.26 | 2.32 | 3.25 | 4.09 |
| 10 | 1.05 | 1.81 | 2.23 | 2.28 | 3.17 | 3.96 |
| ... | ... | ... | ... | ... | ... | ... |
| <u>20</u> | <u>1.03</u> | <u>1.72</u> | <u>2.09</u> | <u>2.13</u> | <u>2.85</u> | <u>3.42</u> |
| ... | ... | ... | ... | ... | ... | ... |
| 30 | 1.02 | 1.70 | 2.04 | 2.09 | 2.75 | 3.27 |
| ... | ... | ... | ... | ... | ... | ... |
| 40 | 1.01 | 1.68 | 2.02 | 2.06 | 2.70 | 3.20 |
| ... | ... | ... | ... | ... | ... | ... |
| 50 | 1.01 | 1.68 | 2.01 | 2.05 | 2.68 | 3.16 |
| 100 | 1.005 | 1.660 | 1.984 | 2.025 | 2.626 | 3.077 |
| ∞ | 1.000 | 1.645 | 1.960 | 2.000 | 2.576 | 3.000 |

A.6 Bootstrap resampling

Bootstrapping is a statistical method for estimating the sampling distribution of an estimator of a limited amount of observations. For example, let a variable x of a particular antenna measurement (e.g. S_{21}) consist of 20 independent observation x_1, x_2, \dots, x_n than this can be expressed as a vector:

$$\vec{x} = (x_1, x_2, \dots, x_{20}) \quad (\text{A.10})$$

From this \vec{x} several measures $\hat{\Theta} = s(\vec{x})$ can be taken, like a mean, for instance. This is done by resampling with replacement. Next a bootstrap sample x^* is computed via sampling of original random variable x by replacement. This means that one random variable x could occur multiple times. As an example the x^{*1} based on \vec{x} consisting of 20 observations could be written as:

$$x^{*1} = (x_{11}, x_3, x_{19}, x_7, x_3) \quad (\text{A.11})$$

The x^{*1} is one bootstrap sample and from this we could compute $\hat{\Theta}^{*n} = s(\vec{x})$ bootstrap samples. After the data is collected from n bootstrap samples the mean of each sample can be plotted in a histogram. The effect of using different amount of random samples with x_n observations is shown in Fig. A.2. The observations are all from the same data set and are bootstrap re-sampled one million times.

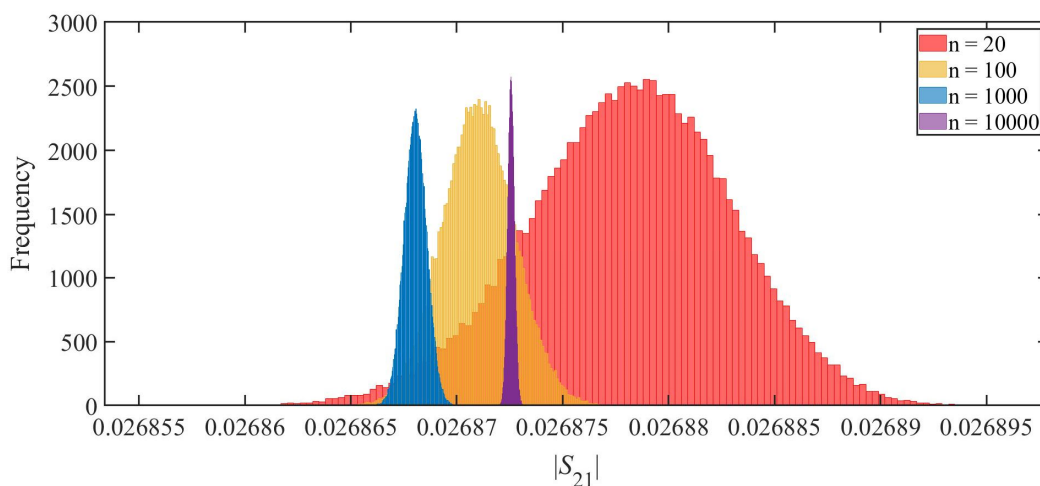


Figure A.2: Bootstrap resampling one million times for different amount of random samples from the same data set (observations) obtaining the mean which are plotted in a histogram.

The results show clearly that with more observations per bootstrap sampling x^* the variance becomes smaller. This is according the LoLN as is discussed in Subsection 2.3.2.

A.7 Antenna characteristics

In Table A.4 the various antenna characteristics are summarized divided in reflection or transmission measurements. For example, the impedance (#2.21) has unit Ω , range from 1 to ∞ .

Table A.4: Antenna characteristics derived from a complex reflection- and transmission-coefficient.

| # | <u>Reflected</u> Incidence | Symbol | Unit | range |
|------|-----------------------------------|----------|-----------------|------------------------|
| 2.9 | Voltage standing wave ratio | VSWR | V | 1 .. ∞ |
| 2.10 | S-Parameter | S_{11} | dB | ≤ 1 |
| | | S_{22} | dB | ≤ 1 |
| 2.11 | Refl. Coeff. <i>magnitude</i> | Γ | dB | 0 .. 1 |
| | | ρ_m | dB | 0 .. 1 |
| 2.12 | Impedance | $R + jX$ | Ω | 1 .. ∞ |
| 2.13 | Admittance | $G + jB$ | Ω | 1 .. 0 |
| 2.14 | Return loss | | dB | ≤ 1 |
| # | <u>Transmitted</u> Incidence | Unit | Symbol | range |
| 2.15 | Gain/loss | G | dB _i | $-\infty.. \infty$ |
| 2.16 | S-Parameter | S_{21} | dB | 0 .. 1 |
| | | S_{12} | dB | 0 .. 1 |
| 2.17 | Trans. Coeff. <i>magnitude</i> | T | dB | 0 .. 1 |
| | | τ_m | dB | 0 .. 1 |
| 2.18 | Insert. phase | Degree | $^\circ$ | $0^\circ .. 359^\circ$ |
| 2.19 | Group delay | τ_g | nS | 0 .. 2π |

B.1 Patch antenna dimensions

A common type of microstrip antenna is the patch antenna. Fig. B.1 shows three rectangular microstrip patch antennas each having a different kind of excitation namely the probe excitation, microstrip edge excitation and microstrip inset excitation, respectively [198]. Fig. B.1(a) shows that the microstrip patch antenna simply consists of two copper plates namely the ground plane and the patch where the latter is tuned in 2-dimensions such that it becomes resonant for a certain frequency. The location of the via i.e., the excitation of the patch is one of the parameters that determines the input impedance Z_{in} . The main disadvantage of this antenna for millimeter wave antennas is the via. The via will be larger than the patch for certain frequencies and can therefore not be used. The edge-fed microstrip antenna, shown in Fig. B.1(b) has no via which simplifies the design. It may be necessary to add an impedance transformer to match the impedance of the excitation Z_0 to the input impedance R_{in} of the patch antenna. This design can be feasible for millimeter wave antennas. However the impedance transformer has a limited bandwidth which can restrict the possible application. The inset-fed antenna shown in Fig. B.1(c) will be designed for this research.

The working of a microstrip patch antenna is illustrated in Fig. B.2. The radiation originates from the fringing E -fields at the edge of the patch, as shown in Fig. B.2(a). We assume that along the width W_p there is no variation of the E -field. As illustrated in Fig. B.2(b) the E -field varies along the length L_p of the patch, which length is about $\lambda/2$ for the fundamental mode TM_{10} [122]. The radiation may now be thought to originate from two slots, [see Fig. B.2(a) black dashed rectangles]. The two slots spaced $\lambda/2$ apart are excited in phase and radiate in the half space above the ground plane [122].

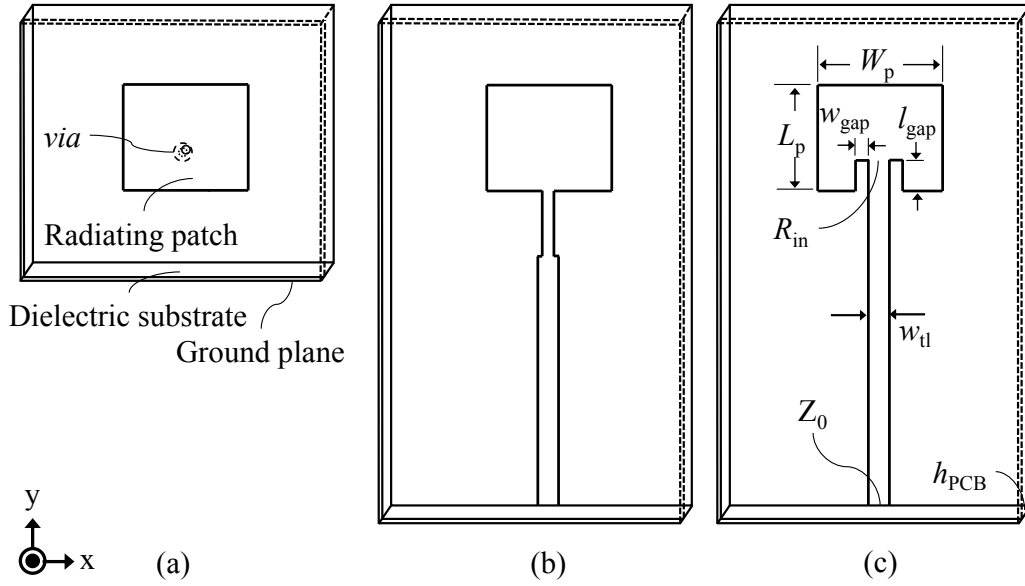


Figure B.1: A rectangular microstrip patch antenna (a) probe-fed, (b) edge-fed and (c) inset-fed.

Fig. B.2(c) illustrates that the voltage v_{ac} is zero in the middle and maximum at the edges of the patch with opposite polarity. The opposite accounts for the current i_{ac} which is maximum in the middle and at minimum at the edges of the patch. From the magnitude of both the v_{ac} and i_{ac} it can be concluded that impedance is zero in the middle and at maximum at the edge of the patch (Approximately 200Ω depending on the Q -factor of the patch) [199].

The patch antenna is relative easy to design with a 2-dimensional geometry where the length of the patch determines the center frequency f_0 . Due to the fringing fields the patch is electrically larger than its physical dimensions based on $\lambda/2$. The physical size of the patch mainly depends on the PCB thickness h_{PCB} and relative permittivity ϵ_r of the substrate. A good approximation of the patch length is the following equation [199]:

$$L_p = 0.49 \frac{\lambda_0}{\sqrt{\epsilon_r}}. \quad (\text{B.1})$$

The minimum dimensions of the ground plane are related to the decaying of the fringe fields and can be calculated with [199]:

$$L_{\text{ground}} = 6h_{PCB} + L_p \quad (\text{B.2})$$

$$W_{\text{ground}} = 6h_{PCB} + W_p \quad (\text{B.3})$$

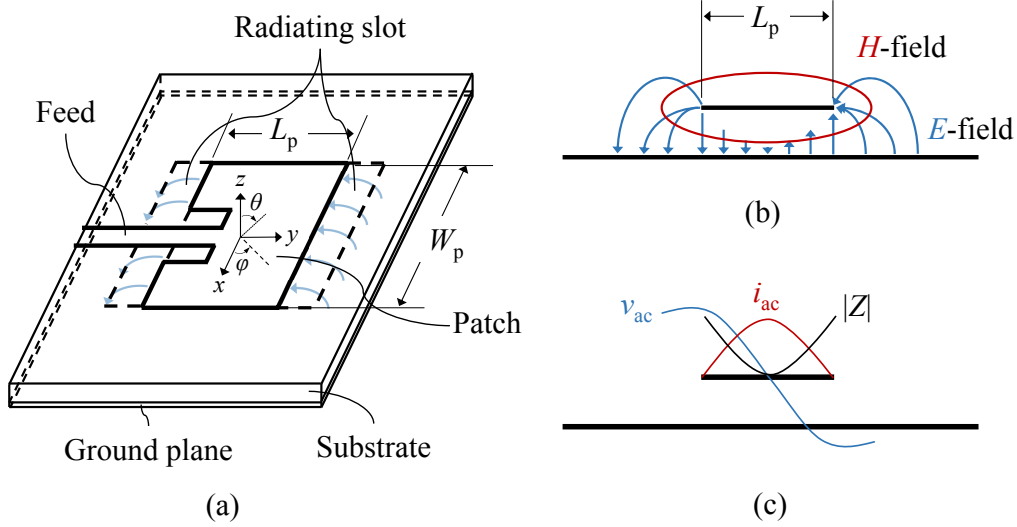


Figure B.2: A patch antenna illustrated in (a) perspective view with fringe fields (blue arcs), radiating slots (dashed lines) and coordinate system, in (b) side view with the E -field (blue arc lines) and H -field (red ellipse), and (c) side view with the current i_{ac} (red line), voltage v_{ac} (blue line) and impedance $|Z|$ (black line).

When the ‘measurable’ antenna is designed for frequencies larger than > 30 GHz then the antenna and its ground plane, determined with equation B.2 and equation B.3, will become very small (< 1 cm). For these so-called millimeter wave antennas it is an option to extend the ground plane to such a size that it easily fits into the measurement setup. This way, the larger ground plane could prevent interaction between the antenna and the close-by environment like an antenna carrier.

The width W_p of the rectangular inset-fed microstrip patch antenna is determined with [200]:

$$W_p = \frac{c_0}{2f_0} \sqrt{\frac{2}{\epsilon_r + 1}}, \quad (\text{B.4})$$

$$f_0 = \left(\frac{c_0}{(W_p / \sqrt{\frac{2}{\epsilon_r + 1}})} \right) / 2, \quad (\text{B.5})$$

where c_0 is the speed of light in vacuum and ϵ_r is the relative permittivity of the substrate. The effective permittivity can be calculated with [200]:

$$\epsilon_{\text{eff}} = \frac{\epsilon_r + 1}{2} + \frac{\epsilon_r - 1}{2} \left[1 + 12 \frac{h_{\text{PCB}}}{W_p} \right]^{-1/2}, \quad (\text{B.6})$$

where h_{PCB} is the thickness of the substrate. Due to fringing fields a length extension ΔL is introduced that is determined as [200]:

$$\frac{\Delta L}{h_{\text{PCB}}} = 0.412 \frac{\epsilon_{\text{eff}} + 0.3 \left(\frac{W_{\text{p}}}{h_{\text{PCB}}} + 0.264 \right)}{\epsilon_{\text{eff}} - 0.258 \left(\frac{W_{\text{p}}}{h_{\text{PCB}}} + 0.8 \right)}. \quad (\text{B.7})$$

The length L_{p} of the rectangular inset-fed microstrip patch antenna and the center frequency f_0 are determined with [200]:

$$L_{\text{p}} = \frac{c_0}{2f_0\sqrt{\epsilon_{\text{eff}}}} - 2\Delta L, \quad (\text{B.8})$$

$$f_0 = \left(\frac{c_0}{L_{\text{p}} + 2\Delta L} \right) / (2\sqrt{\epsilon_{\text{eff}}}). \quad (\text{B.9})$$

As shown in Fig. B.1(c) the antenna is fed with a microstripline inserted into the patch. This inset-fed consist of two dimensions namely the width of the gap w_{gap} between patch and microstrip line and the length of the gap l_{gap} . These parameters are used to achieve an impedance match where the following equations are used [200]:

$$w_{\text{gap}} = \frac{c_0}{\sqrt{2\epsilon_{\text{eff}}}} \frac{4.65 * 10^{-3}}{f_0}, \quad (\text{B.10})$$

$$Z_0 = R_{\text{in}} \cos^2 \left(\frac{\pi}{L_{\text{p}}} d \right), \quad (\text{B.11})$$

$$l_{\text{gap}} = \frac{L_{\text{p}}}{\pi} \cos^{-1} \left(\sqrt{\frac{Z_0}{R_{\text{in}}}} \right). \quad (\text{B.12})$$

Where Z_0 is the characteristic impedance of the microstrip line and R_{in} [see Fig. B.1(c)] the impedance on the radiating edge of the patch.

The microstripline is calculated with one of the following equations depending on the ratio of the width w_{tl} of the microstripline and the thickness h_{PCB} of the substrate:

$$Z_0 = \frac{60}{\sqrt{\epsilon_{\text{eff}}}} \ln \left[\frac{8h_{\text{PCB}}}{w_{\text{tl}}} + \frac{w_{\text{tl}}}{4h_{\text{PCB}}} \right] \quad \text{for} \quad \frac{w_{\text{tl}}}{h_{\text{PCB}}} \leq 1 \quad (\text{B.13})$$

$$Z_0 = \frac{120\pi}{\sqrt{\epsilon_{\text{eff}} \left[\frac{w_{\text{tl}}}{h_{\text{PCB}}} + 1.393 + 0.667 \ln \left(\frac{w_{\text{tl}}}{h_{\text{PCB}}} + 1.444 \right) \right]}} \quad \text{for} \quad \frac{w_{\text{tl}}}{h_{\text{PCB}}} > 1 \quad (\text{B.14})$$

B.2 Circular polarization

Published in [5]

In order to fully characterize a circularly polarized (CP) millimeter wave antenna, it is necessary to determine the polarization ellipse in the x -, y -plane and tilt angle (τ_r), as shown in Fig. B.3, [201]-[203]. Fig. B.3(a) illustrates an elliptically polarized wave propagating along the z -axis measured with help of a linearly polarized (LP) horn antenna. Such measurement does not yield the polarization ellipse (blue curve), but rather the polarization pattern (black peanut curve). From the polarization pattern, besides the axial ratio (AR) also the, tilt angle, the sense of orientation left- or right-hand circular polarization (LHCP or RHCP) and the gain pattern is derived.

Fig. B.3(b) illustrates the relation between the traveling electric-field $\mathbf{E}(z, t)$ (blue arrow) in the z -direction decomposed in an E_x and E_y component [see Fig. B.3(b)] and is which are expressed as [203]:

$$E_x = E_1 \sin(\omega t) \quad (\text{B.15})$$

$$E_y = E_2 \sin(\omega t + \delta) \quad (\text{B.16})$$

Here δ is the time-phased angle by which E_y leads E_x . The tip of the electric field \mathbf{E} describes the polarization ellipse, the variation measured with the LP antenna is given by the polarization pattern. For a given orientation OP [red line in Fig. B.3(b) of the LP antenna, the response is proportional to the largest ellipse dimension measured normally to OP. Fig. B.3(b) shows that this corresponds to length OP' [203]. The minimum and maximum of the polarization ellipse are not aligned with the x - and y -axis, as indicated by the angle τ_r resulting in the $x'y'$ -plane. The AR is now defined as the ratio between the major and minor axis of the polarization ellipse.

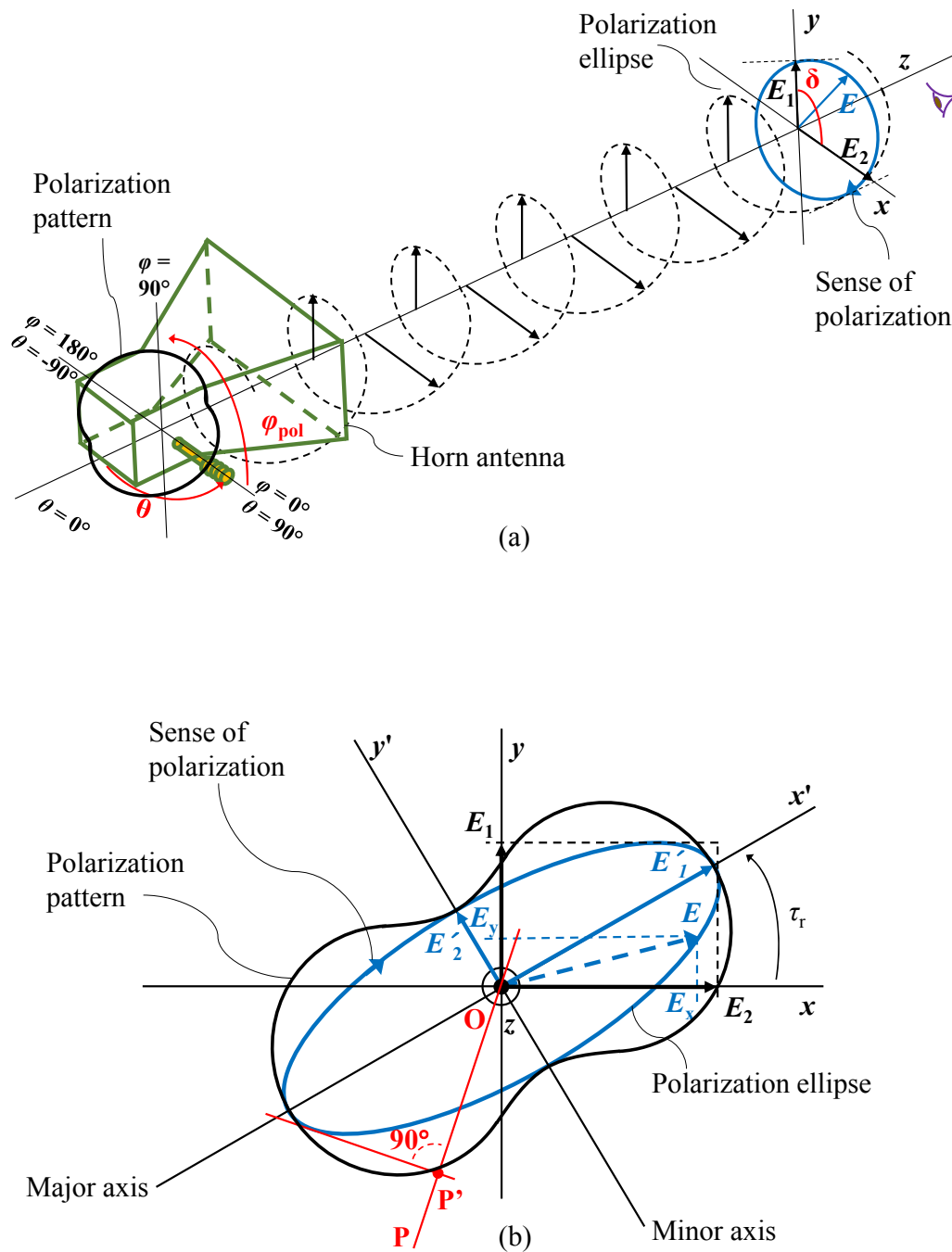


Figure B.3: Polarization pattern and polarization ellipse of an elliptically left-hand polarized antenna (a) perspective view and (b) top view (Drawings are adapted from [201]-[203]).

B.3 Circularly polarized rod antenna uncertainties

Published in [5]

Table B.1: Uncertainties caused by simulation settings, material and manufacturing tolerances [88], [89].

| # | Software settings | Definition | Effect on | Trueness ¹ (%) |
|------|---------------------------------|----------------------|------------------|---------------------------|
| 3.49 | Excitation | Waveguide port | Impedance | 84.3 |
| | | versus | Axial ratio | 99.3 |
| | | discrete port | Realized gain | 99.5 |
| 3.50 | Solver type | Time domain | Impedance | 84.3 |
| | | Solver T = 7h | Axial ratio | 99.3 |
| | | | Realized gain | 99.3 |
| | | | Frequency domain | Impedance |
| | | Solver T = 240h | Axial ratio | 95.8 |
| | | | Realized gain | 99.3 |
| 3.51 | Model complexity | No of mesh cells | Accuracy vs time | |
| # | Material properties | Tolerance (mm) | Effect on | Trueness (%) |
| 3.52 | Permittivity (LCP) | 3.16 ± 0.05 | Impedance | 82.9 |
| | | | Axial ratio | 95.3 |
| | | | Realized gain | 97.7 |
| 3.53 | Loss tangent (LCP) | 0.004 ± 0.0005 | Impedance | 84.3 |
| | | | Axial ratio | 98.4 |
| | | | Realized gain | 98.6 |
| 3.54 | Permittivity (Teflon) | 2.06 ± 0.05 | Impedance | NA |
| | | | Axial ratio | NA |
| | | | Realized gain | NA |
| 3.55 | Loss tangent (Teflon) | 0.00022 ± 0.0001 | Impedance | NA |
| | | | Axial ratio | NA |
| | | | Realized gain | NA |
| # | Manufacturing tol. | Tolerance (mm) | Effect on | Trueness (%) |
| 3.56 | Substrate thickness (LCP) | 0.1 ± 0.010 | Impedance | 81.7 |
| | | | Axial ratio | 96.3 |
| | | | Realized gain | 95.1 |
| 3.57 | Track width | 0.25 ± 0.025 | Impedance | 84.3 |
| | | | Axial ratio | 79.5 |
| 3.58 | Antenna dim. | 1.15 ± 0.115 | Realized gain | 78.3 |
| 3.59 | Layer registration | 33 ± 0.16 | Impedance | 20.1 |
| | | | Axial ratio | 63.5 |
| | | | Realized gain | 65.8 |

B.4 Misalignment in the layer registration of the PCB

Published in [5]

As discussed in Chapter 3, Subsection 3.6.3, the misalignment of the PCB layers causes the largest error affecting the AR and realized gain pattern of the AUT. To inspect the realized PCB, an x-ray photograph has been taken, as shown in Fig. B.4.

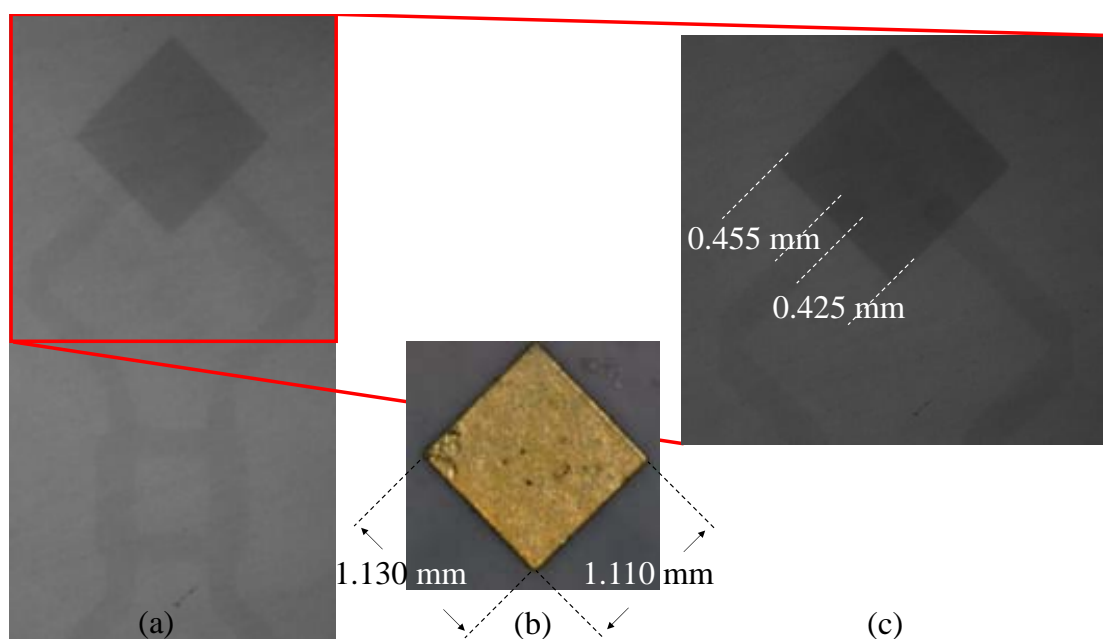


Figure B.4: X-ray photograph of (a) the circularly polarized rod antenna visualizing layer 1 and layer 2 and (b) the actual patch with measured size and (c) showing the misalignment of the feeding network with respect to the patch [137].

The dimensions of the realized patch antenna showed a deviation of $\approx 4.0\%$ compared to the simulated patch (1.15 mm). The layer registration showed an alignment error of $\pm 0.25\%$. This resulted in a positional error of the transmission line of $\approx 3.5\%$. These deviations are many times smaller than simulated [see Chapter , Fig. 3.17(a) and Fig. 3.17(b)], thus falling within specified tolerances.

¹The reference for the various antenna characteristics defining the trueness is taken from the design requirements i.e., the true values (see Table 3.7).

B.5 Polarization pattern methods

Published in [5]

Table B.2 summarizes known polarization pattern methods used to measure the performance of CP antennas [201]. The symbol ‘V’ marks which antenna characteristic is obtained with the specific polarization pattern method and ‘X’ which not. The MAPCM, which has been added as a new method, is preferred over PAM, since PAM requires a very expensive dual-polarized reference antenna that can only be used for characterizing CP antennas. Therefore, a measurement with only a LP antenna is preferred; hence the introduction of the MAPCM.

Table B.2: Measurement methods to determine circularly polarized antenna polarization characteristics.

| # | Measurement method | Acronym | Axial ratio | Tilt angle | Sense of Orientation | Radiation Pattern |
|-----|------------------------------------|---------|-------------|------------|----------------------|-------------------|
| 7.1 | Polarization Pattern | PPM | V | V | X | X |
| 7.2 | Rotating Source | RSM | V | X | X | X |
| 7.3 | Multiple Amplitude Component | MACM | V | V | V | X |
| 7.4 | Phase Amplitude | PAM | V | V | V | V |
| 7.5 | Multiple Phase Amplitude Component | MAPCM | V | V | V | X |
| | | | V | V | V | V |

A **Polarization pattern method (PPM)**. Fig. B.3a shows how a linearly polarized horn antenna is used to measure $\mathbf{E}(z, t)$. When the horn antenna is rotated around the z -axis (φ_{pol}), as illustrated in Fig. B.3(a), the polarization pattern is obtained. As an illustrative example, the polarization pattern is plotted in Fig. B.5. From this graph it is easy to determine the AR and tilt angle τ_r .

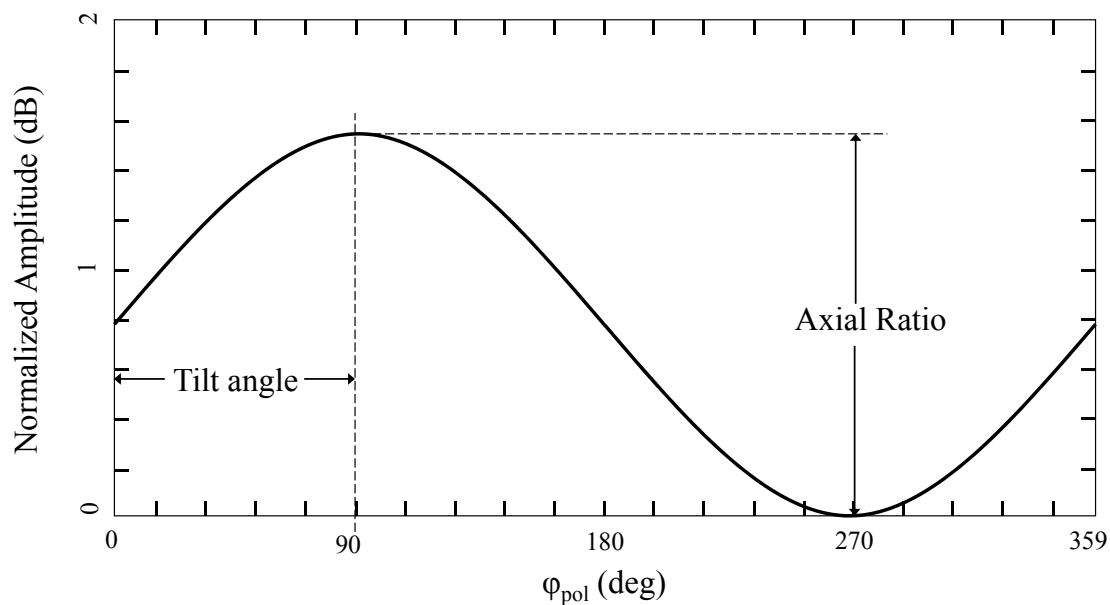


Figure B.5: Illustration of the normalized amplitude of the polarization pattern depicting the axial ratio and tilt angle τ_r .

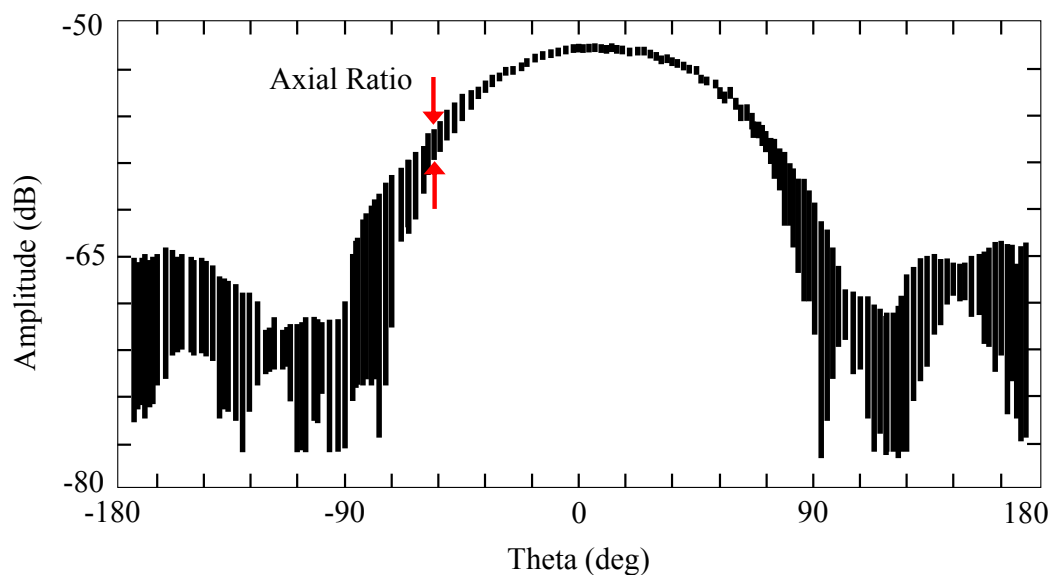


Figure B.6: Illustration of the pattern obtained with the rotating source method with the axial ratio from the envelope boundaries for each θ -angle.

B Rotating source method (RSM). The RSM determines that the measurement is executed with a fast and constant movement of the φ_{pol} rotation of the LP

antenna and a slow and constant movement of the θ -angle [see Fig. B.3(a)]. As shown in Fig. B.6, the advantage of the RSM is that the AR is directly obtained by looking at the envelope, depicted with the red arrows in Fig. B.6, for each θ -angle, without the need of any post processing.

C Multiple amplitude component method (MACM). This method describes a sequence of measurements obtaining the electric field \mathbf{E} . This is done with help of a LP antenna which polarization pattern is illustrated with circles for the $\varphi_{\text{pol}} = 0^\circ$ (E_1) in Fig. B.7(a), $\varphi_{\text{pol}} = 45^\circ$ (E_3) in Fig. B.7(b), $\varphi_{\text{pol}} = 90^\circ$ (E_2) in Fig. B.7(c) and $\varphi_{\text{pol}} = 135^\circ$ (E_4) in Fig. B.7(d). At those four angles the measured response with the LP antenna is proportional to the largest ellipse dimension OP' [203].

It is normally not known whether the maximum of the ellipse is aligned with the co-polarization of the LP. Therefore, it is necessary to determine the tilt angle τ_r . For that we need to determine the δ between E_x and E_y (See Fig. B.3). With help of the four measurements illustrated in Fig. B.7 τ_r is derived following [203]:

$$|E_3|^2 = \frac{1}{2} \left(|E_1|^2 + |E_2|^2 + 2 |E_1| |E_2| \cos\delta \right), \quad (\text{B.17})$$

$$|E_4|^2 = \frac{1}{2} \left(|E_1|^2 + |E_2|^2 - 2 |E_1| |E_2| \cos\delta \right). \quad (\text{B.18})$$

By combining (B.17) and (B.18) δ is determined from [203]:

$$\delta = \cos^{-1} \left(\frac{|E_3|^2 - |E_4|^2}{2 |E_1| |E_2|} \right). \quad (\text{B.19})$$

The corresponding τ_r (see Fig. B.3) is now given by [203]:

$$\tau_r = \frac{1}{2} \tan^{-1} \left(\frac{|E_3|^2 - |E_4|^2}{|E_1|^2 - |E_2|^2} \right). \quad (\text{B.20})$$

The AR is now found by [203]:

$$AR = \sqrt{\frac{|E_1|^2 \cos^2 \tau_r + \frac{1}{2} \left(|E_3|^2 - |E_4|^2 \right) \sin 2\tau_r + |E_2|^2 \sin^2 \tau_r}{|E_1|^2 \sin^2 \tau_r + \frac{1}{2} \left(|E_3|^2 - |E_4|^2 \right) \sin 2\tau_r + |E_2|^2 \cos^2 \tau_r}} \quad (\text{B.21})$$

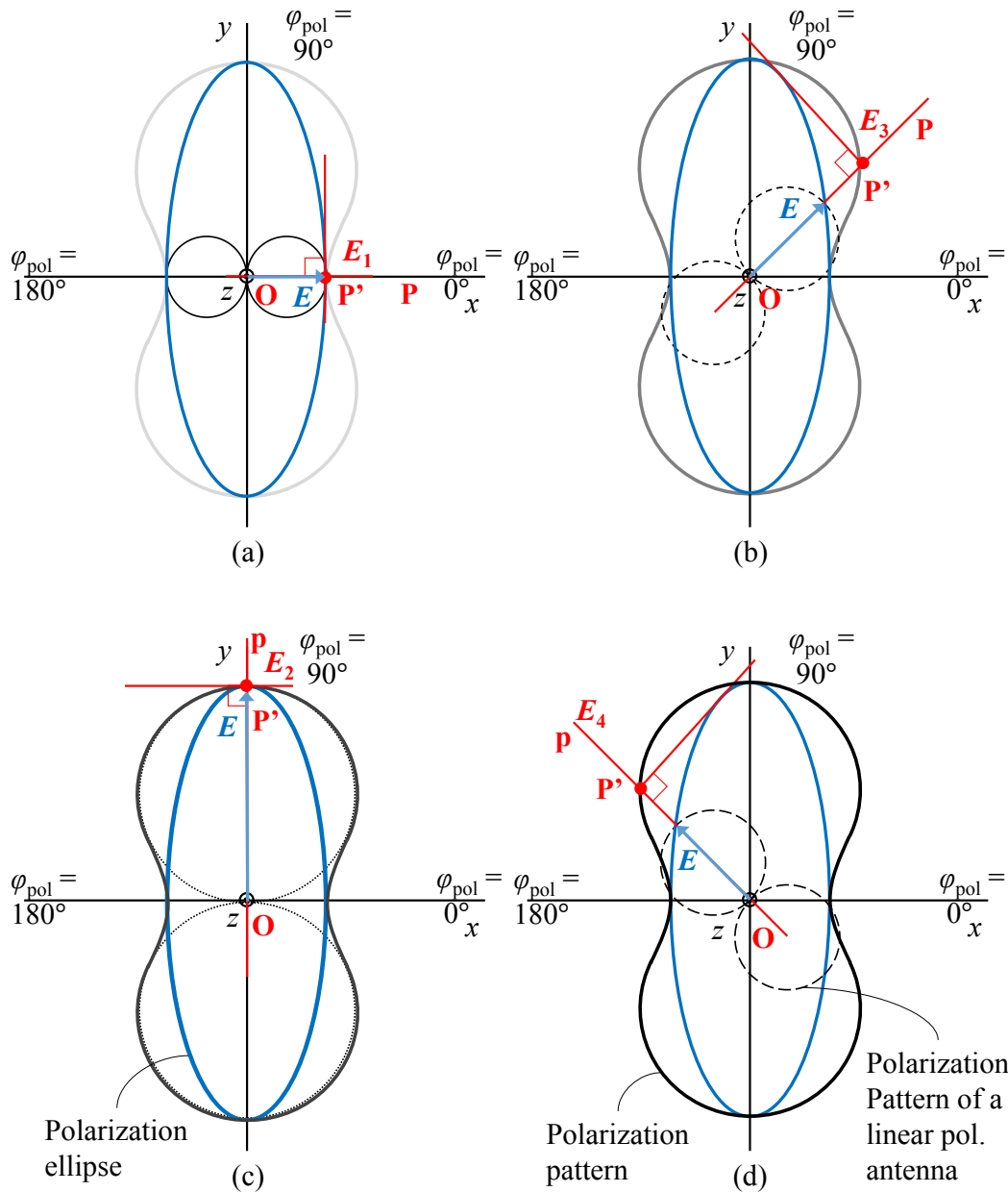


Figure B.7: Both the polarization ellipse of the CP (blue curve) and LP antenna is shown in (a) at $\varphi_{pol} = 0^\circ$ (solid line), (b) $\varphi_{pol} = 45^\circ$ (dashed line), (c) $\varphi_{pol} = 90^\circ$ (dotted line) and (d) $\varphi_{pol} = 135^\circ$ (gray dotted line). Variation measured with the LP antenna results in the polarization pattern (Black peanut curve). For multiple different orientations (red lines) measured with the LP antenna, the response is proportional to the greatest ellipse dimension measured normally to OP [15].

The main difference between this method compared to the PPM and RSM is that

it requires post processing. The advantage of this method is that the data set contains most of the information to retrieve the desired antenna characteristics (see also Table B.2). A disadvantage is that this method is based on retrieving absolute values from which it is not possible to determine the sense of orientation.

D Phase amplitude method (PAM). According to [12], a dual-polarized antenna is used to obtain the phase and magnitude of the orthogonal electric-field \mathbf{E}_1 and \mathbf{E}_2 (see Fig. B.2 and Fig. B.7) at the same time. With this method it is possible to derive all antenna parameters including the sense of orientation. However, this method is less desirable because the dual polarized reference antenna is expensive and only usable for characterizing CP antennas.

E Multiple amplitude phase component method measured with linearly polarized antenna (MAPCM). To avoid the use of a well-defined dual-polarized reference antenna, we can also measure at the angles $\varphi_{\text{pol}} = 0^\circ$ (\mathbf{E}_1) and $\varphi_{\text{pol}} = 90^\circ$ (\mathbf{E}_2) [see Fig. B.2(a)] sequentially. With a VNA it is possible to obtain complex values with which it is possible to calculate the sense of orientation with [203]:

$$E_{\text{LHCP}} = \frac{(\Re\{E_1\} + \Im\{E_2\}) + j(\Im\{E_1\} - \Re\{E_2\})}{\sqrt{2}} \quad (\text{B.22})$$

$$E_{\text{RHCP}} = \frac{(\Re\{E_1\} - \Im\{E_2\}) + j(\Im\{E_1\} + \Re\{E_2\})}{\sqrt{2}} \quad (\text{B.23})$$

From the sense of orientation B.22 and B.23 the AR can be derived as follows [203]:

$$\text{AR}_{\text{dB}} = 20 \log_{10} \left| \frac{E_{\text{RHCP}} + E_{\text{LHCP}}}{E_{\text{RHCP}} - E_{\text{LHCP}}} \right| \quad (\text{B.24})$$

This MAPCM is considered to be a merger of the MACM and PAM. It should be noted that the MAPCM could be sensitive for phase errors caused by the movement of the experimental setup.

B.6 Measurement results of the circularly polarized rod antenna

Published in [5]

The measurement system, shown in Fig. B.8(a) (illustration) and Fig. B.8(b) (realized model) is an in-house-developed, compact, movable mm-wave anechoic chamber. The

enclosure is covered with electromagnetic absorbers [see Figure B.8(b)] to avoid reflections from the environment. An accelerometer is mounted on the scan arm and is used as a mechanical reference to align the scan arm perpendicular to the rotation table [see Figure B.8(a)]. For the measurements discussed in this article, a connector is used, and therefore the probe station is not further described.

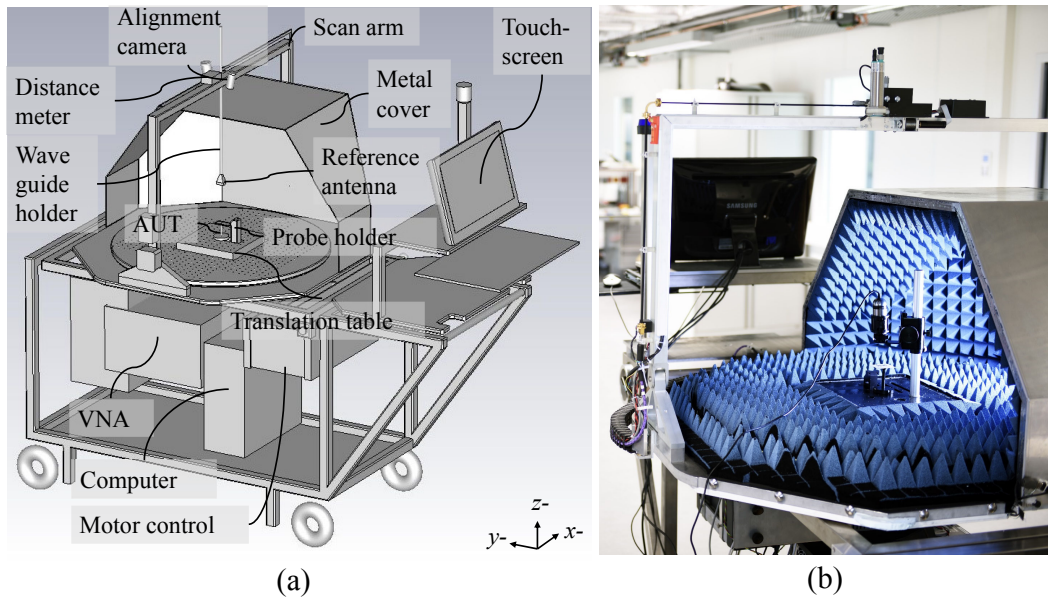
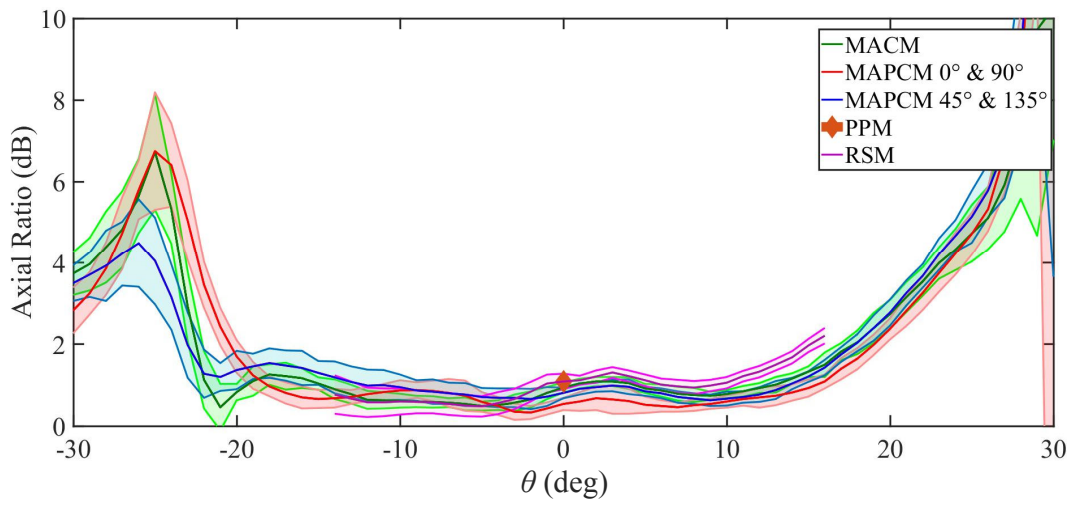
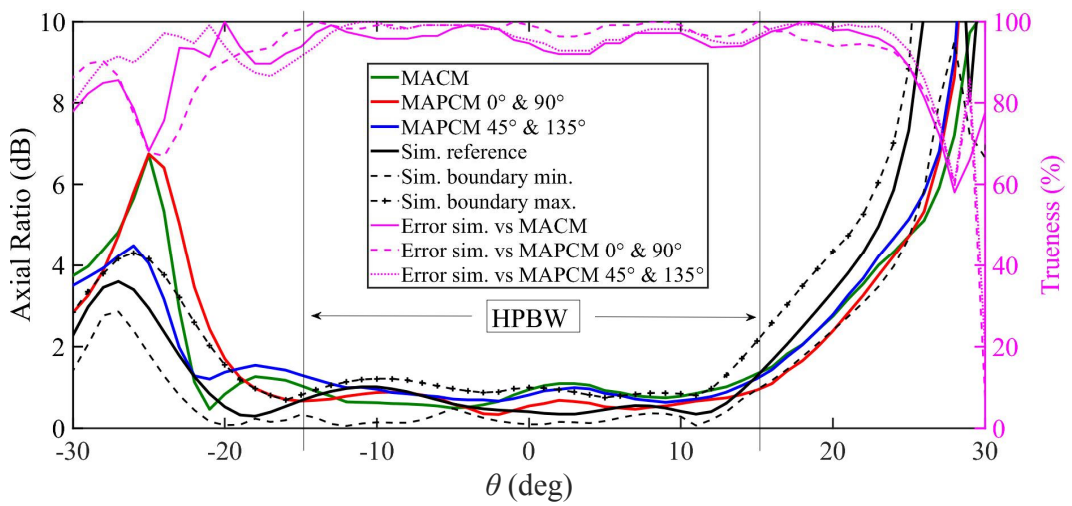


Figure B.8: (a) An illustration of the mm-wave anechoic chamber and (b) a photograph of the realized second generation (2011) millimeter wave anechoic chamber (half open for illustration purposes).

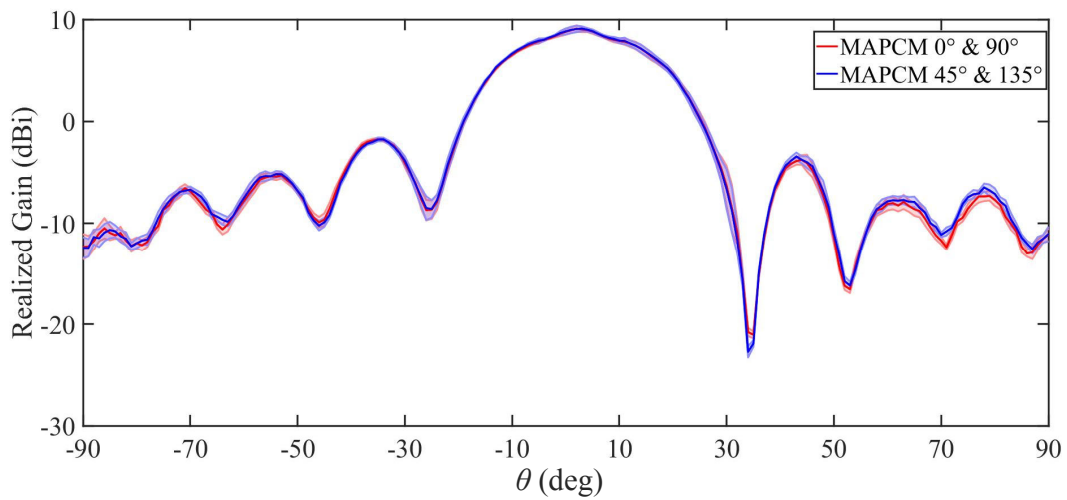
The gain and polarization loss are determined as described in [36]-[38]. A transmission measurement between two identical reference antennas is performed, obtaining the S_{21} scattering coefficient. After the S_{21} measurement, one of the reference antennas is replaced with the AUT. The S_{21} measurement is repeated and the obtained value is compared to the gain of the reference antenna derived from the datasheet. The uncertainty of the misalignment between reference antenna and AUT related to the phase center is calculated to be 0.25 dB. The results for the precision of AR and realized gain pattern are shown in Fig. B.9(a) and Fig. B.9(c). The corresponding trueness is shown in Fig. B.9(b) and Fig. B.9(d).



(a)



(b)



(c)

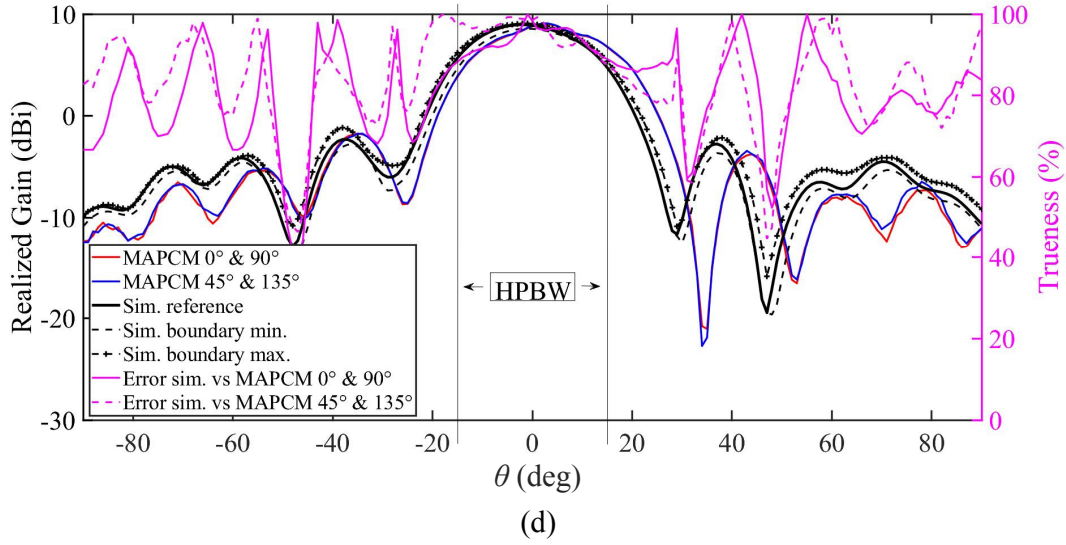


Figure B.9: Accuracy versus θ at 61 GHz. (a) Precision for 1s is indicated with the transparent colored band around the mean and, (b) trueness with the axis on the right side in percentage of the measured AR. (c) Precision and, (d) trueness of the realized gain pattern.

In Fig. B.9(a) and Fig. B.9(c), the standard deviation is indicated by the transparent colored area. It is observed that the repeatability of the measurements is less than 0.1 dB for both AR and realized gain. In Fig. B.9(b) and Fig. B.9(d) the trueness is expressed in percentage of the reference, the reference being the simulation results for the AR in Fig. B.9(b) and realized gain in Fig. B.9(d). The trueness is more than 90% for the AR and more than 85% for the realized gain within the HPBW (see right side of the graph). With an increasing angle, larger than the HPBW, the trueness decreases with more than 20%. The deviation observed in Fig. B.9(d), especially for θ -angles larger than 30° , is caused by the load attached to port 2. The AR obtained by measuring the $\varphi_{\text{pol}} = 0^\circ$ (E_1) and $\varphi_{\text{pol}} = 90^\circ$ (E_2) is different compared to the AR obtained by measuring $\varphi_{\text{pol}} = 45^\circ$ (E_3) and $\varphi_{\text{pol}} = 135^\circ$ (E_4). These differences, as can be observed in Fig. ??, are caused by interference, related to the orientation of the connectors [see Chapter 3, Fig. 3.16(d)].

B.7 Effect of the waveguide port on the realized gain pattern

The effect of the waveguide port, with different sizes (see Fig. B.10), has on the gain patterns is illustrated in Fig. B.11. As can be observed in Fig. B.11(a) the reflection

coefficient is not that much affected. At $f_0 = 85$ GHz in all cases the level is below -10 dB. However, the realized gain pattern all the more where the effect is depending on the solver domain. Fig. B.11(b) shows that the FD causes both blockage and reflection depending on the size of the port. This effect of the different port sizes is illustrated by the ripple and dips at $\theta = 70^\circ$.

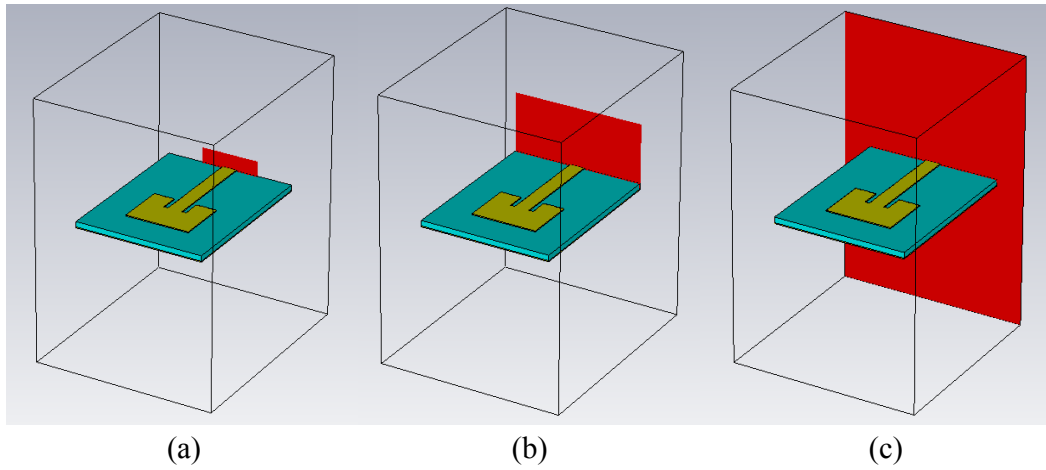


Figure B.10: A rectangular inset-fed microstrip patch antenna (a) waveguide port size k , (b) waveguide port size PCB edge, and (c) waveguide port size boundary box.

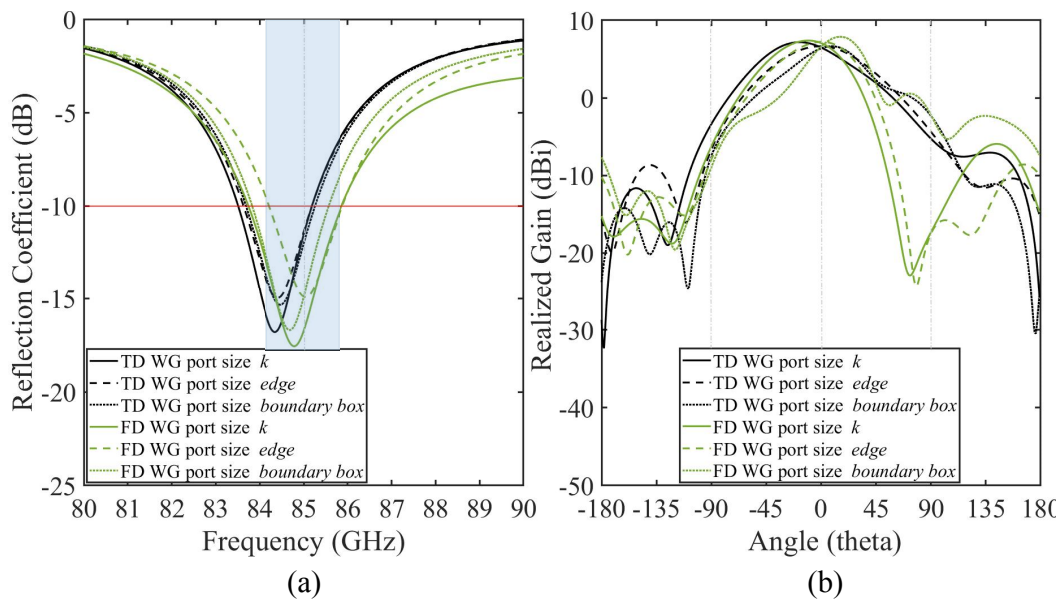


Figure B.11: (a) Reflection coefficient (dB) for various port sizes and solver domain types, and (b) the realized gain (dBi) E -plane with $f_0 = 85$ GHz.

C.1 Surface waves

Surface waves (#4.1) [102] propagate between two media from which one medium has a permittivity larger than one. As illustrated in Fig. C.1 the surface wave is launched into the substrate at an elevation angle θ between $\pi/2$ and $\sin^{-1}(1/\sqrt{\epsilon_r})$. The waves are propagating through the substrate and experiences reflection from the ground plane and the dielectric-air interface. As a rule of thumb surface waves decay as $1/\sqrt{l_{\text{PCB}}}$ thus coupling also decreases away from the point of excitation [204]. In case of the rectangular microstrip patch antenna designed for this research (see Chapter 3, Section 3.5) the length between antenna and interconnection is approximately 15 mm. Traveling this distance the surface wave has attenuated with 13 dB. From the antenna to the edge of the PCB is approximately 5 mm the surface wave will be attenuated with 7 dB.

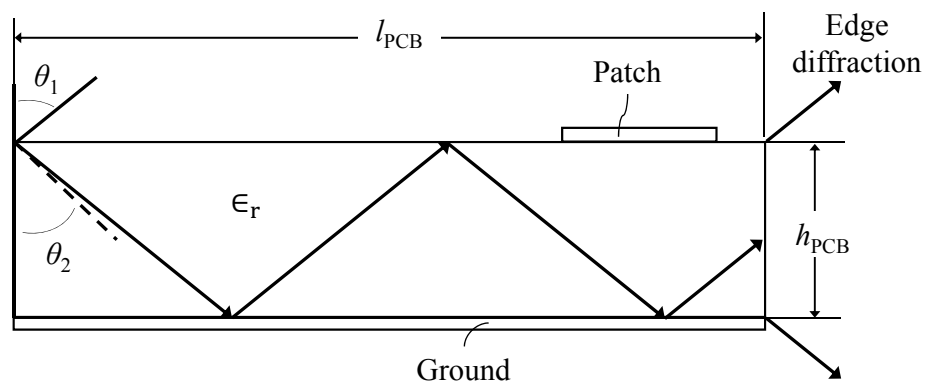


Figure C.1: Illustration of the propagation of a surface wave leading to coupling between elements and diffraction at the edges [204]. Here $\theta_2 = \arcsin(1/\sqrt{\epsilon_r})$

D.1 Dielectric material properties and characteristics

The relative permittivity and loss of a dielectric material are frequency dependent. This can be observed in the dielectric permittivity spectrum [205] as shown in Fig. *D.1*. Zooming in on the millimeter wave frequency range (30 GHz to 300 GHz, dashed area in Fig. *D.1*) both the ϵ' red line and the ϵ'' blue line are decreasing in this frequency range. In this frequency range the electromagnetic wave causes dipolar polarization of the molecules in the dielectric material [see Fig. *D.1(b)*]¹.

The dielectric material composition can be defined as homogeneous and / or isotropic (see Fig. *D.2*). Where [205]:

- **Homogeneous** means that the material properties are equal at each location, and
- **isotropic** means that the material properties are equal in all directions.
- **Linearity** means that materials in which the dielectric polarization is linearly related to the electric field².

Because no material is perfectly homogeneous and/or isotropic, this can be seen as an uncertainty. This means that the value of the relative permittivity and loss tangent obtained via measurement from a dielectric material will vary depending on the location of the area measured. Even more, with most of the material characterizing techniques a certain area is measured at the same time meaning that the relative permittivity

¹It should be noted that the polarization shifts from dipolar to atomic already at a 100 GHz. This phenomena is not further investigated during this research.

²The dielectric constant is not dependent on the electric field.

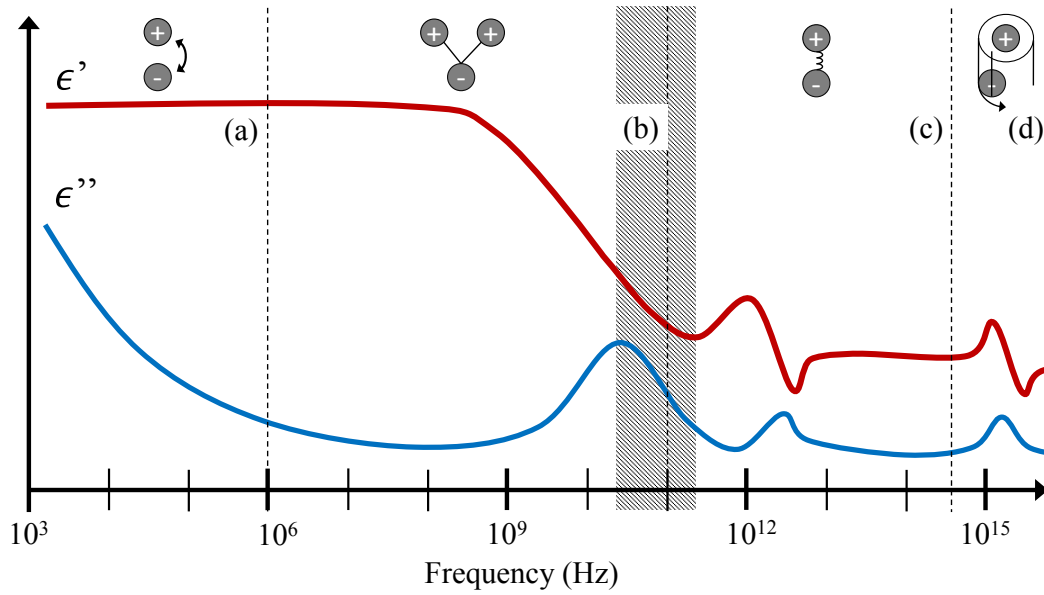


Figure D.1: Trend lines of a dielectric permittivity spectrum with ϵ' indicated by the red line and ϵ'' indicated by the blue line. The dashed area indicates the millimeter wave range. Various polarization mechanisms per frequency range (a) ionic (Maxwell-Wagner), (b) dipolar, (c) atomic, and (d) electronic [206].

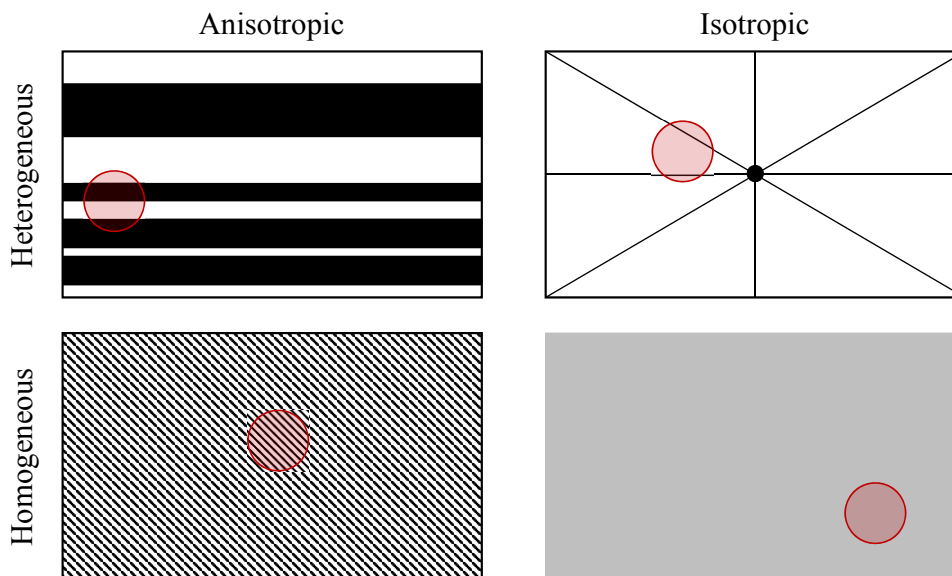


Figure D.2: Illustration of the meaning of homogeneous, heterogeneous, isotropic and an-isotropic. The red circle is an example of an observation area or a measurement area where the material is characterized.

and loss tangent is an average over that area. So, the value of the derived relative

permittivity and loss tangent also depends on the area size.

The dielectric materials can be tested if they are both homogeneous and/or isotropic. The homogeneity is determined by measuring the material on different locations. The isotropy of the material is determined by rotating the dielectric material (different direction).

According to [205], PTFE meets the requirements as discussed earlier in this section and is referred to in [207] - [208] for instance, as reference material. PTFE will be used during this research.

D.2 Optimization of a coupling aperture or iris

According to [181] the diameter of the iris is experimentally determined. What is important are the coupling of the electromagnetic-field from the waveguide to the cavity through the iris, also known as the coupling factor, and the degradation of the Q -factor. Optimization is paramount because these two parameters contradict each other.

In [181] it is concluded that changing the diameter of the iris within a certain range has little influence on the different unwanted modes. According to [181] is the TEM_{10q} , where q is the axial mode, hardly visible with a diameter of the iris of $\sim 80\%$ and $\sim 64\%$ compared to the height of the waveguide³. In the case of the setup as presented in this chapter, the iris has a diameter of 100% with respect to the height of the waveguide (see Table 5.2). The reason that the 100% diameter of the iris is chosen is to see the effect if several modes were to propagate in the cavity. This is not the case at the near-concentric distance (see Fig. D.5).

D.3 Relationship between the size of the mirror and the size of the Gaussian beam

A Gaussian beam as shown in Fig. D.3 is formed between the two spherical mirrors as shown in Fig. D.4. As for the Gaussian beam, there are two beam waists that are of interest. This is the beam waist in the middle of the two mirrors $2w_0$ and the beam waist on the mirror surface $2B_m$, [see Fig. D.3 and Fig. 5.5(a)]. The size of the beam waist on the mirror determines the size of the mirror. Using (5.7) and (5.8) the beam waist for the different focus distances has been calculated and illustrated in Fig. 5.6. When the mirrors are at the largest focus distance e.g., the concentric distance, the beam waist on the mirror $2B_m$ is largest.

³The height of the waveguide (WR 90) used in the setup that for this research is $h = 10.16$ mm and the width $w = 22.86$ mm [see Fig. 5.5(c)].

A beam with a radius B_m centered on the aperture of a spherical mirror, the power P passing through a circle with mirror radius r_m in the transverse plane at position z (see Fig. D.3) is [171]:

$$P(r_m, z) = P_0 \left[1 - e^{-2r_m^2/B_m^2(z)} \right], \quad (\text{D.1})$$

where P_0 is the total power of the beam. For a spherical mirror with radius $r_m = B_m$, the fraction of power transmitted through a circle is [171]:

$$\frac{P(z)}{P_0} = (1 - e^{-2}) 100\% \approx 86.5\%. \quad (\text{D.2})$$

Similarly, about 90% of the beam's power will flow through a circle with a mirror radius $r_m = 1.07B_m$, 95% through the mirror radius $r_m = 1.224B_m$, and 99% through a circle with mirror radius $r_m = 1.52B_m$.

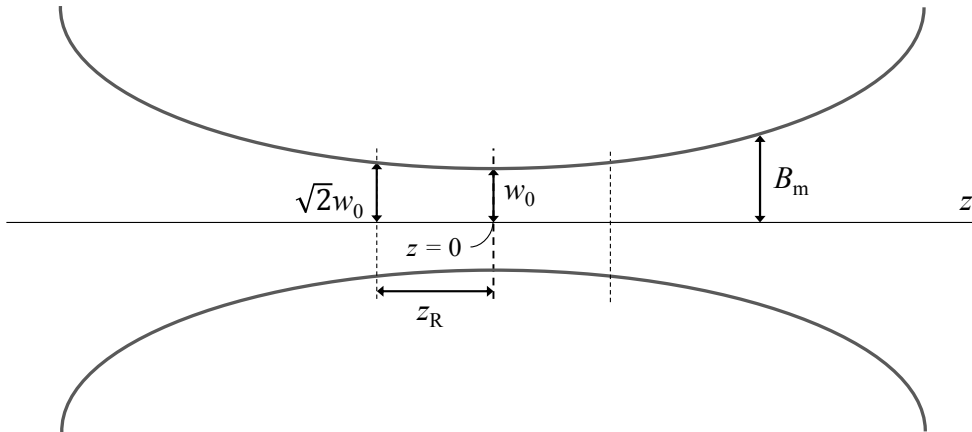


Figure D.3: Gaussian beam width $B_m(z)$ as a function of the distance z along the beam, which forms a hyperbola, w_0 is the beam waist and z_R : Rayleigh range.

D.3.1 Simulation settings of the Fabry-Perot open-cavity resonator

In [209] a full-wave modeling of various types of Fabry-Perot resonators in the millimeter range are described. This simulation model includes a dielectric material. It mentions that the solver time is ~ 1.5 hour. The Fabry-Perot open-cavity resonator designed for this research is simulated with help of [210] where the settings of the software are mentioned in Table D.1.

Table D.1: Simulation settings of the Fabry-Perot open-cavity resonator [210].

| # | Parameter | Value |
|------|----------------------------|---------------|
| 5.93 | Solver | Time-domain |
| 5.94 | Mesh cells per wavelength | 10 |
| 5.95 | Total amount of mesh cells | 20696067 |
| 5.96 | N_x, N_y, N_z | 208, 484, 208 |
| 5.97 | Amount of pulses | 100 |
| 5.98 | Simulation time | 34 : 29 : 51 |

D.3.2 Simulation results of the Fabry-Perot open-cavity resonator

The design and simulated results for the E -field in dB(V/m) of the Fabry-Perot open-cavity resonator are shown in Fig. D.4(a) and in perspective in Fig. D.4(b) with a contour plot. A 3D view consisting of arrows of the E -field is shown in Fig. D.4(c). Clearly visible is the Gaussian shape where the beam waist w_0 , the beam waist on the mirror B_m and, the mirror size r_m are indicated. It shows that most of the energy is falling on the mirror where a small part of the field is diffracted on the edges of the mirror and a part is caused by spill-over escaping the cavity. According to (D.2) the ratio between r_m and B_m which is ~ 1.44 then $\sim 98\%$ of the power falls on the mirror and stays within the cavity.

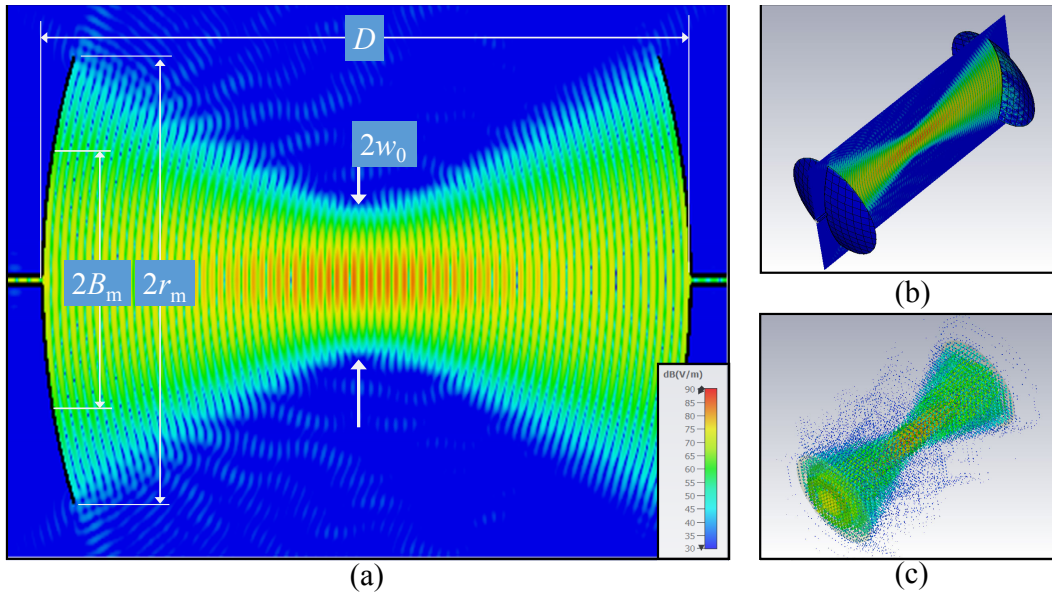


Figure D.4: Simulation result of a spherical mirror setup at concentric distance D at 66.528 GHz. The E -field in dBV/m (a) contour plot, (b) perspective view and, (c) perspective view in 3D illustrated with arrows.

Fig. D.5 shows the simulated and measured resonance spectrum of the Fabry-Perot open-cavity resonator.

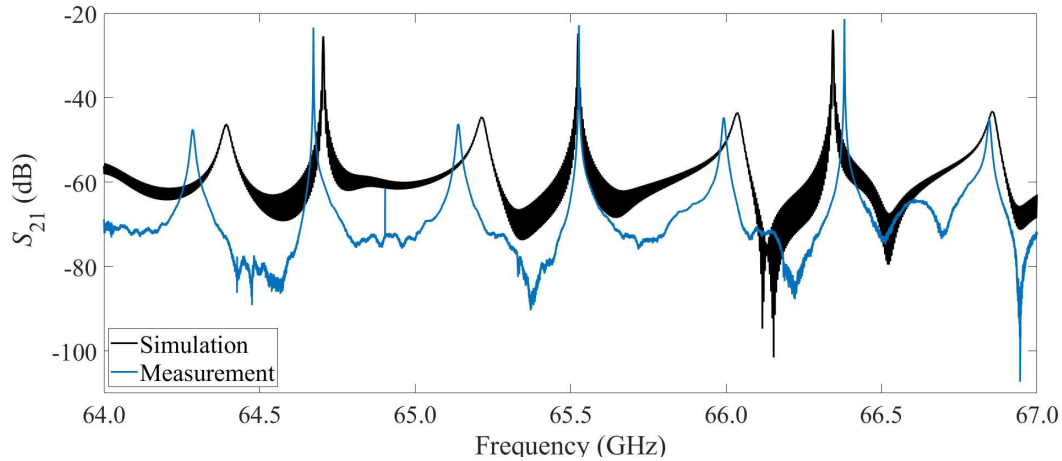


Figure D.5: Simulation and measurement results of the Fabry-Perot open-cavity resonator at concentric distance.

The small deviation in resonance frequency as shown in Fig. D.5 is possibly due to a limited amount of mesh-cells and number of pulses⁴ (see Table D.1).

D.4 Amount of q 's with maximum Q -factor per frequency

The distance between the mirrors D is optimized by choosing q such that the Q -factor is at maximum. This only works when the mirrors are positioned at the concentric distance [see Chapter 5, Fig. 5.3(a)].

⁴The simulation duration has to reach a steady state criterium and can be set by a number of pulses. The simulation duration is calculated by multiplying a given number with the Gaussian pulse width that is used as stimulation signal. The pulse width depends on the frequency range of the reference excitation signal.

Table D.2: q versus Q per frequency for the E -band (60 GHz to 90 GHz).

| # | Frequency-band (GHz) | f_0 (GHz) | λ (mm) | q @ f (GHz) | Q -factor |
|-------|-------------------------|----------------|-------------------|--------------------|-------------|
| 5.99 | 58 – 61 | 60.654 | 4.9412 | 33 @ 60 GHz | 92817 |
| 5.100 | 61 – 64 | 63.654 | 4.7083 | 36 @ 63 GHz | 103318 |
| 5.101 | 64 – 67 | 66.510 | 4.5061 | 38 @ 65 GHz | 110486 |
| 5.102 | 67 – 70 | 68.653 | 4.3654 | 40 @ 68 GHz | 106532 |
| 5.103 | 70 – 73 | 72.501 | 4.1338 | 42 @ 71 GHz | 93535 |
| 5.104 | 74 – 77 | 76.490 | 3.9182 | 45 @ 75 GHz | 82122 |
| 5.105 | 77 – 80 | 79.487 | 3.7705 | 47 @ 78 GHz | 73199 |
| 5.106 | 80 – 83 | 82.485 | 3.6334 | 49 @ 81 GHz | 65625 |
| 5.107 | 84 – 87 | 84.844 | 3.5324 | 52 @ 85 GHz | 60996 |
| 5.108 | 87 – 90 | 89.476 | 3.3495 | 54 @ 88 GHz | 51713 |

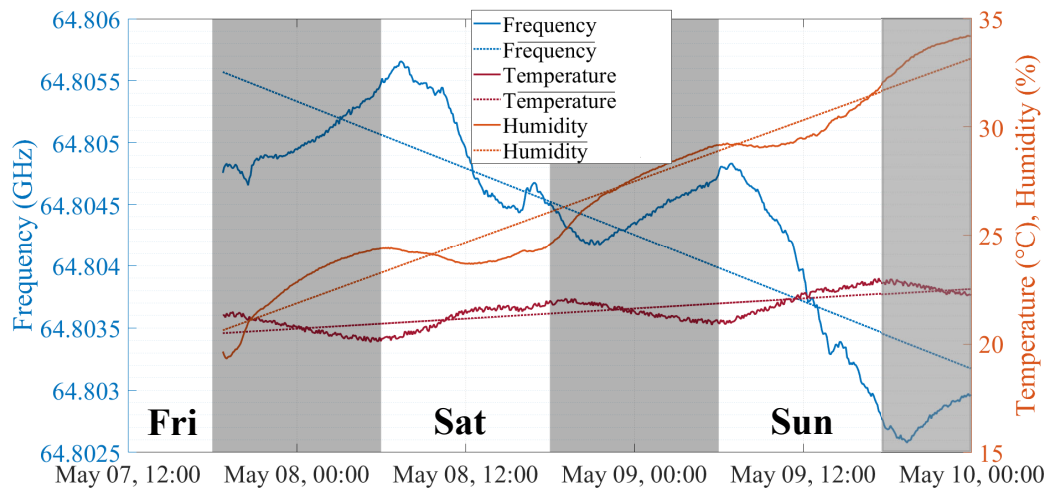
D.5 Measurement results of the temperature, humidity and resonance frequency

During two weekends and a midweek in the month May of 2021 the environmental conditions were recorded while the Fabry-Perot was measuring a resonance frequency, which is also recorded. The results of the frequency (GHz) blue solid line, temperature ($^{\circ}$ C) red solid line and humidity (%) orange solid line are shown in Fig. *D.6*. The data is sampled over 9 consecutive days, consisting of two weekends [see Fig. *D.6*(a) and Fig. *D.6*(c)] and one midweek [see Fig. *D.6*(b)]. The transparent black rectangles represent nighttime.

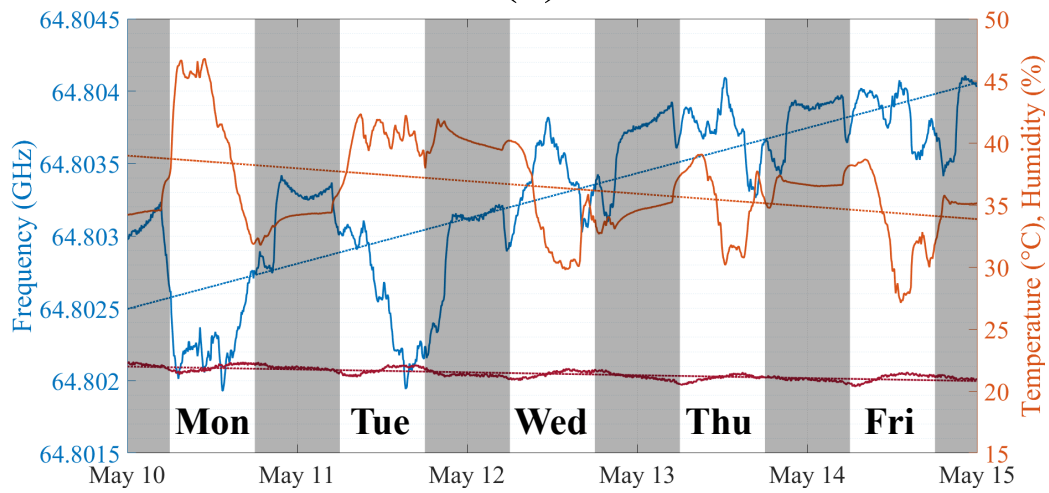
The first thing to notice is a significant difference in temperature, humidity and frequency drift between the weekends [see Fig *D.6*(a) and] Fig *D.6*(c)] and the mid-week [see Fig. *D.6*(b)]. This is caused by the fact that there is only human activity during the mid-week. Another cause is that during the weekends and the nights the climate control is turned off.

The second effect that can be observed from Fig. *D.6* is that if the average (dotted lines) of the temperature and humidity increase the average frequency decreases and vice versa.

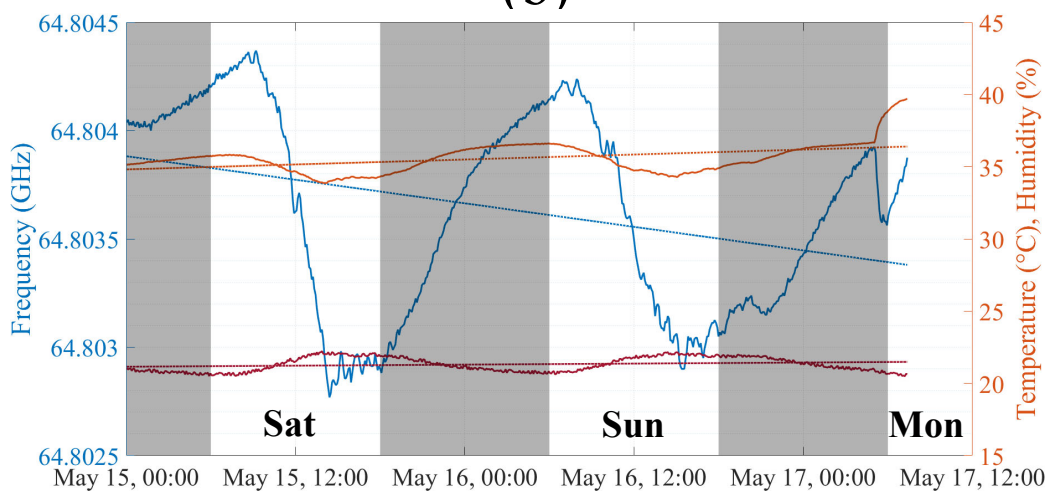
The third thing to notice is that when the temperature decreases the frequency increases where the peak in the data of the frequency corresponds with the dip in the data of the temperature and vice versa.



(a)



(b)



(c)

Figure D.6: Measurement results, obtained in May 2021, of the temperature (°C), humidity (%) and frequency drift (GHz), (a) from the first weekend, (b) midweeks, and (c) from the second weekend.

@Commentjabref-meta: databaseType:bibtex;

Bibliography

- [1] JCGM:100:2008. (2008) Jcgm 100: Evaluation of measurement data - guide to the expression of uncertainty in measurement. [Online]. Available: https://www.bipm.org/documents/20126/2071204/JCGM_100_2008_E.pdf/cb0ef43f-baa5-11cf-3f85-4dcd86f77bd6?msclkid=4e750d84ba6111eca8fc24805fd1e830
- [2] JCGM:2008. (2008) Jcgm 2008, international vocabulary of metrology - basic and general concepts and associated terms (vim). [Online]. Available: <https://www.bipm.org/en/publications/guides/vim.html>
- [3] D. Titz, F. Ferrero, and C. Luxey, "Development of a millimeter-wave measurement setup and dedicated techniques to characterize the matching and radiation performance of probe-fed antennas [measurements corner]," *IEEE Antennas and Propagation Magazine*, vol. 54, no. 4, pp. 188–203, Aug 2012.
- [4] L. Boehm, F. Boegelsack, M. Hitzler, S. Wiehler, and C. Waldschmidt, "Accuracy evaluation for antenna measurements at mm-wave frequencies," in *2016 10th European Conference on Antennas and Propagation (EuCAP)*, April 2016, pp. 1–5.
- [5] A. Reniers, Q. Liu, M. Rousstia, M. Herben, H. Visser, and A. B. Smolders, "Statistical analysis applied to simulating and measuring circularly-polarized millimeter-wave antennas [measurements corner]," *IEEE Antennas and Propagation Magazine*, vol. 61, no. 1, pp. 98–138, Feb 2019.
- [6] M. Ozawa, "Universally valid reformulation of the heisenberg uncertainty principle on noise and disturbance in measurement," *A Physical Review*, 2003.
- [7] "Ieee standard definitions of terms for antennas," *IEEE No 145-1973*, pp. 1–18, Aug 1973.
- [8] J. C. Maxwell, "On physical lines of force," *Philosophical Magazine*, vol. 90, pp. 11–23, Feb. 2010.
- [9] J. C. Maxwell, "A dynamical theory of the electromagnetic field," *Philosophical Transactions of the Royal Society of London*, vol. 155, pp. 459–513, 1865.
- [10] D. J. Cichon and W. Wiesbeck, "The heinrich hertz wireless experiments at karlsruhe in the view of modern communication," in *Proceedings of the 1995 International Conference on 100 Years of Radio*, Sep. 1995, pp. 1–6.
- [11] J. L. Gonzalez, F. Badets, B. Martineau, and D. Belot, "A 56-ghz lc-tank vco with 17% tuning range in 65-nm bulk cmos for wireless hdmi," *IEEE Transactions on Microwave Theory and Techniques*, vol. 58, no. 5, pp. 1359–1366, May 2010.

- [12] G. Pelosi, S. Selleri, and B. Valotti, "From poldhu to the italian station of coltano: Marconi and the first years of transcontinental wireless," *IEEE Antennas and Propagation Magazine*, vol. 46, no. 3, pp. 47–54, June 2004.
- [13] C. A. Balanis, "Antenna theory: a review," *Proceedings of the IEEE*, vol. 80, no. 1, pp. 7–23, Jan 1992.
- [14] G. A. T. Warren L. Stutzman, *Antenna Theory and Design, 3rd Edition*. John Wiley & Sons, 2012.
- [15] F. Braun. (1909) Nobel lecture: Electrical oscillations and wireless telegraphy. [Online]. Available: http://www.nobelprize.org/nobel_prizes/physics/laureates/1909/braun-lecture.html
- [16] R. Appleyard. (1927) Pioneers of electrical communication part 5 - heinrich rudolph hertz. [Online]. Available: <http://www.americanradiohistory.com/Archive-ITT/20s/ITT-Vol-06-1927-02.pdf>
- [17] S. Uda, *On the Wireless Beam of Short Electric Waves*, ser. Journal of the Institute of electrical engineers of Japan. Institute of electrical engineers of Japan, 1927. [Online]. Available: <https://books.google.nl/books?id=hbkmGwAACAAJ>
- [18] D. T. Emerson, "The work of jagadis chandra bose: 100 years of mm-wave research," in *1997 IEEE MTT-S International Microwave Symposium Digest*, vol. 2, June 1997, pp. 553–556 vol.2.
- [19] G. C. Southworth and A. P. King, "Metal horns as directive receivers of ultra-short waves," *Proceedings of the IRE*, vol. 27, no. 2, pp. 95–102, Feb 1939.
- [20] R. D. Richtmyer, "Dielectric resonators," *Journal of Applied Physics*, vol. 10, no. 6, pp. 391–398, 1939. [Online]. Available: <https://doi.org/10.1063/1.1707320>
- [21] R. King, C. Harrison, and D. Denton, "Transmission-line missile antennas," *IRE Transactions on Antennas and Propagation*, vol. 8, no. 1, pp. 88–90, January 1960.
- [22] G. Borgiotti and Q. Balzano, "Mutual coupling analysis of a conformal array of elements on a cylindrical surface," *IEEE Transactions on Antennas and Propagation*, vol. 18, no. 1, pp. 55–63, Jan 1970.
- [23] J. Howell, "Microstrip antennas," *IEEE Transactions on Antennas and Propagation*, vol. 23, no. 1, pp. 90–93, January 1975.
- [24] D. M. Pozar, S. D. Targonski, and H. D. Syrigos, "Design of millimeter wave microstrip reflectarrays," *IEEE Transactions on Antennas and Propagation*, vol. 45, no. 2, pp. 287–296, Feb 1997.
- [25] Y. P. Zhang and D. Liu, "Antenna-on-chip and antenna-in-package solutions to highly integrated millimeter-wave devices for wireless communications," *IEEE Transactions on Antennas and Propagation*, vol. 57, no. 10, pp. 2830–2841, Oct 2009.
- [26] U. Johannsen, A. B. Smolders, and A. C. F. Reniers, "Measurement package for mm-wave antennas-on-chip," in *2010 Conference Proceedings ICECom, 20th International Conference on Applied Electromagnetics and Communications*, Sept 2010, pp. 1–4.
- [27] M. D. Huang, M. H. A. J. Herben, and M. I. Kazim, "Design of cylindrically bent antenna array on lcp substrate with large coverage at 60 ghz," in *Proceedings of the 5th European Conference on Antennas and Propagation (EUCAP)*, April 2011, pp. 1117–1121.

- [28] M. I. Kazim, M. H. A. J. Herben, and A. B. Smolders, "Wide angular coverage deflector: 60-ghz three-dimensional passive electromagnetic deflector achieves wide angular coverage." *IEEE Antennas and Propagation Magazine*, vol. 58, no. 2, pp. 47–59, April 2016.
- [29] M. W. Rousstia, A. C. F. Reniers, and M. H. A. J. Herben, "Switched-beam array of dielectric rod antenna with rf-mems switch for millimeter-wave applications," *Radio Science*, vol. 50, no. 3, pp. 177–190, March 2015.
- [30] A. Al-Rawi, A. Dubok, S. J. Geluk, M. H. A. J. Herben, and A. B. Smolders, "A comparative study on the parabolic and spherical fpa-fed reflector antenna," in *2016 10th European Conference on Antennas and Propagation (EuCAP)*, April 2016, pp. 1–4.
- [31] S. UDA, "On the wireless beam of short electric waves. (i)," *The Journal of the Institute of Electrical Engineers of Japan*, vol. 46, no. 452, pp. 273–282, 1926.
- [32] H. H. Beverage and H. O. Peterson, "Radio transmission measurements on long wave lengths," *Proceedings of the Institute of Radio Engineers*, vol. 11, no. 6, pp. 661–673, Dec 1923.
- [33] R. Bown, C. R. Englund, and H. T. Friis, "Radio transmission measurements," *Proceedings of the Institute of Radio Engineers*, vol. 11, no. 2, pp. 115–152, April 1923.
- [34] E. H. Newman, "A brief history of early computational electromagnetics at the ohio state university electroscience laboratory," in *IEEE Antennas and Propagation Society International Symposium. Digest. Held in conjunction with: USNC/CNC/URSI North American Radio Sci. Meeting (Cat. No.03CH37450)*, vol. 4, June 2003, pp. 606–609 vol.4.
- [35] G. E. Evans, *Antenna measurement techniques*, 1990.
- [36] Rosenberger. (2017). [Online]. Available: <http://rosenberger.de/ok/index.php?caller=xlink&url=detail.php&oldcaller=searchcritax&itemID=943>
- [37] OIML. (2007) International vocabulary of metrology - basic and general concepts and associated terms (vim). [Online]. Available: <http://www.bipm.org/en/publications/guides/vim.html>
- [38] J. Turner. Beauty, form, and euclid's elements part 3. [Online]. Available: <https://thinkingbeautifully.org/beauty-form-and-euclids-elements-part-3/>
- [39] R. Ash, *A Primer of Abstract Algebra*, ser. Chandler & Sharp Publications in Political Science. Mathematical Association of America, 1998. [Online]. Available: <https://books.google.nl/books?id=3o5OypsFdFcC>
- [40] A. Ferrero, D. Petri, P. Carbone, and M. Catelani, *Modern Measurements: Fundamentals and Applications*. Wiley, 2015. [Online]. Available: <https://books.google.nl/books?id=Q6uBCgAAQBAJ>
- [41] J. Maxwell. (1871) Report of the fortieth meeting of the british association for the advancement of science. [Online]. Available: <https://www.biodiversitylibrary.org/item/93095#page/7/mode/1up>
- [42] L. Kelvin, *Electrical Units of Measurement, a Lecture Given on 3 May 1883, Published in the Book, Popular Lectures and Addresses, Volume 1,*, P. Lectures and Addresses, Eds., 1891.
- [43] A. Furuta, "One thing is certain: Heisenberg's uncertainty principle is not dead," *Scientific American*, 2012.
- [44] W. Heisenberg, *Physics and Philosophy: The Revolution in Modern Science*. Prometheus Books, 1958.

- [45] J. S. Bell and A. Aspect, *Speakable and Unsayable in Quantum Mechanics: Collected Papers on Quantum Philosophy*, 2nd ed. Cambridge University Press, 2004.
- [46] E. Schrödinger, “Die gegenwärtige situation in der quantenmechanik,” *Naturwissenschaften*, vol. 23, no. 50, pp. 844–849, Dec 1935. [Online]. Available: <https://doi.org/10.1007/BF01491987>
- [47] J. von Neumann and R. Beyer, *Mathematical Foundations of Quantum Mechanics*, ser. Goldstine Printed Materials. Princeton University Press, 1955. [Online]. Available: <https://books.google.nl/books?id=JLyCo3RO4qUC>
- [48] K. Neill. (2020) Quantum theory, perception, reality and consciousness. [Online]. Available: <https://theobservereffect.wordpress.com/schrodingers-cat/>
- [49] E. B. Goldstein, *Cognitive Psychology: Connecting Mind, Research and Everyday Experience*. Wadsworth Publishing, 2007.
- [50] Merriam-Webster Online, “Merriam-Webster Online Dictionary,” 2009. [Online]. Available: <http://www.merriam-webster.com>
- [51] A. Blake, G. Stapleton, P. Rodgers, L. Cheek, and J. Howse, “The impact of shape on the perception of euler diagrams,” in *Diagrammatic Representation and Inference*, T. Dwyer, H. Purchase, and A. Delaney, Eds. Berlin, Heidelberg: Springer Berlin Heidelberg, 2014, pp. 123–137.
- [52] G. Upton and I. Cook, *A Dictionary of Statistics*. [Online]. Available: <http://www.oxfordreference.com/view/10.1093/acref/9780199541454.001.0001/acref-9780199541454>
- [53] Y. Dodge, *The Oxford Dictionary of Statistical Terms*. Oxford University Press, 2006. [Online]. Available: https://books.google.nl/books?id=_OnjBgpWcC
- [54] H. Beyer, “Tukey, john w.: Exploratory data analysis. addison-wesley publishing company reading, mass. -menlo park, cal., london, amsterdam, don mills, ontario, sydney 1977, xvi, 688 s.” *Biometrical Journal*, vol. 23, no. 4, pp. 413–414, 1981. [Online]. Available: <https://onlinelibrary.wiley.com/doi/abs/10.1002/bimj.4710230408>
- [55] W. Kirch, Ed., *Level of MeasurementLevel of measurement*. Dordrecht: Springer Netherlands, 2008, pp. 851–852. [Online]. Available: https://doi.org/10.1007/978-1-4020-5614-7_1971
- [56] S. S. Stevens, “On the theory of scales of measurement,” *Science*, vol. 103, no. 2684, pp. 677–680, 1946. [Online]. Available: <http://science.sciencemag.org/content/103/2684/677>
- [57] —, *On the theory of scales of measurement*, 1946, vol. 103,.
- [58] F. Mosteller and J. Tukey, *Data Analysis and Regression: A Second Course in Statistics*, ser. Addison-Wesley series in behavioral science. Addison-Wesley Publishing Company, 1977. [Online]. Available: <https://books.google.nl/books?id=pGIHAAAAMAAJ>
- [59] N. R. Chrisman, “Rethinking levels of measurement for cartography,” *Cartography and Geographic Information Systems*, vol. 25, no. 4, pp. 231–242, 1998. [Online]. Available: <https://doi.org/10.1559/152304098782383043>
- [60] D. P. R. Rakesh Kumar, S. Richa, “Deciphering the dilemma of parametric and nonparametric tests,” *Journal of the Practice of Cardiovascular Sciences*, vol. 2, pp. 95–98, 2016.
- [61] J. Kenney, *Mathematics of Statistics*, ser. Mathematics of Statistics. Van Nostrand, 1946, no. v. 2. [Online]. Available: <https://books.google.nl/books?id=UdILAAAAMAAJ>

- [62] D. P. Kroese, T. Brereton, T. Taimre, and Z. I. Botev, “Why the monte carlo method is so important today,” *WIREs Computational Statistics*, vol. 6, no. 6, pp. 386–392, 2014. [Online]. Available: <https://onlinelibrary.wiley.com/doi/abs/10.1002/wics.1314>
- [63] B. S. M. Dobbert, “Uncertainty propagation for measurement with multiple output quantities,” *White paper*, 2014.
- [64] J. G. B. F.R.A.S., “Liv. on a class of definite integrals.-part ii,” *The London, Edinburgh, and Dublin Philosophical Magazine and Journal of Science*, vol. 42, no. 282, pp. 421–436, 1871. [Online]. Available: <https://doi.org/10.1080/14786447108640600>
- [65] L. C. Andrews, “Special functions of mathematics for engineers,” *Oxford Science Publications*, vol. 372, pp. 375–378, 1998.
- [66] H. Fischer, *A History of the Central Limit Theorem: From Classical to Modern Probability Theory*, ser. Sources and Studies in the History of Mathematics and Physical Sciences. Springer New York, 2010. [Online]. Available: <https://books.google.nl/books?id=v7kTwaffiPsC>
- [67] D. Freedman and P. Diaconis, “On the histogram as a density estimator:12 theory,” *Zeitschrift für Wahrscheinlichkeitstheorie und Verwandte Gebiete*, vol. 57, no. 4, pp. 453–476, Dec 1981. [Online]. Available: <https://doi.org/10.1007/BF01025868>
- [68] H. Pishro-Nik. (2020) Introduction to probability. [Online]. Available: https://www.probabilitycourse.com/chapter7/7_0_0_intro.php
- [69] Student, “The probable error of a mean,” *Biometrika*, vol. 6, no. 1, pp. 1–25, 1908. [Online]. Available: <http://www.jstor.org/stable/2331554>
- [70] R. Fisher, “Applications of “student’s” distribution,” *Metron*, vol. 5, pp. 90–104, 1925.
- [71] AS. (2022) Glossary of statistical terms. [Online]. Available: <http://www.animatedsoftware.com/statglos/sgdegree.htm>
- [72] K. Meier, J. Brudney, and J. Bohte, *Applied Statistics for Public and Nonprofit Administration*. Cengage Learning, 2011. [Online]. Available: <https://books.google.nl/books?id=1zwxtL0Axe4C>
- [73] J. Rice, *Mathematical Statistics and Data Analysis*, ser. Advanced series. Cengage Learning, 2006, no. p. 3. [Online]. Available: <https://books.google.nl/books?id=EKA-yeX2GVgC>
- [74] C. Dietrich, *Uncertainty, Calibration and Probability: The Statistics of Scientific and Industrial Measurement*, ser. A Halsted pressbook. Hilger, 1973. [Online]. Available: <https://books.google.nl/books?id=IokxAAAAIAAJ>
- [75] H. Akoglu, “User’s guide to correlation coefficients,” *Turkish Journal of Emergency Medicine*, vol. 18, pp. 91 – 93, 2018.
- [76] M. Disha. (2020) Correlation meaning types and its computation. [Online]. Available: <https://www.yourarticlelibrary.com/statistics-2/correlation-meaning-types-and-its-computation-statistics/92001>
- [77] S. L. R. Ellison. (2003) Traceability in chemical measurement. [Online]. Available: http://www.eurachem.org/images/stories/Guides/pdf/EC_Trace.2003.pdf
- [78] T. C. (ISO/REMCO). (2015) Reference materials contents of certificates, labels and accompanying documentation. [Online]. Available: <https://www.iso.org/standard/52468.html>
- [79] ISO. (2019) Iso guide 30:2015 reference materials – selected terms and definitions. [Online]. Available: <https://www.iso.org/standard/46209.html>

- [80] LNM. (2019) Definition of tolerance. [Online]. Available: <https://www.coursehero.com/file/p42mtiq3/Principle-of-Interchangeability-When-the-parts-that-are-manufactured-at-the/>
- [81] F. Scholz, "Tolerance stack analysis methods." *Information & Support Services*, 1995.
- [82] N. Johnson, S. Kotz, and N. Balakrishnan, *Continuous univariate distributions*, ser. Wiley series in probability and mathematical statistics: Applied probability and statistics. Wiley & Sons, 1995, no. v. 2. [Online]. Available: <https://books.google.nl/books?id=0QzvAAAAMAAJ>
- [83] V. J. R. Sapsford, *Data Collection and Analysis*, Sage, Ed., 2006.
- [84] Y. I. Alexandrov, "Uncertainty of measurement. twenty years afterwards," *Fresenius' Journal of Analytical Chemistry*, vol. 370, no. 6, pp. 690–693, Jul 2001. [Online]. Available: <https://doi.org/10.1007/s002160100882>
- [85] J. D. Stemwedel. (2014) Brief thoughts on uncertainty. [Online]. Available: <http://blogs.scientificamerican.com/doing-good-science/brief-thoughts-on-uncertainty/>
- [86] J. M. Hickey, M. G. Keane, D. A. Kenny, A. R. Cromie, H. A. Mulder, and R. F. Veerkamp, "Estimation of accuracy and bias in genetic evaluations with genetic groups using sampling1," *Journal of Animal Science*, vol. 86, no. 5, pp. 1047–1056, 2008. [Online]. Available: <http://dx.doi.org/10.2527/jas.2007-0653>
- [87] E. Prenesti and F. Gosmaro, "Trueness, precision and accuracy: a critical overview of the concepts as well as proposals for revision," *Accreditation and Quality Assurance*, vol. 20, no. 1, pp. 33–40, Feb 2015. [Online]. Available: <https://doi.org/10.1007/s00769-014-1093-0>
- [88] J. Csavina, J. A. Roberti, J. R. Taylor, and H. W. Loescher, "Traceable measurements and calibration: a primer on uncertainty analysis," *Ecosphere*, vol. 8, no. 2, pp. e01683–n/a, 2017, e01683. [Online]. Available: <http://dx.doi.org/10.1002/ecs2.1683>
- [89] A. Menditto, M. Patriarca, and B. Magnusson, "Understanding the meaning of accuracy, trueness and precision," *Accreditation and Quality Assurance*, vol. 12, no. 1, pp. 45–47, Jan 2007. [Online]. Available: <https://doi.org/10.1007/s00769-006-0191-z>
- [90] S. Kokoska, *Introductory Statistics (Preliminary Edition): A Problem-Solving Approach*. W. H. Freeman, 2008. [Online]. Available: <https://books.google.nl/books?id=LEIsZMd9YhgC>
- [91] E. W. Weisstein. (2019) Bessel's correction. [Online]. Available: <http://mathworld.wolfram.com/BesselsCorrection.html>
- [92] B. D. Hall, "Evaluating methods of calculating measurement uncertainty," *Metrologia*, vol. 45, no. 2, p. L5, 2008. [Online]. Available: <http://stacks.iop.org/0026-1394/45/i=2/a=N01>
- [93] R. Hogan. (2018) Type a and type b uncertainty evaluating uncertainty components. [Online]. Available: <https://www.isobudgets.com/type-a-and-type-b-uncertainty/>
- [94] B. Taylor and C. Kuyatt, "Guidelines for evaluating and expressing the uncertainty of nist measurement results," NIST, Tech. Rep., 1994.
- [95] L. Stant, P. Aaen, and N. Ridler, "Comparing methods for evaluating measurement uncertainty given in the jcgM evaluation of measurement data documents," *Measurement*, vol. 94, pp. 847 – 851, 2016. [Online]. Available: <http://www.sciencedirect.com/science/article/pii/S0263224116304766>
- [96] A. Gelman, J. B. Carlin, H. S. Stern, and D. B. Rubin, *Bayesian Data Analysis*, 2nd ed. Chapman and Hall/CRC, 2004.

- [97] BIPM. (2019) Supplement 1 to the “guide to the expression of uncertainty in measurement” - propagation of distributions using a monte carlo method. [Online]. Available: http://www.bipm.org/utis/common/documents/jcgm/JCGM_101_2008_E.pdf
- [98] ——. (2019) Supplement 2 to the “guide to the expression of uncertainty in measurement” - extension to any number of output quantities. [Online]. Available: http://www.bipm.org/utis/common/documents/jcgm/JCGM_102_2011_E.pdf
- [99] S. Kar and A. Ramalingam, “Is 30 the magic number? issues in sample size estimation,” *Natl. J. Commun. Med.*, vol. 4, pp. 175–179, 01 2013.
- [100] B. N. Taylor, C. E. Kuyatt, N. I. of Standards, and T. (U.S.), *Guidelines for evaluating and expressing the uncertainty of NIST measurement results*, 1994th ed. Gaithersburg, MD : U.S. Department of Commerce, Technology Administration, National Institute of Standards and Technology, 1994, “September 1994.”
- [101] A. Sinha, K. T. Flood, D. Kessel, S. Johnson, C. Hunt, H. Woolnough, F. P. Vidal, P.-F. Villard, R. Holbray, M. Crawshaw, A. Bulpitt, N. W. John, F. Bello, R. Phillips, and D. Gould, “The Role of Simulation in Medical Training and Assessment,” in *Radiological Society of North America - RSNA 2009*, Chicago, United States, Nov. 2009. [Online]. Available: <https://hal.archives-ouvertes.fr/hal-00509830>
- [102] R. G. Kouyoumjian and P. H. Pathak, “A uniform geometrical theory of diffraction for an edge in a perfectly conducting surface,” *Proceedings of the IEEE*, vol. 62, no. 11, pp. 1448–1461, Nov 1974.
- [103] D. Jordan, “The maxwellians by bruce j. hunt,” *Isis: A Journal of the History of Science*, vol. 84, pp. 595–596, 1993.
- [104] “Bakerian lecture. on relaxation methods: A mathematics for engineering science,” *Proceedings of the Royal Society of London A: Mathematical, Physical and Engineering Sciences*, vol. 184, no. 998, pp. 253–288, 1945. [Online]. Available: <http://rspa.royalsocietypublishing.org/content/184/998/253>
- [105] K. Yee, “Numerical solution of initial boundary value problems involving maxwell’s equations in isotropic media,” *IEEE Transactions on Antennas and Propagation*, vol. 14, no. 3, pp. 302–307, May 1966.
- [106] A. Winslow, L. L. Laboratory, and B. L. R. L. University of California, *Numerical calculation of static magnetic fields in an irregular triangle mesh*. University of California Lawrence Radiation Laboratory, 1964. [Online]. Available: <https://books.google.nl/books?id=hDHOKr7IqbIC>
- [107] R. H. Macneal, “An asymmetric finite difference network,” *Quarterly of Applied Mathematics*, vol. 11, no. 3, pp. 295–310, 1953. [Online]. Available: <http://www.jstor.org/stable/43634052>
- [108] M. L. Brown, “Comparison of alternative formulations of 3-dimensional magnetic-field and eddy-current problems at power frequencies,” *IEE Proceedings B - Electric Power Applications*, vol. 127, no. 5, pp. 331–332, September 1980.
- [109] NEC. (1975). [Online]. Available: <http://www.nec.com/en/global/solutions/software.html><http://www.nec.com/en/global/solutions/software.html>
- [110] Ansys. (1970). [Online]. Available: <http://www.ansys.com/products/electronics/ansys-hfss>
- [111] FEKO. (1991). [Online]. Available: <https://www.feko.info/>

- [112] CST. (2022) Electromagnetic field simulation software. [Online]. Available: <https://www.3ds.com/products-services/simulia/products/cst-studio-suite/>
- [113] J.-P. Berenger, "A perfectly matched layer for the absorption of electromagnetic waves," *Journal of Computational Physics*, vol. 114, no. 2, pp. 185–200, 1994. [Online]. Available: <https://www.sciencedirect.com/science/article/pii/S0021999184711594>
- [114] J. S. Carson, "Model verification and validation," in *Proceedings of the Winter Simulation Conference*, vol. 1, Dec 2002, pp. 52–58 vol.1.
- [115] R. Johnson and H. Jasik, *Antenna Engineering Handbook*, ser. McGraw-Hill handbook. McGraw-Hill, 1984. [Online]. Available: https://books.google.nl/books?id=_mxGAAAYAAJ
- [116] C. A. Magus. (2019). [Online]. Available: <https://www.cst.com/products/antennamagus>
- [117] A. C. F. Reniers, Q. Liu, M. H. A. J. Herben, and A. B. Smolders, "Review of the accuracy and precision of mm-wave antenna simulations and measurements," in *2016 10th European Conference on Antennas and Propagation (EuCAP)*, April 2016, pp. 1–5.
- [118] R. G. Sargent, "Verification and validation of simulation models," in *Proceedings of the 2011 Winter Simulation Conference (WSC)*, Dec 2011, pp. 183–198.
- [119] H. Yao, H. Kumar, T. Ei, N. Ashrafi, S. Ashrafi, D. L. MacFarlane, and R. Henderson, "Patch antenna array for the generation of millimeter-wave hermite 8211;gaussian beams," *IEEE Antennas and Wireless Propagation Letters*, vol. 15, pp. 1947–1950, 2016.
- [120] Y. Li and K. M. Luk, "Wideband perforated dense dielectric patch antenna array for millimeter-wave applications," *IEEE Transactions on Antennas and Propagation*, vol. 63, no. 8, pp. 3780–3786, Aug 2015.
- [121] A. Mavaddat, S. H. M. Armaki, and A. R. Erfanian, "Millimeter-wave energy harvesting using 4times4 microstrip patch antenna array," *IEEE Antennas and Wireless Propagation Letters*, vol. 14, pp. 515–518, 2015.
- [122] I. J. Bahl and P. Bhartia, *Microstrip antennas*. Dedham, Mass. : Artech House, 1980, includes index.
- [123] J. Mosig and F. Gardiol, "The near field of an open microstrip structure," in *1979 Antennas and Propagation Society International Symposium*, vol. 17, June 1979, pp. 379–382.
- [124] N. Alexopoulos, N. Uzunoglu, and I. Rana, "Radiation by microstrip patches," in *1979 Antennas and Propagation Society International Symposium*, vol. 17, Jun 1979, pp. 722–727.
- [125] P. Agrawal and M. Bailey, "An analysis technique for microstrip antennas," *IEEE Transactions on Antennas and Propagation*, vol. 25, no. 6, pp. 756–759, Nov 1977.
- [126] J. R. James and G. J. Wilson, "Microstrip antennas and arrays. part 1: Fundamental action and limitations," *Microwaves, Optics and Acoustics, IEE Journal on*, vol. 1, no. 5, pp. 165–174, September 1977.
- [127] Y. Lo, D. Solomon, and W. Richards, "Theory and experiment on microstrip antennas," *IEEE Transactions on Antennas and Propagation*, vol. 27, no. 2, pp. 137–145, Mar 1979.
- [128] W. F. Richards, Y. T. Lo, and D. D. Harrison, "Improved theory for microstrip antennas," *Electronics Letters*, vol. 15, no. 2, pp. 42–44, January 1979.
- [129] E. L. Carver, Keith R ; Coffey, "Theoretical investigation of the microstrip antenna." 1979.

- [130] M. Gangopadhyaya, P. Mukherjee, U. Sharma, B. Gupta, and S. Manna, "Design optimization of microstrip fed rectangular microstrip antenna using differential evolution algorithm," in *2015 IEEE 2nd International Conference on Recent Trends in Information Systems (ReTIS)*, July 2015, pp. 49–52.
- [131] R. Munson, "Conformal microstrip antennas and microstrip phased arrays," *IEEE Transactions on Antennas and Propagation*, vol. 22, no. 1, pp. 74–78, Jan 1974.
- [132] QPI. (1988) Quality products international. [Online]. Available: <http://www.qpigroup.com/support/documentatie>
- [133] M. Rousstia, "Gigabit wireless connector and multibeam antenna design and implementation using 60 ghz technology," 2015.
- [134] CST. (2018) Recommended hardware. [Online]. Available: <https://www.cst.com/products/csts2/hardwarerecommendation>
- [135] M. W. Rousstia and M. H. A. J. Herben, "60-ghz wideband branchline coupler and patch antenna with dielectric rod for full-duplex gigabit wireless communication," in *The 8th European Conference on Antennas and Propagation (EuCAP 2014)*, April 2014, pp. 201–205.
- [136] D. C. Thompson, O. Tantot, H. Jallageas, G. E. Ponchak, M. M. Tentzeris, and J. Papapolymerou, "Characterization of liquid crystal polymer (lcp) material and transmission lines on lcp substrates from 30 to 110 ghz," *IEEE Transactions on Microwave Theory and Techniques*, vol. 52, no. 4, pp. 1343–1352, April 2004.
- [137] A. Kazempour, M. Hudlicka, S. Yee, M. A. Salhi, D. Allal, T. Kleine-Ostmann, and T. Schrader, "Design and calibration of a compact quasi-optical system for material characterization in millimeter/submillimeter wave domain," *IEEE Transactions on Instrumentation and Measurement*, vol. 64, no. 6, pp. 1438–1445, June 2015.
- [138] K. A. Goldberg. (2022) Let's talk about good agreement. [Online]. Available: <https://goldberg.lbl.gov/publications1/good-agreement/>
- [139] M. W. Rousstia and M. H. A. J. Herben, "High performance 60-ghz dielectric rod antenna with dual circular polarization," in *2013 European Microwave Conference*, Oct 2013, pp. 1671–1674.
- [140] GGB. (2018) The originator of the picoprobe. [Online]. Available: <https://www.cascademicrotech.com/products/probes/rf-microwave/t-wave-probe/t-wave-probe>
- [141] T. Zwick, C. Baks, U. R. Pfeiffer, D. Liu, and B. P. Gaucher, "Probe based mmw antenna measurement setup," in *IEEE Antennas and Propagation Society Symposium, 2004.*, vol. 1, June 2004, pp. 747–750 Vol.1.
- [142] W. Simon, M. Werthen, and I. Wolff, "A novel coplanar transmission line to rectangular waveguide transition," in *1998 IEEE MTT-S International Microwave Symposium Digest (Cat. No.98CH36192)*, vol. 1, June 1998, pp. 257–260 vol.1.
- [143] W. Menzel and A. Klaassen, "On the transition from ridged waveguide to microstrip," in *1989 19th European Microwave Conference*, Sept 1989, pp. 1265–1269.
- [144] A. C. F. Reniers, A. R. van Dommele, A. B. Smolders, and M. H. A. J. Herben, "The influence of the probe connection on mm-wave antenna measurements," *IEEE Transactions on Antennas and Propagation*, vol. 63, no. 9, pp. 3819–3825, Sept 2015.

- [145] J. Huang, "Uniform geometrical theory of diffraction in the calculation of microstrip antenna radiation patterns," in *1982 Antennas and Propagation Society International Symposium*, vol. 20, May 1982, pp. 152–155.
- [146] J. V. Hughes and H. L. Armstrong, "The Dielectric Constant of Dry Air," *Journal of Applied Physics*, vol. 23, no. 5, pp. 501–504, May 1952.
- [147] S. P. Parker, *McGraw-Hill Dictionary of Scientific and Technical Terms (5th Ed.)*. USA: McGraw-Hill, Inc., 1994.
- [148] T. Maleszka and G. Jaworski, "Broadband stripline to microstrip transition with constant impedance field matching section for applications in multilayer planar technologies," in *18-th International Conference on Microwaves, Radar and Wireless Communications*, 2010, pp. 1–4.
- [149] N. Marcuvitz, *Waveguide Handbook*. GBR: Institution of Electrical Engineers, 1986.
- [150] GGB. (2018). [Online]. Available: <http://www.ggb.com/67a.html>
- [151] A. J. Van den Biggelaar, E. Galesloot, A. C. F. Reniers, A. B. Smolders, and U. Johannsen, "Verification of a contactless characterization method for millimeter-wave integrated antennas," *IEEE Transactions on Antennas and Propagation*, pp. 1–1, 2020.
- [152] E. Heidrich and W. Wiesbeck, "Features of advanced polarimetric rcs-antenna measurements," in *Digest on Antennas and Propagation Society International Symposium*, June 1989, pp. 1026–1029 vol.2.
- [153] B. Monsalve, S. Blanch, and J. Romeu, "Input impedance measurements of cell phone antennas using backscattering modulation," in *2012 6th European Conference on Antennas and Propagation (EUCAP)*, March 2012, pp. 1549–1551.
- [154] B. Monsalve, S. Blanch, and J. Romeu, "Multiport small integrated antenna impedance matrix measurement by backscattering modulation," *IEEE Transactions on Antennas and Propagation*, vol. 61, no. 4, pp. 2034–2042, April 2013.
- [155] A. J. van den Biggelaar, D. P. P. Daverveld, A. C. F. Reniers, U. Johannsen, and A. B. Smolders, "Assessment of a contactless characterization method for integrated antennas," in *2019 16th European Radar Conference (EuRAD)*, Oct 2019, pp. 381–384.
- [156] Keysight. (2021). [Online]. Available: <https://www.keysight.com/nl/en/home.html>
- [157] R. N. Clarke and C. B. Rosenberg, "Fabry-perot and open resonators at microwave and millimetre wave frequencies, 2-300 GHz," *Journal of Physics E: Scientific Instruments*, vol. 15, no. 1, pp. 9–24, Jan 1982. [Online]. Available: <https://doi.org/10.1088%2F0022-3735%2F15%2F1%2F002>
- [158] M. D. Huang, M. H. A. J. Herben, A. C. F. Reniers, and P. F. M. Smulders, "Causes of discrepancies between measurements and em simulations of millimeter-wave antennas [measurements corner]," *IEEE Antennas and Propagation Magazine*, vol. 55, no. 6, pp. 139–149, Dec 2013.
- [159] O. Huber, T. Faseth, G. Magerl, and H. Arthaber, "Dielectric characterization of rf-printed circuit board materials by microstrip transmission lines and conductor-backed coplanar waveguides up to 110 ghz," *IEEE Transactions on Microwave Theory and Techniques*, vol. 66, no. 1, pp. 237–244, Jan 2018.
- [160] J. Barowski and I. Rolfes, "Millimeter wave material characterization using fmcw-transceivers," in *2017 IEEE MTT-S International Microwave Workshop Series on Advanced Materials and Processes for RF and THz Applications (IMWS-AMP)*, Sept 2017, pp. 1–3.

- [161] J. Degenford and P. Coleman, "A quasi-optics perturbation technique for measuring dielectric constants," *Proceedings of the IEEE*, vol. 54, no. 4, pp. 520–522, 1966.
- [162] I. Wolff and N. Knoppik, "Microstrip ring resonator and dispersion measurement on microstrip lines," *Electronics Letters*, vol. 7, pp. 779–781, 1971.
- [163] T. Karpisz, B. Salski, P. Kopyt, and J. Krupka, "Measurement of dielectrics from 20 to 50 ghz with a fabry-perot open resonator," *IEEE Transactions on Microwave Theory and Techniques*, vol. 67, no. 5, pp. 1901–1908, 2019.
- [164] H. Wheeler, "Transmission-line properties of parallel strips separated by a dielectric sheet," *IEEE Transactions on Microwave Theory and Techniques*, vol. 13, no. 2, pp. 172–185, 1965.
- [165] O. Rybin and T. Abbas, "Broadband microwave measurements of relative permittivity and permeability of materials," 11 2021.
- [166] V. Degli-Esposti, M. Zoli, E. M. Vitucci, F. Fuschini, M. Barbiroli, and J. Chen, "A method for the electromagnetic characterization of construction materials based on fabry-perot resonance," *IEEE Access*, vol. 5, pp. 24 938–24 943, 2017.
- [167] G. Federico, A. Reniers, A. Roc'h, L. Bronckers, and H. Visser, "Complex permittivity measurements with a low cost parabolic resonant cavity," in *The Loughborough Antennas Propagation Conference (LAPC 2018)*, 2018, pp. 1–6.
- [168] E. I. Green, "The story of q," *American Scientist*, vol. 43, no. 4, pp. 584–594, 1955. [Online]. Available: <http://www.jstor.org/stable/27826701>
- [169] R. P. encyclopedia. (2021). [Online]. Available: https://www.rp-photonics.com/q_factor.html
- [170] W. Culshaw, "Resonators for millimeter and submillimeter wavelengths," *IRE Transactions on Microwave Theory and Techniques*, vol. 9, no. 2, pp. 135–144, 1961.
- [171] A. Siegman, *Lasers*. University Science Books, 1986. [Online]. Available: <https://books.google.nl/books?id=1BZVwUZLTkAC>
- [172] H. Kogelnik and T. Li, "Laser beams and resonators," *Proceedings of the IEEE*, vol. 54, no. 10, pp. 1312–1329, 1966.
- [173] *Stable Resonators*. New York, NY: Springer New York, 2005, pp. 219–279. [Online]. Available: https://doi.org/10.1007/0-387-25110-3_6
- [174] R. N. Clarke and C. B. Rosenberg, "Fabry-perot and open resonators at microwave and millimetre wave frequencies, 2-300 GHz," *Journal of Physics E: Scientific Instruments*, vol. 15, no. 1, pp. 9–24, jan 1982. [Online]. Available: <https://doi.org/10.1088/0022-3735/15/1/002>
- [175] "Translated journals," *IEEE Spectrum*, vol. 5, no. 3, pp. 120–122, 1968.
- [176] R. Cook and R. Jones, "Precise dielectric measurement techniques for the frequency range 10 ghz to 150 ghz," in *1978 8th European Microwave Conference*, 1978, pp. 528–532.
- [177] G. X. Shu, Y. Luo, Q. S. Zhang, J. Su, L. Wang, Y. Xu, and S. F. Wang, "Millimeter wave measurement of the low-loss dielectric in vacuum electronic devices with reflection type hemispherical open resonator," *Journal of Infrared, Millimeter, and Terahertz Waves*, vol. 36, no. 6, pp. 556–568, Jun 2015. [Online]. Available: <https://doi.org/10.1007/s10762-015-0160-x>
- [178] T. M. Hirvonen, P. Vainikainen, A. Lozowski, and A. V. Raisanen, "Measurement of dielectrics at 100 ghz with an open resonator connected to a network analyzer," *IEEE Transactions on Instrumentation and Measurement*, vol. 45, no. 4, pp. 780–786, 1996.

- [179] ———, “Measurement of dielectrics at 100 ghz with an open resonator connected to a network analyzer,” *IEEE Transactions on Instrumentation and Measurement*, vol. 45, no. 4, pp. 780–786, 1996.
- [180] W. Quan and M. N. Afsar, “Ultra high-q 60ghz open resonator system for precision dielectric permittivity and loss tangent measurements,” in *2018 IEEE International Instrumentation and Measurement Technology Conference (I2MTC)*, 2018, pp. 1–5.
- [181] A. L. Cullen and P. K. Yu, “The accurate measurement of permittivity by means of an open resonator,” *Proceedings of the Royal Society of London. Series A, Mathematical and Physical Sciences*, vol. 325, no. 1563, pp. 493–509, 1971. [Online]. Available: <http://www.jstor.org/stable/77945>
- [182] G. X. Shu, Y. Luo, Q. S. Zhang, J. Su, L. Wang, Y. Xu, and S. F. Wang, “Millimeter wave measurement of the low-loss dielectric in vacuum electronic devices with reflection type hemispherical open resonator,” *Journal of Infrared, Millimeter, and Terahertz Waves*, vol. 36, no. 6, pp. 556–568, Apr 2015. [Online]. Available: <http://dx.doi.org/10.1007/s10762-015-0160-x>
- [183] PI. [Online]. Available: <https://www.physikinstrumente.com/en/products/>
- [184] (2018). [Online]. Available: <https://www.rohacell.com/product/rohacell/en>
- [185] MathWorks. (2018) Matlab and statistics toolbox. [Online]. Available: <https://nl.mathworks.com/products/matlab.html>
- [186] L. G. Hector and H. L. Schultz, “The dielectric constant of air at radiofrequencies,” *Physics*, vol. 7, pp. 133–136, 1936.
- [187] L. Essen and K. D. Froome, “The refractive indices and dielectric constants of air and its principal constituents at 24,000 mc/s,” *Proceedings of the Physical Society. Section B*, vol. 64, no. 10, pp. 862–875, oct 1951. [Online]. Available: <https://doi.org/10.1088/0370-1301/64/10/303>
- [188] VDI. (2020). [Online]. Available: <https://www.vadiodes.com/en/products/vector-network-analyzer-extension-modules>
- [189] Rohde-schwarz. [Online]. Available: https://www.rohde-schwarz.com/ae/about/news-press/details/press-room/press-releases-detailpages/rohde-schwarz-presents-the-first-moveable-over-the-air-test-chamber-for-5g-antennas-and-transceivers-press-releases_detailpage_229356-529001.html?rusprivacypolicy=1
- [190] A. Bianconi, “Ugo fano and shape resonances,” *X-ray and inner-shell processes*, vol. 652, pp. 13–18, 2003.
- [191] N. Pompeo, K. Torokhtii, F. Leccese, A. Scorza, S. Sciuto, and E. Silva, “Fitting strategy of resonance curves from microwave resonators with non-idealities,” in *2017 IEEE International Instrumentation and Measurement Technology Conference (I2MTC)*, 2017, pp. 1–6.
- [192] G. P. Watkins, “Knight’s risk, uncertainty and profit,” *The Quarterly Journal of Economics*, vol. 36, no. 4, pp. 682–690, 1922. [Online]. Available: <http://www.jstor.org/stable/1884757>
- [193] J. F. Hair, R. L. Tatham, R. E. Anderson, and W. Black, *Multivariate Data Analysis (5th Edition)*, 5th ed. Prentice Hall, March 1998. [Online]. Available: <http://www.amazon.ca/exec/obidos/redirect?tag=citeulike09-20&path=ASIN/0138948585>
- [194] G. E. P. Box and D. R. Cox, “An analysis of transformations,” *Journal of the Royal Statistical Society. Series B (Methodological)*, vol. 26, no. 2, pp. 211–252, 1964. [Online]. Available: <http://www.jstor.org/stable/2984418>

- [195] J. W. Tukey, *Exploratory data analysis*, M. . A.-W. P. C. Reading, Ed., 1977.
- [196] M. Rosenblatt, “Remarks on some nonparametric estimates of a density function,” no. 3, 1956.
- [197] E. Parzen, “On estimation of a probability density function and mode,” *The Annals of Mathematical Statistics*, vol. 33, no. 3, pp. 1065–1076, 1962. [Online]. Available: <http://www.jstor.org/stable/2237880>
- [198] R. Garg, P. Bhartia, I. Bahl, and A. Ittipiboon, *Microstrip Antenna Design Handbook*. Artech House, 2001.
- [199] G. M. D. Orban. (2018) Basics of patch antennas. [Online]. Available: <http://orbanmicrowave.com/wp-content/uploads/2014/12/Orban-Patch-Antennas-2009-rev.pdf>
- [200] M. A. Matin and A. I. Sayeed, “A design rule for inset-fed rectangular microstrip patch antenna,” *WTOC*, vol. 9, no. 1, pp. 63–72, Jan. 2010.
- [201] “Ieee standard test procedures for antennas,” *ANSI/IEEE Std 149-1979*, pp. 01–, 1979.
- [202] W. H. R. A. Marino, “Computation and measurement of the polarization ellipse,” 1999.
- [203] J. Kraus, *Antennas*, 1950.
- [204] R. Garg, *Microstrip antennas design handbook*. Boston, Mass. ; London : Artech House, 2001, includes bibliographical references and index.
- [205] R. Geyer, “Dielectric characterization and reference materials,” 2017.
- [206] ———, “Dielectric characterization and reference materials,” 1990-04-01 1990.
- [207] T. Zwick, A. Chandrasekhar, C. W. Baks, U. R. Pfeiffer, S. Brebels, and B. P. Gaucher, “Determination of the complex permittivity of packaging materials at millimeter-wave frequencies,” *IEEE Transactions on Microwave Theory and Techniques*, vol. 54, no. 3, pp. 1001–1010, 2006.
- [208] S. Khanal, T. Kiuru, J. Mallat, O. Luukkonen, and A. Räisänen, “Measurement of dielectric properties at 75-325 ghz using a vector network analyzer and full wave simulator,” *Radioengineering*, vol. 21, no. 2, pp. 551–556, 2012.
- [209] P. Piksa, S. Zvanovec, P. Cerny, and M. Mazanek, “Full-wave modeling of fabry-perot resonator in millimeter waves,” in *2008 14th Conference on Microwave Techniques*, 2008, pp. 1–4.
- [210] CST. (1991). [Online]. Available: <https://www.cst.com/products/cstmws>.

List of publications

Journal publications

- [J1] Reniers, A.C.F., Dommele, van, A.R., Smolders, A.B. & Herben, M.H.A.J., “The influence of the probe connection on mm wave antenna measurements,” *IEEE Transactions on Antennas and Propagation*, vol. 63, no. 9, pp. 3819-3825, sept. 2015.
- [J2] Reniers, A., Liu, Q., Rousstia, M., Herben, M., Visser, H. & Smolders, A. B., “Statistical analysis applied to simulating and measuring circularly-polarized millimeter wave antennas,” *IEEE Antennas and Propagation Magazine*, 61, 1, p. 98-138, Feb 2019.
- [J3] Reniers, A. C. F., Johannsen, U. & Smolders, A. B., 6 Mar 2020, “Antenna in Package Technology and Applications: Antenna in Package Measurements.” Liu, D. & Zhang, Y. (eds.). Wiley, p. 115-145 31 p.
- [J4] Rousstia, M.W., Reniers, A.C.F. & Herben, M.H.A.J., “Switched-beam array of dielectric rod antenna with RF-MEMS switch for millimeter wave applications,” *Radio Science*, vol. 50, no. 3, pp. 177 -190, march. 2015.
- [J5] Huang, M.D., Herben, M.H.A.J., Reniers, A.C.F. & Smulders, P.F.M., ”Causes of discrepancies between measurements and EM-simulations of millimeter-wave antennas,” *IEEE Antennas and Propagation Magazine*, vol. 55, no. 5, pp. 139-149, may. 2013.
- [J6] Deckmyn, T., Agneessens, S., Reniers, A.C.F., Smolders, A.B., Cauwe, M., Vande Ginste, D. & Rogier, H., ”A novel 60 GHz wideband coupled half-mode/quarter-mode substrate integrated waveguide antenna,” *IEEE Transactions on Antennas and Propagation*, vol. 65, no. 12, pp. 6915-6926, dec. 2017.

Conference publications

- [C1] A. C. F. Reniers; Q. Liu; M. H. A. J. Herben; A. B. Smolders, “Review of the accuracy and precision of mm-wave antenna simulations and measurements,” *10th European Conference on Antennas and Propagation (EuCAP), 2016*, 2016, pp. 1-5.
- [C2] Reniers, A. C. F., Dommele, van, A. R., Huang, M. D. & Herben, M. H. A. J., “Disturbing effects of microwave probe on mm-wave antenna pattern measurements,” *Proceedings of the 8th European Conference on Antennas and Propagation (EuCAP 2014)*, 6-11 April 2014, The Hague, The Netherlands. Piscataway: Institute of Electrical and Electronics Engineers, p. 161-164.
- [C3] Reniers, A. C. F., Dommele, van, A. R., Huang, M. D. & Herben, M. H. A. J., “Analyzing the disturbing effects of microwave probe on mm-wave antenna pattern measurements,” *COST IC1004 Cooperative Radio Communications for Green Smart Environments 9th MC & Scientific Meeting*, 5-7 February 2014, Ferrara, Italy.
- [C4] Reniers, A. C. F., van Dommele, A. R. & Herben, M. H. A. J., “Antenna measurement techniques : measurement hardware-induced pattern distortions,” *Cooperative radio communications for green smart environments*. Cardona, N. (ed.). Delft: River Publishers, p. 416-418
- [C5] Rousstia, M. W., Reniers, A. C. F. & Herben, M. H. A. J., “An 11-GHz multi-beam dielectric rod antenna using non-planar array approach,” *Proceedings of the 8th European Conference on Antennas and Propagation (EuCAP)*, 6-11 April 2014, The Hague, The Netherlands. Piscataway: Institute of Electrical and Electronics Engineers, p. 1697-1701.
- [C6] Liu, Q., Reniers, A., Johannsen, U., van Beurden, M. C. & Smolders, A. B., “Improved probing reliability in antenna-on-chip measurement,” *IEEE Antennas and Wireless Propagation Letters*. 17, 9, p. 1745-1749, Sep 2018.
- [C7] van den Biggelaar, A. J., Daverveld, D. P. P., Reniers, A. C. F., Johannsen, U. & Smolders, A. B., “Assessment of a contactless characterization method for integrated antennas,” *49th European Microwave Conference, EuMC 2019*. Piscataway: Institute of Electrical and Electronics Engineers, p. 1016-1019, Oct 2019.
- [C8] Federico, G., Reniers, A. C. F., Roc’h, A., Bronckers, L. A. & Visser, H. J., “Complex permittivity measurements with a low cost parabolic resonant cavity,” *Proceedings of the 14th Loughborough Antennas and Propagation Conference (LAPC)*. Institution of Engineering and Technology (IET), Feb 2019.

-
- [C9] de Nooij, J. N. D., Kleijer, M. & Reniers, A. C. F., “Modified Coupling Aperture to Optimize the Power Transfer in a Fabry-Pérot Open-Cavity Resonator,” 24 Mar 2022, (Accepted/In press).

Presentations

- [p1] Ad C.F. Reniers (Participant), Tom van Nunen (Participant) & Hubregt J. Visser (Organiser), Wireless Power Week 2019, 17 Jun 2019.
- [p2] Ad Reniers (Contributor) & A.B. Smolders (Contributor), 12th European Conference on Antennas and Propagation (EuCAP 2018), 2018.
- [p3] Ad Reniers (Contributor), A.B. Smolders (Chair) & U. Johannsen (Contributor), 12th European Microwave Integrated Circuits Conference (EuMIC 2017), 9 Oct 2017.
- [p4] Ad Reniers (Speaker), conference; 2009 CST European User Group Meeting, March 16-18, 2009, Darmstadt, Germany, 10 Apr 2010.

Acknowledgements

In recent years, I have had the opportunity to meet many special people who have contributed in one way or another to the completion of my research that is described in this thesis. I would like to thank them individually as much as possible.

I want to start with my first promotor, Bart Smolders. I am grateful for the opportunities you have given me to work on PhD research alongside my work for the EM group. In addition, you facilitated that I was allowed to invest in measurement systems with which I was able to validate my hypothesis with measurements. Furthermore, I want to thank you for the review comments and your support for not giving up. Your comment: “There is life after your Ph.D.” in other words, round it off because after your PhD you can still do enough research, I will not forget. I would like to thank my second promotor, Mark Bentum, for reviewing my thesis and providing valuable feedback. I also want to thank you for the sincere conversations we’ve had about education, where I fully share your vision. I am grateful for the many years of collaboration with my co-promotor, Matti Herben. I have learned a lot from you regarding research, supervising students and teaching. Your critical view and comments about my research at the time laid the foundation for my Ph.D. research. Thanks also for the many social conversations we have had, there is more to life than just work. I would also like to thank Martijn van Beurden for thoroughly reviewing my thesis. This certainly helped to take the content of my thesis to a higher level. I would also like to thank you for the various discussions that have helped me to formulate some research topics more sharply. Many thanks to Rob Maaskant for reviewing my thesis and discussing my research topic in detail. This definitely prepared me for my defense. Furthermore, I would like to thank you for the many discussions that we have had in the office over the past years on various research topics that have given me new research ideas. Many thanks to Peter Baltus and Guus Pemen for your time and effort to review and assess my thesis and for your sincere compliments. I would also like to thank Huib Visser for your time spent reviewing the first part of my thesis. Your comments have helped to take the writing of my research work to the a higher level. I would also like to thank you for the many years that we have worked together on various research projects at both TNO and TU/e.

Specifically, I would like to thank the following people, starting with Anouk Hubrechen. I think we've been working together on various research projects for about seven years. Your curiosity and enthusiasm are contagious and has given me inspiration for my current research. I would like to thank you for the collaboration and the many conversations about science, among other things and hope we can do this for years to come. Thank you also for being a paronymph during my defense. I would also like to thank Elles Raaijmakers for the many conversations about all kinds of things including statistics. Your creativity has helped me to visualize some science topics in my thesis. Thank you also for your contribution to the presentations for my defense. Thank you Marjolijn Kleijer for being my sparring partner in the development of the Fabry-Pérot open-cavity resonator. With your decisiveness and the many hours you have spent on implementing the algorithm, we now have a working system whose measurement data has been used for my research. Paola Escobari, you have done a lot of measurements and the outcome of those measurements provided me with progressive insight that will form the basis for further research. Julie de Nooij, thank you for your help in performing numerous measurements to characterize the Fabry-Pérot open-cavity resonator. It's great to see how enthusiastically you are working on this research topic, which has led to new ideas to improve the measurement system. Thank you Gabriele Federico for the discussions we had about material characterization. Looking forward to do some research together in the future. Thank you also for being a paronymph during my defense. I would like to thank Teun van den Biggelaar for the various discussions we have had about new techniques measuring antennas accurately, and for collaborating on some scientific papers on the subject. I would also like to thank Sander Bronckers for the ideas and suggestions regarding doing research in the field of materials characterization and metrology in general.

Next, I would like to thank my colleagues and students in the EM group for their collegiality and support. Thank you Bas de Hon for the discussion and explanation on specific topics of computational electromagnetics which is not my area of expertise. Thank you Suzanne Kuijlaars for administrative support and your personal interest in my well-being. Rainier van Dommele, thanks for providing the various measuring instruments needed to be able to obtain measurement results for my research.

I would also like to thank the indoor soccer team (waht was the name again? Something with Maxwell) which includes Ali Al-Rawi, Radovan Bojanic, Shady Keyrouz and several others already mentioned in the preceding paragraphs. With you I have spent many hours to de-stress from daily work.

I would have loved to skip this paragraph, but unfortunately I cannot ignore the event that changed my life, made me the person I am today and influenced the outcome of my research and this thesis. The event that happened on August 16, 2019, the day my oldest son Owen died in a tragic accident. I would therefore like to mention the

following people who have a major influence on my life and helped me in one way or another to get my life back on track, to cope with this terrible loss and to put a little smile on my face again. It was partly because of them that I was able to complete my research. Therefore, besides my family, the following people have a special place in my heart.

First of all, Peter and Marianne Engels, thank you for the sincere comfort you have offered me, for your attention, the many conversations, the dinners and the walks. I would also like to thank Stef, Caroline and Victor Snels for the meals, comforting conversations and the pleasant company. Stef, how cool and emotional it was to cycle through half of Germany together. I am already looking forward to the tour of tours, through the Alps. I would also like to thank Henrico, Ilse, Rhiannon, Daphne and Liz Stacie for your care and attention, for the emotional conversations, your advice and suggestions. I want you all to know that they helped me make decisions that contributed to my partial recovery (kintsukuroi). Tsjimkje, Harm, Linda, Thijn and Wes Kohne thank you for the company, comfort, attention, apps, the beautiful drawings, advice and suggestions. Attila, Ellen and Levi thank you for the attention and hospitality. Dunstan, Hanneke and kids Midlane and Martin, Anouk and kids for your sincere attention, conversations and drawings. There are many more, too many to mention, who have shown interest and shared my grief with me. I want you all to know that this has helped me to find myself, to cope with grief and life as it is now, and indirectly to complete my research with a little smile and due pride.

Mom and Dad, I am so grateful for your love and care. It made me the person I am today, being able to complete this research and the writing of this thesis. Thank you Isabel for the years we spent together raising our two sons, where both contributed to the content of my research, which I am proud of.

Dear Noah, I couldn't be more proud of what you've accomplished despite the sad things you've been through. I am glad that we have been able to work together in recent years and that we share the love for technology. Your contribution to the development of the software for the anechoic chamber has ensured that we can continue to do research on this subject for years to come. I hope we can enjoy each other's company in the different aspects of life for many years to come.

Dear Owen, you have been my son for 22 years. In this far too short time that you have lived you have achieved so much and touched so many people. I am grateful for the time we had together. Grateful for the short collaboration in which your graduation work has laid the foundation for part of my research, which has been recorded in chapter five. Although I miss you terribly, I am convinced that we will see each other again, one hundred percent sure!

Curriculum Vitae

Adrianus, Cornelis, Franciscus Reniers was born on september 30, 1968 in Eindhoven, the Netherlands. He has a bachelor's degree in electrical engineering and followed various master courses. In 2016 he started as a parttime Ph.D.-student in addition to his work on research and education for the electromagnetics group of the faculty of Electrical Engineering of Eindhoven University of Technology (TU/e). From 1999 to 2009 he worked at TNO Industry and Technology on various engineering and research projects related to antenna design and measurements in both the commercial and medical domain. Since 2009 he is affiliated with the EM-group of the Department of Electrical Engineering of the TU/e where he has focused on millimeter wave antenna design and measurements with a key focus on metrology.

